Qubit and Cavity Measurement in Circuit Quantum Electrodynamics

Dissertation

zur Erlangung des Grades

des Doktors der Naturwissenschaften

der Naturwissenschaftlich - Technischen Fakultät II

- Physik und Mechatronik -

der Universität des Saarlandes

von

Luke C. G. Govia

Saarbrücken

2015

Tag des Kolloquiums:	21.09.2015
Dekan:	Univ.-Prof. Dr. Georg Frey
Mitglieder des Prüfungsausschusses:	Prof. Dr. Christoph Becher Prof. Dr. Frank Wilhelm-Mauch Prof. Dr. Giovanna Morigi Dr. Reza Shaebani

To my parents.

Contents

List of Figures

Acknowledgements

First and foremost I would like to thank my supervisor Professor Frank Wilhelm-Mauch. He has been a constant source of inspiration for me, both on a professional and personal level. His excellent managerial skills have made him a pleasure to work for, and I think that no amount of time would ever be sufficient for him to teach me all he knows about physics. He has fostered an amazing culture in his group, one of a dedication to excellence and integrity, and I am proud to have been part of it.

I would like to thank and acknowledge Professor Giovanna Morigi for being the second examiner of my thesis. In addition, my time at Saarland University has been enlightened by the excellent discussions I have had with her and members of her group.

I have worked with many great post doctoral researchers during my PhD, and I would like to briefly mention them. Working with Dr. Emily Pritchett has been a very productive and rewarding experience for which I am eternally thankful. She taught me how to solve master equations numerically, the importance of which goes without saying. Dr. Bruno Taketani has listened to my (sometimes crazy) ideas without hesitation, and helped turn them into something useful. Obrigado. My thanks go to Dr. Markku Stenberg for our always interesting discussions on physics, running, and life. Though our time together has been short, I would also like to thank Dr. Felix Motzoi and Dr. Elie Assemat for the engaging discussions we have had.

It has been my pleasure to collaborate with several excellent research groups on the project for qubit readout with a JPM. My stay in Wisconsin was very productive in a large part due to Professors Robert McDermott and Maxim Vavilov, who made ample time from their busy schedules to meet with me. I would also like to thank their students Guilhem Ribeill and Canran Xu, as well as postdoc Dr. Ted Thorbeck for working with me and helping me understand the experiments. Also, I would like to thank Professor Britton Plourde for his help, and the discussions we had while he was on sabbatical in Saarbrücken.

I was not alone in my time at Saarland University. I have had the privilege

of knowing my fellow PhD students, and friends, Dr. Daniel Egger, Pierre-Luc Dallaire-Demers, and Per Liebermann. We have had too many good times to ever list, but thank you for being a big part of the best memories of my time in Saarbrücken. Also, I am very grateful for Per and Daniel's help with German throughout the years.

I have also had the pleasure of working with many Bachelor and Master students while at Saarland University. Marius Schöndorf, Michael Kaicher, Peter Schuhmacher, Zoë Ashwood, Maximilian Riem, and Johannes Görlitz, I am a better physicist because of my time spent working with you.

Monika Francois is amazing. She makes complicated university bureaucracy simple and transparent, even for those of us who cannot understand what the regulations are saying. She has made my life so much easier than it could have been, and for that I am eternally grateful.

None of this would have been possible without my parents, Nicholas and Cathy. Thank you for always believing in me, and fostering in me the courage to chase my dreams. Your support has never wavered, no matter our separation in time and space. Thanks also to my sister, Leah, and my brother, Zach, for their friendship, and for helping me laugh and remember to enjoy life. You two make me less serious, which is undoubtedly a daunting task.

I have met many people in Saarbrücken who have made my time here an enjoyable one, and thanks especially go to Jan and the rest of HTC Neunkirchen for the great times we have had together. To my oldest and dearest friend, Etienne, thank you for always being there for me, and your timely words of support and wisdom.

I will never be able to thank Mina Bionta enough for her constant support, understanding, and love, but I will continue to try. You accept me for who I am, and I am lucky to have you in my life.

Finally, to all those I have mentioned here, and to everyone else who has influenced me over the years, thank you. I owe all that I am to you.

Abstract

Quantum information and computing are rapidly evolving fields that explore and make use of the fundamental quantum mechanical aspects of nature. Applications of these fields are far reaching, and touch the fields of computer science, chemistry and biology. Integral to much of quantum information is the ability to measure a quantum system, and this thesis focuses on novel quantum measurement techniques in superconducting integrated circuits, a leading physical architecture for quantum information. A scalable protocol to read out the state of a superconducting qubit via a coupled microwave cavity and a photon counter is presented. Inspired by this protocol, a protocol is developed for readout of a binary multi-qubit operator, the qubit parity, that overcomes the fundamental limits of previous parity readout schemes. Furthermore, this thesis explores the full quantum description of the state formed when a semi-classical drive is applied to an electromagnetic cavity coupled to a qubit. It is found that this state exhibits novel properties, such as qubit evolution dependent on the cavity-phase, and sets fundamental limits on the accuracy and repeatability of qubit measurement via a cavity. Finally, a protocol is presented to create nonclassical states in an electromagnetic cavity using a nonlinear photon detector, including states for which no preparation technique was previously known.

Zusammenfassung

Quanteninformation ist ein sich schnell entwickelnder Bereich der Physik, der die fundamentalen quantenmechanischen Aspekte der Natur untersucht und sie sich zunutze macht. Die Anwendungsmöglichkeiten dieses Gebiets sind vielfältig und liegen beispielsweise in der Informatik, Chemie und Biologie. Für einen großen Teil der Quanteninformation ist es essenziell ein Quantensystem messen zu können; diese Arbeit fokussiert sich auf neuartige Messtechniken in integrierten supraleitenden Schaltkreisen, einer führenden Architektur der Quanteninformation. Es wird ein skalierbares Protokoll zum Auslesen des Zustandes eines supraleitenden Quantenbits (Qubit) mithilfe eines an ihn gekoppelten Mikrowellenresonators (Kavität) und eines Photonenzählers vorgestellt. Ausgehend von diesem Verfahren wird ein weiteres zum Messen eines binären Multi-Qubit Operators, der Qubit Parität, entwickelt, welches die fundamentalen Grenzen bisheriger Auslesemethoden überschreitet. Des Weiteren wird in dieser Arbeit die vollständig quantenmechanische Beschreibung des Zustandes, der bei semiklassischem Antrieb einer an einen Qubit gekoppelten elektromagnetischen Kavität entsteht, untersucht. Es stellt sich heraus, dass dieser Zustand neuartige Eigenschaften wie beispielsweise die Abhängigkeit der Zeitentwicklung des Qubits von der Phase der Kavität aufweist und wesentliche Beschränkungen bezüglich Genauigkeit und Reproduzierbarkeit von Qubitmessungen mittels einer Kavität setzt. Zum Schluss wird ein Verfahren vorgestellt, das nichtklassische Zustände in einer Kavität erzeugt, wobei der Photonendetektor die einzige Nichtlinearität darstellt. Die zuvor genannten nichtklassischen Zustände umfassen auch solche, für die bisher keine Präparationsverfahren bekannt waren.

Chapter 1

Introduction

1.1 Quantum Information Processing and Computation

The field of quantum information processing and computation is concerned with the study of quantum physics applied to informatic and computational tasks. Since first proposed by Feynman [1], a universal quantum simulator promises the ability to efficiently simulate any quantum system, which has far ranging applications, not only within physics, but in fields such as chemistry and biology.

The idea of applying quantum mechanics to computational problems in computer science was first formulated by Deutsch [2], and since then it has been shown that algorithms running on a quantum computer can be more efficient than their classical counterparts [3]. Famous examples include Grover's search algorithm for an unsorted database [4], which is provably faster than the fastest classical implementation, and Shor's algorithm for factoring large numbers [5], which may offer an exponential decrease in computation time (with the caveat being that their is no proven lower bound on the classical algorithm; however, all known classical algorithms are exponentially slower than Shor's algorithm).

Given the broad and significant applications of a working quantum computer, the last few decades have seen considerable theoretical and experimental effort devoted to the development of quantum computation. The Loss-DiVincenzo criteria [6] describe the components required for a working circuit-model quantum computer, and they will briefly be reviewed here.

(i) Identification of well-defined qubits

A qubit is an effective two-level quantum system, which can often be defined by a state of lower energy (ground state) and a state of higher energy (excited state), though only controllable evolution between the two states is required. The density matrix of a qubit can be completely described in the basis of the Pauli matrices by the formula

$$\rho = \frac{1}{2}\left(\mathbb{I} + \vec{s}.\vec{\sigma}\right), \tag{1.1}$$

where $\mathbb{I}$ is the identity operator, $\vec{\sigma} = (\hat{\sigma}_x, \hat{\sigma}_y, \hat{\sigma}_z)$ is the "vector" of Pauli matrices, and $\vec{s} = (\mathrm{Tr}[\rho\hat{\sigma}_x], \mathrm{Tr}[\rho\hat{\sigma}_y], \mathrm{Tr}[\rho\hat{\sigma}_z])$ is the Pauli spin vector. The energy difference between the ground and excited states of the qubit is often referred to as the energy splitting or qubit frequency (ignoring the factor of $\hbar$). Physically, a well-defined qubit is one that can be isolated from others, so that it can be controlled and measured as its own entity. In the physical architecture of superconducting integrated circuits, effective two-level systems can be created using Josephson junctions, and these form the so called superconducting qubits (see section 1.3 for further information).

(ii) Low decoherence

Decoherence refers to interactions between a qubit and its environment. This has two major effects: energy relaxation (state decay), where the qubit loses energy to the environment and decays to its ground state, and dephasing, where superposition states of the qubit loss coherence and become mixed. The former is caused by interaction between the qubit and environmental systems at the qubit's energy splitting, while the latter is often caused by low frequency noise that results in frequency broadening of the qubit's energy splitting. Decoherence limits the useful lifetime over which a qubit can be used for computation, and introduces errors into any computation. Qubits are designed to have as little decoherence as possible, and in recent years schemes have been developed to correct for errors caused by deocherence [7].

(iii) Reliable state preparation

Once qubits have been identified, it is necessary to prepare the initial state required by the desired algorithm. Often, the desired initial state is such that all qubits are in their ground energy eigenstate. In this case, for initially non-interacting qubits and zero effective qubit temperature, simply waiting long enough will initialize the qubits to their ground state, as they are driven

their by decoherence. However, as the decoherence time of the qubits should be as long as possible, and as the effective temperature is never zero, initialization by environmental decay can be very time consuming, and will be inherently imperfect. As a result, active initialization schemes have been developed, such as initialization by projective measurement and coherent feedback, which requires highly accurate qubit measurement and control, as will now be discussed.

(iv) Accurate quantum gate operations

To perform arbitrary unitary operations (quantum gates) on a register of qubits, it is sufficient to be able to perform all members of a universal gate set. As proven by Solovay and Kitaev [7], it is possible to define a universal gate set with a discrete number of elements that can approximate any unitary with arbitrary precision. In particular, it is sufficient to be able to perform a single two-qubit entangling gate and a discrete number of distinct single-qubit gates to achieve universal control of an arbitrary number of qubits. The challenge for theorists and experimentalists is to design and achieve single- and two-qubit gates that are accurate enough to be used repeatedly in a complicated quantum algorithm. The applied unitary transformation must have high fidelity with the desired unitary of the quantum gate, which requires excellent control of the evolution of the quantum system.

(v) Reliable quantum measurement

The final criteria required for quantum computation, and the central focus of this thesis, is the ability to measure the state of the qubit register, typically at the end of the computation, in order to extract the output of the computation. The measurement must be fast enough that it can determine the state of the qubits before environmental decoherence sullies the result. However, because of the relationship between measurement and decoherence, the challenge is in designing a measurement scheme that is fast and reliable, while not introducing extra undesired decoherence to the system. Quantum measurement will be discussed in greater detail in section 1.5.

For further information on quantum information and computation, the reader is directed to the seminal textbook of Nielsen and Chuang [7].

1.2 Quantized Electromagnetic Fields

As this thesis deals with aspects of the quantum nature of electromagnetic radiation, it will be necessary to understand the quantization of electromagnetic fields. This is a topic that has been studied extensively, with many excellent resources available [8, 9, 10]. In this section the necessary concepts will be briefly reviewed.

1.2.1 The Hamiltonian of an Electromagnetic Cavity

Following [8], we begin with the normal modes of the electric field contained with in an electromagnetic cavity

$$E_x(z,t) = \sum_n A_n q_n(t) \sin(k_n z), \tag{1.2}$$

where without loss of generality, we have assumed the electric field to be polarized along the x-direction. $A_n q_n(t)$ is the amplitude (where $q_n(t)$ is a 1D function), and $k_n = n\pi/L$ the wave number of the n'th normal mode, where L is the length of the cavity (in the z-direction). The factor A_n depends on the specific dimension of the cuboidal cavity and is defined as

$$A_n = \sqrt{\frac{2\omega_n^2 m_n}{V\epsilon_0}}, \tag{1.3}$$

where $\omega_n = cn\pi/L$ is the normal mode frequency, V is the volume of the cavity, ϵ_0 is the permittivity of free space, and m_n is a constant of unit mass that depends on both the mode frequency and the geometry of the cavity.

Using Maxwell's equations and equation (1.2) one can calculate the magnetic field inside the cavity to be

$$B_y(z,t) = \sum_n A_n \left(\frac{\dot{q}_n(t)\epsilon_0}{k_n}\right) \cos(k_n z), \tag{1.4}$$

which is only nonzero along the y-direction. Equations (1.2) and (1.4) together with the relation

$$\mathcal{H} = \frac{1}{2}\int_V d\tau \left(\epsilon_0 E_x^2 + \mu_0 H_y^2\right) \tag{1.5}$$

can be used to calculate the classical Hamiltonian of the system $\mathcal{H}$. This is given by

$$\mathcal{H} = \frac{1}{2}\sum_n \left(m_n\omega_n^2 q_n^2 + \frac{p_n^2}{m_n}\right), \tag{1.6}$$

where $p_n = m_n \dot{q}_n$ is the canonical momentum for q_n. The reason for the introduction of the parameter m_n is now clear, as the Hamiltonian for each normal mode has the standard form of the Hamiltonian for a harmonic oscillator.

Quantization of this Hamiltonian proceeds as normally done for the quantization of a harmonic oscillator, and after a canonical transformation for each mode the Hamiltonian can be written as

$$\hat{H} = \hbar \sum_n \omega_n \left(\hat{a}_n^\dagger \hat{a}_n + \frac{1}{2} \right) = \sum_n \hat{H}_n, \tag{1.7}$$

where $\hat{a}_n^\dagger$ and $\hat{a}_n$ are the raising and lowering operators for the n'th normal mode, and ω_n is the mode eigenfrequency as defined before. For a single mode, the eigenstates of the Hamiltonian $\hat{H}_n$ are known as the Fock states, where the m'th Fock state $|m\rangle$ corresponds to a state with m photons. The lowering and raising operators connect the Fock states by the relations

$$\hat{a}|m\rangle = \sqrt{m}|m-1\rangle, \tag{1.8}$$

$$\hat{a}^\dagger|m\rangle = \sqrt{m+1}|m+1\rangle. \tag{1.9}$$

The previous discussion was independent of the eigenfrequencies of the modes ω_n, and applies equally well to all frequency regimes, including both optical and microwave. In microwave electronics, the LC circuit (shown in FIG. 1.1) is a physical system with a similar classical Hamiltonian to that of the electromagnetic cavity, given by

$$\mathcal{H}_{\mathrm{LC}} = \frac{\phi^2}{2L} + \frac{1}{2} L \omega_{\mathrm{LC}}^2 Q^2 \tag{1.10}$$

where ϕ is the magnetic flux across the inductor (of inductance L), and Q the charge on the capacitor (of capacitance C). $\omega_{LC} = 1/\sqrt{LC}$ is the resonance frequency of the circuit, and we see that the inductance L plays the role of an effective mass. This system is often referred to as the LC resonator or lumped element resonator due to its harmonic oscillator Hamiltonian.

The quantized version of this Hamiltonian [11] is

$$\hat{H}_{\mathrm{LC}} = \frac{\hat{\phi}^2}{2L} + \frac{1}{2} L \omega_{\mathrm{LC}}^2 \hat{Q}^2. \tag{1.11}$$

The important thing to notice is that this lumped element device has a harmonic oscillator Hamiltonian, and thus its eigenstates are the equally spaced (in energy) Fock states. Therefore, if one is attempting to design a qubit from integrated circuits, the LC resonator is not a suitable candidate, as it is not possible to address two states of the system independently from the others. To get around this problem, a suitable nonlinearity needs to be introduced, as will be discussed in section 1.3.

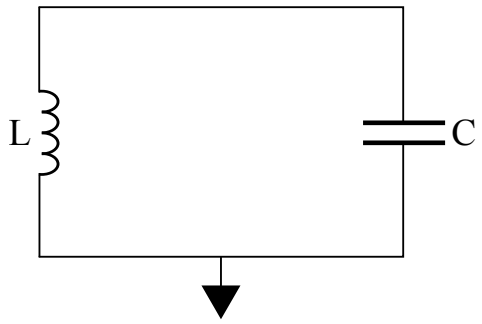

Figure 1.1: Circuit diagram of the LC resonator.

1.2.2 The Semi-Classically Driven Harmonic Oscillator

We focus on a single mode harmonic oscillator with Hamiltonian

$$\hat{H} = \omega \hat{a}^\dagger \hat{a}, \tag{1.12}$$

where we have ignored the constant energy shift and set $\hbar = 1$. A classical drive field applied to this system can be described by the off-diagonal Hamiltonian

$$\hat{H}_\mathrm{d} = 2\cos(\omega_\mathrm{d} t)\left(\epsilon \hat{a} + \epsilon^* \hat{a}^\dagger\right), \tag{1.13}$$

where ω_d is the frequency of the applied drive field, and ϵ is the complex drive amplitude. As the external field is treated classically and the harmonic oscillator is treated quantum mechanically this situation is referred to as semi-classically driven [9]. In the interaction frame with respect to the system self-Hamiltonian of equation (1.12), and after performing the rotating-wave approximation, the full Hamiltonian of the system is

$$\hat{H}'_\mathrm{d} = \left(\epsilon \hat{a} e^{-i\Delta t} + \epsilon^* \hat{a}^\dagger e^{i\Delta t}\right), \tag{1.14}$$

where $\Delta = \omega - \omega_\mathrm{d}$. The rotating wave approximation drops all nonsecular terms proportional to $e^{\pm i(\omega+\omega_\mathrm{d})t}$, as on the timescale under consideration these terms average to zero. This approximation is valid provided $|\epsilon| \ll \omega + \omega_\mathrm{d}$.

The evolution operator generated by this interaction Hamiltonian is

$$\hat{U}'_\mathrm{d}(t) = \hat{D}\left(\alpha(t)\right) = e^{\alpha \hat{a}^\dagger - \alpha^* \hat{a}}, \tag{1.15}$$

where $\hat{D}\left(\alpha(t)\right)$ is known as the displacement operator, and $\alpha(t)$ is given by

$$\alpha(t) = \frac{-\epsilon^*}{\Delta}\left(e^{i\Delta t} - 1\right). \tag{1.16}$$

For a non-cosine shaped classical drive the expression for $\alpha(t)$ is the same as that of the Green's function solution for a driven classical harmonic oscillator.

Starting from the vacuum state $|0\rangle$, application of the displacement operator creates the set of states known as the coherent states [12], defined by

$$|\beta\rangle = \hat{D}(\beta)|0\rangle = e^{-\frac{|\beta|^2}{2}} \sum_{n=0}^{\infty} \frac{\beta^n}{\sqrt{n!}}|n\rangle, \tag{1.17}$$

where $\{|n\rangle\}_{n=0}^{\infty}$ are the Fock states, and $\beta \in \mathbb{C}$ is referred to as the coherent state amplitude. The coherent states are the quantum states that best describe classical electromagentic radiation, as would be expected given the fact that the Hamiltonian model underlying their creation is a semi-classically driven electromagnetic cavity.

The coherent states form an over complete basis of the Hilbert space for a harmonic oscillator, and in particular any state ρ can be written as

$$\rho = \int d^2\alpha P(\alpha)|\alpha\rangle\langle\alpha|, \tag{1.18}$$

where $P(\alpha)$ is a quasiprobability function known as the Glauber-Sudarshan P-function [13]. Such quasiprobability distributions (of which there are many) can be used to visualize the state ρ in phase space, just as classical probability distributions are used in classical mechanics.

1.2.3 Nonclassical States of Electromagnetic Radiation

Nonclassical states of electromagnetic radiation (or any harmonic oscillator) exhibit properties that are uniquely quantum mechanical in nature. A common definition of a classical state is that it can be written as a convex sum or incoherent mixture of coherent states, which implies that the P-function is non-negative (and non-singular) for all α. A nonclassical state is therefore any state that cannot be expressed as a mixture of coherent states. More quantitative measures of nonclassicality will be discussed in chapter 6.

Canonical examples of nonclassical states include the Fock states, the even and odd Schrödinger cat states, defined by

$$|\Psi\rangle_{\text{SC}} = (|\alpha\rangle \pm |-\alpha\rangle)/\sqrt{\mathcal{N}}, \tag{1.19}$$

where $\mathcal{N}$ is the normalization, and the squeezed vacuum state, given by

$$|\Psi\rangle_{\text{SV}} = \hat{S}(z)|0\rangle = e^{\left(z^*\hat{a}^2 - z\hat{a}^{\dagger 2}\right)/2}|0\rangle, \tag{1.20}$$

where $\hat{S}(z)$ is the squeezing operator with complex squeezing amplitude $z \in \mathbb{C}$. Schrödinger cat states are interesting as for large enough $|\alpha|$ they are a superposition of macroscopically distinguishable classical states, and thus

allow one to experimentally probe the quantum-classical boundary. In addition, both Schrödinger cat states and squeezed states are useful in metrology and sensing, as they can allow for quantum-limited precision [14, 15].

While it is simple to define a state ρ in terms of its P-function, for a given state ρ it is often difficult to do the reverse. Also, as it is often highly singular for interesting states, the P-function can be an inconvenient way to represent a state in phase space. Conveniently, there are other commonly used quasiprobability distributions, two of which we will highlight here. They are the Husimi Q-function, and the Wigner function [16, 17, 18], defined for the state ρ by

$$Q(\alpha) = \frac{1}{\pi}\langle\alpha|\rho|\alpha\rangle, \tag{1.21}$$

$$W(\alpha) = \frac{1}{\pi^2}\int d^2\beta e^{-\beta\alpha^* + \beta^*\alpha}\chi_{\mathrm{W}}(\beta), \tag{1.22}$$

respectively, where we have introduced the Wigner characteristic function $\chi_{\mathrm{W}}(\beta)$, defined by

$$\rho = \frac{1}{\pi}\int d^2\beta \chi_{\mathrm{W}}(\beta)\hat{D}(-\beta), \tag{1.23}$$

to remain within the coherent state basis.

For a given state ρ the Q-function is the easiest to compute, and is useful for visualizing states that are superpositions of coherent states, such as the Schrödinger cat state. However, as it is always bounded and non-negative, it is not a good nonclassicality witness. The Wigner function is better in this regard, as for most nonclassical states it will be negative for some α (a notable exception to this is the squeezed vacuum state), and for superposition states it displays interference fringes in phase space between coherent state components.

The Q-function and Wigner function for an even Schrödinger cat state with $\alpha \in \mathbb{R}$ are shown in FIGs. 1.2(a), and 1.2(b). The Q-function clearly shows the two coherent state components, each centered at the right amplitude, but would not well distinguish between a superposition and a mixture of the two coherent states. This distinction is better captured in the Wigner function, which shows clear interference fringes (and negativity) between the two coherent state components.

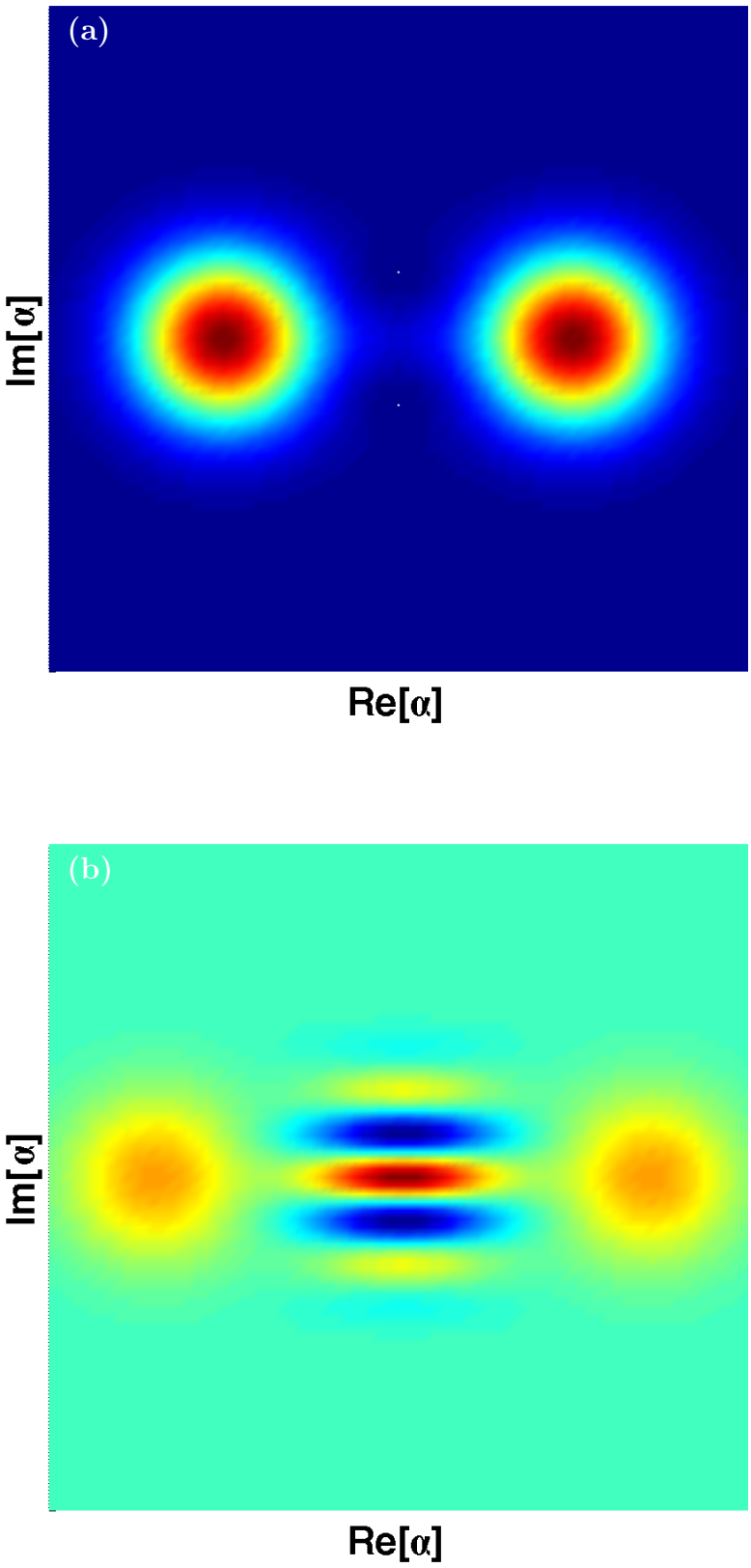

Figure 1.2: **(a)** Husimi Q-function and **(b)** Wigner function of an even Schrödinger cat state.

1.3 Quantum Computing with Integrated Circuits

In many quantum computing architectures, the qubit is an effective two-level system found in nature, such as two addressable levels in the electronic structure of an atom, ion or molecule. The benefit of these systems is that under the same environmental conditions the qubit parameters are always the same, while the challenge is in designing control and measurement technology to work within the parameter regime set by nature.

From the opposite side of the problem, one could design a qubit to be in a desirable parameter regime. Such tailor-made quantum systems are not commonplace, but integrated circuits made from superconducting qubits are a leading candidate. They allow for integration with the well developed field of microwave electronics, and offer a planar geometry well suited for scaling to large size quantum computers. The circuits need to be superconducting to avoid loss from electrical resistance, and without this protection coherence would be very difficult, if not impossible, to achieve.

While a relatively young field, superconducting qubits have been extensively studied in both theory and experiment, with many great reviews of the field already available [19, 20, 21, 22, 23]. In this section, we will briefly discuss the key element underlying all superconducting qubits, the Josephson junction, before going over the basics of a few relevant qubit designs, and how these devices can be coupled to microwave resonators.

1.3.1 The Josephson Junction

As previously mentioned, the simple LC resonator circuit has the same Hamiltonian as a harmonic oscillator, preventing its use as a qubit. In order to isolate a useful qubit from the eigenstates of some integrated circuit, it is necessary to have a nonlinear element that breaks the degeneracy of the transition energies between neighboring eigenstates. For superconducting circuits, the simplest nonlinear element is the Josephson junction.

The Josephson junction is a tunnel junction consisting of two layers of superconducting material with a layer of non-superconducting material between them, shown in FIG. 1.3(a). Due to quantum tunneling, Cooper pairs are able to cross the non-superconducting barrier in the junction, allowing for nonzero current and voltage across the junction. The Josephson equations

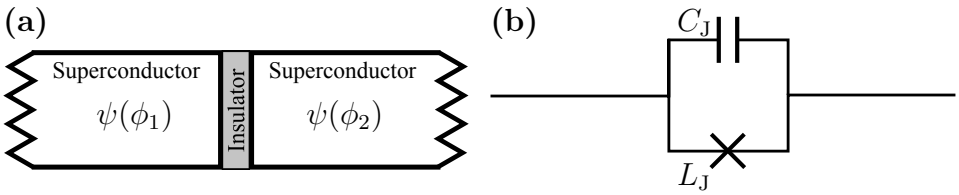

Figure 1.3: **(a)** Schematic and **(b)** effective circuit diagram for a Josephson junction.

[24], given by

$$I = I_c \sin(\phi) \tag{1.24}$$

$$V = \Phi_0 \dot{\phi} \tag{1.25}$$

describe the current and voltage across the junction, where $\phi = \phi_1 - \phi_2$ is the superconducting phase difference across the junction, and $\Phi_0 = \hbar/2e$ is the reduced magnetic flux quantum for superconductors. I_c is the critical current of the junction; if the junction is biased with an external current that exceeds I_c superconductivity in the junction will break down. The Josephson junction can also be thought of as a capacitor (with capacitance C_J) in parallel to a nonlinear inductor (of inductance L_J), as shown in FIG. 1.3(b).

1.3.2 Superconducting Qubits

Using the Josephson junction, a variety of superconducting qubits have been developed, each broadly originating from one of three basic designs. Biasing the junction in series with a bias current creates a phase qubit [25], for which the qubit states are the ground and first excited state of one metastable potential well in a cosine washboard potential. Connecting the junction in series with a capacitor and a voltage source creates a charge qubit [26, 27]. Here, a superconducting island is formed between the capacitor and the Josephson junction, and the number of Cooper pairs on this island defines the qubit state. Finally, connecting one or more Josephson junctions in a ring and threading a magnetic field through the ring forms a flux qubit [28]. Magnetic flux quantization in the ring forces the supercurrent in the flux qubit to flow either clockwise or anticlockwise, and these two directions of current flow form the qubit states.

While the specific kind of superconducting qubit is not important to much of the discussion in this thesis, the nature of the charge qubit will be briefly expanded upon, as from the charge qubit the contemporary Transmon [29, 30] and Xmon [31] were developed. The charge qubit circuit is shown in FIG. 1.4,

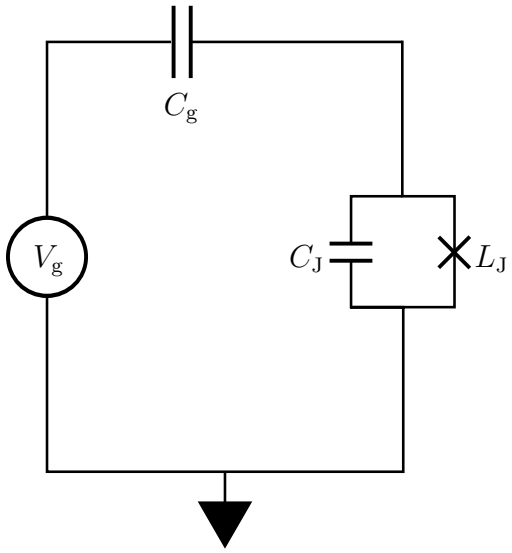

Figure 1.4: Circuit diagram of the charge qubit.

where V_g is referred to as the gate voltage, and C_g the gate capacitance. The circuit Hamiltonian for the charge qubit is given by

$$\hat{H} = E_C \left(\hat{N} - N_g\right)^2 - E_J \cos(\hat{\phi}), \tag{1.26}$$

where the Cooper pair number $\hat{N} = \hat{Q}/(2e)$ is the charge (conjugate to $\hat{\phi}$) scaled by $1/(2e)$. We have also defined the gate charge number, $N_g = -C_g V_g/(2e)$, the Josephson coupling energy $E_J = I_c \Phi_0$, and the charging energy $E_C = (2e)^2/2(C_J + C_g)$. The charging energy is the energy required to increase by one the difference in the number of Cooper pairs on either side of the Josephson junction.

As described in [32], we work in the eigenstate basis of $\hat{N}$, which satisfies $\hat{N}|n\rangle = n|n\rangle$. The operator $E_C \left(\hat{N} - N_g\right)^2$ has an anharmonic energy spectrum, allowing one to selectively address two eigenstates, and in doing so define a qubit. Typically, the two lowest energy eigenstates are chosen as the qubit, with an energy separation of $E_C(1 - 2N_g)$, while the second excited state is separated from the first excited state by an energy of $E_C(3 - 2N_g)$, which is $2E_C$ above the qubit transition. The charge qubit is operated in the $E_C \gg E_J$ regime to maximize the anharmonicity of the Hamiltonian. However, nonzero E_J is required, along with tunable N_g, to generate universal control of the charge qubit.

Since $\hat{\phi}$ and $\hat{N}$ are conjugate variables it follows that $e^{i\hat{\phi}}|n\rangle = |n+1\rangle$. Taking this into account, one can describe $\cos(\hat{\phi})$ in the Cooper pair number

basis, and restricted to the qubit subspace the Hamiltonian becomes

$$\hat{H}_{\mathrm{CQ}} = E_{\mathrm{C}} \left(N_{\mathrm{g}} - \frac{1}{2} \right) \hat{\sigma}_z - \frac{E_{\mathrm{J}}}{2} \hat{\sigma}_x. \tag{1.27}$$

Unfortunately, as the qubit energy spacing depends on N_{g}, which depends on the gate voltage, noise in the voltage source will dephase the qubit. Working at the charge degeneracy point $N_{\mathrm{g}} = 1/2$ minimizes this effect, however, this effect can be quite large even slightly away from the charge degeneracy point.

To reduce the effect of charge noise from the voltage source, the Transmon and Xmon work in the $E_{\mathrm{J}} \gg E_{\mathrm{C}}$ regime by adding a large capacitance in parallel to the Josephson junction. As a consequence this reduces the anharmonicity of the system eigenspectrum, making it more difficult to define a qubit subspace. However, addressing only the qubit states is still possible by using more sophisticated control pulses [33], and it is therefore still possible to define a qubit subspace for this weakly anharmonic system.

1.3.3 Circuit Quantum Electrodynamics

The interaction between microwave resonators, such as stripline resonators or the lumped element LC-resonators described previously, and superconducting qubits is the domain of the field of circuit Quantum Electrodynamics (cQED). The coupling between these devices is achieved either by galvanic or direct electrostatic coupling when the qubit is fabricated inside the resonator [34, 35], or by capacitive or inductive coupling when the qubit is fabricated outside the resonator [36, 31].

In all cases, the right choice of system parameters leads to Rabi interaction between the microwave resonator and the superconducting qubit, described by the Hamiltonian

$$\hat{H}_{\mathrm{Rabi}} = g \hat{\sigma}_x \left(\hat{a} + \hat{a}^\dagger \right). \tag{1.28}$$

In most cases the coupling strength g is small enough that the rotating wave approximation (RWA) is valid, which neglects nonsecular terms and leads to the Jaynes-Cummings interaction [37], given by the Hamiltonian

$$\hat{H}_{\mathrm{JC}} = g \left(\hat{\sigma}^+ \hat{a} + \hat{\sigma}^- \hat{a}^\dagger \right), \tag{1.29}$$

where $\hat{\sigma}^\pm$ are the raising and lowering operators for the qubit. The Jaynes-Cummings coupling strength can be calculated from circuit parameters, and depends on the specific implementation of the superconducting qubit and the microwave cavity. Further details about this coupling strength for some specific qubit/resonator set-ups can be found in Refs. [38, 30, 39].

Though the coupling strength in cQED experiments is normally weak enough that the RWA is valid, contemporary cQED experiments still operate in the strong coupling regime, as the coupling strength is much larger than the dissipation rates of the system. Recent experiments have even reached the ultrastrong coupling regime, at which point the RWA begins to break down and the Jaynes-Cummings Hamiltonian is no longer valid [34].

1.4 Open Quantum Systems

While theoretically it is convenient to study closed systems, in reality and in experiments it is often necessary to study an open system, which includes interactions between the system and its environment. The naïve way to do this would be to enlarge the definition of "the system" to include the relevant parts of the environment, and solve for all degrees of freedom. However, this can introduce a very large overhead, as it is now necessary to describe the dynamics of many more variables than are of interest, and often, solving the full equations of motion for both the system and environment is simply not possible.

Fortunately, in many situations it is possible to derive an effective evolution for the system state alone, which while describing the system's interaction with the environment, does not describe the evolution of the environment itself. In quantum mechanics, one commonly used equation for open system evolution is the Lindblad master equation, which we will describe here, as it was used extensively throughout this thesis.

1.4.1 The Lindblad Master Equation

The Lindblad master equation (in diagonal form) for the evolution of the system state $\rho(t)$ is given by the equation

$$\dot{\rho}(t) = -i[\hat{H}, \rho(t)] + \sum_{\mu} \gamma_{\mu} \left(\hat{L}_{\mu} \rho(t) \hat{L}_{\mu}^{\dagger} - \frac{1}{2} \left\{ \hat{L}_{\mu}^{\dagger} \hat{L}_{\mu}, \rho(t) \right\} \right), \tag{1.30}$$

where $[A, B] = AB - BA$ is the commutator and $\{A, B\} = AB + BA$ the anticommutator of A and B. The first term of equation (1.30) is the von Neumann equation for the coherent evolution of the system state under the Hamiltonian $\hat{H}$, which includes both the system self-Hamiltonian and any coherent evolution due to the environment (such as Lamb shifts). The operators $\hat{L}_{\mu}$ and the real and positive coefficients γ_{μ} are referred to as the Lindblad operators and Lindblad rates, respectively. They describe the incoherent system evolution due to the environment, and the second term of equation (1.30) is commonly called the dissipator.

In superoperator language, the Lindblad master equation can be written as

$$\dot{\rho}(t) = \mathcal{L}\rho(t), \tag{1.31}$$

which has the simple solution

$$\rho(t) = e^{\mathcal{L}t}\rho(0), \tag{1.32}$$

and we see that the Lindblad generator $\mathcal{L}$ generates the quantum map $\rho(t) = \Lambda_t\rho(0) = e^{\mathcal{L}t}\rho(0)$. The usefulness and widespread application of the Lindblad equation comes from the fact that it is the most general form of the generator of the semigroup of quantum maps that satisfy the following properties [40]:

1. Λ_t is completely positive and trace preserving (CPTP).
2. $\mathrm{Tr}\left[\Lambda_t\rho(0)\hat{O}\right]$ is continuous in t for all valid observables $\hat{O}$.
3. Λ_t is Markovian, such that $\Lambda_{(t+t')} = \Lambda_t \circ \Lambda_{t'}$ and $\Lambda_0 = \mathcal{I}$.

The first property ensures that the open system evolution maps valid quantum states to valid quantum states, and in particular ensures that if the evolving system is a component of a larger system, the state of the larger system remains a valid quantum state. The second property ensures that there are no discontinuous jumps in the expectation values of valid observables, which would be nonphysical. Finally, the third property implies that the evolution of the system at time t depends only on the state at time t, and not on the history of the state, and that for $t = 0$ the mapping is the identity mapping $\mathcal{I}$.

Properties one and two are necessary for the quantum map to describe physical evolution of the state $\rho(t)$, while property three is convenient and holds for many physical situations. As the Lindblad master equation is the most general form of the generator for quantum maps with all three properties, it is unsurprising that it accurately describes many physical systems.

1.4.2 Microscopic Derivations of the Master Equation

While the Lindblad master equation is easily defined and has a wide range of application, it can be quite challenging to formally derive a Lindblad master equation starting from the Hamiltonian description of the coherent evolution between the system and its environment. These so called microscopic derivations of the master equation are covered extensively (and excellently) in Ref. [41], and only a few relevant points will be mentioned here.

The Lindblad master equation is often microscopically derived in the weak coupling limit [42], where the interaction between the system and its environment is the smallest energy scale of the full Hamiltonian. Assuming weak coupling, one can make the following three approximations to the system-environment dynamics:

1. Born approximation. The full state of the system and environment is given by $\eta(t) = \rho(t) \otimes \rho_{\mathrm{E}}$, that is, the environment state is negligibly affected by interaction with the system and is stationary.

2. Markov approximation. The evolution of the system at time t only depends on the state of the system at time t. This implies that correlations between the system and the environment decay much faster than the timescale of interest.

3. Rotating wave approximation. Nonsecular terms in the evolution that oscillate quickly in time are averaged over and vanish as a result.

After these approximations have been made, it is possible to trace out the environment and obtain an effective evolution equation for the system that is a Lindblad master equation.

It is important here to note that in the weak coupling limit the master equation is derived in the energy eigenbasis of the system, and therefore, combining the Lindblad equations for two systems cannot be done in the weak coupling limit. Instead, it is necessary to consider the joint system, and derive the master equation for both systems in the energy eigenbasis of the joint system [43].

A Lindblad master equation can also be derived in the situation where the system-environment interaction is stronger than the system self-Hamiltonian, known as the singular coupling limit [44], such as is the case when the relevant system eigenenergies are all degenerate. In this situation, both the Born and Markov approximations are still necessary, however, no secular approximation is necessary as there are no longer nonsecular terms in the evolution equation after the Born and Markov approximations have been made.

1.5 Quantum Measurement and Parity

The study of quantum measurement has a long and storied history in physics. One can argue that understanding the nature of quantum measurement was for a long time a significant portion of the field of quantum foundations, and that it has been a driving force behind the development of the myriad of interpretations of quantum mechanics that currently exist. We will not focus on these issues here, but instead discuss the aspects of the formalism of quantum measurement that are relevant to this thesis. Quantum measurement is a broad and extensively studied field, and for further reading on the topics mentioned here, as well as many others, the reader is directed to the excellent references [45] and [7].

1.5.1 von Neumann Projective Measurement

In quantum mechanics, a measurement operator is a Hermitian matrix $\hat{O}$, whose eigenvalues $\{\lambda_i\}$ correspond to the outcomes of the measurement. As $\hat{O}$ is Hermitian, we can write it in its spectral decomposition as

$$\hat{O} = \sum_i \lambda_i |\lambda_i\rangle\langle\lambda_i|, \tag{1.33}$$

where $\{|\lambda_i\rangle\}$ is the set of eigenvectors of $\hat{O}$. For a nondegenerate eigenspectrum, a von Neumann or projective measurement of the observable $\hat{O}$ with outcome λ_i will project the state of the system to the corresponding eigenvector $|\lambda_i\rangle$ at the end of the measurement. For a degenerate eigenspectrum, the final state of the system will be a superposition of the eigenstates of $\hat{O}$ corresponding to outcome λ_i.

More concretely, for an initial state ρ_{in}, at the end of a projective measurement, the unconditioned final state of the system is given by

$$\rho_{\text{fin}}^{\text{uncon}} = \sum_i \text{Tr}\Big[\rho_{\text{in}}|\lambda_i\rangle\langle\lambda_i|\Big]|\lambda_i\rangle\langle\lambda_i|, \tag{1.34}$$

which is a classical mixture of the output states of all possible measurement outcomes. When the measurement outcome is known, the state is described by a single component of the above sum. As is evident from the form of equation (1.34), a hallmark of projective measurement is that repeated measurements that occur immediately after one another will always result in the same measurement outcome.

1.5.2 Quantum Non-Demolition Measurement

Quantum non-demolition (QND) measurement extends the concept of repeatable measurements, such that repeated QND measurements will always give the same result, no matter the time between them, provided no external manipulation of the system occurs between measurements. For a closed system, this requirement is satisfied if the system's self-Hamiltonian $\hat{H}_{\mathrm{S}}$ and the observable $\hat{O}$ commute, so that evolution under $\hat{H}_{\mathrm{S}}$ applies only a global phase to the eigenvectors of $\hat{O}$ [46]. This criterion is automatically satisfied for measurement of a system in its eigenbasis. For an open system, QND measurements can normally only be repeated on a timescale shorter than the decoherence time, otherwise interactions with the environment will change the state of the system and prevent repeatable measurement outcomes.

In actual experiments, measurement of an observable that commutes with the system Hamiltonian is often quite challenging. In fact, even when the goal is to measure the system in its eigenbasis, the simplest way to do this often destroys the system being measured. The typical example of this is a number resolving photon detector used to measure an electromagnetic state in the Fock basis. Regardless of the initial state, after detection the electromagnetic field will be in vacuum and the field has been measured in a destructive way, making repeated measurements impossible.

Many measurement techniques have been developed to avoid destructive measurement and implement QND measurement of a system, and we will highlight here the most relevant schemes in circuit QED. QND measurement of the qubit state can be achieved by coupling dispersively to a microwave cavity, and encoding the state of the qubit in either the phase or photon number of a coherent state in the cavity [47, 39]. By a similar set-up, it is also possible to measure the photon number of an incoming microwave signal in a QND way [48].

1.5.3 Parity Measurement

One interesting and useful measurement is that of the parity of a register of qubits, which distinguishes whether an even or odd number of qubits are in the excited state. For N qubits, the parity observable is given by

$$\hat{O}_{\mathrm{P}} = \bigotimes_{n=1}^{N} \hat{\sigma}_z. \tag{1.35}$$

Parity is a binary outcome measurement, which is to say that the parity observable has two eigenvalues ± 1 (even or odd parity respectively), which

each have highly degenerate eigenspaces. As a result, measurement of the parity results in decoherence between states of different parity, but leaves the coherence of states with the same parity unaffected.

Parity measurement has many applications to quantum information protocols, including error correction [49] and entanglement generation [50, 51]. Despite the simple nature of its observable, measurement of parity, and only parity, has proven to be quite difficult experimentally. One key reason for this is that most natural interactions are two-body, while in general N-qubit parity measurement requires N-body interactions. Hence, the N-body interactions need to be broken down into long control sequences of two-body interactions, which introduces considerable overhead.

In many cases only a partial parity measurement is performed, which distinguishes between parity subspaces but also extracts additional information about the state of the qubits. This results in unwanted decoherence within a parity subspace. Chapter 3 of this thesis introduces a new parity measurement scheme designed to avoid this problem.

1.6 The Josephson Photomultiplier

In the optical frequency regime, photon detectors that operate via the photoelectric effect are commonplace [52], as many natural or easily synthesized materials exist with work functions in the optical frequency spectrum. In these devices the photoemission of electrons creates an avalanche effect, which results in a large and easily measurable current.

However, there are no known naturally occurring materials with work functions in the microwave frequency regime, and as such, microwave photon detectors were for a long time an unrealized technology. To circumvent this limitation, it was necessary to develop artificial atoms with effective "work functions" in the microwave regime, that can also produce a large signal when detecting a photon [53]. The first such device, developed using superconducting integrated circuits, was the Josephson photomultiplier [54]. More recently, protocols to non-destructively detect propagating microwave photons have been developed [55, 48]. These protocols circumvent the work function limitation of photon counters by using the dispersive interaction with an ancilla superconducting qubit to observe the presence of the photon.

1.6.1 Circuit Design and the Full Hamiltonian

The Josephson photomultiplier (JPM) consists of a current biased Josephson junction, for which the circuit diagram is shown in FIG. 1.5(a), where I_b is the applied bias current, and ϕ is the superconducting phase across the Josephson junction. As a function of ϕ, the potential energy of the JPM has what is known as a cosine washboard shape, shown in FIG. 1.5(b), and has the functional form

$$U(\phi) = -I_c\Phi_0\cos\phi - I_b\Phi_0\phi \tag{1.36}$$

where I_c is the critical current of the Josephson junction, and $\Phi_0 = \hbar/2e$ is the reduced magnetic flux quantum for Cooper pairs.

The JPM is similar in design to the phase qubit [25], however, for the JPM the applied bias current is large enough that only two quasi-bound states exist in each metastable well of the JPM potential, with the excited quasi-bound state being very near in energy to the potential local maximum. When the system tunnels out of a quasi-bound well, it finds itself in a state with more energy then the neighboring local minima. As a result, it quickly "runs down" the well, resulting in a rapid change in the flux ϕ, which results in a large voltage in the circuit that can be detected by classical circuitry connected to the JPM.

If the JPM bias is tuned such that tunneling events occur after interaction with incident microwave radiation, then the large voltage generated will

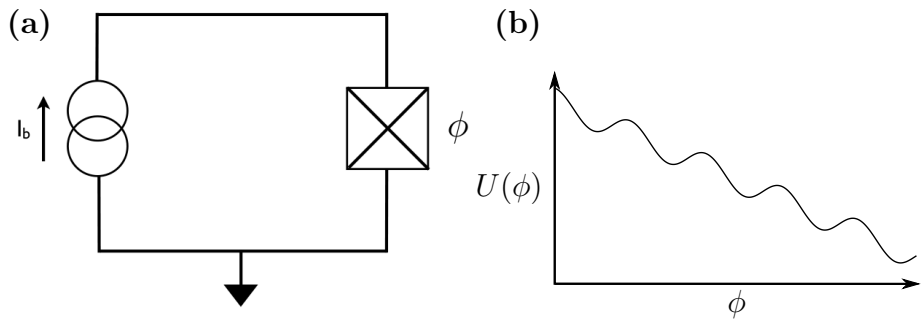

Figure 1.5: **(a)** Circuit diagram and **(b)** potential energy landscape of the Josephson Photomultiplier.

indicate the detection of a microwave photon. This process is analogous to the avalanche effect in optical photon detectors. Much like optical detectors, the detection response (voltage signal) of the JPM is both unambiguous and easily observed, satisfying the necessary criteria of a useful photon detector.

The JPM was first realized experimentally in Ref. [54], where two JPM's were used to demonstrate the Hanbury Brown and Twiss effect [56] in the microwave regime. State of the art experiments with the JPM involve integrating the JPM with cavity-qubit systems in order to perform the single-qubit readout protocol proposed in Ref. [47] and chapter 2. At the time of writing of this thesis the first experimental progress towards single-qubit readout was recently reported [57].

1.6.2 Effective Three Level Model

To study the interaction between a JPM and a microwave cavity, an effective three level model of the JPM was introduced [58, 59], similar to as was done in [53]. In this model, the two quasi-bound states in a single potential well constitute the ground and excited states of the JPM, and we amalgamate all states outside the potential well into the measured state $|m\rangle$. The ground and excited states of the JPM are coupled coherently via the operators $\hat{\sigma}^{\pm}$, while the measured state can only be reached via incoherent tunneling from the ground or excited state, at rates γ_D and γ_J respectively. For typically experimental systems $\gamma_J \approx (10^2 - 10^3)\gamma_D$ [54]. Two other incoherent processes affect the JPM, namely inelastic relaxation from the excited state to the ground state, and pure dephasing, which are characterized by timescales T_1 and T_2 respectively.

The tunneling between the excited state of the JPM and the measured state is accurately described by an incoherent rate and a unidirectional pro-

cess for a reason similar to that of Fermi's golden rule. The states outside the quasi-bound well form a quasi-continuum and have much higher excitation numbers relative to their local minimum than do the quasi-bound states. As a result, once they state tunnels out of the quasi-bound well it is very quickly driven by the environment to states existing solely outside of the well (which we describe by the measured state), enforcing the incoherent and unidirectional nature of the process.

In this model, the microwave cavity and the JPM interact via the Jaynes-Cummings interaction, $g\left(\hat{\sigma}^{+}\hat{a}+\hat{\sigma}^{-}\hat{a}^{\dagger}\right)$, where g is the coupling strength. When the cavity and JPM are on resonance, a photon from the cavity can excite the JPM, which can then tunnel into the measured state, producing a classically observable voltage pulse. If the JPM starts in its ground state, since $\gamma_{\mathrm{J}} \gg \gamma_{\mathrm{D}}$ we can say that an observed tunneling event was likely to have been caused by interaction with the cavity, and indicate the detection of a microwave photon.

In Ref. [59] it was found that for $\gamma_{\mathrm{J}} \approx g$ the JPM often imparts a back action on the cavity that has the form of the photon subtraction operator

$$\hat{B}_{-} = \sum_{n=1} |n-1\rangle\langle n|. \tag{1.37}$$

A detector with such a back action is a true binary detector, distinguishing between the vacuum and its compliment without obtaining any further information about the photon number. The JPM is closest to the subtraction operator when $1/T_2$ is the largest rate in the system. The subtraction-like qualities of the JPM imply that it is blind to the phase of a coherent state in the cavity, a quality that will be useful in chapter 3. The subtraction operator also implements a nonlinear back action, which will be used in chapter 6 to create nonclassical states in the cavity.

1.7 Layout of this Thesis

This thesis is in a cumulative format, as it contains research done on several projects that all fall under the general research theme on the interaction between a qubit and electromagnetic radiation, with applications to measurement. Chapters 2 through 6 are all either published, submitted for peer review, or being prepared for submission, and in all cases the correct author list and publication information is described on the first page of the chapter.

Chapters 2 and 3 describe novel single-qubit and multi-qubit parity readout schemes, respectively, where, in both cases an electromagnetic cavity is used as an ancilla. Chapter 4 contains a new description of the evolution of a dispersively coupled qubit-cavity system when the cavity is driven by classical radiation. Chapter 5 describes an application of this effect to qubit readout. Finally, in chapter 6, a scheme to create nonclassical states in an electromagnetic cavity by photon counting is introduced. Each chapter contains appendices describing calculations supplemental to the results contained in the main text of the chapter. In addition, this thesis contains a single global appendix that describes the methodology used in the numerical simulations done in all chapters of this thesis.

Chapters 2, 3, and 6 describe work done in collaboration with individuals other than the author of this thesis and his supervisor F.K. Wilhelm. The contribution of other authors will be briefly described here.

In chapter 2 the majority of the text was written by L.C.G. Govia, with parts also written by R. McDermott, B.L.T. Plourde and F.K. Wilhelm. In chapter 3 the text was written by L.C.G. Govia with editing done by E.J. Pritchett and F.K. Wilhelm. In both chapters all numerical simulations and analytic calculations were done by L.C.G. Govia, except for appendix 2.A of chapter 2, which was done by M.G. Vavilov and C. Xu. The readout schemes of these chapters were discovered and developed in collaborative discussions between all authors. In chapter 6 the text was written by L.C.G. Govia with editing done by E.J. Pritchett and F.K. Wilhelm. L.C.G. Govia and E.J. Pritchett performed the numerical simulations, the results of which are shown in the chapter's figures.

Chapter 2

High-fidelity qubit measurement with a microwave photon counter

Luke C. G. Govia, Emily J. Pritchett, Canran Xu, B. L. T. Plourde, Maxim G. Vavilov, Frank K. Wilhelm, and R. McDermott

Tis safer to be that which we destroy,
Than by destruction dwell in doubtful joy.
-William Shakespeare

Abstract

High-fidelity, efficient quantum nondemolition readout of quantum bits is integral to the goal of quantum computation. As superconducting circuits approach the requirements of scalable, universal fault tolerance, qubit readout must also meet the demand of simplicity to scale with growing system size. Here we propose a fast, high-fidelity, scalable measurement scheme based on the state-selective ring-up of a cavity followed by photodetection with the recently introduced Josephson photomultiplier (JPM), a current-biased Josephson junction. This scheme maps qubit state information to the binary digital output of the JPM, circumventing the need for room-temperature heterodyne detection and offering the possibility of a cryogenic interface to superconducting digital control circuitry. Numerics show that measurement contrast in excess of 95% is achievable in a measurement time of 140 ns. We discuss perspectives to scale this scheme to enable readout of multiple qubit channels with a single JPM.

Published in Phys. Rev. A **90**, 062307 (2014).

2.1 Introduction

Over the past decade, circuit quantum electrodynamics (cQED) has emerged as a powerful paradigm for scalable quantum information processing in the solid state [39, 60, 61, 62]. Here a superconducting qubit plays the role of an artificial atom, and a thin-film coplanar waveguide or bulk cavity resonator is used to realize a bosonic mode with strong coupling to the atom. Interaction between the qubit and the cavity is described by the Jaynes-Cummings Hamiltonian [37]. Strong interaction between the qubit and the cavity has been used to realize high-fidelity multi-qubit gates [63, 64, 65, 66]; moreover, the qubit has been used to prepare highly nonclassical states of the resonator [67, 68]. In the limit where the qubit is far detuned from the cavity resonance so that $\Delta \equiv \omega_C - \omega_Q$ satisfies $|\Delta| \gg g_Q$, where ω_C is the cavity frequency, ω_Q is the qubit frequency, and g_Q is the qubit-cavity coupling strength, the following dispersive approximation to the Jaynes-Cummings Hamiltonian is realized [39] (with $\hbar = 1$):

$$\hat{H}_{\text{eff}} = (\omega_C + \chi_Q \hat{\sigma}_z)\, \hat{a}^\dagger \hat{a} - \frac{1}{2}(\omega_Q - \chi_Q)\hat{\sigma}_z; \tag{2.1}$$

here $\chi_Q = g_Q^2/\Delta$ is the dispersive coupling strength of the resonator to the qubit, and $\hat{\sigma}_z$ is the Pauli-z operator. One sees from the first term that the effective cavity frequency acquires a shift that depends on the qubit state. It is therefore possible to perform a quantum nondemolition measurement of the qubit by monitoring the microwave transmission across the cavity at a frequency close to the cavity resonance, for example, by using standard homodyne or heterodyne techniques [39, 69]. This approach for reading out the qubit state through cavity transmission measurements has become standard practice.

Recently much effort has been devoted to the development of near quantum-limited superconducting amplifiers for single-shot detection of the qubit state. Specific milestones include observation of quantum jumps in a transmon qubit [70], heralded state preparation of single qubit states to eliminate initialization errors [71, 72], deterministic preparation of entangled states [50], stabilization of qubit Rabi oscillations using quantum feedback [73], and quantum teleportation [74]. The technology allows high readout speed [75] and entanglement over large distances [76]. While this approach works well for a small number of readout channels, the required superconducting amplifiers, cryogenic semiconducting postamplifiers, and quadrature mixers entail significant experimental overhead: the amplifiers often require biasing with a strong auxiliary microwave pump tone which must be isolated from the qubit circuit with bulky cryogenic isolators; moreover, there is no clear path to in-

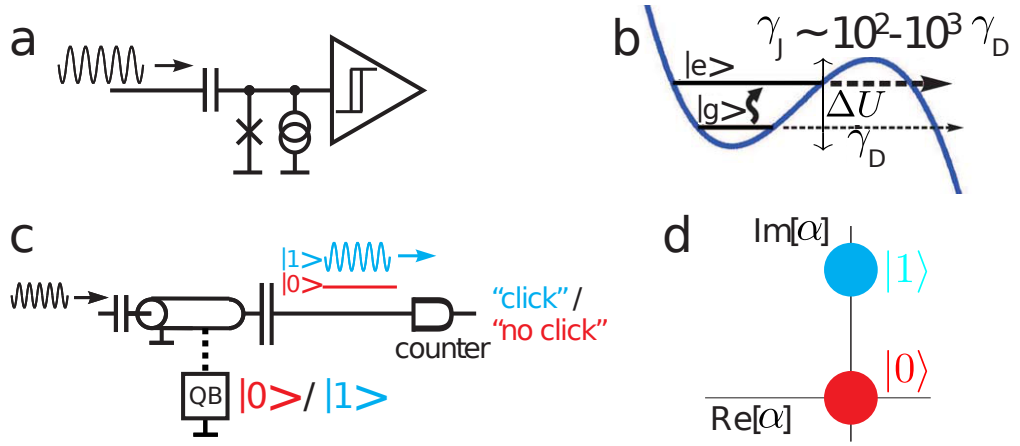

Figure 2.1: **(a)** Schematic diagram of the Josephson photomultiplier (JPM) circuit. The junction is biased with a dc current, and microwaves are coupled to the junction *via* an on-chip capacitor. In the simplest implementation, switching of the junction creates a voltage pulse that is read out by a room temperature comparator circuit. **(b)** Junction potential energy landscape. The junction is initialized in the ground state $|g\rangle$. An incident photon induces a transition to the first excited state $|e\rangle$, which rapidly tunnels to the continuum with rate γ_J. **(c)** Counter-based measurement in cQED. "Bright" and "dark" cavity pointer states result in binary digital output from the JPM: "click" or "no click". **(d)** In-phase (I) and quadrature (Q) phase space portrait of the cavity state after the ring-up, highlighting pointers to the $|0\rangle$ state in red and to the $|1\rangle$ state in blue.

tegrating heterodyne detection at low temperature to provide for a compact, scalable architecture.

An alternative approach that has not yet been considered is to measure the state of the qubit using a photon counter. In contrast to an amplifier, which performs a linear mapping of input modes $\hat{a}, \hat{a}^\dagger$ to output modes $\hat{b}, \hat{b}^\dagger$, a photon counter responds to the total power of the input signal $\hat{a}^\dagger\hat{a}$ in a nonlinear fashion: the presence or absence of photons projects the counter into one of two possible classical output states, irrespective of the phase of the input signal. In the optical frequency range, the prototypical photon counter is the avalanche photodiode [52, 77]: here, absorption of a single photon creates an electron-hole pair; the reverse bias of the *pn* junction sweeps the charge away from the depletion region and impact ionization generates additional

electron-hole pairs, leading to a large and easily measured classical current.

We have recently introduced a superconducting device that performs as a microwave-frequency analog of the avalanche photodiode [54, 59, 58]. The detector is a Josephson junction that is biased with a current such that the energy separation between the ground $|g\rangle$ and first excited $|e\rangle$ states in the metastable minima of the junction potential energy landscape is resonant with the energy of the incident microwaves (see Fig. 2.1a-b). Absorption of a single microwave photon promotes the junction from the $|g\rangle$ to the $|e\rangle$ state, which tunnels rapidly to the continuum, producing a large and easily measured voltage of order twice the superconducting gap voltage. We refer to the detector as the Josephson photomultiplier (JPM). The JPM provides an intrinsically broadband frequency response; as we will show here, single-shot measurement contrast around 95% – suitable for scalable surface codes [49] – is achievable; the detector requires no microwave biasing, facilitating wireup of complex multi-qubit circuits comprising many measurement channels; finally, the detector produces a binary digital output that interfaces well to scalable cold control circuitry based on Single Flux Quantum (SFQ) digital logic [78].

This paper is organized as follows. In Section II, we describe the basic principles of the JPM and discuss detector operation. In Section III, we present a detailed theoretical model of the proposed measurement protocol, with a focus on measurement contrast and back action. In Section IV, we discuss how close this scheme comes to a quantum non-demolition (QND) measurement, and in Section V we consider interactions with the environment, taking into account the full Jaynes-Cummings Hamiltonian between the cavity and the qubit. Section VI is devoted to a discussion of issues related to scaling this measurement approach to a large number of readout channels. In Section VII we present our conclusions.

2.2 Microwave Photon Counter Based on a Josephson Junction

A schematic diagram of the JPM is shown in Fig. 2.1a. The Josephson junction is biased in the supercurrent state with a current I_b that is slightly below the junction critical current I_0. The potential energy landscape $U(\delta)$ for the phase difference δ across the junction takes on a tilted-washboard form [79], with local potential minima characterized by a barrier height ΔU and plasma frequency ω_p (Fig. 2.1b). The circuit design and bias parameters are chosen so that there is a handful of discrete energy levels in each local

minimum of the potential; the JPM initially occupies the ground state $|g\rangle$. Microwaves that are tuned to the junction resonance induce a transition to the first excited state $|e\rangle$, which rapidly tunnels to the continuum. This tunnelling transition in turn leads to the appearance of a large voltage across the junction of order twice the superconducting gap. Absorption of a photon thus yields an unambiguous and easily measured "click".

The experimental protocol involves pulsing the bias point of the JPM for a finite interval of order 10s of ns so that the transition frequency between the $|g\rangle$ and $|e\rangle$ states is close to the frequency of the incident photons: at this point, the junction is in the "active" state, and there is high probability that absorption of a photon will induce a transition to the continuum. In the absence of resonant photons, there is a small, nonzero probability that the JPM will transition due to quantum tunnelling from $|g\rangle$, a dark-count event. JPM intrinsic contrast peaks for a bias such that $\Delta U/\hbar\omega_p \sim 2$ for a measurement interval that is roughly equal to the Rabi period of the coherent drive [58, 80]; for very short times, the interaction with the drive field is too weak to induce a transition, while for longer measurement times dark counts due to quantum tunnelling from the ground state degrade performance. In prior work, we have demonstrated efficiencies of order 90% for coherent drive corresponding to Rabi frequencies around 100 MHz for junctions with extremely modest coherence times of order a few ns [54].

In the context of qubit measurement, the utility of the JPM is its ability to map bright and dark cavity states to two distinct classical output states: "click" or "no click". It hence presents a measurement paradigm different from that of a linear amplifier and should be discussed in different terminology [81]. For example, the gain of a JPM at an infinitesimal input signal is negligible as such a signal will not activate it into the voltage state, whereas above a certain threshold the nonlinear gain is extremely high. A performance comparison can, however, be done on the level of the overall qubit measurement protocol.

In a conventional cQED measurement, the state of the qubit is encoded in the quadrature amplitudes of a weak microwave signal that is transmitted across the readout cavity. It is possible to access these amplitudes by preamplifying the signal using a low-noise linear amplifier followed by homodyne or heterodyne detection; assignment of the detected signal to the qubit $|0\rangle$ or $|1\rangle$ states is performed by subsequent post-processing and thresholding. In the following, we analyze an alternative protocol in which the state of the qubit is mapped to the photon occupation of the cavity. The JPM then provides a high-fidelity digital detector of cavity occupation (see Fig. 2.1c-d). The measurement provides no information about the phase of the transmitted microwaves, or indeed about the amplitude of the transmitted signal beyond the digital "click" / "no click" output of the JPM. As we show below, mea-

surement contrast achievable with the JPM is comparable to that achieved with quantum-limited linear amplifiers, while the JPM provides unique advantages in terms of scaling to a large number of measurement channels. We note that related proposals for photon counters were put forth recently that include both irreversible photon absorption [82, 53, 83] and non-destructive photon detection via nonlinearity of a transmission line coupled to transmons [55, 48].

2.3 cQED Measurement with a Microwave Photon Counter

The basic scheme for qubit measurement with the JPM is shown in Fig. 2.2. The qubit (resonating around 5 GHz) is coupled to a readout cavity (resonating around 6 GHz). As in the usual dispersive limit of the Jaynes-Cummings Hamiltonian (2.1), the cavity acquires a dispersive shift $\chi_Q \equiv g_Q^2/\Delta$ that depends on the state of the qubit. For the purposes of realizing a fast measurement, it is desirable to engineer a dispersive shift $\chi_Q/\pi \approx 10$ MHz, as opposed to the smaller dispersive shifts of order 1 MHz realized in typical cQED experiments. The measurement proceeds in three stages: (1) *Drive stage.* Here, we map the qubit state to microwave photon occupation of the readout cavity. A microwave pulse applied to the dressed frequency corresponding to qubit state $|1\rangle$ creates a "bright" cavity if and only if the qubit is in the excited state. If the qubit is in the ground state, the cavity acquires a non-negligible occupation at the start of the pulse, but it coherently oscillates back to the "dark" vacuum state upon completion of the drive pulse. During the drive stage the JPM idles at a frequency that is blue detuned from the cavity by around 1 GHz. (2) *Measurement stage.* Here, we map photon occupation of the cavity to the voltage state of the JPM ("click" or "no click"). The JPM is rapidly tuned into resonance with the cavity. A bright cavity induces a transition to the voltage state, while a dark cavity leaves the JPM in the supercurrent state. (3) *Reset stage.* It is advantageous to coherently depopulate the bright cavity in order to circumvent the need for the cavity to decay *via* spontaneous emission. However, since the depletion of the cavity due to interaction with the JPM is a stochastic process, so that neither the number of photons removed nor the back action on the cavity is perfectly known or reproducible, it is not possible to return the cavity precisely to the vacuum state. Nevertheless, an appropriate coherent pulse can return the cavity to a state that is close to the vacuum. The measurement pulse sequence is shown in the upper panel of Fig. 2.2.

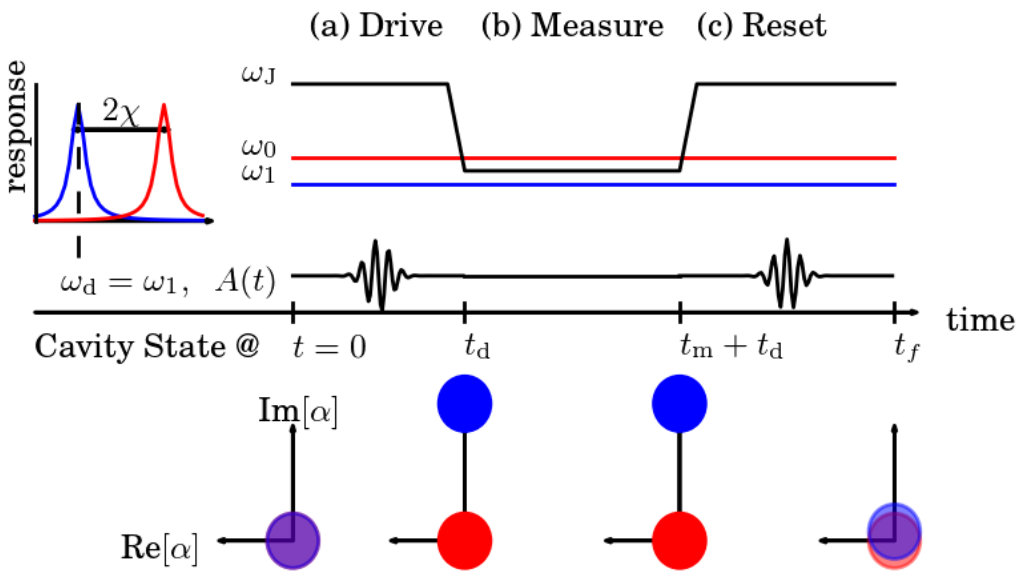

Figure 2.2: Schematic of the three-stage measurement protocol: the upper panel describes the relevant control, while the lower panel represents the corresponding cavity state. **(a)** In the drive stage, the cavity is driven strongly and coherently at the cavity frequency dressed by the qubit $|1\rangle$ state, $\omega_d = \omega_1 = \omega_C - \chi_Q + \chi_J$, for a duration $t_d = \pi/\chi_Q$ (assuming a square pulse). This projects the qubit onto either $|0\rangle$ or $|1\rangle$ and conditionally populates the cavity with a large number of photons $n \sim |\alpha_1|^2$ when the qubit is projected onto the $|1\rangle$ state. **(b)** During the measurement phase, the JPM is tuned into resonance with the cavity and allowed to interact; a bright cavity switches the JPM to its voltage state while a dark cavity leaves the JPM in the supercurrent state. This conditionally squeezes the cavity state by a small amount (not shown here). **(c)** In the reset stage, the cavity is again driven coherently at ω_d, conditionally displacing the cavity to a near-vacuum state.

In the dispersive regime of the qubit-resonator sytem, the unitary evolution of the full system is described by the Hamiltonian

$$\hat{H} = \hat{H}_{\text{eff}} + A(t)\left(\hat{a} + \hat{a}^\dagger\right) - \frac{\omega_J(t)}{2}\hat{\sigma}_z^J + g_J\left(\hat{a}\hat{\sigma}_J^+ + \hat{a}^\dagger\hat{\sigma}_J^-\right), \tag{2.2}$$

where $\omega_J(t)$ is the frequency of the JPM, $A(t)$ is the classical drive applied to the cavity, g_J is the cavity-JPM coupling, and $\hat{H}_{\text{eff}}$ is defined in Eq. (2.1). The JPM operators $\hat{\sigma}_J^\pm$ couple the ground and excited state of the JPM, which are separated by a frequency $\omega_J(t)$ but do not couple to the measured state. The JPM self-Hamiltonian contains $\hat{\sigma}_z^J = \text{diag}(1, -1, E)$. Here, the

energy of the measured state E is irrelevant once the tunnelling rates (which are not contained in this Hamiltonian as they require interaction with an environment) have been fixed independently. The measured state plays no role in the unitary dynamics of the system as it only couples incoherently to all other states, and the full dynamics of the JPM are described by a Lindblad-type master equation.

In the following we analyze the three stages of the measurement in detail.

2.3.1 Drive Stage

The goal of this stage is to prepare a photonic state in the cavity that is dependent on the qubit state, such that the conditional cavity states can later be distinguished by the JPM in the measurement stage. The JPM idles in this stage, biased far off-resonance from the cavity such that the effective interaction between the cavity and the JPM is dispersive, with a dispersive shift $\chi_{\mathrm{J}} \equiv g_{\mathrm{J}}^2/(\omega_{\mathrm{C}} - \omega_{\mathrm{J}})$.

The effective Hamiltonian for the cavity becomes

$$\hat{H}_{\mathrm{C}} = \tilde{\omega}_{\mathrm{C}} \hat{a}^\dagger \hat{a} + A(t) \left(\hat{a} + \hat{a}^\dagger \right), \tag{2.3}$$

where $\tilde{\omega}_{\mathrm{C}} \equiv (\omega_{\mathrm{C}} \pm \chi_{\mathrm{Q}} + \chi_{\mathrm{J}})$. We choose a classical drive $A(t) = a_0 \cos(\omega_{\mathrm{d}} t)$ for $0 \leq t \leq t_{\mathrm{d}}$ where a_0 is the drive strength, ω_{d} the drive frequency, and t_{d} the pulse length (for simplicity here we assume a square pulse). By setting $\omega_{\mathrm{d}} = \omega_{\mathrm{C}} - \chi_{\mathrm{Q}} + \chi_{\mathrm{J}}$ we obtain an effective cavity-drive detuning $\delta\omega = \tilde{\omega}_{\mathrm{C}} - \omega_{\mathrm{d}}$ that depends on the state of the qubit:

$$\delta\omega = \begin{cases} 2\chi_{\mathrm{Q}} & \text{for qubit in state } |0\rangle \\ 0 & \text{for qubit in state } |1\rangle. \end{cases} \tag{2.4}$$

For such a classical drive of duration t_{d}, the solution to Eq. (2.3) is easily obtained. Depending on the state of the qubit, the cavity will be in the coherent state $|\alpha_{0/1}\rangle$, with

$$\alpha_0 = -\frac{a_0}{4\chi_{\mathrm{Q}}} \left(e^{i2\chi_{\mathrm{Q}} t_{\mathrm{d}}} - 1 \right); \quad \alpha_1 = -\frac{i a_0}{2} t_{\mathrm{d}} \tag{2.5}$$

up to a global phase. We see that when the qubit is in state $|0\rangle$, the cavity occupation oscillates sinusoidally at a frequency set by the detuning of the drive pulse from the dressed cavity resonance. On the other hand, when the qubit is in state $|1\rangle$, the cavity occupation $|\alpha_1|^2$ grows monotonically in time. This is shown in Fig. 2.3, where we plot cavity occupation *versus* coherent drive time for the qubit in states $|0\rangle$ and $|1\rangle$. In order to maximize contrast

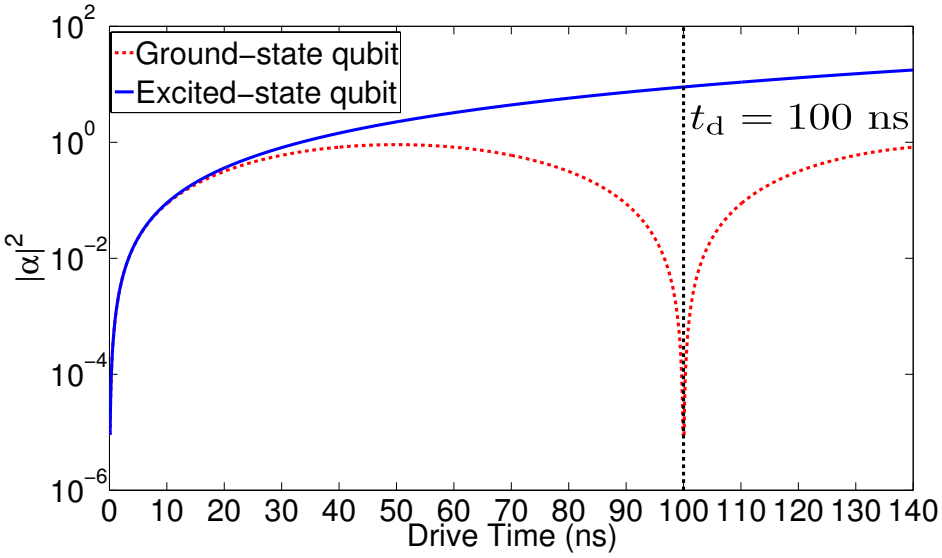

Figure 2.3: Cavity occupation as a function of the duration of the applied drive, t_d, for the qubit in states $|0\rangle$ and $|1\rangle$. Here $\chi_Q/\pi = 10$ MHz, such that the optimal drive time is $t_d = 100$ ns.

between the dark and bright cavity states to which the qubit states $|0\rangle$ and $|1\rangle$ are mapped, it is optimal to choose $t_d = \pi/\chi_Q$ such that $\alpha_0 = 0$ at the end of the drive stage. The length of the drive stage is therefore set by the requirement that $\alpha_0(t_d) = 0$ and not by the input cavity coupling, which is the inverse of the decay time of the cavity through its input port.

We assume the system starts in the state

$$|\Psi(0)\rangle = |0\rangle_C \otimes |\psi\rangle_Q \otimes |0\rangle_J, \tag{2.6}$$

where the qubit state $|\psi\rangle_Q = a|0\rangle + b|1\rangle$ can be prepared independently by the qubit drive line. After the drive stage, the system is left in the state

$$|\Psi(t_d)\rangle = \left(a|\alpha_0\rangle_C \otimes |0\rangle_Q + b|\alpha_1\rangle_C \otimes |1\rangle_Q\right) \otimes |0\rangle_J, \tag{2.7}$$

which can be verified by solving Eq. (2.2) analytically. In the case that $\alpha_0 = 0$, the cavity has nonzero occupation only when the qubit is in the excited state.

The drive stage can be thought of as the first step in a quantum measurement of the qubit state, as described in the pointer basis formalism of Zurek [84]. In this language, the cavity states $|\alpha_{0/1}\rangle$ form the pointer basis that is entangled with the qubit. Examining the reduced density matrix of

the qubit state

$$\hat{\rho}_{\mathrm{Q}} = \begin{pmatrix} |a|^2 & a^* b D \\ a b^* D & |b|^2 \end{pmatrix}, \tag{2.8}$$

we see that qubit coherence has been suppressed by a factor

$$D = \exp\left(-|\alpha_1 - \alpha_0|^2\right), \tag{2.9}$$

which quantifies the dephasing of the qubit induced by the interaction with the pointer basis (cavity). The dephasing would be complete if the pointer states were orthogonal. Moreover, mapping of the qubit $|1\rangle/|0\rangle$ states to bright/dark cavity states can be viewed as a coherent amplification step, as the information about the qubit state is now contained in a large number of photons. A more detailed discussion of the consequences of this overlap on the detection contrast and back action will be presented later.

As a result of the strong dephasing of the qubit state during the drive stage (quantified by the factor D), our multi-stage protocol explicitly exposes the role of the pre-measurement stage in quantum non-demolition (QND) readout. In particular, our protocol highlights the fact that in QND readout of the qubit state, measurement of the cavity pointer states is not the major source of qubit state dephasing. The qubit states are dephased during the pre-measurement, when qubit states and cavity pointer states are entangled, which in our case corresponds to the drive stage. The main role of the subsequent pointer state measurement (the measurement stage in our protocol) is to break unitarity and "freeze" the qubit in a dephased state. This distinction between pre-measurement and measurement is less obvious in qubit readout using a continuous cavity signal with linear amplification and heterodyne detection. The clear distinction between pre-measurement and measurement in our protocol allows for independent control of each stage, which can be used to achieve higher readout fidelity (as has been done here), and to study, both in theory and experiment, QND measurement and the pointer basis formalism with an explicit physical system in mind. A similar distinction between pre-measurement and measurement exists in a readout scheme in atomic cavity QED, albeit in a rather different parameter regime. This scheme employs dispersive coupling between the cavity and a travelling atom (pre-measurement) followed by atomic state detection via ionization (measurement) to read out the cavity state [85, 86].

2.3.2 Measurement Stage

After the drive stage, the qubit state information has been transferred to the cavity occupation. In the measurement stage, a measurement of the

cavity by the JPM will reveal the state of the qubit. During this stage, the JPM is brought into resonance with the dressed frequency of the cavity corresponding to the qubit $|1\rangle$ state, $\omega_J = \omega_C - \chi_Q$, in order to maximize detection in the case that the qubit is excited. In practice, precise tuning of the JPM bias point is not required due to the broad detection bandwidth of the JPM [58].

The Hamiltonian during this stage is that of Eq. (2.2) with $A(t) = 0$. In the following, we assume a cavity-JPM coupling $g_J/2\pi = 50$ MHz. In addition, the system evolves incoherently as a result of tunnelling (both bright and dark) and relaxation of the JPM. We consider tunnelling from both the JPM excited and ground states to the measured state, and relaxation from the excited state to the ground state, with corresponding rates γ_J, γ_D, and γ_R, respectively. Here we take $\gamma_J = 200$ MHz, $\gamma_D = 1$ MHz, and $\gamma_R = 200$ MHz; this relaxation rate corresponds to a junction with capacitance 100 pF directly connected to an environmental impedance of 50 Ω. The total evolution of the system can therefore be described by a Lindblad-type master equation with Lindblad operators corresponding to each incoherent process of the JPM, as outlined in more detail in our previous work [59, 58].

As the cavity-JPM coupling and bright count rate can be controlled independently of one another, they can be adjusted into an optimal regime for good measurement. As explained in more detail in our previous work [54, 58], the optimal regime for good measurement is when $g_J \sim \gamma_J$, as in this regime the bright count rate is large enough for a bright count to occur within the occupation time of the JPM (per Rabi cycle), while not so large as to result in a Zeno effect suppression of the cavity-JPM interaction. The coupling and bright count rate chosen for the numerical simulations presented here are well within the optimal regime for good measurement.

Starting from the output state of the drive stage, we numerically solve the master equation for the measurement stage to obtain the detection probability $P\left(|\alpha|^2, t_m\right)$ as a function of cavity occupation and measurement time t_m. In the case that the qubit starts in the $|0\rangle/|1\rangle$ state, the detection probability reduces to $P\left(|\alpha_{0/1}|^2, t_m\right)$. We define the qubit measurement contrast as the difference in detection probability between these two cases:

$$C = P\left(|\alpha_1|^2, t_m\right) - P\left(|\alpha_0|^2, t_m\right). \tag{2.10}$$

Clearly, the measurement contrast is optimized when $P\left(|\alpha_0|^2, t_m\right) = 0$, which requires that $\alpha_0 = 0$ and $\gamma_D = 0$. The measurement contrast has a maximal value of one if $|\alpha_1| \to \infty$, indicating a perfect measurement.

Figure 2.4(a) shows the detection probability as a function of both $|\alpha|^2$ and t_m for the system parameters previously discussed. For all coherent states

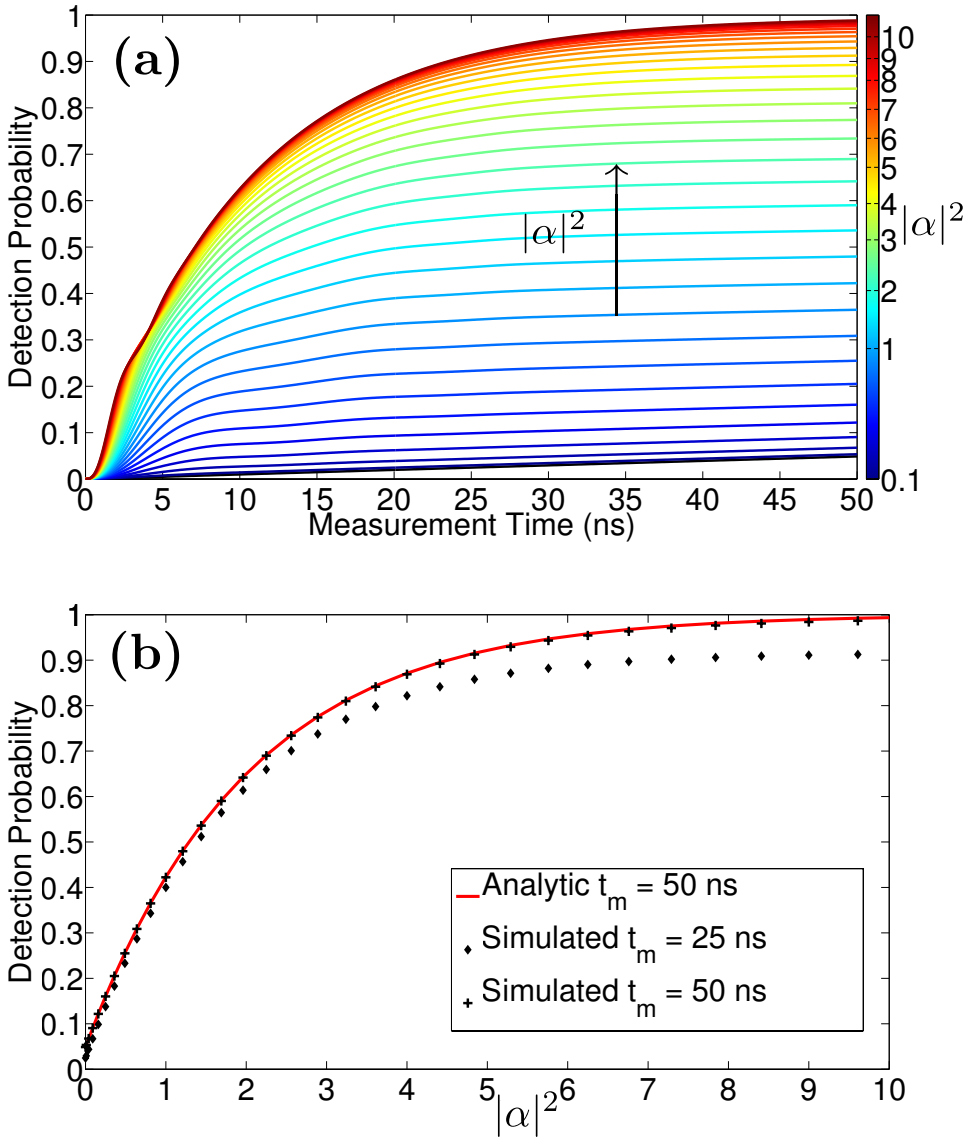

Figure 2.4: **(a)** Detection probability $P(|\alpha|^2, t_\mathrm{m})$ as a function of measurement time t_m (horizontal axis) and cavity occupation $|\alpha|^2$ (color) for system parameters $g_\mathrm{J}/2\pi = 50$ MHz, $\gamma_\mathrm{J} = 200$ MHz, $\gamma_\mathrm{D} = 1$ MHz and $\gamma_\mathrm{R} = 200$ MHz. **(b)** Detection probability $P(|\alpha|^2, t_\mathrm{m})$ as a function of cavity occupation $|\alpha|^2$, both numerical simulations and analytic fit, for $t_\mathrm{m} = 25$ and 50 ns.

with average photon number $|\alpha|^2 > 0$ we see similar behavior as a function of time, with saturation of the detection probability around 40 ns, irrespective of cavity occupation. The fact that the detection probability saturates at a value less than unity is explained by the two competing mechanisms for excitation loss in the JPM: measurement tunnelling and inelastic relaxation, only the former of which results in a bright count. The black curve in Fig. 2.4(a), $\alpha = 0$, is the detection probability for the cavity when the qubit is in the ground state, $P\left(|\alpha_0|^2 = 0, t_\mathrm{m}\right)$, and the fact that it is nonzero is due only to dark counts, which occur with a probability $P_\mathrm{D}(0,t) = 1 - e^{-\gamma_\mathrm{D} t}$.

In a simplified picture where energy in the detector automatically leads to a click, we would have

$$P(|\alpha|^2) = P_\mathrm{B}(|\alpha|^2) + (1 - P_\mathrm{B}(|\alpha|^2))P_\mathrm{D}, \tag{2.11}$$

where $P_\mathrm{B}(|\alpha|^2)$ is the bright count probability and $P_\mathrm{D} = P_\mathrm{D}(0,t)$ is the dark count probability, which we take to be independent of α. However, the detection mechanism of a JPM involves the coherent absorption of energy prior to a tunnelling transition to the classically observable voltage state. In the interval following absorption of a photon but prior to tunnelling, dark counts cannot occur as the JPM is in its excited state. This breaks the dark/bright symmetry of Eq. (2.11); as a result, this equation may no longer be valid. However, as it shows how dark counts are detrimental to measurement contrast, Eq. (2.11) is a good reference point to compare against, and will still be valid in some situations, such as when the JPM coupling rate is smaller than the bright tunnelling rate, i.e., $g_\mathrm{J} < \gamma_\mathrm{J}$.

Figure 2.4(b) shows the detection probability as a function of $|\alpha|^2$ for $t_\mathrm{m} = 25$ and 50 ns, along with an analytic fit to the data by Eq. (2.11), with P_B given by the curve

$$P_\mathrm{B}(|\alpha|^2, t_\mathrm{m} \to \infty) = 1 - \exp\left(-|\alpha|^2 \frac{\gamma_\mathrm{J}}{\gamma_\mathrm{J} + \gamma_\mathrm{R}}\right). \tag{2.12}$$

See Appendix 2.A for a derivation. The analytic curves for both $t_\mathrm{m} = 25$ and 50 ns are so similar on this scale that only $t_\mathrm{m} = 50$ ns is plotted. As can be seen, the analytic fit is valid when t_m is sufficiently large. For small t_m, Eq. (2.11) remains close to correct, but the approximation for P_B in Eq. (2.12) breaks down.

We have calculated detection probability $P\left(|\alpha|^2, t_\mathrm{m}\right)$ and measurement contrast *versus* measurement time t_m for $|\alpha_0|^2 = 0$, and $|\alpha_1|^2 = 10$; the results are shown in Fig. 2.5(a). The measurement contrast peaks at $\approx 95\%$ around 40 ns, indicating that a good choice for t_m is 40 ns. At longer times the measurement contrast will eventually begin to decrease, as $P\left(|\alpha_0|^2, t_\mathrm{m}\right)$

continues to increase while $P\left(|\alpha_1|^2, t_\mathrm{m}\right)$ asymptotes to near unity. In general, we observe that increasing α_1 increases the contrast, ultimately limited by the breakdown of the dispersive approximation to the Jaynes-Cummings Hamiltonian.

The contrast shown in Fig. 2.5(a) is for one set of system parameters, and in principle it is possible to obtain higher values of measurement contrast by optimizing over parameter space. Figure 2.5(b) shows the optimal measurement contrast as a function of bright count rate, γ_J, for various bright states $|\alpha_1|^2$. The ratio of the bright and dark count rates is set by fabrication parameters of the JPM, and therefore remains fixed at $\gamma_\mathrm{J}/\gamma_\mathrm{D} = 200$. However, the inelastic relaxation rate remains fixed as γ_J changes, such that $\gamma_\mathrm{R} = 200$ MHz regardless of the value of γ_J. As can be seen in Fig. 2.5(b), within experimentally reachable parameter regimes contrast greater than 95% is possible.

Measurement contrast is ultimately limited by the possibility of misidentifying the qubit state. Misidentification of the excited state as the ground state is due to the nonzero vacuum component of the coherent state $|\alpha_1\rangle$ as well as to internal photon loss. This occurs with a probability $1-P\left(|\alpha_1|^2, t_\mathrm{m}\right)$, which is bounded below by $e^{-|\alpha_1|^2}$ (occuring when $\gamma_\mathrm{R} = 0$). Misidentification of the ground state as the excited state is the result of a dark count (assuming $\alpha_0 = 0$), and the probability of misidentification in this case is exactly $P_\mathrm{D}(0, t_\mathrm{m})$ discussed earlier. The problem of misidentification, and the fact that measurement contrast is less than unity even for $\gamma_\mathrm{R}, \gamma_\mathrm{D} = 0$, is related to the basis of our measurement protocol and will be discussed in more detail in Section IV.

After the measurement stage, if the JPM absorbs a photon and switches out of the supercurrent state, classical emission due to this switching process could induce relaxation in the qubit or produce a spurious population in the readout cavity that would spoil the reset pulse [87]. The resulting population is proportional to the energy spectral density of the classical current drive at the qubit or cavity frequency. A straightforward approach to address this would be to install a microwave isolator between the cavity and JPM, as in conventional cQED experiments, where one inserts one or more cryogenic isolators between the measurement cavity and the superconducting preamplifier. The breaking of time-reversal symmetry by the isolator allows signals to travel from the cavity to the readout device with minimal loss, while back action noise is heavily attenuated. However, we anticipate that this classical back action can be greatly suppressed by an appropriate choice of JPM parameters to suppress harmonics of the switching transients at the qubit and cavity frequencies, or by shunting the JPM by an appropriate admittance to prevent a full switch of the JPM phase to the running state. Alternatively, it

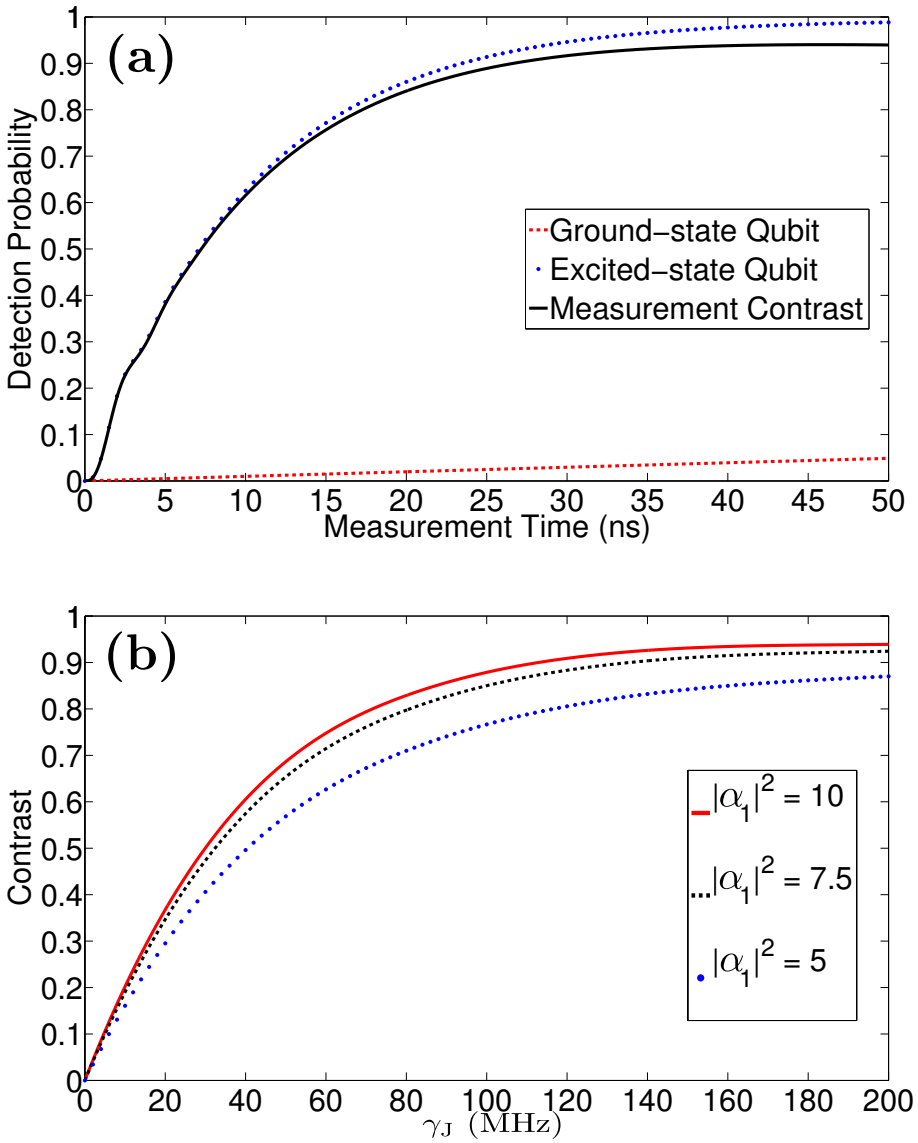

Figure 2.5: **(a)** Excited qubit detection probability $P(|\alpha_1|^2, t_m)$, ground qubit detection probability $P(|\alpha_0|^2, t_m)$, and measurement contrast *versus* measurement time. Here $|\alpha_1|^2 = 10$ and $|\alpha_0|^2 = 0$, with system parameters as before. **(b)** Measurement contrast as a function of bright count rate γ_J, for various $|\alpha_1|^2$ and $t_m = 50$ ns. The relaxation rate remains fixed at $\gamma_R = 200$ MHz, while the dark count rate changes such that the ratio $\gamma_J/\gamma_D = 200$ is unchanged.

might also be possible to eliminate a cryogenic isolator by incorporating on the JPM chip tunable impedance-matching circuitry, as this would allow for the realization of a strong impedance mismatch between the cavity output and JPM immediately after the end of the measurement stage.

2.3.3 Reset Stage

The final stage is to remove the energy from the cavity, ideally leaving the cavity-qubit system in the conditional states $|0\rangle_C|0\rangle_Q$ or $|0\rangle_C|1\rangle_Q$ to allow for additional operations on the qubit. This can be achieved through cavity decay by simply waiting long enough; however, because the total cavity decay time may be comparable to the qubit T_1, it is preferable to actively reset the cavity.

After the measurement stage, the cavity is either in the vacuum state or the state $\hat{B}_J\hat{B}_1^{N-1}|\alpha_1\rangle$. Here, $\hat{B}_{J,1}$ are the back action operators [59] on the cavity due to JPM tunnelling and inelastic relaxation, respectively, and N is the number of photons removed from the cavity by the JPM. These back action operators interpolate between the standard lowering operator $\hat{B} = \hat{a}$ and the subtraction operator $\hat{B} = \hat{a}\hat{n}^{-1/2}$ [59]. We neglect for the moment the classical back action on the cavity due to the transient current that develops when the JPM switches to the voltage state. As a starting point for reset, we will assume that $\hat{B}_J\hat{B}_1^{N-1}|\alpha_1\rangle \approx |\alpha_M\rangle$ even with large γ_R, with

$$|\alpha_M|^2 = \mathrm{Tr}\left[\hat{a}^\dagger\hat{a}\hat{B}_J\hat{B}_1^{N-1}|\alpha_1\rangle\langle\alpha_1|\hat{B}_J^\dagger\hat{B}_1^{\dagger N-1}\right], \tag{2.13}$$

the average photon number of the cavity state after measurement.

At the end of the reset stage, we desire the cavity to be in the vacuum state independent of the qubit state, and thus we must invert the drive stage. Consider a Hamiltonian of the form of Eq. (2.3), with a more general drive $A(t) = a_1\cos(\omega_d t + \phi)\Theta(t_d - t)$, where $t_d = \pi/\chi_Q$ as before. The unitary operation applied to the cavity is then

$$\hat{U}_r = \mathbb{I}_C \otimes |0\rangle\langle 0|_Q + \hat{D}(\beta) \otimes |1\rangle\langle 1|_Q. \tag{2.14}$$

Here $\hat{D}(\beta)$ is the displacement operator on the cavity, with

$$\beta = \frac{-ia_1 t_d}{2} e^{-i\phi}.$$

Thus, by choosing a_1 such that $(a_1 t_d)/2 = |\alpha_M|$ and setting $\phi = (2n+1)\pi, n \in \mathbb{Z}$, we have $\beta = -\alpha_M$. Under these conditions, the operation $\hat{U}_r$ will leave the cavity in the vacuum state independent of the qubit state, and will do

so with an operation time $t_r = t_d$, significantly shorter than the total decay time of the cavity.

However, after detection by a JPM the state of the cavity is not a coherent state; thus there does not exist a displacement operator $\hat{D}(\beta)$ that will map it identically to the vacuum state. One can quantify the resulting deviation from vacuum by calculating

$$E(\alpha_1, N) = 1 - \frac{1}{A^2}|\langle 0|D(-\alpha_M)\hat{B}_J\hat{B}_1^{N-1}|\alpha_1\rangle|^2, \tag{2.15}$$

where A is the normalization of the state after measurement. This error will depend on the form of the back action. Assuming all back actions can be expressed in terms of subtraction operators as in [59], we find

$$\begin{aligned} E(\alpha_1, N) &= 1 - \frac{1}{P_N}|\langle -\alpha_M|\hat{B}_-^N|\alpha_1\rangle|^2 \\ &= 1 - \frac{1}{P_N}\left| e^{-\frac{|\alpha_M|^2+|\alpha_1|^2}{2}} \sum_{n=0}^{\infty} \frac{\alpha_M^n \alpha_1^{n+N}}{\sqrt{n!(n+N)!}} \right|^2 . \end{aligned} \tag{2.16}$$

Here, the normalization A^2 is the probability of N photons being subtracted [88], $P_N = 1 - \frac{\Gamma(N,|\alpha_1|^2)}{\Gamma(N)}$, where $\Gamma(N, |\alpha_1|^2)$ is the upper incomplete Gamma function. The error of this reset pulse is shown in Fig. 2.6 for different values of N and as a function of $|\alpha_1|^2$. As can be seen, the maximal error increases with increasing N, but for all N the error tends to zero as $|\alpha_1| \to \infty$. In reality, as the value of N is not fixed, a better estimate for the average error can be obtained by averaging over the error traces shown in Fig. 2.6. Note that if the back action operator is closer to the standard photon lowering operator $\hat{a}$, this figure of merit will improve as the coherent states are eigenstates of this operator, and can be moved to vacuum exactly.

The possibility exists that more complicated pulse sequences during the reset phase will be able to map the cavity state identically to the vacuum; however, consideration of such sequences is beyond the scope of this work. In any case, the error of the reset pulse shown here does not affect the success of qubit readout.

2.4 QNDness of the Measurement

Ideally, we would like our measurement to project the qubit into its bare basis, $\{|0/1\rangle_Q\}$, hence implementing a quantum nondemolition (QND) measurement. A hallmark of QND measurement is that a repeated measurement leads to the same result with certainty. Our measurement scheme starts from

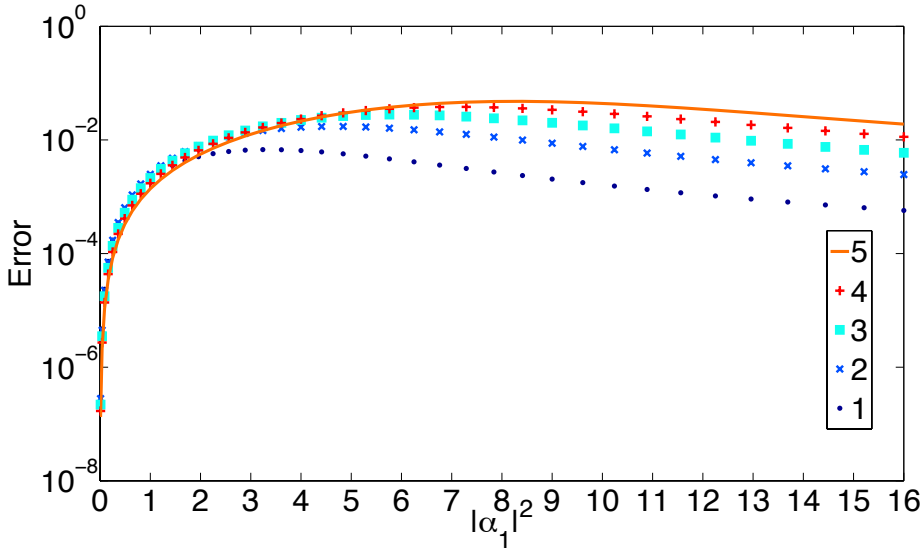

Figure 2.6: Numerically evaluated overlap error for the reset pulse described in the text. The number of photons N removed from the cavity is shown in the legend.

the dispersive Hamiltonian of Eq. (2.1) in the cavity ring-up phase, which is QND in the sense that the qubit and the pointer coupling commute. However, the process of destructive photon absorption necessarily results in a deviation from QNDness, which we analyze in detail below. Even in the case of an ideal measurement ($\gamma_R, \gamma_D = 0$ and $t_m \to \infty$), the potential misidentification of the two states leads to a QND error. Starting from the state in Eq. (2.7), the measurement projects the qubit conditionally onto the states

$$|\psi_0\rangle = \frac{ae^{-|\alpha_0|^2/2}|0\rangle_Q + be^{-|\alpha_1|^2/2}|1\rangle_Q}{\sqrt{|a|^2e^{-|\alpha_0|^2} + |b|^2e^{-|\alpha_1|^2}}} \tag{2.17}$$

$$|\psi_1\rangle = \frac{a\sqrt{1-e^{-|\alpha_0|^2}}|0\rangle_Q + b\sqrt{1-e^{-|\alpha_1|^2}}|1\rangle_Q}{\sqrt{|a|^2(1-e^{-|\alpha_0|^2}) + |b|^2(1-e^{-|\alpha_1|^2})}}. \tag{2.18}$$

Even for $\alpha_0 = 0$ these states are non-orthogonal (and not equal to the ideal QND post-measurement states), and their overlap is related to the overlap of the cavity pointer states $|\alpha_{0/1}\rangle$. This overlap is what allows misidentification to occur, ultimately limiting the contrast and QNDness.

If we do not condition on the measurement outcome, the effect of a perfect QND measurement is the quantum process defined by the map

$$a|0\rangle + b|1\rangle \longrightarrow |a|^2|0\rangle\langle 0| + |b|^2|1\rangle\langle 1|, \tag{2.19}$$

which completely destroys all coherence in the qubit state, while maintaining relative populations. We can describe this quantum process by its Choi matrix $\hat{\mathcal{C}}_{\text{per}}$ (see Appendix 2.B), and can compare this to the Choi matrix $\hat{\mathcal{C}}_{t_\text{m}}$ describing our measurement protocol (which is a function of the measurement time t_m) using the following Choi matrix fidelity

$$\mathcal{F}_{t_\text{m}} = \frac{\left(\text{Tr}\left[\sqrt{\sqrt{\hat{\mathcal{C}}_{\text{per}}}\hat{\mathcal{C}}_{t_\text{m}}\sqrt{\hat{\mathcal{C}}_{\text{per}}}}\right]\right)^2}{\text{Tr}\left[\hat{\mathcal{C}}_{\text{per}}\right]\text{Tr}\left[\hat{\mathcal{C}}_{t_\text{m}}\right]}. \tag{2.20}$$

As this fidelity compares the unconditional measurement protocol, it does not contain information about the success of the measurement (which we believe is well described by the contrast), but instead quantifies how close the possible qubit output states are to the desired ones. As a result, by choosing ideal QND measurement as our reference process, we can directly quantify the QNDness of our measurement protocol.

As we are examining the unconditional measurement process, any measurement time dependence in $\hat{\mathcal{C}}_{t_\text{m}}$ will be due to changes in the back action of JPM measurement on the cavity that change the post-measurement cavity state, and therefore modify the coherence of the post-measurement qubit state. However, for $\alpha_1 \gg \alpha_0$ sufficient decoherence of the qubit state has occurred during the drive stage that the resultant measurement time dependence of the fidelity is several orders of magnitude smaller than the average value, and in practice we can set $\mathcal{F}_{t_\text{m}} = \mathcal{F}_\infty$. Using Eqs. (2.17) and (2.18) we can calculate $\mathcal{F}_\infty$ analytically in the ideal case when $\gamma_\text{R}, \gamma_\text{D} = 0$ (see Appendix 2.B):

$$\begin{aligned}\mathcal{F}_\infty &= \frac{1}{2}\left(1 + \sqrt{1 - K(\alpha_0,\alpha_1)^2}\right) \\ K(\alpha_0,\alpha_1) &= e^{-\frac{1}{2}\left(|\alpha_0|^2+|\alpha_1|^2\right)} + \sqrt{\left(1-e^{-|\alpha_0|^2}\right)\left(1-e^{-|\alpha_1|^2}\right)}.\end{aligned} \tag{2.21}$$

For $|\alpha_0|^2 = 0$ and $|\alpha_1|^2 = 4$, we already have $\mathcal{F}_\infty > 99\%$. For $|\alpha_1|^2 = 10$ as used elsewhere, $\mathcal{F}_\infty > 99.99\%$. Ultimately, this value of the fidelity should be considered the fundamental limit of our protocol as it corresponds to the ideal case, ignoring both JPM relaxation and dark counts, as well as other environmental interactions.

When JPM relaxation is non-negligible ($\gamma_\text{R} \neq 0$), even for $t_\text{m} \to \infty$ the measurement conditionally projects the qubit onto mixed states rather than the pure states of Eqs. (2.17) and (2.18), as even for $\alpha_0 = 0$, $|\psi_0\rangle$ is mixed incoherently with a $|1\rangle\langle 1|_\text{Q}$ component. Similarly, dark counts cause

mixing of the state $|\psi_1\rangle$ as they incoherently add a $|0\rangle\langle 0|$ component to $|\psi_1\rangle$. Therefore, to describe back action, we can use POVM (positive-operator valued measure) elements for the qubit state to describe the map onto the post-measurement state. While full determination of these POVM elements is beyond the scope of this work, the unconditional quantum process $\hat{\mathcal{C}}_{t_\mathrm{m}}$ is also directly affected by changes in the POVM elements, such that it is quantitatively different when $\gamma_\mathrm{R}, \gamma_\mathrm{D} \neq 0$. However, the average value of the fidelity is nearly the same, and as changes to the fidelity with measurement time are several orders of magnitude smaller than the average value, the fidelity is not a good measure to compare the ideal case with that for $\gamma_\mathrm{R}, \gamma_\mathrm{D} \neq 0$.

Therefore, to qualitatively study the deviations from QNDness introduced by JPM relaxation and dark counts, we examine the probability that repeated measurements (within qubit T_1) will give the same measurement result. Consider single measurement probabilities P_a, where $a \in \{0, 1\}$ is the measurement outcome, and joint measurement probabilities P_{ab} where a, b are the outcomes of the second and first measurements, respectively. For an ideal QND measurement as defined above, we have

$$P_{00} = P_0, \quad P_{01} = P_{10} = 0, \quad P_{11} = P_1. \tag{2.22}$$

When JPM relaxation and dark counts are taken into account, none of these relationships hold. This is generally a result of the fact that our protocol can misidentify the qubit state (due to dark counts, energy relaxation, or less than unit contrast), so that the second event does not occur with unit probability. In particular, due to dark counts $P_0 \neq P_{00}$; similarly, due to the probability of not detecting a photon for a given cavity state or mistakenly measuring the vacuum component of the $|\alpha_1\rangle$ state, we have $P_{11} \neq P_1$. P_{11} can also be further modified by imperfect reset of the cavity. The symmetry between P_{01} and P_{10} is not broken by misidentification; however, they are both nonzero. On top of these misidentifications, QNDness can also be limited by corrections beyond the dispersive Hamiltonian as discussed in the next section.

2.5 Environmental Interactions and Corrections Beyond the Dispersive Hamiltonian

So far the discussion has focused on a closed qubit-cavity subsystem. When we consider interactions with the environment, it is apparent that the dominant effects are qubit and cavity relaxation. The timescale of these effects

depends heavily on the frequency of the JPM, as it is most strongly coupled to environmental modes.

During the drive and reset stages of the measurement protocol, the JPM idles at a frequency that is far blue detuned from the cavity or qubit resonances. As a result, the leading order decay channel for both the cavity and the qubit is through the cavity's input port. If we take a cavity decay rate $\kappa \approx 100$ kHz, we find a qubit lifetime limitation of $T_1^\kappa \approx 2$ ms for vacuum in the cavity [43] (see Appendix 2.C for further details), and this T_1^κ will in fact increase with higher cavity occupation [89], though this is a higher order effect not considered in our evaluation. This Purcell limited qubit T_1 can only be calculated by first considering the full Jaynes-Cummings Hamiltonian when deriving the master equation for the coupled system, and so it is inherently not contained in the dispersive picture. Essentially, induced qubit T_1 can be understood by observing that the eigenstates of the full JC Hamiltonian are always dressed (albeit weakly at strong detuning), and thus decay of the dressing cloud can lead to decay of the eigenstate.

In addition, while spontaneous emission of the cavity through its input port is inconsequential, emission toward the JPM during the drive stage will degrade the preparation of the cavity pointer states, with the dominant effect being a nonzero occupation $|\alpha_0|^2$ of the $|0\rangle_Q$-state pointer upon completion of the drive stage. However, this effect is very small due to the large cavity-JPM detuning during the drive stage, and so it only minimally affects the contrast.

During the measurement stage, the JPM is brought on resonance with the cavity, and cavity decay through the JPM is desirable, since it amounts to bright tunnelling or JPM relaxation. However, as the cavity-JPM states hybridize, qubit decay through the JPM is also possible, as a result of beyond-dispersive effects identical to those for qubit Purcell decay discussed previously. Through a procedure similar to that of [43], we obtain a JPM-limited qubit lifetime of $T_1^{\gamma_R} \approx 2$ μs during the measurement stage for vacuum in the cavity, considerably shorter than $T_1^\kappa \approx 2$ ms (see Appendix 2.C for further details). For an occupied cavity the situation is more complex, due to additional excitations as well as stimulated emission channels, but we find that to lowest order in g_Q/Δ the qubit lifetime increases as cavity occupation increases, and that for $|\alpha|^2 = 10$ one would expect a qubit lifetime of $T_1^{\gamma_R} \approx 40$ μs.

However, numerical simulations (see Fig. 2.7(a)) indicate that there is no appreciable qubit decay probability during the overall measurement process. We attribute this to the fact that the global state of the system is frozen once the JPM is in the measured state, and since $\gamma_J \gg 1/T_1^{\gamma_R}$, this occurs long before any appreciable qubit decay. In fact, we expect only a 0.05% change

in the qubit state due to JPM-mediated decay (see Appendix 2.C for further details), which is completely washed out by other effects in Fig. 2.7(a). In other words, a seemingly short induced lifetime during the measurement stage is inconsequential if the associated relaxation channel is only open for a short time. This implies that a working point with a very fast bright tunnelling rate is optimal.

The qubit also experiences dephasing due to low frequency noise at the JPM with a characteristic timescale $T_\phi^{\gamma_J}$. However, as the ideal cQED measurement protocol should maximally dephase the qubit state, this low frequency noise does not affect the fidelity or measurement contrast of our protocol.

To quantify measurement degradation due to beyond-dispersive effects, we compare the process fidelity of Eq. (2.20) for dispersive qubit-cavity coupling with that for the full Jaynes-Cummings Hamiltonian. Figure 2.7(b) shows the fidelity as a function of measurement time, for similar parameters as used throughout and $|\alpha_1|^2 = 9$. As expected, the dispersive fidelity changes only minimally as a function of measurement time, while the Jaynes-Cummings fidelity both oscillates and grows with measurement time. Crucially, the fidelity for the full Jaynes-Cummings Hamiltonian is still approximately 98%, i.e., not significantly less than for the dispersive Hamiltonian. It is the focus of future study to improve this number.

Finally, we have examined both the cavity occupation during the drive stage and the measurement contrast for the full Jaynes-Cummings Hamiltonian. For the drive stage the major effect is a small shift in the time t_d at which the cavity occupation is minimized for the qubit in the ground state, and an increase in the minimum occupation $|\alpha_0|^2$ (Fig. 2.8(a)). This results in a reduction of the contrast (as can be seen Fig. 2.8(b)); however, this reduction in contrast is not significant enough to seriously degrade the success of our measurement protocol.

2.6 Scalability of Counting Measurement

A useful multiqubit processor comprising hundreds if not thousands of qubits will require a large number of measurement channels with their associated wiring, filtering, and isolation. It is therefore important not only to examine the ultimate performance of a single measurement channel, but also to consider prospects for scaling to many measurement channels. From the standpoint of scalability, JPM-based counter measurement possesses several unique advantages compared to conventional heterodyne measurement based on low-noise superconducting amplifiers.

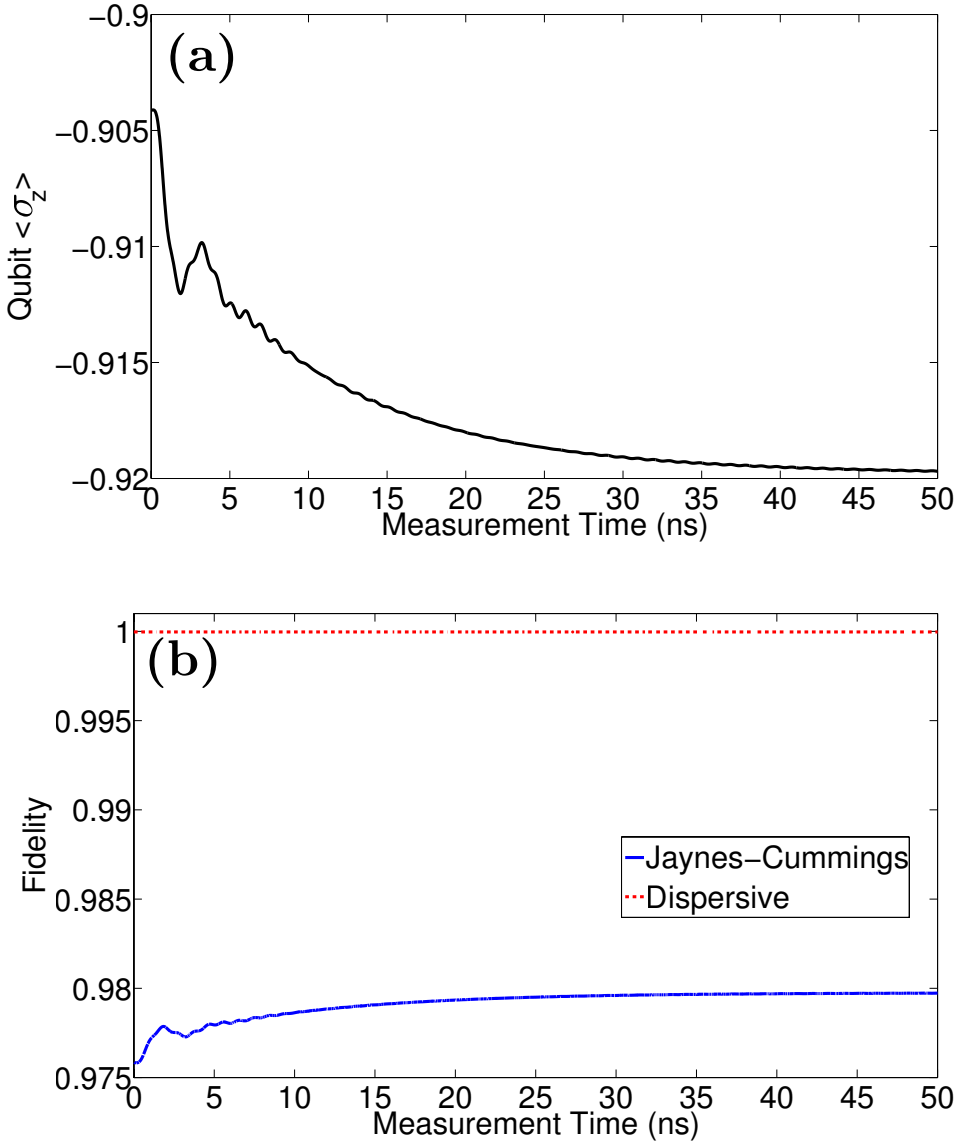

Figure 2.7: **(a)** Qubit σ_z expectation for the qubit initially in the excited state versus measurement time (Jaynes-Cummings Hamiltonian) and **(b)** process fidelity of qubit readout for both the dispersive Hamiltonian and the Jaynes-Cummings Hamiltonian. Coupling strength and tunnelling rates are as used throughout. Here $|\alpha_0|^2 = 0$ and $|\alpha_1|^2 = 9$.

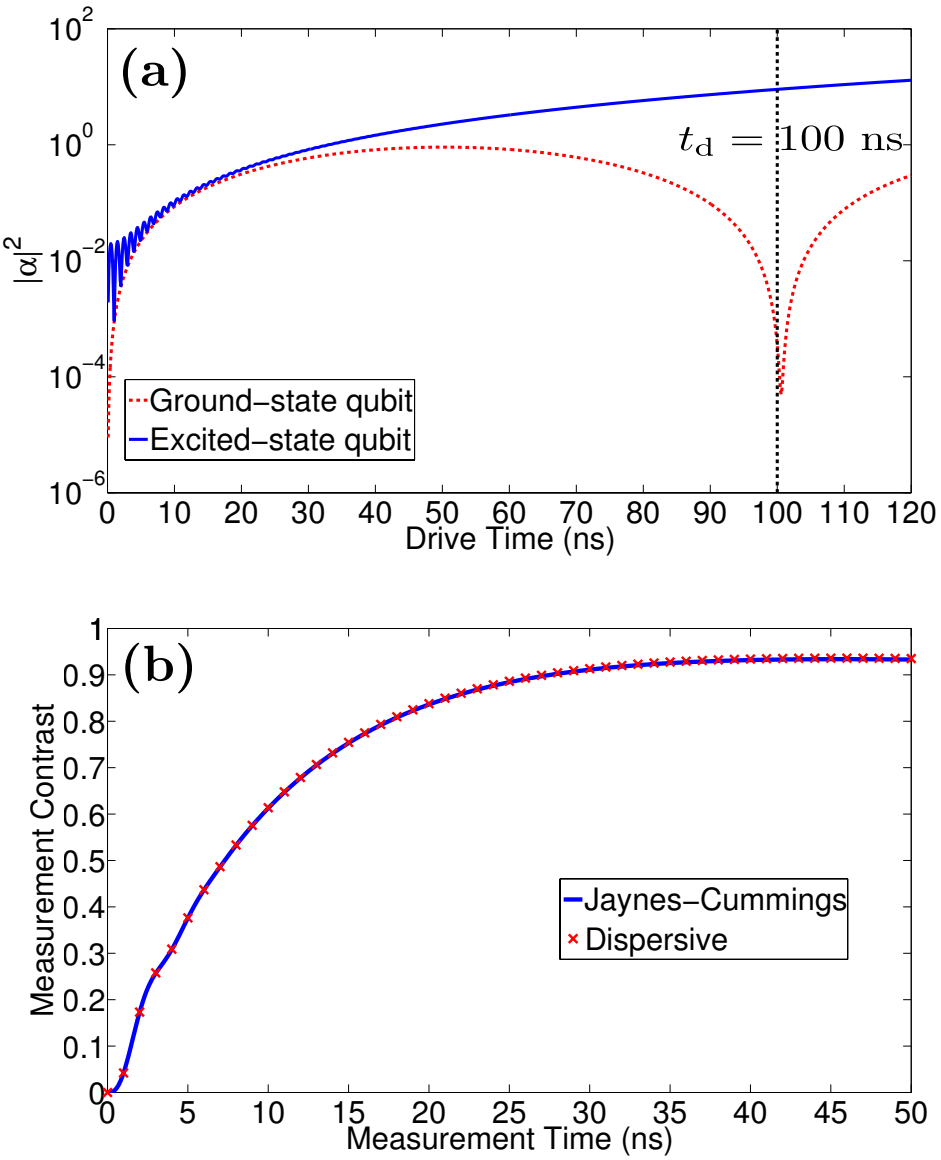

Figure 2.8: **(a)** Cavity occupation during the drive stage for the full Jaynes-Cummings Hamiltonian. **(b)** Measurement contrast for the dispersive Hamiltonian and the Jaynes-Cummings Hamiltonian. As elsewhere, $\chi_Q/\pi = 10$ MHz, $g_J/2\pi = 50$ MHz, $\gamma_J = 200$ MHz, $\gamma_D = 1$ MHz and $\gamma_R = 200$ MHz. In both plots, the drive strength is chosen such that $|\alpha_1|^2 = 9$ for $t_d = 100$ ns for the dispersive Hamiltonian.

The JPM requires only relatively low-bandwidth dc wiring for biasing, thus eliminating the need for bulkier cryogenic coaxial lines and microwave attenuators. Moreover, operation of the JPM requires no microwave pump tone, eliminating a major source of cost, complexity, and deleterious crosstalk in conventional cQED circuits. In addition, because the output signal of the JPM is of the order of twice the superconducting gap, no cryogenic amplifiers are needed and the JPM signal can be detected with straightforward room-temperature electronics. Alternatively, the binary digital output of the JPM provides a natural interface to the SFQ-logic family. Here, classical bits are stored in the form of quantized voltage pulses whose time integral equals the superconducting flux quantum $\Phi_0 = h/2e$. Optimized SFQ circuits can be clocked at 100s of GHz, and they offer orders of magnitude lower dissipation than conventional CMOS logic. The integration of a classical SFQ control circuit in the multiqubit cryostat would yield significant reductions in power consumption, latency, and overall system footprint.

The large intrinsic bandwidth of the JPM (approaching 1 GHz) [58] also allows for the possibility of time-domain multiplexing. Multiple qubits, each with a separate readout cavity at slightly different frequencies, could be interrogated with a single JPM by selectively addressing each cavity with drive pulses at different frequencies. While the "click"/"no click" output of the JPM does not enable frequency-domain multiplexing of the cavity readout, it is possible to multiplex instead by staggering the readout of the cavities in time, with an offset between cavity measurements of order 10s of ns.

2.7 Conclusion

In conclusion, we have outlined a new readout scheme for superconducting quantum bits using selective cavity ring-up and photodetection. We show that even without detailed optimization, our measurement protocol is compatible with the requirements of fault tolerance, with achievable measurement contrast greater than 95% in measurement times of order 100 ns. Counter-based qubit measurement possesses distinct advantages in terms of scalability, with simple wireup and dc biasing requirements and the prospect of multiplexing in the time domain. Finally, as the counter maps quantum information to a binary digital output without the need for room-temperature heterodyne detection and post-processing, our scheme provides a natural interface between a superconducting quantum processor and cryogenic classical control circuitry based on the SFQ digital logic family.

Acknowledgements

Supported by the Army Research Office under contract W911NF-14-1-0080. LCGG, EJP, and FKW also acknowledge support from the European Union through ScaleQIT and LCGG from NSERC through an NSERC PGS-D. CX, MV and RM were also supported by NSF grant No. DMR-1105178.

Appendix

2.A Derivation of the Analytic Expression for the Bright Count Rate

Following [58], we begin by assuming we have a dark count-free JPM coupled to a cavity in an N-photon Fock state. A single photon in the cavity would cause a bright count with probability $P_1 = \gamma_J/(\gamma_R + \gamma_J)$, where γ_J is the bright tunnelling rate and γ_R is the inelastic relaxation rate of the JPM, as defined before. However, if instead the JPM relaxes back to the ground state, the second photon in the cavity will cause a bright count with probability $P_2 = [\gamma_R/(\gamma_R + \gamma_J)]P_1$, where the first factor is the probability that the first photon is lost due to inelastic relaxation. Therefore, for the nth photon, we have

$$P_n = \left(\frac{\gamma_R}{\gamma_R + \gamma_J}\right)^{n-1} \frac{\gamma_J}{\gamma_R + \gamma_J}.$$

Summing up all probabilities for $n = 1, \ldots, N$, we obtain

$$P_N = 1 - \left(\frac{\gamma_R}{\gamma_R + \gamma_J}\right)^N = 1 - \exp\left(-N \ln\left(1 + \frac{\gamma_J}{\gamma_R}\right)\right).$$

For a coherent state, we improve the estimate by averaging over N for a state with given $|\alpha|^2$:

$$P(|\alpha|^2) = \sum \frac{|\alpha|^{2N}}{N!} e^{-|\alpha|^2} P_N = 1 - \exp\left(-|\alpha|^2 \frac{\gamma_J}{(\gamma_J + \gamma_R)}\right). \tag{2.23}$$

This analytic expression is valid for $\gamma_R \gtrsim \gamma_J$, assuming that all rates are independent of the number of photons in the cavity. This assumption implies that the photon excites the JPM faster than both rates γ_R and γ_J, and is valid for long measurement times.

2.B Analytic Derivation of Fidelity in the Ideal Case

To calculate $\mathcal{F}_\infty$, we begin by defining the unconditional map on the qubit state (with $\gamma_\mathrm{D}, \gamma_\mathrm{R} = 0$) using Eqs. (2.17) and (2.18) by

$$\mathcal{E}_\infty\left(|\psi\rangle\langle\psi|\right) = P_0|\psi_0\rangle\langle\psi_0| + P_1|\psi_1\rangle\langle\psi_1|, \tag{2.24}$$

for an arbitrary initial qubit state $|\psi\rangle = a|0\rangle + b|1\rangle$. The "click"/"no click" probabilities for such an input state are given by

$$P_0 = |a|^2 e^{-|\alpha_0|^2} + |b|^2 e^{-|\alpha_1|^2}, \tag{2.25}$$

$$P_1 = |a|^2(1 - e^{-|\alpha_0|^2}) + |b|^2(1 - e^{-|\alpha_1|^2}). \tag{2.26}$$

In light of this, Eq. (2.24) becomes

$$\begin{aligned}\mathcal{E}_\infty\left(|\psi\rangle\langle\psi|\right) = |a|^2|0\rangle\langle 0| + |b|^2|1\rangle\langle 1| \\ + ab^* K(\alpha_0,\alpha_1)|0\rangle\langle 1| + a^* b K(\alpha_0,\alpha_1)|1\rangle\langle 0|,\end{aligned} \tag{2.27}$$

where $K(\alpha_0, \alpha_1)$ is as defined in Eq. (2.21):

$$K(\alpha_0,\alpha_1) = e^{-\frac{1}{2}\left(|\alpha_0|^2+|\alpha_1|^2\right)} + \sqrt{\left(1 - e^{-|\alpha_0|^2}\right)\left(1 - e^{-|\alpha_1|^2}\right)}.$$

Now that the map is fully determined, we can calculate the Choi matrix elements

$$\left[\hat{\mathcal{C}}_\infty\right]_{ijkl} = \langle j|\mathcal{E}_\infty\left(|i\rangle\langle k|\right)|l\rangle, \tag{2.28}$$

and find that the Choi matrix is given by

$$\hat{\mathcal{C}}_\infty = \begin{pmatrix} 1 & 0 & 0 & K(\alpha_0,\alpha_1) \\ 0 & 0 & 0 & 0 \\ 0 & 0 & 0 & 0 \\ K(\alpha_0,\alpha_1) & 0 & 0 & 1 \end{pmatrix}. \tag{2.29}$$

By a similar procedure, the Choi matrix for perfect QND measurement is given by

$$\hat{\mathcal{C}}_\mathrm{per} = \begin{pmatrix} 1 & 0 & 0 & 0 \\ 0 & 0 & 0 & 0 \\ 0 & 0 & 0 & 0 \\ 0 & 0 & 0 & 1 \end{pmatrix}. \tag{2.30}$$

With both Choi matrices defined, using Eq. (2.20) we can calculate the fidelity to be

$$\mathcal{F}_\infty = \frac{1}{2}\left(1 + \sqrt{1 - K(\alpha_0,\alpha_1)^2}\right), \tag{2.31}$$

as in Eq. (2.21).

2.C Cavity and JPM-Limited Qubit Lifetimes

We first summarize the results of [43] for a qubit coupled dispersively to a cavity with decay rate κ; next we extend this result to include the JPM. For a qubit coupled dispersively to a cavity, the dressed qubit-cavity eigenstates to second order are

$$\overline{|1,n-1\rangle} \approx \left(1-\frac{g_{\mathrm{Q}}^2 n}{2\Delta^2}\right)|1,n-1\rangle - \frac{g_{\mathrm{Q}}\sqrt{n}}{\Delta}|0,n\rangle, \tag{2.32}$$

$$\overline{|0,n\rangle} \approx \left(1-\frac{g_{\mathrm{Q}}^2 n}{2\Delta^2}\right)|0,n\rangle + \frac{g_{\mathrm{Q}}\sqrt{n}}{\Delta}|1,n-1\rangle, \tag{2.33}$$

where $|0/1,n\rangle$ are the uncoupled eigenstates of the cavity-qubit system and $\Delta=\omega_{\mathrm{C}}-\omega_{\mathrm{Q}}$. We are interested in Purcell-limited qubit relaxation, i.e. transitions from $\overline{|1,n\rangle}$ to $\overline{|0,n\rangle}$ mediated by the cavity's coupling to the external environment, which we assume takes the standard form with the cavity coupling operator given by $\hat{X}=\hat{a}+\hat{a}^\dagger$. From [43], the decay rate for this process is given by

$$\Gamma_\kappa^{\overline{1n},\overline{0n}} = \kappa(\Delta_{\overline{0n},\overline{1n}})|\overline{\langle 1,n|}\hat{X}\overline{|0,n\rangle}|^2; \tag{2.34}$$

here $\kappa(\omega)$ is the coupling constant that depends on the spectral density of the cavity's environment, which should be evaluated at $\Delta_{\overline{n0},\overline{n1}}=\omega_{\mathrm{Q}}+\chi_{\mathrm{Q}}$. To lowest order in g_{Q}/Δ,

$$|\overline{\langle 1,n|}\hat{X}\overline{|0,n\rangle}|^2 \approx \frac{g_{\mathrm{Q}}^2}{\Delta^2}. \tag{2.35}$$

Assuming an Ohmic spectral density and using as a reference value the coupling constant at the uncoupled cavity frequency $\kappa(\omega_{\mathrm{C}})$, we have $\kappa(\omega)\approx\kappa(\omega_{\mathrm{C}})\omega/\omega_{\mathrm{C}}$, where ω_{C} is the bare cavity frequency, not the ultraviolet cutoff frequency of the Ohmic spectral density [80]. Setting $\kappa(\omega_{\mathrm{C}})=100$ kHz (the input coupling to the cavity), $\Delta/2\pi=1$ GHz, and a corresponding g_{Q} that gives $\chi_{\mathrm{Q}}/2\pi=5$ MHz, we obtain a Purcell limited qubit lifetime of 2 ms. To next order in g_{Q}/Δ the qubit lifetime is dependent on the cavity occupation; however, as shown in [89], the lifetime increases for higher photon numbers in the cavity.

When the JPM is brought on resonance with the cavity, the cavity-JPM states hybridize, so that the eigenstates are now

$$|n,a\rangle = \frac{1}{\sqrt{2}}\left(|n,0\rangle + (-1)^a|n-1,1\rangle\right), \tag{2.36}$$

where the ground state $|0,a\rangle=|0,0\rangle$, and the index a labels what is normally labelled by $\pm$. In light of this, to study qubit relaxation via the JPM, we must

examine transitions from the two states $\overline{|1,n,a\rangle}$ to the two states $\overline{|0,n,b\rangle}$ via the JPM-environment coupling operator $\hat{\sigma}_x^{\mathrm{J}}$, where now

$$\overline{|1,n,a\rangle} \approx \left(1 - \frac{g_{\mathrm{Q}}^2(n+1)}{2\Delta^2}\right)|1,n,a\rangle - \frac{g_{\mathrm{Q}}\sqrt{n+1}}{\Delta}|0,n+1,a\rangle, \tag{2.37}$$

$$\overline{|0,n,b\rangle} \approx \left(1 - \frac{g_{\mathrm{Q}}^2 n}{2\Delta^2}\right)|0,n,b\rangle + \frac{g_{\mathrm{Q}}\sqrt{n}}{\Delta}|1,n-1,b\rangle. \tag{2.38}$$

Similar to the case for cavity-mediated decay, the decay rates for these processes are given by

$$\Gamma_{\gamma_{\mathrm{R}}}^{\overline{1na},\overline{0nb}} = \gamma_{\mathrm{R}}(\Delta_{\overline{0na},\overline{1nb}})|\overline{\langle 1,n,a|}\hat{\sigma}_x^{\mathrm{J}}\overline{|0,n,b\rangle}|^2, \tag{2.39}$$

where $\gamma_{\mathrm{R}}(\omega)$ is the JPM's coupling constant with the environment. Using the fact that

$$\langle n+1,a|\sigma_x^{\mathrm{J}}|n,b\rangle = \frac{(-1)^a}{2}, \qquad n>0 \tag{2.40}$$

$$\langle 1,a|\sigma_x^{\mathrm{J}}|0,b\rangle = \frac{(-1)^a}{\sqrt{2}}, \qquad n=0 \tag{2.41}$$

and all other matrix elements are zero, we find that

$$\overline{\langle 1,n,a|}\hat{\sigma}_x^{\mathrm{J}}\overline{|0,n,b\rangle} = (-1)^a\frac{g_{\mathrm{Q}}}{2\Delta}\left(\sqrt{n}-\sqrt{n+1}\right) \tag{2.42}$$

$$\overline{\langle 1,0,a|}\hat{\sigma}_x^{\mathrm{J}}\overline{|0,0,b\rangle} = (-1)^a\frac{g_{\mathrm{Q}}}{\sqrt{2}\Delta}, \tag{2.43}$$

to first order in g_{Q}/Δ. As before, assuming an Ohmic spectral density we approximate $\gamma_{\mathrm{R}}(\Delta_{\overline{0na},\overline{1nb}})$ by $\gamma_{\mathrm{R}}(\omega_{\mathrm{J}})\omega_{\mathrm{Q}}/\omega_{\mathrm{J}}$, which assumes that the qubit energy-shifts due to both the cavity and the JPM are sufficiently smaller than ω_{Q} (i.e. $\Delta_{\overline{0na},\overline{1nb}} \approx \omega_{\mathrm{Q}}$). Using $\gamma_{\mathrm{R}}(\omega_{\mathrm{J}}) = 200$ MHz as in the main text and other quantities as before, we obtain a JPM-limited qubit lifetime $T_1^{\gamma_{\mathrm{R}}} \approx 2\ \mu$s for vacuum in the cavity. For cavity Fock states with $n>0$ this lifetime scales as

$$T_1^{\gamma_{\mathrm{R}}} \propto \frac{1}{\left(\sqrt{n}-\sqrt{n+1}\right)^2} = \left(\sqrt{n}+\sqrt{n+1}\right)^2, \tag{2.44}$$

and so we have $T_1^{\gamma_{\mathrm{R}}} \propto 2n$ to leading order. Thus, for $n=10$ we have an improvement of the qubit lifetime to $T_1^{\gamma_{\mathrm{R}}} \approx 40\ \mu$s.

In addition, there are several competing incoherent processes in the JPM, namely bright and dark counts, which block the JPM-mediated qubit decay channel. Numerical simulations indicate that due to the fact that $\gamma_{\mathrm{J}} \gg$

$\Gamma_{\gamma_R}^{\overline{1na},\overline{0nb}}$ for relevant photon numbers in the cavity, there is almost no appreciable decay of the qubit during the measurement process (see Fig. 2.7(a)). This can be understood by the fact that $\Gamma_{\gamma_R}^{\overline{1na},\overline{0nb}}/\gamma_J \propto g_Q^2/(n\Delta^2)$, which for $n = 10$ is only 0.05%, and so we expect no more than a 0.05% change in the qubit state due to JPM-mediated decay during the measurement protocol. Detailed study of qubit decay during JPM measurement will be the subject of future work.

Chapter 3

Scalable Two- and Four-Qubit Parity Measurement with a Threshold Photon Counter

Luke C. G. Govia, Emily J. Pritchett, B. L. T. Plourde, Maxim G. Vavilov, R. McDermott, and Frank K. Wilhelm

Abstract

Parity measurement is a central tool to many quantum information processing tasks. In this chapter, we propose a method to directly measure two- and four-qubit parity with low overhead in hard- and software, while remaining robust to experimental imperfections. Our scheme relies on dispersive qubit-cavity coupling and photon counting that is sensitive only to intensity; both ingredients are widely realized in many different quantum computing modalities. For a leading technology in quantum computing, superconducting integrated circuits, we analyze the measurement contrast and the back action of the scheme and show that this measurement comes close enough to an ideal parity measurement to be applicable to quantum error correction.

Submitted for peer review. Available at arXiv:1502.03340.

3.1 Introduction

The ability to measure a quantum system in a high fidelity and quantum non-demolition (QND) way is fundamental to most aspects of quantum information processing (QIP). In the circuit quantum electrodynamics (cQED) community, great success has been achieved in qubit readout by linear amplification and homodyne detection of the signal in a dispersively coupled microwave resonator (cavity) [39, 69, 75, 70]. However, the macroscopic size and complicated circuitry required for this readout scheme is a major obstacle to scalability. For this reason a simpler, scalable, high-fidelity, QND single-qubit readout scheme based on threshold photodetection was recently introduced [47].

In addition, QND readout of multi-qubit operators is increasingly important in contemporary QIP. In particular, readout of the parity of multiple qubits has applications to quantum error correction [7] such as the surface code [49], to quantum phase estimation [90], to the implementation of multi-qubit gates [91, 92], and to entanglement generation [93, 50, 94]. Parity measurement of two superconducting qubits has been proposed [95] and demonstrated [50, 51], as has Bell-state measurement [74], and parity measurement of a cavity state using a superconducting qubit [96]. However, adapting these protocols to more than two qubits requires a significant increase in complexity, either in the number of resonators necessary for amplification-based direct parity measurement [97, 98], or in the number of costly entangling gates in gate-based parity measurement.

In this chapter, we propose a protocol for QND parity readout of multiple qubits coupled to one resonator, over a timescale comparable to that of a single entangling gate. We describe the physical model, briefly review the similar protocol of single-qubit readout [47], and then present the protocol for N-qubit single-shot parity measurement. Finally, we analyze the main sources of error.

We describe parity measurement on N qubits, each coupled to the same single-mode cavity, which is also coupled to a tunable photon counter. Each qubit Q_n of transition frequency ω_{Q_n} couples to the cavity via a Jaynes-Cummings interaction in the dispersive regime, leading to the full cavity-qubit Hamiltonian ($\hbar = 1$)

$$H = H_{\mathrm{D}} + \omega_{\mathrm{C}}\hat{a}^\dagger\hat{a} + \sum_n^N \left(\chi_{\mathrm{Q}_n}\hat{a}^\dagger\hat{a} - \frac{\omega_{\mathrm{Q}_n} - \chi_{\mathrm{Q}_n}}{2}\right)\hat{\sigma}_z^n, \tag{3.1}$$

where $\chi_{\mathrm{Q}_n} \equiv g_{\mathrm{Q}_n}^2/(\omega_{\mathrm{C}} - \omega_{\mathrm{Q}_n})$ is the dispersive shift for coupling strength g_{Q_n}, and $H_{\mathrm{D}} \equiv A(t)\left(\hat{a} + \hat{a}^\dagger\right)$ is a time-dependent classical drive that controls

the cavity. For this Hamiltonian the computational basis states are defined as the eigenvectors of $\sum_n^N \hat{\sigma}_z^n$. We assume that the qubits are far enough detuned that cavity-mediated qubit-qubit coupling is negligible. This model is sufficiently general to encompass many qubit architectures [23, 75, 50, 99, 97, 39].

Our protocol can be applied to any physical system with a threshold photon counter and strong dispersive coupling between qubits and electromagnetic radiation. In the microwave regime, where photon counting is possible with a Josephson Photomultiplier (JPM) [54], other examples include NV centers in diamond [100], Rydberg atoms [101, 102], and lateral quantum dots [103]. At higher frequencies, where photon counters are commonplace, candidate systems include trapped atoms [104] and self-assembled quantum dots [105].

Described in Ref. [47], the cavity-mediated QND measurement of a single qubit with a photon counter is performed in a three-stage protocol. First the cavity, initialized to vacuum, is driven at its shifted resonance frequency for an excited qubit, populating the cavity conditionally upon the state of the qubit. In the following measurement stage, the photon counter distinguishes between the two conditional cavity states (one of which is above and one below its threshold), and therefore detects the state of the qubit. Finally, an additional microwave drive resets the cavity to the vacuum state for further computation. Two properties of the counter are crucial: it should be an intensity detector that responds to the total energy only (insensitive to phase), and it should have threshold behavior at a suitable number of photons that is well between vacuum and the selectively excited state of the cavity. Number resolution and single-photon sensitivity are *not* required.

3.2 N-Qubit Parity Readout Protocol

During the drive stage, the reduced Hamiltonian of the cavity coupled to a single qubit,

$$\hat{H}_{\mathrm{C}} = \tilde{\omega}_{\mathrm{C}} \hat{a}^\dagger \hat{a} + A(t) \left(\hat{a} + \hat{a}^\dagger \right), \tag{3.2}$$

is that of a single mode oscillator with resonance frequency $\tilde{\omega}_{\mathrm{C}} = \omega_{\mathrm{C}} + \tilde{\chi}_{\mathrm{Q}}$, where $\tilde{\chi}_{\mathrm{Q}} = s\chi_{\mathrm{Q}}$ encodes the state of the qubit through $s = \pm 1$, with s the respective eigenvalue of $\hat{\sigma}_z$. By a carefully timed classical drive at frequency $\omega_{\mathrm{D}} = \omega_{\mathrm{C}} - \chi_{\mathrm{Q}}$, we put the cavity in a high-amplitude coherent state if the qubit is excited, but in the vacuum state if the qubit is in its ground state, thus dephasing the qubit. The cavity is populated conditionally upon the

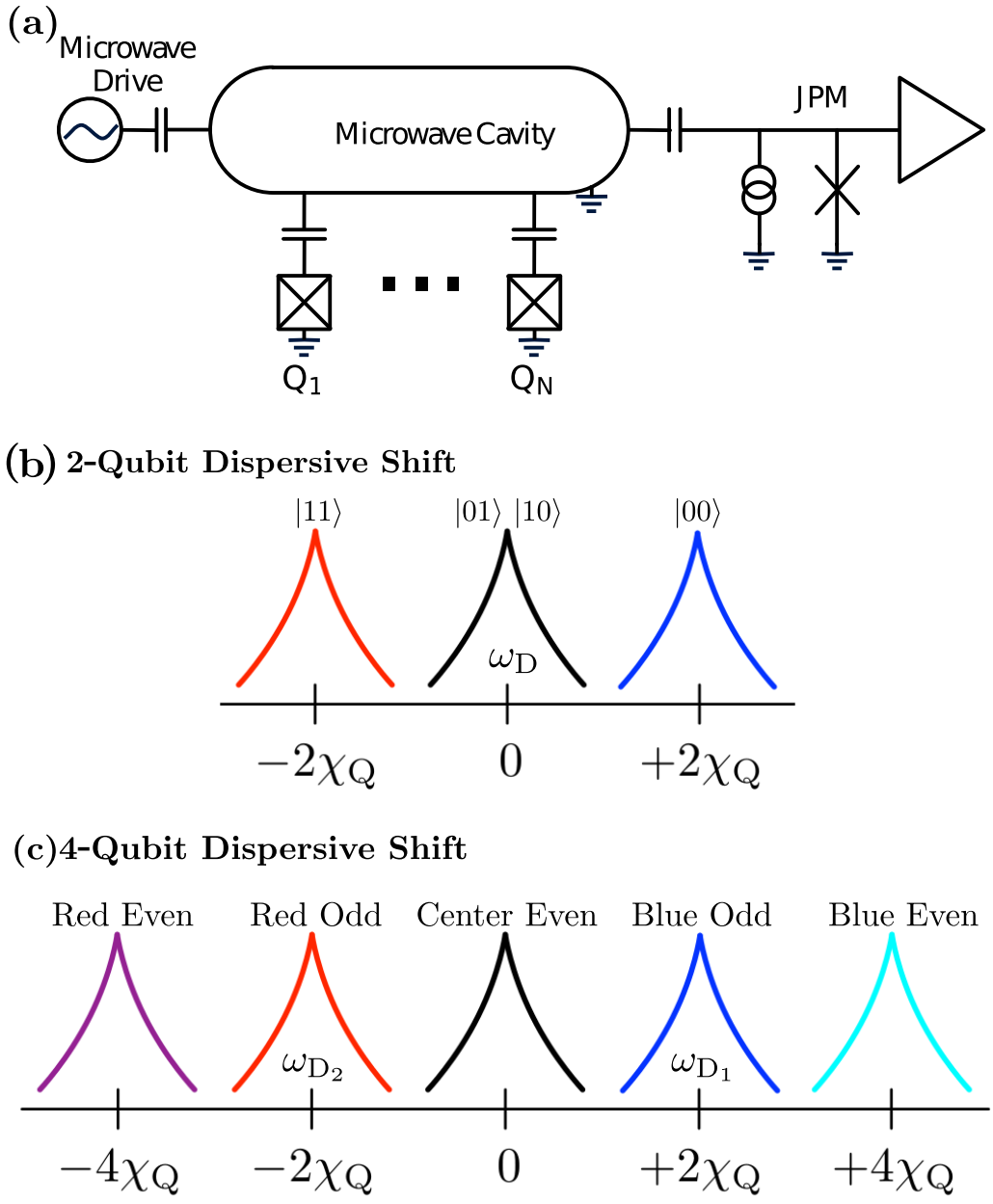

Figure 3.1: **(a)** Schematic of the experimental design showing the cavity, N coupled qubits, and the photon counter (a JPM in this case). **(b)** and **(c)** Illustration of the dispersive shifts on the cavity for two- and four-qubit computational basis states.

qubit having odd parity (excited state), via the unitary

$$\hat{U}_{\mathrm{D}} = \hat{P}_{\mathrm{Q}}^{\mathrm{E}} \otimes \mathbb{I}_{\mathrm{C}} + \hat{P}_{\mathrm{Q}}^{\mathrm{O}} \otimes \hat{D}(\beta), \tag{3.3}$$

where $\hat{D}(\beta)$ is the displacement operator. Here $\hat{P}_{\mathrm{Q}}^{\mathrm{E/O}}$ are the projectors onto the even/odd parity subspaces, which are projectors onto the ground and excited states for single-qubit readout, while for $N > 1$ are sums of projectors onto a set of states spanning each parity subspace. This unitary is a quantum eraser that transfers parity information to the cavity amplitude and all other qubit-state information to the phase.

Now consider two qubits coupled to the cavity with equal dispersive shifts. For the computational basis states the total dispersive shift on the cavity is $\tilde{\chi}_{\mathrm{Q}} = \pm 2\chi_{\mathrm{Q}}$ when both qubits are in the same eigenstate (even parity), and $\tilde{\chi}_{\mathrm{Q}} = 0$ when the qubits are in different eigenstates (odd parity), illustrated in FIG. 3.1(b). By driving with frequency $\omega_{\mathrm{D}} = \omega_{\mathrm{C}}$ we entangle the qubit parity subspaces with distinguishable cavity states, implementing the unitary of Eq. (3.17). At the end of the drive pulse $A(t) = a_0 \cos(\omega_{\mathrm{D}} t + \phi)\Theta(t_{\mathrm{D}} - t)$, the qubit-dependent cavity occupations are

$$|\alpha_{\mathrm{E}}|^2 = \left(\frac{a_0}{\Delta_{\mathrm{D}}}\right)^2 \frac{1 - \cos(\Delta_{\mathrm{D}} t_{\mathrm{D}})}{2}, \quad |\alpha_{\mathrm{O}}|^2 = \left(\frac{a_0}{2} t_{\mathrm{D}}\right)^2,$$

where $\Delta_{\mathrm{D}} = \tilde{\omega}_{\mathrm{C}} - \omega_{\mathrm{D}}$. Setting $\omega_{\mathrm{D}} = \omega_{\mathrm{C}}$ gives $|\Delta_{\mathrm{D}}| = 2\chi_{\mathrm{Q}}$ for even-parity states, and therefore $|\alpha_{\mathrm{E}}|^2 = 0$ at $t_{\mathrm{D}} = \pi/\chi_{\mathrm{Q}}$ ($\Delta_{\mathrm{D}} = 0$ for the odd states). As $\alpha_{\mathrm{E}} = 0$, the even-parity states are indistinguishable and all state information other than parity has been erased. Thus, while inter-subspace coherence is reduced to $\langle \alpha_{\mathrm{O}} | \alpha_{\mathrm{E}} \rangle$, intra-subspace coherence is protected, unlike in direct parity measurement [50].

For $N > 2$ qubits, the degeneracy within the odd and even subspaces splits and we can no longer perform parity measurement by a single frequency cavity drive. However, with

$$A(t) = a_0 \sum_i \cos(\omega_{\mathrm{D}_i} t + \phi) \quad 0 \leq t \leq t_D \tag{3.4}$$

where $\omega_{\mathrm{D}_i} = \omega_{\mathrm{C}} + \tilde{\chi}_{\mathrm{Q}_i}$ are the dispersively-shifted cavity frequencies for each band of the odd-parity subspace, we apply the unitary of Eq. (3.17) by simultaneously driving all odd-parity spectral lines resonantly with a multi-tone drive (see appendix 3.A for further details). Here, multiplexing is used to measure a binary observable, extracting less qubit information than full multiplexed readout [36, 106], but at a reduced cost in complexity.

For four qubits, basis states with odd parity produce dispersive shifts of $\pm 2\chi_{\mathrm{Q}}$ (blue and red odd-parity bands), while basis states with even parity cause shifts of 0 or $\pm 4\chi_{\mathrm{Q}}$, as shown in FIG. 3.1(c). Therefore, with two drive frequencies $\omega_{\mathrm{D}_{1,2}} = \omega_{\mathrm{C}} \pm 2\chi_{\mathrm{Q}}$ we can simultaneously drive both odd-parity spectral lines. The cavity occupations for the four-qubit parity bands

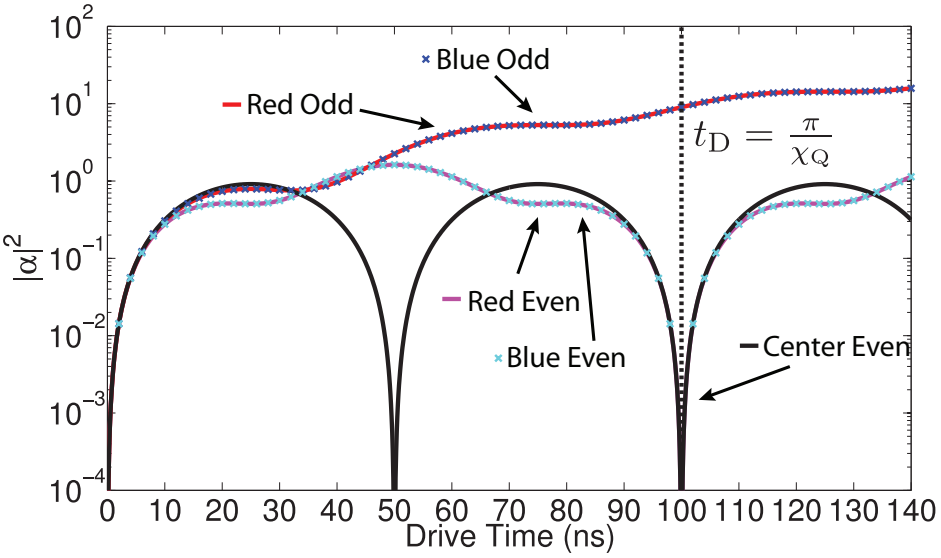

Figure 3.2: Cavity photon number as a function of the length of the drive pulse, t_D, for the four qubit parity bands. $\chi_Q/\pi = 10$ MHz, so the optimal drive time is $t_D = 100$ ns, which for $|\alpha_O|^2 = 9$ sets $a_0 = 0.06$ MHz.

are shown in FIG. 3.2 (see appendix 3.A for their analytic form). Crucially, $|\alpha_E|^2 = 0$ for all even-parity states at $t_D = \pi/\chi_Q$, while $|\alpha_O|^2$ is equal for all odd-parity states. Therefore, qubit parity information has been mapped onto cavity occupation in a way that erases all state information other than parity.

In the measurement stage we distinguish between the qubit-parity dependent cavity states in a frequency and phase insensitive way (to avoid intra-subspace decoherence) by using a high-bandwidth photon counter. We tune the counter on resonance with the bare cavity frequency ω_C. For two qubits, the counter and cavity are resonant if the qubits have odd parity, maximizing the detection probability of $|\alpha_O\rangle$. For four qubits, the counter is resonant with the cavity if the qubits are in the center even-parity band; however, this is not an issue because the cavity is unoccupied for even-parity qubits. The counter will be $\pm 2\chi_Q$ off resonance from the cavity for odd-parity qubits, symmetrically between the two odd-parity cavity frequencies. For a counter with bandwidth $> 4\chi_Q$ this ensures the detection probabilities for all odd-parity states are identical, minimizing intra-subspace decoherence.

For $N = 4$, the bright count detection probability for the two odd-parity bands is shown in FIG. 3.3, as is the false "even-state detection probability" due to dark counts. As expected, the two bright count curves are identical. These curves are calculated by solving the master equation with relevant

experimental parameters (for further information see appendix 3.B). As an example of a threshold photon counter we have chosen the JPM, which coupled to a cavity approaches unit detection probability with large bandwidth ($\gg \chi_{\mathrm{Q}}$) [59, 58]. Recent progress has been made with a JPM coupled to a cavity-qubit system with initial steps towards single-qubit readout [57]. We note that similar detectors exist in the optical [107, 108] and near infrared [109] regimes.

As a figure of merit we consider the parity measurement contrast, defined as

$$C\left(t_{\mathrm{M}}\right) \equiv P\left(|\alpha_{\mathrm{O}}|^2, t_{\mathrm{M}}\right) - P\left(|\alpha_{\mathrm{E}}|^2, t_{\mathrm{M}}\right), \tag{3.5}$$

the difference in detection probability between odd/even parity states, which is a function of the measurement time t_{M}. The drive time t_{D} is chosen such that $\alpha_{\mathrm{E}} = 0$, so the parity measurement contrast reduces to the detection probability of the odd-parity cavity state minus the dark count probability. In reality there will be thermal photons in the cavity. However, because of the threshold nature of the photon counter it is not necessary to have an initially empty cavity to maximize measurement contrast; it is sufficient that the detection probability has a sharp threshold between α_{O} and α_{E}. This is important for the JPM, where, while in principle the threshold can be set at zero occupation [59, 58], this is often difficult to engineer. Nonetheless, a suitable threshold between α_{O} and α_{E} is easily obtained [47].

Parity measurement contrast is limited by misidentification of the parity, which occurs either due to a dark count or the nonzero probability of not detecting the state $|\alpha_{\mathrm{O}}\rangle$. These errors are controlled by the bright count/dark count ratio of the photon counter and the cavity occupation $|\alpha_{\mathrm{O}}|^2$, and control over these parameters is sufficient to obtain contrast arbitrarily close to unity. As seen in FIG. 3.3, measurement contrast that approaches 95% is achievable, compatible with the readout threshold for error correction [49][1], in a 40 ns time-frame with experimentally relevant bright count/dark count ratio and $|\alpha_{\mathrm{O}}|^2$.

In the reset stage we again implement the qubit-dependent cavity displacement of Eq. (3.17), but with $\beta = -\alpha_{\mathrm{M}}$. For odd parity states, the cavity begins approximately in the coherent state $|\alpha_{\mathrm{M}}\rangle$ and is returned to vacuum, where $|\alpha_{\mathrm{M}}|$ is calculated given the input magnitude $|\alpha_{\mathrm{O}}|$ and the form of the detection back action on the cavity [88]. For a JPM, after measurement the cavity is not a coherent state, and reset is imperfect. However, single-shot parity measurement is unaffected by reset error, and though repeated measurements are affected, for experimentally relevant parameters

[1] To the best of our knowledge the imbalanced thresholds between gates and measurement have not been explored in detail in the fault tolerance literature.

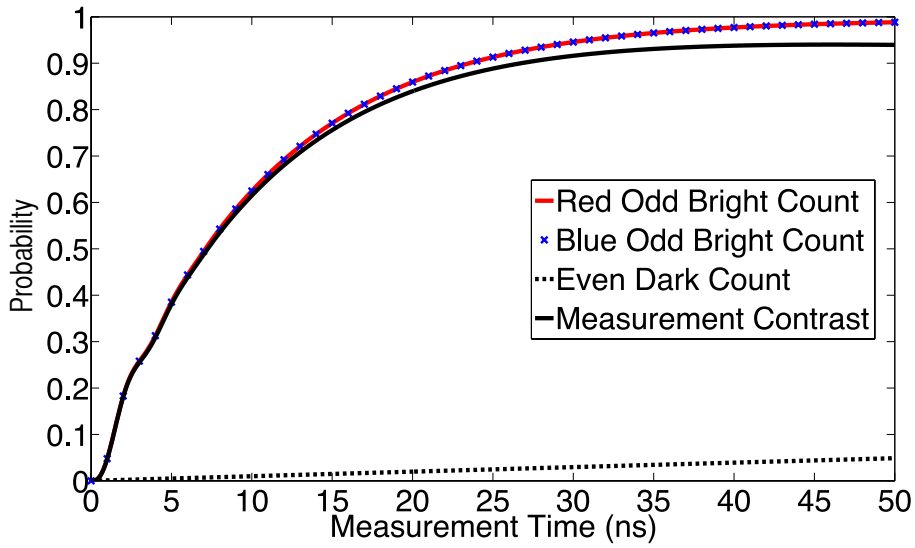

Figure 3.3: Bright count probability for the four-qubit odd-parity bands, dark count probability for even parity, and measurement contrast as functions of measurement time. The JPM bright count rate, inelastic relaxation rate, and dark count rate are $\gamma_J = 200$ MHz, $\gamma_R = 200$ MHz, and $\gamma_D = 1$ MHz. The cavity-JPM coupling is $g_J/2\pi = 50$ MHz.

reset error is on the order of 1% [47].

3.3 Error Analysis

In a realistic experiment it is unlikely that all qubit-cavity dispersive shifts will be identical. Therefore, we examine the robustness of our protocol under variations in the dispersive shifts, defining the dispersive shift error ϵ, such that $\chi_{Q_1} = \chi_Q$, and $\chi_{Q_2} = \chi_Q + \epsilon$ for two qubits. For four qubits there are three dispersive shift errors: ϵ_2, ϵ_3, and ϵ_4. We assume this error is small, such that $\epsilon_i/\chi_Q \ll 1$. For a superconducting qubit with coherence time 5 μs, the uncertainty in χ_Q due to homogeneous broadening is no more than $\pm 0.1\%$, and thus $|\epsilon_i/\chi_Q| < 0.2\%$. Mismatch in χ_Q causes a reduction in measurement contrast and intra-subspace decoherence (dephasing of a superposition of qubit states of the same parity). We provide quantitative estimates of these effects, leaving further details to appendices 3.C and 3.D. Errors in the drive frequencies ω_{D_i} cause similar errors as χ_Q mismatch, but can be corrected for during tune-up.

Imperfect resonance between the applied drives and the cavity due to χ_Q

mismatch leads to a reduced $|\alpha_{\mathrm{O}}|^2$ and an increased $|\alpha_{\mathrm{E}}|^2$. The reduction in measurement contrast due to this is second order in $\epsilon_i/\chi_{\mathrm{Q}}$, commensurate with a square-law detector. As shown in FIG. 3.4, even for 10% χ_{Q} mismatch the resulting measurement error (even-state detection probability) is on the order of 1%.

The intra-subspace decoherence caused by χ_{Q} mismatch is due to qubit states with the same parity being entangled to cavity states with different phases, which are distinguishable in principle. The resulting decoherence is at most second order in $\epsilon_i/\chi_{\mathrm{Q}}$. Shown in FIG. 3.4 is the coherence of odd- and even-parity two-qubit superposition states, quantified by the relevant off-diagonal matrix element of the reduced two-qubit density matrix. Though the decoherence of an odd-parity superposition is nontrivial for larger values of $\epsilon/\chi_{\mathrm{Q}}$, perfect reset returns full coherence by depopulating the cavity in a phase insensitive way.

However, any cavity decay prior to perfect reset will cause irreversible decoherence, as would the decay of residual photons after imperfect reset. Up to the limit of strong χ_{Q}-mismatch (ϵ approaching χ_{Q}), the intra-subspace coherence decays to $\exp(-N_{\mathrm{C}}(1-\cos(\pi\epsilon/\chi_{\mathrm{Q}})))$ in the steady state, where N_{C} is the average photon number in the cavity prior to decay, hence requiring $\epsilon < \chi_{\mathrm{Q}}/\sqrt{N_{\mathrm{C}}}$. For a high-$Q$ cavity, decay during the short measurement time is unlikely, and post-reset cavity decay is the significant source of loss. For the parameters considered here, the residual photons after imperfect reset result in coherence loss less than 1% in the worst case, which is inconsequential.

For two qubits with χ_{Q} mismatch, no intra-subspace decoherence occurs during the measurement stage as cavity states corresponding to qubit states of the same parity have equal detection probability. For four qubits the detection probabilities of cavity states within the same parity subspace can be different, with their difference scaling as $(\epsilon_i^2 - \epsilon_j^2)/\chi_{\mathrm{Q}}^2$. This changes the basis of measurement, changing the output qubit state at the protocol's end. This effect can be mitigated by a square-law photon counter that quickly saturates with photon number above threshold, such as the JPM, for which the error in the output qubit state is negligible.

Higher order effects beyond the dispersive Hamiltonian can affect the parity readout protocol presented here. As a result of the formation of cavity-qubit dressed states, there is residual cavity occupation for even-parity states, which reduces parity measurement contrast. For four qubits the contrast is reduced to $\approx 92\%$ (see appendix 3.E). However, contrast can be improved by increasing cavity-qubit detuning, and/or using better drive pulse sequences. The protocol's QNDness will also be affected by higher order terms; however, as shown for single-qubit readout in [47], this change in QNDness is minimal. As the measurement stages of single-qubit readout and parity readout are

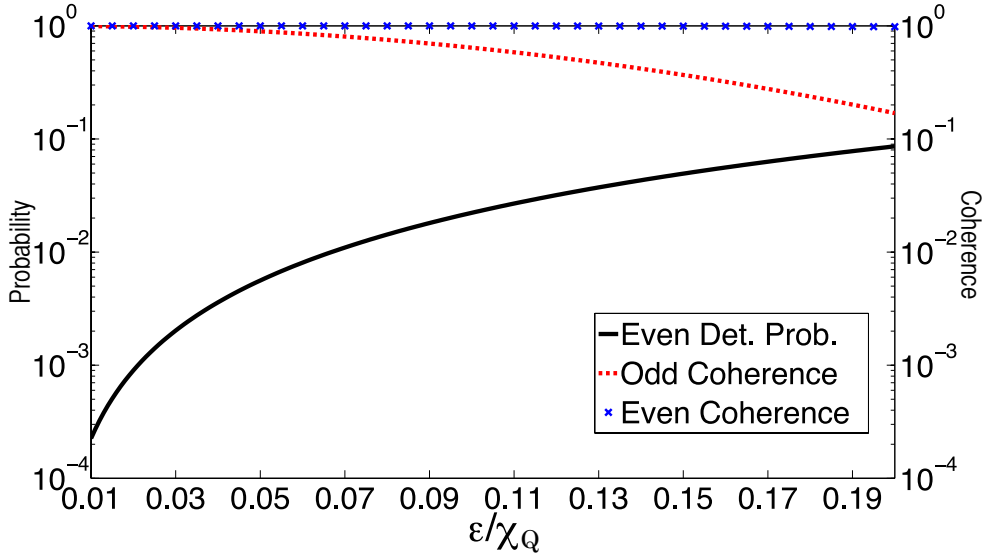

Figure 3.4: Even-parity detection probability, odd-parity coherence, and even-parity coherence as functions of the χ_Q mismatch for two-qubit parity measurement. ϵ/χ_Q ranges from 1% to 20%, well within experimental expectations. $\chi_Q/2\pi = 5$ MHz, and the drive power a_0 is such that $|\alpha_O|^2 = 9$.

very similar, this is also true for parity readout.

Our protocol involves an entangling operation that maps qubit information to the cavity such that destructive readout of the cavity non-destructively determines the qubits' parity. It provides a tailored and efficient quantum circuit that maps parity information onto an ancilla (the cavity), and then measures the ancilla in a way that is insensitive to qubit-resolving information. It occupies a middle ground between the direct parity measurement of [97, 98] and gate-based parity measurement. The advantage of our protocol over gate-based protocols is the reduced number of entangling gates required: one for our proposal *versus* N for the gate-based N-qubit protocol, which allows for a readout fidelity that is not bounded by gate fidelity. Our protocol also requires fewer cavities than direct four-qubit parity readout [97, 98], and avoids the intra-subspace decoherence often introduced by these protocols.

3.4 Conclusion

In conclusion we have presented a high-fidelity, scalable, QND protocol for parity readout of two or four qubits via photon counting of a dispersively coupled cavity. Measurement contrast is limited by the bright/dark count

ratio of the photon counter, and with the limited optimization in this chapter approaches 95%. Our protocol introduces no decoherence of qubit states with the same parity, and is robust against the major sources or error. Future work will focus on protocol optimization and higher order corrections.

Acknowledgements

Supported by the Army Research Office under contract W911NF-14-1-0080. L.C.G.G., E.J.P., and F.K.W. also acknowledge support from the European Union through ScaleQIT and LCGG from NSERC through an NSERC PGS-D. M.G.V., and R.M. were also supported by NSF Grant No. DMR-1105178.

Appendix

In the following appendices we expand on the details of the calculations and simulations presented in the main text. While not essential to understanding the results presented in the main text, these details complete the explanation of the results in a more mathematically rigorous way.

In appendix 3.A we present the details of the analytic derivation of FIG. 3.2, which shows the driven cavity occupation as a function of time, and how this is used to create a qubit-parity dependent cavity population. In appendix 3.B we describe the master equation formalism used to simulate the interaction of the cavity with our example threshold square-law photon counter, the Josephson Photomultiplier (JPM). In appendix 3.C we expand on the error analysis of the main text to describe the effect of χ_Q mismatch. In appendix 3.D we discuss the effect of this χ_Q mismatch when cavity photon loss occurs. Finally, in appendix 3.E we describe how consideration of the full Jaynes-Cummings Hamiltonian affects the results of the main text.

3.A Derivation of the qubit-parity dependent drive for four qubits

In this appendix we derive the driven cavity evolution for four qubits, as shown in FIG. 3.2. The full system Hamiltonian is block diagonal, with one block for each state of the qubits. In each block the effective cavity Hamiltonian is

$$\hat{H}_C = \tilde{\omega}_C \hat{a}^\dagger \hat{a} + a_0[\cos(\omega_{D_1} t + \phi_1) + \cos(\omega_{D_2} t + \phi_2)]\Theta(t_D - t)\left(\hat{a} + \hat{a}^\dagger\right), \tag{3.6}$$

where the shifted cavity frequency $\tilde{\omega}_C = \omega_C + \tilde{\chi}_Q$ depends on the qubit-state dependent dispersive shift $\tilde{\chi}_Q = \chi_Q \langle \hat{\sigma}_z \rangle$, which defines the state of the qubits, and therefore, the corresponding block of the full Hamiltonian. $\tilde{\chi}_Q = \pm 2\chi_Q$ for odd-parity states and $\tilde{\chi}_Q = 0, \pm 4\chi_Q$ for even parity.

We go to a frame rotating with the shifted cavity frequency $\tilde{\omega}_{\mathrm{C}}$ to obtain

$$\hat{H}'_{\mathrm{C}} = \frac{a_0}{2}\Theta(t_{\mathrm{D}} - t)\left[\hat{a}\left(e^{-i\Delta_1 t} + e^{-i\Delta_2 t}\right) + \mathrm{h.c.}\right], \tag{3.7}$$

where $\Delta_i = \tilde{\omega}_{\mathrm{C}} - \omega_{\mathrm{D}_i}$. We formally solve for the evolution operator in each block for times $t \geq t_D$ as

$$\hat{U}(t,0) = \mathcal{T}\exp\left\{-i\int_0^{t_{\mathrm{D}}} \hat{H}'_{\mathrm{C}}(t')dt'\right\}, \tag{3.8}$$

where $\mathcal{T}$ is the time ordering operator. The evolution operator for the full system then has the form

$$\hat{U}_{\mathrm{D}} = \sum_j |j\rangle\langle j| \otimes \hat{U}_j(t,0), \tag{3.9}$$

where $\hat{U}_j(t,0)$ are the solutions to equation (3.8) for each qubit state $|j\rangle$ in the computational basis.

We evaluate the integral in equation (3.8) using the Magnus expansion [110] to take care of the time ordering. Because $\left[\hat{a}, \hat{a}^\dagger\right] = 1$ the Magnus expansion truncates at second order, and conveniently the second order term is a global phase that we can ignore. We evaluate the integral in two regimes, corresponding to even or odd parity, and in so doing obtain the solution for the blocks of the full Hamiltonian. For even parity, $\Delta_1 \neq 0$ and $\Delta_2 \neq 0$, and to first order we have

$$\int_0^{t_{\mathrm{D}}} \hat{H}'_{\mathrm{C}}(t')dt' = \frac{a_0}{2}\left[\hat{a}\left(\frac{i}{\Delta_1}\left(e^{-i\Delta_1 t_{\mathrm{D}}} - 1\right) + \frac{i}{\Delta_2}\left(e^{-i\Delta_2 t_{\mathrm{D}}} - 1\right)\right) + \mathrm{h.c.}\right].$$

The evolution operator of equation (3.8) for even parity is then

$$\hat{U}_{\mathrm{E}}(t,0) = \hat{D}(\alpha_{\mathrm{E}}(t_{\mathrm{D}})), \tag{3.10}$$

where

$$\alpha_{\mathrm{E}}(t_{\mathrm{D}}) = -\frac{a_0}{2}\left[\frac{e^{i\Delta_1 t_{\mathrm{D}}} - 1}{\Delta_1} + \frac{e^{i\Delta_2 t_{\mathrm{D}}} - 1}{\Delta_2}\right]. \tag{3.11}$$

In general $\alpha_{\mathrm{E}}(t_{\mathrm{D}})$ varies in phase for different even-parity qubit states as $\Delta_{1,2}$ depend on the specific state.

For an odd-parity qubit basis state, the shifted cavity will be on resonant with one of the two applied drives, and therefore, one Δ_i is zero, while the other is nonzero. Since the solution is symmetric in regards to which $\Delta_i = 0$,

we will examine $\Delta_1 = 0$ and $\Delta_2 \neq 0$ without loss of generality. The integral in equation (3.8) now gives

$$\int_0^{t_\mathrm{D}} \hat{H}'_\mathrm{C}(t')dt' = \frac{a_0}{2}\left[\hat{a}\left(t_\mathrm{D} + i\frac{e^{-i\Delta_2 t_\mathrm{D}} - 1}{\Delta_2}\right) + \mathrm{h.c.}\right],$$

which leads to the odd-parity evolution operator

$$\hat{U}_\mathrm{O}(t,0) = \hat{D}(\alpha_\mathrm{O}(t_\mathrm{D})) = \hat{D}\left(\beta(t_\mathrm{D}) + \eta(t_\mathrm{D})\right), \tag{3.12}$$

where

$$\beta(t_\mathrm{D}) = -\frac{ia_0}{2}t_\mathrm{D} \tag{3.13}$$

$$\eta(t_\mathrm{D}) = -\frac{a_0}{2\Delta_2}\left(e^{i\Delta_2 t_\mathrm{D}} - 1\right). \tag{3.14}$$

In this case it is important to note that while $\eta(t_\mathrm{D})$ varies between odd-parity states, $\beta(t_\mathrm{D})$ is the same for all odd-parity states.

If $\omega_{\mathrm{D}_1} = 2\chi_\mathrm{Q}$ and $\omega_{\mathrm{D}_2} = -2\chi_\mathrm{Q}$ as in the main text, then for even parity we have $\Delta_1, \Delta_2 \in \{\pm 2\chi_\mathrm{Q}, \pm 6\chi_\mathrm{Q}\}$. For odd parity, we have chosen $\Delta_1 = 0$, which means that $\Delta_2 = 4\chi_\mathrm{Q}$. Thus, if we set $t_\mathrm{D} = \pi/\chi_\mathrm{Q}$, we have that $\alpha_\mathrm{E}(t_\mathrm{D}) = 0$, and $\eta(t_\mathrm{D}) = 0$, while $\beta(t_\mathrm{D}) \neq 0$. As a result of this,

$$\hat{U}_\mathrm{E}(t,0) = \hat{D}(0) = \mathbb{I}, \tag{3.15}$$

$$\hat{U}_\mathrm{O}(t,0) = \hat{D}\left(\beta(t_\mathrm{D})\right), \tag{3.16}$$

and the evolution operators are the same for all states within the same parity subspace. This, along with the block diagonal form of the full system Hamiltonian implies that the unitary on the full system will have the form

$$\begin{aligned}\hat{U}_\mathrm{D} &= \sum_{j\in\mathrm{even}} |j\rangle\langle j| \otimes \hat{U}_\mathrm{E}(t,0) + \sum_{j\in\mathrm{odd}} |j\rangle\langle j| \otimes \hat{U}_\mathrm{O}(t,0) \\ &= \hat{P}_\mathrm{Q}^\mathrm{E} \otimes \mathbb{I}_\mathrm{C} + \hat{P}_\mathrm{Q}^\mathrm{O} \otimes \hat{D}(\beta),\end{aligned} \tag{3.17}$$

where $\hat{P}_\mathrm{Q}^{\mathrm{E,O}}$ are projectors onto the even- and odd-parity subspaces respectively.

3.B Master equation for the cavity-JPM coupled system

In this appendix we describe the methodology of the numerical simulations used to obtain FIG. 3.3, which shows the detection probability and parity contrast for our example threshold detector, the JPM.

We start with the cavity-JPM coupled system for four-qubit odd parity, where the shifted cavity frequencies $\tilde{\omega}_C = \omega_C \pm 2\chi_Q$ and the JPM frequency $\omega_J = \omega_C$ are such that the JPM is $\pm 2\chi_Q$ detuned from the cavity. This leads to the Hamiltonian

$$\hat{H}_{JC} = \tilde{\omega}_C \hat{a}^\dagger \hat{a} - \frac{\omega_J}{2}\hat{\sigma}_J + g_J \left(\hat{a}\hat{\sigma}_J^+ + \hat{a}^\dagger \hat{\sigma}_J^-\right),$$

where $\hat{\sigma}_J^\pm$ couple the ground and excited state of the JPM. As shown previously [54, 53, 58, 59], the JPM is well-approximated as a three-level system with self-Hamiltonian $H_J = -\frac{\omega_J}{2}\sigma_J$, where $\hat{\sigma}_J \equiv \mathrm{diag}(1, -1, k)$. The energy of the third 'measurement' state is arbitrary in our model; the JPM only tunnels into it incoherently at fixed rates [59, 58].

In addition, the JPM experiences a number of incoherent processes. Tunneling from the JPM excited state to the measured state corresponds to photon detection and occurs at the bright count rate γ_J, with the corresponding Lindblad operator

$$\hat{L}_2 = \sqrt{\gamma_J}\left(\mathbb{I}_C \otimes |\mathrm{m}\rangle\langle 1|_J\right). \tag{3.18}$$

Inelastic relaxation takes the JPM from the excited state to the ground state at a rate γ_R, with corresponding Lindblad operator

$$\hat{L}_1 = \sqrt{\gamma_R}\left(\mathbb{I}_C \otimes |0\rangle\langle 1|_J\right). \tag{3.19}$$

Finally, false detections, where the JPM tunnels from the ground state to the measured state, can occur at the dark count rate γ_D, with Lindblad operator

$$\hat{L}_0 = \sqrt{\gamma_D}\left(\mathbb{I}_C \otimes |m\rangle\langle 0|_J\right). \tag{3.20}$$

We ignore the effects of pure dephasing on the JPM as they do not affect the parity measurement protocol of the main text.

We solve the master equation

$$\begin{aligned}\dot{\rho}(t) = &-i[\hat{H}_{JC}, \rho(t)] \\ &+ \sum_{\mu=0}^{2}\left(\hat{L}_\mu \rho(t) \hat{L}_\mu^\dagger - \frac{1}{2}\{\hat{L}_\mu^\dagger \hat{L}_\mu, \rho(t)\}\right),\end{aligned} \tag{3.21}$$

with $\gamma_J = 200$ MHz, $\gamma_R = 200$ MHz, $\gamma_D = 1$ MHz, and $g_J/2\pi = 50$ MHz, for both $\tilde{\omega}_C - \omega_C = 2\chi_Q$, and $-2\chi_Q$ (where $\chi_Q/2\pi = 5$ MHz) to generate the detection probability curves of the main text FIG. 3.3 .

3.C Qubit Dispersive Shift Mismatch

In this appendix we examine in detail the possible sources of error caused by χ_Q mismatch that were described in the main text and shown in FIG. 3.4. Firstly, we quantify the decrease in measurement contrast and the coherence loss for two qubits. As described in the main text, this coherence loss can be restored by perfect reset. We then examine these effects for four qubits, and also quantify the change in the measurement basis due to detection probability mismatch, which is unique to four qubits.

3.C.1 Two Qubits

If the dispersive shifts for the two qubits vary, such that $\chi_{Q_1} = \chi_Q$ and $\chi_{Q_2} = \chi_Q + \epsilon$, then the cavity-drive detunings within a parity subspace split, such that we now have

$$\begin{aligned}\Delta_{00} &= -2\chi_Q - \epsilon \\ \Delta_{11} &= 2\chi_Q + \epsilon \\ \Delta_{01} &= \epsilon \\ \Delta_{10} &= -\epsilon\end{aligned} \tag{3.22}$$

where Δ_{ij} is the cavity-drive detuning for the state $|ij\rangle$.

After a time $t_D = \pi/\chi_Q$ the cavity will be in a qubit-state dependent coherent state with amplitude

$$\begin{aligned}\alpha_{00} &= \frac{a_0}{2(2\chi_Q + \epsilon)}\left(e^{-i\frac{\pi}{\chi_Q}\epsilon} - 1\right), \\ \alpha_{11} &= -\frac{a_0}{2(2\chi_Q + \epsilon)}\left(e^{i\frac{\pi}{\chi_Q}\epsilon} - 1\right), \\ \alpha_{01} &= -\frac{a_0}{2\epsilon}\left(e^{i\frac{\pi}{\chi_Q}\epsilon} - 1\right), \\ \alpha_{10} &= \frac{a_0}{2\epsilon}\left(e^{-i\frac{\pi}{\chi_Q}\epsilon} - 1\right).\end{aligned} \tag{3.23}$$

For the even-parity qubit states we have that $\alpha_{11} = -\bar{\alpha}_{00}$, and for the odd-parity states $\alpha_{10} = -\bar{\alpha}_{01}$. As a result, states within the same parity subspace will have the same detection probability, and so there will be no intra-subspace decoherence during the measurement stage. However, as $|\alpha_{00}| \neq 0$ there will be a reduction of measurement contrast due to the increased probability of misidentification. As the coherent states for each parity subspace are out of phase with one another there also will be intra-subspace decoherence during the drive stage. We will now quantify these effects in the $\epsilon/\chi_Q < 1$ regime.

For the measurement contrast and misidentification we can quantify the effect of χ_{Q} mismatch by looking at the cavity occupation for odd parity, $|\alpha_{\mathrm{O}}|^2 = |\alpha_{01}|^2 = |\alpha_{10}|^2$, and for even parity, $|\alpha_{\mathrm{E}}|^2 = |\alpha_{00}|^2 = |\alpha_{11}|^2$. For odd parity

$$\begin{aligned} |\alpha_{\mathrm{O}}|^2 &= \left(\frac{a_0}{2\epsilon}\right)^2 \left(2 - 2\cos\left(\frac{\pi\epsilon}{\chi_{\mathrm{Q}}}\right)\right) \\ &= \left(\frac{a_0}{2}\right)^2 \left(\frac{\pi}{\chi_{\mathrm{Q}}}\right)^2 \left(1 - \frac{1}{12}\left(\frac{\pi\epsilon}{\chi_{\mathrm{Q}}}\right)^2\right) + \mathcal{O}\left(\varepsilon^4\right), \end{aligned} \tag{3.24}$$

where $\varepsilon = \epsilon/\chi_{\mathrm{Q}}$, and we see that the reduction of $|\alpha_{\mathrm{O}}|^2$ from that when the dispersive shifts are perfectly matched is second order in $\epsilon/\chi_{\mathrm{Q}}$. Similarly, for even parity

$$\begin{aligned} |\alpha_{\mathrm{E}}|^2 &= \left(\frac{a_0}{2(2\chi_{\mathrm{Q}} + \epsilon)}\right)^2 \left(2 - 2\cos\left(\frac{\pi\epsilon}{\chi_{\mathrm{Q}}}\right)\right) \\ &= \left(\frac{a_0}{2(2\chi_{\mathrm{Q}} + \epsilon)}\right)^2 \left(\frac{\pi\epsilon}{\chi_{\mathrm{Q}}}\right)^2 + \mathcal{O}\left(\varepsilon^4\right) \\ &= \left(\frac{a_0}{2}\right)^2 \left(\frac{\pi}{\chi_{\mathrm{Q}}}\right)^2 \left(\frac{\epsilon}{2\chi_{\mathrm{Q}}}\right)^2 + \mathcal{O}\left(\varepsilon^4\right), \end{aligned} \tag{3.25}$$

and the increase in $|\alpha_{\mathrm{E}}|^2$ from that when the dispersive shifts are perfectly matched is again second order in $\epsilon/\chi_{\mathrm{Q}}$. The fact that the lowest order dependence is quadratic originates from the expansion of the cosine, and can be physically explained by the fact that the amplitude is originally tuned to zero, and a square-law detector responds to intensity which is $|\alpha|^2$.

To quantify the intra-subspace decoherence during the drive stage, we consider an arbitrary superposition of odd-parity states with the cavity initially in vacuum, to which we apply the modified qubit state dependent drive (accounting for χ_{Q} mismatch). The resulting state

$$|\Psi\rangle = a|01\rangle|\alpha_{01}\rangle + b|10\rangle|\alpha_{10}\rangle, \tag{3.26}$$

where $|a|^2 + |b|^2 = 1$, is no longer a product state and as such there will necessarily be decoherence of the reduced qubit state. The reduced qubit state is

$$\rho_{\mathrm{Q}} = \begin{pmatrix} 0 & 0 & 0 & 0 \\ 0 & |a|^2 & \bar{D}a\bar{b} & 0 \\ 0 & D\bar{a}b & |b|^2 & 0 \\ 0 & 0 & 0 & 0 \end{pmatrix}, \tag{3.27}$$

with the complex decoherence factor

$$D = \langle \alpha_{01} | \alpha_{10} \rangle = \exp\left\{ - \left(|\alpha_{01}|^2 + \bar{\alpha}_{01}^2 \right) \right\}. \tag{3.28}$$

From equation (3.23) we see that

$$|\alpha_{01}|^2 = 2A_{\mathrm{O}}^2 \left(1 - \cos\left(\frac{\pi\epsilon}{\chi_{\mathrm{Q}}} \right) \right), \tag{3.29}$$
$$\bar{\alpha}_{01}^2 = A_{\mathrm{O}}^2 \left[1 - 2\left(\cos\left(\frac{\pi\epsilon}{\chi_{\mathrm{Q}}} \right) - i \sin\left(\frac{\pi\epsilon}{\chi_{\mathrm{Q}}} \right) \right) + \cos\left(2\frac{\pi\epsilon}{\chi_{\mathrm{Q}}} \right) - i \sin\left(2\frac{\pi\epsilon}{\chi_{\mathrm{Q}}} \right) \right],$$

where $A_{\mathrm{O}} = a_0/2\epsilon$.

Keeping only the first nonzero term in the Taylor series expansion we find

$$\begin{aligned} |\alpha_{01}|^2 + \bar{\alpha}_{01}^2 &= A_{\mathrm{O}}^2 \left(\frac{1}{2} \left(\frac{\pi\epsilon}{\chi_{\mathrm{Q}}} \right)^4 + i \left(\frac{\pi\epsilon}{\chi_{\mathrm{Q}}} \right)^3 \right) \\ &= \left(\frac{a_0}{2} \right)^2 \left(\frac{\pi}{\chi_{\mathrm{Q}}} \right)^2 \left(\frac{1}{2} \left(\frac{\pi\epsilon}{\chi_{\mathrm{Q}}} \right)^2 + i \frac{\pi\epsilon}{\chi_{\mathrm{Q}}} \right) + \mathcal{O}\left(\varepsilon^3 \right). \end{aligned} \tag{3.30}$$

As can be seen, for an odd-parity superposition, χ_{Q} mismatch causes decoherence at a rate that is second order in the small parameter ϵ/χ, and also introduces a complex phase factor that is first order in ϵ/χ.

For an even-parity superposition, we simply replace A_{O} with the corresponding expression for even states, and we find

$$\begin{aligned} |\alpha_{00}|^2 + \bar{\alpha}_{00}^2 &= \left(\frac{a_0}{2(2\chi_{\mathrm{Q}} + \epsilon)} \right)^2 \left(\frac{1}{2} \left(\frac{\pi\epsilon}{\chi_{\mathrm{Q}}} \right)^4 + i \left(\frac{\pi\epsilon}{\chi_{\mathrm{Q}}} \right)^3 \right) \\ &= \left(\frac{a_0}{4\chi_{\mathrm{Q}}} \right)^2 \left(\frac{1}{2} \left(\frac{\pi\epsilon}{\chi_{\mathrm{Q}}} \right)^4 + i \left(\frac{\pi\epsilon}{\chi_{\mathrm{Q}}} \right)^3 \right) + \mathcal{O}\left(\varepsilon^5 \right). \end{aligned} \tag{3.31}$$

Thus the even parity situation is even better, as the decoherence rate is now fourth order in ϵ/χ, and the complex phase factor now third order.

For both odd- and even-parity superpositions full intra-subspace coherence will be returned to the two qubits by perfect reset, as it disentangles the qubits and the cavity in a unitary and phase insensitive way. However, if cavity decay occurs before reset, or imperfect reset leaves residual photons which subsequently decay, the qubit state will lose coherence, as will be discussed in appendix 3.D.

3.C.2 Four Qubits

The situation is considerably more complex in the four qubit case as the cavity-drive detunings split into sixteen distinct frequencies, one for each qubit state. Correspondingly, after the qubit state dependent drive there are sixteen possible cavity states $|\alpha_{ijkl}\rangle$, where $i, j, k, l \in \{0, 1\}$ index the qubit state $|ijkl\rangle$. As a result of the double frequency drive each α_{ijkl} will have two components oscillating at different frequencies, with each component similar in form to those of equation (3.23). Cavity states for even qubit parity will have both components of the form of α_{00}, where the amplitude is suppressed by a factor $1/(2\chi_Q + \epsilon)$, as both drives are off resonance by at least $2\chi_Q$. For odd qubit parity the cavity state will have one component that is similar in form to α_{00} from the off resonance drive and one component similar to α_{01} from the nearly on resonance drive.

Given the similar structure of α_{ijkl} in the four qubit case to α_{ij} of the two qubit case it is clear that the errors introduced by χ_Q mismatch in the four qubit case will be a generalization of those in the two qubit case. There will be a reduction of measurement contrast due to an increase in the probability of misidentification, which will again be at most second order in the small parameters ϵ_i/χ_Q. The overlap between any two states $|\alpha_{ijkl}\rangle$ corresponding to qubits in the same parity subspace is very similar to equations (3.30) and (3.31) for the two qubit case, and as a result, the intra-subspace decoherence during the drive phase will be at most second order in ϵ_i/χ_Q for odd-parity superpositions and fourth order for even parity. As in the two qubit case full coherence will be returned to the qubits by perfect cavity reset.

Despite the χ_Q mismatch the two qubit case exhibits symmetry in α_{ij} within a parity subspace that ensures the detection probabilities are the same for cavity states corresponding to qubit states of the same parity. However, in the four qubit case this symmetry is no longer present, as in general $\epsilon_2 \neq \epsilon_3 \neq \epsilon_4$, and as a result, detection probabilities will differ within a parity subspace.

For example, consider an equal superposition of odd-parity states $|a\rangle$ and $|b\rangle$, which after the drive stage are entangled to cavity stages $|\alpha_{a/b}\rangle$ respectively. Detection by the photon counter results in back action on the cavity described by the non-unitary back action operator $\hat{B}$. Defining the normalized states

$$|\psi_{a,b}\rangle = \frac{\hat{B}|\alpha_{a,b}\rangle}{\langle\alpha_{a,b}|\hat{B}^\dagger\hat{B}|\alpha_{a,b}\rangle} = \frac{\hat{B}|\alpha_{a,b}\rangle}{P_{a,b}}, \tag{3.32}$$

where $P_{a,b}$ is the detection probability of the state $|\alpha_{a,b}\rangle$, then the resulting

state of the cavity-qubits system after detection by the photon counter is

$$|\Psi\rangle = \frac{1}{\sqrt{N}}\left(\sqrt{P_a}|a\rangle|\psi_a\rangle + \sqrt{P_b}|b\rangle|\psi_b\rangle\right), \tag{3.33}$$

where the normalization factor $N = P_a + P_b$.

The four qubit states of equation (3.33) are entangled to distinguishable cavity states such that the reduced four qubit density matrix's coherence is reduced by the overlap $\langle\psi_b|\psi_a\rangle$. To remove this effect and focus solely on detection probability mismatch we assume that we can perform perfect reset of the cavity and create the state

$$|\Psi\rangle = \frac{1}{\sqrt{N}}\left(\sqrt{P_a}|a\rangle + \sqrt{P_b}|b\rangle\right)|0\rangle, \tag{3.34}$$

for which the reduced qubit state is the pure state

$$|\Psi\rangle_{\mathrm{Q}} = \left(\sqrt{P_a}|a\rangle + \sqrt{P_b}|b\rangle\right)/\sqrt{N}. \tag{3.35}$$

Clearly, the output state $|\Psi\rangle_{\mathrm{Q}}$ is no longer the input state and this change is a result of the fact that different detection probabilities for states within the same parity subspace change the basis of measurement of the protocol. To quantify this effect we calculate the magnitude of the overlap between the target state $|\Psi_{\mathrm{T}}\rangle_{\mathrm{Q}} = (|a\rangle + |b\rangle)/\sqrt{2}$ and the state $|\Psi\rangle_{\mathrm{Q}}$, given by

$$O = |\langle\Psi_T|\Psi\rangle_{\mathrm{Q}}|^2 = \frac{1}{2}\left(1 + \frac{2\sqrt{P_a}\sqrt{P_b}}{P_a + P_b}\right), \tag{3.36}$$

which is unity for $P_a = P_b$ as expected.

If we assume the photon counter is a JPM with a subtraction operator back action [88], then the detection probability of the state $|\alpha_i\rangle$ is

$$P_i = 1 - \exp\left\{-|\alpha_i|^2\right\}. \tag{3.37}$$

By Taylor expanding the overlap and discarding terms smaller than $e^{-2|\alpha_{a/b}|^2}$ we obtain the approximate overlap

$$O = 1 - \frac{e^{-\left(|\alpha_a|^2+|\alpha_b|^2\right)}\left(\cosh\left(|\alpha_a|^2 - |\alpha_b|^2\right) - 1\right)}{4\left(2 - e^{-|\alpha_a|^2} - e^{-|\alpha_b|^2}\right)} + \mathcal{O}\left(e^{-3|\alpha_{a/b}|^2}\right). \tag{3.38}$$

Since we are interested in the effect of detection probability mismatch we can assume $\alpha_{a/b}$ differ in magnitude only and set $|\alpha_a| = |\alpha|$ and $|\alpha_b| = |\alpha|(1+\delta)$ without loss of generality. The overlap can then be rewritten as

$$O = 1 - \frac{e^{-|\alpha|^2\left(2+2\delta+\delta^2\right)}\left(\cosh\left(|\alpha|^2(2\delta+\delta^2)\right) - 1\right)}{4\left(2 - e^{-|\alpha|^2} - e^{-|\alpha|^2(1+\delta)^2}\right)}. \tag{3.39}$$

To examine the scaling of the overlap, we assume that $\delta \ll 1$ and only keep terms up to order δ^2 in the Taylor series, which gives

$$O = 1 - \frac{\delta^2 |\alpha|^4 e^{-2|\alpha|^2}}{4\left(1 - e^{-|\alpha|^2}\right)} + \mathcal{O}\left(\delta^3\right). \tag{3.40}$$

Four qubit χ_{Q} mismatch causes a difference in the cavity coherent state amplitude for states in the same parity subspace that scales as $\delta^2 \propto (\epsilon_i^2 - \epsilon_j^2)/\chi_{\mathrm{Q}}^2$. As we assume $\epsilon_i/\chi_{\mathrm{Q}}$ is a small parameter, then $(\epsilon_i^2 - \epsilon_j^2)/\chi_{\mathrm{Q}}^2$ is as small or smaller, so the assumption that $\delta \ll 1$ is valid.

From equation (3.40) we see that the error in the output state scales as $(\epsilon_i^2 - \epsilon_j^2)/\chi_{\mathrm{Q}}^2$ and is damped by the factor $|\alpha|^4 e^{-2|\alpha|^2}/4$. For $|\alpha| = 3$ as used in the main text this damping factor is on the order of 10^{-6}, and so any error in the output state caused by detection probability mismatch is negligible.

A better approximation to the detection probability in the case where the JPM can also relax inelastically is [47]

$$P_i \approx 1 - \exp\left\{-|\alpha_i|^2 \frac{\gamma_{\mathrm{J}}}{\gamma_{\mathrm{J}} + \gamma_{\mathrm{R}}}\right\}. \tag{3.41}$$

Using $\gamma_{\mathrm{J}} = \gamma_{\mathrm{R}}$ as elsewhere, then the error of equation (3.40) is damped by a factor $\propto |\alpha|^4 e^{-|\alpha|^2}$. For $|\alpha| = 3$ as before, this is on the order of 10^{-2}, which again results in a negligible effect that will only decrease with increasing cavity photon number.

3.D Qubit decoherence and cavity decay

When χ_{Q} mismatch is present there can be a phase difference between cavity states corresponding to qubit states with the same parity, as discussed for two qubits in appendix 3.C.1. In this section we examine the effect this has on intra-subspace coherence when a cavity decay mechanism is introduced, as described in the main text.

We start with a typical post drive or imperfect reset state of the form

$$\hat{\rho}(0) = \sum_{s,s'} c(s,s') |s\rangle\langle s'| \otimes \hat{\rho}_{s,s'}(0) \otimes \hat{\rho}_{\mathrm{B}}, \tag{3.42}$$

where s, s' label the state of the qubits, $\hat{\rho}_{s,s'}(0)$ are the qubit dependent cavity matrices, and the environmental bath is represented by the state $\hat{\rho}_{\mathrm{B}}$, which is assumed to be stationary and a thermal state. Additionally we assume that the qubit states have no intrinsic time dependence, i.e. we work in the rotating frame of the qubits.

We consider the intial state of the qubits to be an equal superposition of two states in the same parity subspace, which for simplicity we have labelled as $|0\rangle$ and $|1\rangle$. This results in the initial system state

$$\hat{\rho}_{\mathrm{S}}(0) = \frac{1}{2}\Big(|0\rangle\langle 0| \otimes |\alpha_0\rangle\langle\alpha_0| + |0\rangle\langle 1| \otimes |\alpha_0\rangle\langle\alpha_1| \\ +|1\rangle\langle 0| \otimes |\alpha_1\rangle\langle\alpha_0| + |1\rangle\langle 1| \otimes |\alpha_1\rangle\langle\alpha_1|\Big), \tag{3.43}$$

where $\hat{\rho}_{s,s'}(0) = |\alpha_s\rangle\langle\alpha_{s'}|$. Due to χ_{Q} mismatch α_0 and α_1 differ in their phase only and we can set

$$\alpha_0 = |\tilde{\alpha}|e^{i\varphi_0},\ \alpha_1 = |\tilde{\alpha}|e^{i\varphi_1}. \tag{3.44}$$

Assuming that the cavity is in a coherent state is accurate for a post drive stage state, but the post reset state will be a more general state of the form $\hat{\rho}_{s,s'}(0) = |\psi_s\rangle\langle\psi_{s'}|$. Nevertheless, we are eventually interested in steady state dynamics which are independent of the initial state of the cavity (under the Born-Markov approximation). We will treat the post drive stage situation first and then generalize to the post reset state.

To solve for $\hat{\rho}_{s,s'}(t)$, we will use the Wigner characteristic function approach. We define the Wigner characteristic function $\chi_{ss'}(\alpha, t)$ of the state $\hat{\rho}_{s,s'}(t)$ as

$$\hat{\rho}_{s,s'}(t) = \frac{1}{\pi}\int d^2\alpha \chi_{ss'}(\alpha, t)\hat{D}(-\alpha), \tag{3.45}$$

where $\hat{D}(\beta)$ is the displacement operator.

If we assume a Jaynes-Cumming type interaction between the cavity and a bosonic environment with smooth spectral density, then following [111] we arrive at the analytic solution for $\chi_{ss'}(\alpha, t)$

$$\chi_{ss'}(\alpha, t) = \chi_{ss'}(\alpha e^{-t(\kappa - i\omega)}, 0)e^{\left(\frac{\eta}{2}|\alpha|^2(e^{-2t\kappa}-1)\right)}, \tag{3.46}$$

where κ is the decay rate of the cavity, ω is the frequency of the cavity mode, and $\eta = 1 + 2n(\omega)$ with $n(\omega)$ the Bose distribution at frequency ω.

In order to quantify the absolute maximum amount of decoherence, we are interested in the steady state solution ($t \to \infty$) of equation (3.46)

$$\tilde{\chi}_{ss'}(\alpha) = \chi_{ss'}(0, 0)e^{-\frac{\eta}{2}|\alpha|^2}. \tag{3.47}$$

Using the facts that

$$\chi_{ss'}(0, 0) = \frac{1}{4\pi}\mathrm{Tr}[\hat{\rho}_{s,s'}(0)] \tag{3.48}$$

$$\chi_{10}(\alpha, t) = \bar{\chi}_{01}(-\alpha, t) \tag{3.49}$$

we obtain

$$\tilde{\chi}_{00}(\alpha) = \tilde{\chi}_{11}(\alpha) = \frac{1}{4\pi} e^{-\frac{\eta}{2}|\alpha|^2}, \tag{3.50}$$

$$\tilde{\chi}_{01}(\alpha) = \exp\left(|\tilde{\alpha}|^2 (e^{i(\varphi_1 - \varphi_0)} - 1)\right) \frac{1}{4\pi} e^{-\frac{\eta}{2}|\alpha|^2}, \tag{3.51}$$

$$\tilde{\chi}_{10}(\alpha) = \exp\left(|\tilde{\alpha}|^2 (e^{i(\varphi_0 - \varphi_1)} - 1)\right) \frac{1}{4\pi} e^{-\frac{\eta}{2}|\alpha|^2}. \tag{3.52}$$

Each of equations (3.50), (3.51) and (3.52) can be reduced to $\tilde{\chi}_{ss'}(\alpha) = F_{ss'}(\alpha_0, \alpha_1)\chi_{\text{Thermal}}(\alpha, \omega)$, where $\chi_{\text{Thermal}}(\alpha, \omega) = e^{-\frac{\eta}{2}|\alpha|^2}/4\pi$ is the Wigner characteristic function for a thermal state at frequency ω.

In light of this simplification the steady state solution for the full system reduces to

$$\hat{\rho}_S = \sum_{s,s'} c(s, s') F_{ss'}(\alpha_0, \alpha_1) |s\rangle\langle s| \otimes \frac{1}{\pi} \int d^2\alpha \chi_{\text{Thermal}}(\alpha, \omega) \hat{D}(-\alpha), \tag{3.53}$$

where $F_{ss'}(\alpha_s, \alpha_{s'}) = \exp\left(|\tilde{\alpha}|^2 (e^{i(\varphi_s - \varphi_{s'})} - 1)\right)$. As this is a product state it is the trivial to trace out the state of the cavity and obtain the state of the qubits alone

$$\hat{\rho}_Q = \frac{1}{2}\Big(|0\rangle\langle 0| + F_{01}(\alpha_0, \alpha_1)|0\rangle\langle 1| + F_{10}(\alpha_1, \alpha_0)|1\rangle\langle 0| + |1\rangle\langle 1|\Big). \tag{3.54}$$

For two qubits, we examine the damping envelope of the off diagonal elements, given by

$$F_{01}(\alpha_0, \alpha_1) = \exp\left(-|\tilde{\alpha}|^2 (e^{2i\varphi_0} + 1)\right), \tag{3.55}$$

where we have used the fact that $\varphi_0 - \varphi_1 = 2\varphi_0 - \pi$ for two qubits, as can be calculated from either pair of expressions in equation (3.23). We are interested in the absolute value of this envelope, which is given by

$$\begin{aligned} |F_{01}(\alpha_0, \alpha_1)| &= \exp\left(-|\tilde{\alpha}|^2 \text{Re}\left\{(e^{2i\varphi_0} + 1)\right\}\right) \\ &= \exp\left[-|\tilde{\alpha}|^2 \left(1 - \cos\left(\frac{\pi}{\chi_{\text{Q}}}\epsilon\right)\right)\right], \end{aligned} \tag{3.56}$$

where the second equality comes from using equation (3.23) to define $e^{2i\varphi_0}$. From this we see that the decoherence depends on both the cavity occupation and the magnitude of the χ_{Q} mismatch, being maximal when $\epsilon/\chi_{\text{Q}} = 1$. Using $|\alpha|^2 = 9$ as used elsewhere, and a strong mismatch of $\epsilon/\chi_{\text{Q}} = 0.1$, the qubit coherence is reduced to 64% in the steady state. However, for a high-Q

cavity we do not expect any photon loss during the parity readout protocol, and as such, the post reset state is of greater interest.

Generalizing to the post reset state we need only change the definition of the damping envelope to

$$F_{ss'} = \mathrm{Tr}[\hat{\rho}_{s,s'}(0)] = \langle \psi_{s'} | \psi_s \rangle, \tag{3.57}$$

where $|\psi_s\rangle$ is the state after detection and imperfect reset for an initial cavity state $|\alpha_s\rangle$. We will consider the worst case scenario for the states $|\alpha_{0/1}\rangle$, where the damping envelope of equation (3.56) reduces to $\exp(-2|\tilde{\alpha}|^2)$. This occurs for $\epsilon = \chi_{\mathrm{Q}}$, where the states $|\alpha_{0/1}\rangle$ lie on the real axis with $\alpha_0 = -\alpha_1$. This is the worst case as the states are maximally distinguishable, and correspondingly we expect the states $|\psi_{0/1}\rangle$ to also be maximally distinguishable in this case.

Figure 3.5 shows a numerical simulation of $1 - F_{01}$ for the worst case post reset state as a function of both the initial cavity occupation $|\tilde{\alpha}|^2$, and the number of photons removed by the photon detector. For these simulations, the detector was assumed to be a JPM with subtraction operator back action [88]. Multiple photons can be removed due to JPM inelastic relaxation. As can be seen, even for the worst case scenario, qubit coherence is reduced by less than 1%. As we expect $\epsilon \ll \chi_{\mathrm{Q}}$ in a realistic experiment, the decoherence caused by post reset state photon loss will be far from the upper bound presented here, and can be considered inconsequential.

3.E Higher Order Effects Beyond the Dispersive Hamiltonian

While the dispersive Hamiltonian is the first order approximation to the cavity-qubit coupling in the relevant regime of our protocol, it is worthwhile to consider the effects on the protocol of the full Jaynes-Cummings Hamiltonian for the cavity-qubit coupling, given by

$$\hat{H}_{\mathrm{JC}} = \omega_{\mathrm{C}} \hat{a}^\dagger \hat{a} - \sum_{k=0}^{N} \frac{1}{2} \omega_{\mathrm{Q}} \hat{\sigma}_z^k + \sum_{k=0}^{N} g_k \left(\hat{\sigma}_+^k \hat{a} + \hat{\sigma}_-^k \hat{a}^\dagger \right), \tag{3.58}$$

where g_k is the cavity-qubit coupling for qubit k. The major effects of the full Jaynes-Cummings Hamiltonian occur during the drive stage.

The first is an asymmetric shift to the cavity frequency within a parity subspace, due to the Kerr-like interaction term, which is one order of approximation higher than the dispersive Hamiltonian. The result of this is

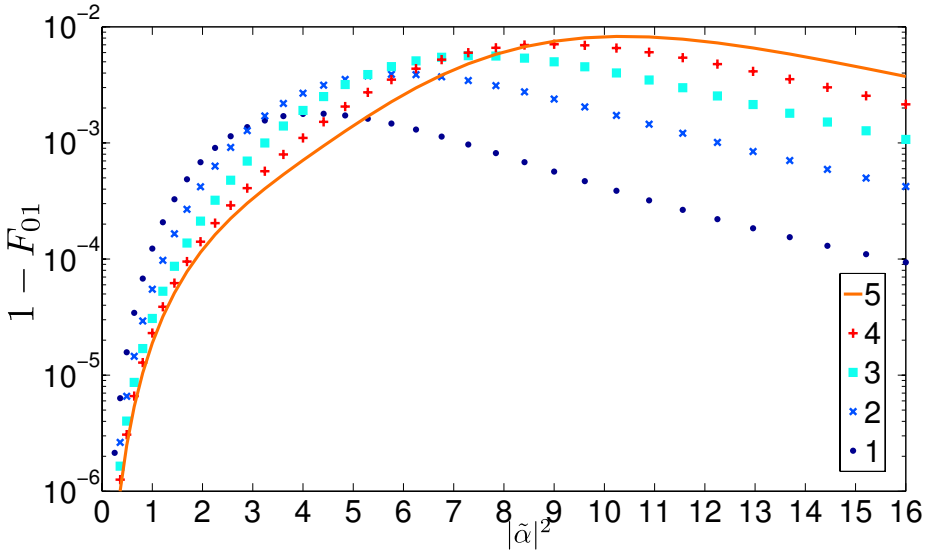

Figure 3.5: $1 - F_{01}$ as a function of the cavity occupation prior to detection and imperfect reset (horizontal axis), and the number of photons removed from the cavity by the photon detector (color and line style). The initial cavity states considered are maximally distinguishable, and so this represents the worst case scenario.

that the minima of the even qubit parity cavity occupation curves no longer coincide, as can be seen in FIG. 3.6(a) for the four qubit case. The second major effect is the formation of dressed cavity-qubit states, the result of which is that there is residual cavity occupation for even-parity states, and the minima are no longer zero for all even-parity states. Therefore, for no choice of t_D will the cavity be in the vacuum state if the qubits are in an even-parity state. This reduces the measurement contrast, though as can be seen in figure FIG. 3.6(b) this reduction is only on the order of a few percent, and measurement contrasts approaching 92% can still be achieved with the same parameters as in the main text.

These effects can be mitigated by increasing the cavity-qubit detuning, in which case the parity measurement contrast asymptotes to the dispersive value. However, this either decreases χ_Q and therefore increases the length of the drive stage, or necessitates also increasing the cavity-qubit couplings (to keep χ_Q constant), which is only advisable to the point where the rotating wave approximation begins to break down. It is also possible to improve the contrast by better pulse shaping in the drive stage, and this will be the focus of future work. As can also be seen in FIG. 3.6(a), the fact that the even qubit parity cavity photon states are not the same between parity bands would

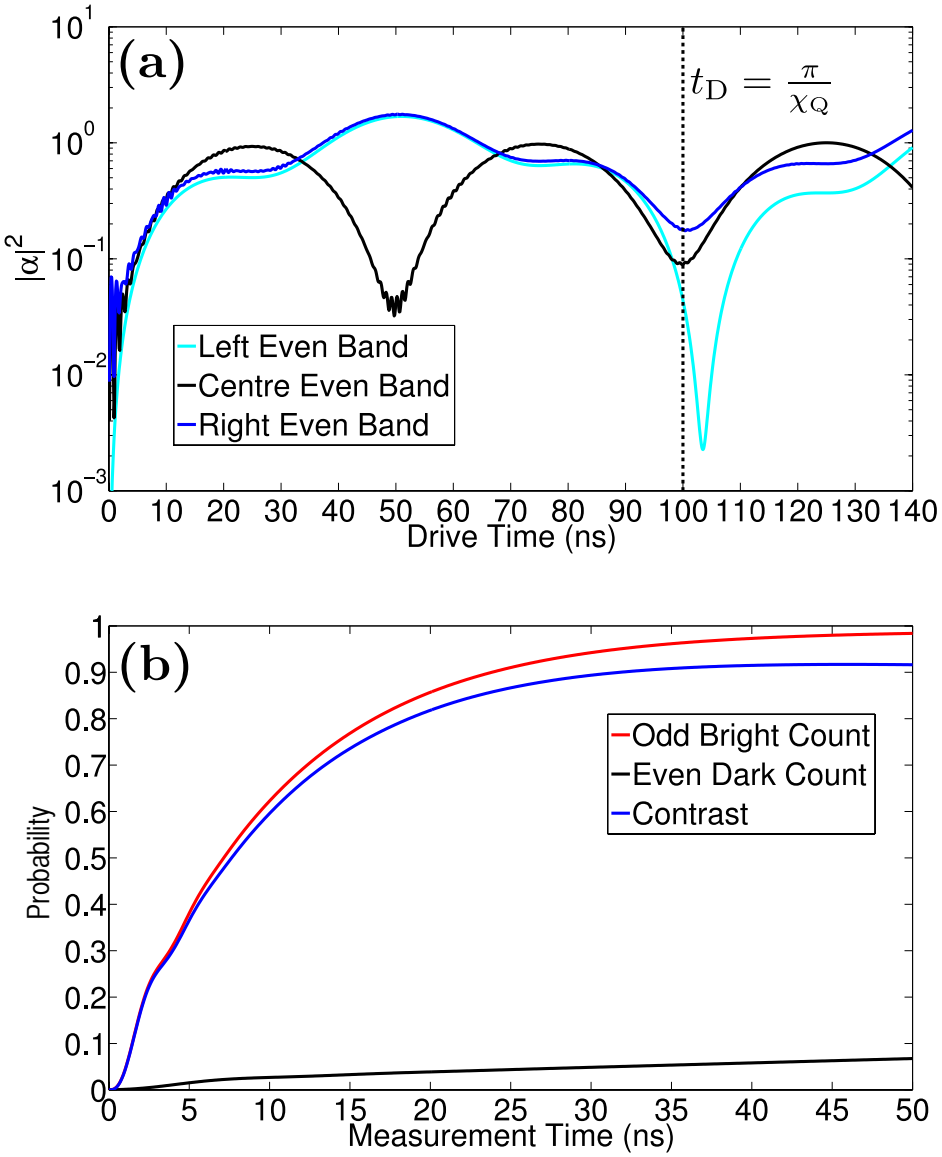

Figure 3.6: **(a)** Cavity occupation for even-parity qubit states with Jaynes-Cummings cavity-qubit coupling. **(b)** Bright and dark count rates, and measurement contrast for the cavity photon numbers of **(a)**, assuming the even state is from the right band (worst case).

cause intra-subspace qubit decoherence. Full coherence would be returned by perfect reset, unless photon loss occurs (either through a detection or other mechanism). However, photon loss of any kind is so unlikely for these low occupation cavity states that the effect on qubit coherence is minimal,

on the order of a few percent at most.

Chapter 4

Entanglement Generated by the Dispersive Interaction: The Dressed Coherent State

Luke C. G. Govia and Frank K. Wilhelm

Nothing can come of nothing.

-William Shakespeare

Abstract

In the dispersive regime of qubit-cavity coupling, classical cavity drive populates the cavity, but leaves the qubit state unaffected. However, the dispersive Hamiltonian is derived after both a frame transformation and an approximation. Therefore, to connect to external experimental devices, the inverse frame transformation from the dispersive frame back to the lab frame is necessary. In this work, we show that in the lab frame the system is best described by an entangled state known as the dressed coherent state, and thus even in the dispersive regime, entanglement is generated between the qubit and the cavity. Also, we show that further qubit evolution depends on both the amplitude and phase of the dressed coherent state, and use the dressed coherent state to calculate the measurement contrast of a recently developed dispersive readout protocol.

4.1 Introduction

The interaction between a two level system (TLS) and quantized electromagnetic radiation has been studied extensively since the beginnings of quantum mechanics, with much effort devoted to the study of physical systems described by the Jaynes-Cummings Hamiltonian [37]. Over the last few decades the fields of cavity quantum electrodynamics (CQED) and more recently circuit quantum electrodynamics (cQED) have significantly developed, allowing for the exploration of the Jaynes-Cummings interaction in a wide range of parameter regimes and physical systems. In particular in cQED, both the strong coupling regime ($g \gg \kappa, \gamma$, first achieved in Rydberg atoms [112]) and the strong dispersive regime ($\chi \gg \kappa, \gamma$) have been reached within the last decade [60]. In cQED, a superconducting qubit serves as the TLS, while the quantized electromagnetic fields are microwaves in either a strip-line resonator or 3D microwave cavity.

Contemporary experiments in cQED often work in the strong dispersive regime, where the qubit and microwave cavity are off resonance, and the Jaynes-Cummings interaction reduces to an effective second order shift in system eigen-energies. In this regime, a wide range of quantum information protocols has been demonstrated [23], including quantum teleportation [74], entanglement generation by measurement and feedback [50, 51], non-classical microwave state generation [113], and error correction by stabilization measurements [106].

When an empty electromagnetic cavity is driven by classical radiation, the state of the cavity is described quantum mechanically by the coherent state $|\alpha\rangle$, where the complex amplitude α depends on the strength and length of the classical drive. In the dispersive regime of qubit-cavity coupling, when a classical cavity drive is applied the state of the joint system is typically described by the product state $a|g\rangle|\alpha_g\rangle + b|e\rangle|\alpha_e\rangle$, with no qubit-cavity entanglement generated if the qubit is not initially in a superposition state.

What is typically overlooked is that the state $a|g\rangle|\alpha_g\rangle + b|e\rangle|\alpha_e\rangle$ is an accurate description of the joint system state under the dispersive approximation, which involves a frame transformation to the *dispersive frame*, and thus this state is not an accurate description of the qubit-cavity system in the lab frame of the experiment. In this chapter, we will show that in the lab frame of the experiment a more accurate description of the joint state is the dressed coherent state $\overline{|g/e, \alpha\rangle}$ [114]. Unlike the description in the dispersive frame, the dressed coherent state of the lab frame is entangled, even if the qubit is not initially in a superposition state. This has profound implications on the future evolution of the system, and we will show that future qubit evolution is dependent on both the amplitude and phase of the dressed coherent

state. Similar effects have previously been studied for a driven qubit-cavity system where the qubit and cavity are resonant [115, 116].

This chapter is organized as follows: in section 4.2 we describe the physical system of interest and the unitary frames we will be working in; in section 4.3 we define the dressed coherent state and give analytical and numerical evidence that this is the state created after an electromagnetic cavity is driven classically; in section 4.4 we discuss applications of the dressed coherent state to quantum information protocols; finally, in section 4.5 we make concluding remarks.

4.2 The Physical System

We consider a qubit and cavity coupled via the Jaynes-Cummings interaction, described by the lab frame Hamiltonian

$$\hat{H} = \omega_c \hat{a}^\dagger \hat{a} - \frac{\omega_q}{2}\hat{\sigma}_z + g\left(\hat{\sigma}^- \hat{a}^\dagger + \hat{\sigma}^+ \hat{a}\right), \tag{4.1}$$

where $\hat{a}$ and $\hat{a}^\dagger$ are the usual bosonic annihilation and creation operators, $\hat{\sigma}_z$ is the Pauli matrix whose eigenstates are the qubit logical states, $\hat{\sigma}^\pm$ are the qubit raising and lowering operators, $\omega_{c/q}$ are the cavity and qubit frequencies, g is the Jaynes-Cummings coupling strength, and we set $\hbar = 1$ from here on. The eigenbasis for this Hamiltonian is given by the dressed states [9]

$$\overline{|g,n\rangle} = \cos\theta_n |g,n\rangle - \sin\theta_n |e,n-1\rangle, \tag{4.2}$$

$$\overline{|e,n-1\rangle} = \cos\theta_n |e,n-1\rangle + \sin\theta_n |g,n\rangle, \tag{4.3}$$

where the unbarred kets are the eigenstates of the uncoupled system, and the mixing angle θ_n is given by the relation

$$\theta_n = \frac{1}{2}\arctan\left(2\lambda\sqrt{n}\right). \tag{4.4}$$

where, $\lambda = g/\Delta$ with $\Delta = \omega_q - \omega_c$ the cavity-qubit detuning. We work in the dispersive regime, defined by $|\lambda| \ll 1$. In this regime the mixing angle is well approximated as $\theta_n \approx \lambda\sqrt{n}$, provided $n \ll n_{\text{crit}}$, where n_{crit} is the critical photon number at which the approximation breaks down due to the product $\sqrt{n}\lambda$ approaching unity [39]. The dressed states then reduce to

$$\overline{|g,n\rangle} = \cos\left(\lambda\sqrt{n}\right)|g,n\rangle - \sin\left(\lambda\sqrt{n}\right)|e,n-1\rangle, \tag{4.5}$$

$$\overline{|e,n-1\rangle} = \cos\left(\lambda\sqrt{n}\right)|e,n-1\rangle + \sin\left(\lambda\sqrt{n}\right)|g,n\rangle, \tag{4.6}$$

In this regime, it is then possible to transform to the *dispersive frame* by applying the unitary rotation $\hat{U}_{\mathrm{D}} = \exp\left\{\lambda\left(\hat{\sigma}^{+}\hat{a} - \hat{\sigma}^{-}\hat{a}^{\dagger}\right)\right\}$, and keeping terms up to first order in the dispersive shift $\chi = g^2/\Delta$. The result of this procedure is the dispersive frame Hamiltonian

$$\hat{H}_{\mathrm{D}} = \omega_{\mathrm{c}}\hat{a}^{\dagger}\hat{a} - \frac{\omega_{\mathrm{q}} + \chi}{2}\hat{\sigma}_z - \chi\hat{\sigma}_z\hat{a}^{\dagger}\hat{a}, \tag{4.7}$$

which we emphasize is not in the lab frame, but in the dispersive frame defined by $\hat{U}_{\mathrm{D}}$. To highlight the in-equivalence of the two frames, we note the identities (which will be useful later)

$$\hat{U}_{\mathrm{D}}^{\dagger}|g,n\rangle = \overline{|g,n\rangle}, \tag{4.8}$$

$$\hat{U}_{\mathrm{D}}^{\dagger}|e,n\rangle = \overline{|e,n\rangle}, \tag{4.9}$$

where the dressed states are given by equations (4.5) and (4.6).

4.3 The Dressed Coherent State

4.3.1 Analytic Derivation

We are interested in the effect on the full system of a classical drive applied to the cavity, as described in the lab frame and to lowest order in the dispersive frame by the Hamiltonian

$$\hat{H}_{\mathrm{d}}(t) = 2\cos(\omega_{\mathrm{d}}t)\left(\epsilon\hat{a} + \epsilon^{*}\hat{a}^{\dagger}\right), \tag{4.10}$$

where ω_{d} and ϵ are the frequency and complex amplitude of the drive respectively. In the interaction frame of the system Hamiltonian $\hat{H}_{\mathrm{D}}$ of equation (4.7) (which we refer to as the "dispersive-interaction" frame), after the rotating wave approximation the full system Hamiltonian is then

$$\hat{H}_{\mathrm{I}}(t) = \epsilon e^{-i\delta t}e^{i\chi\hat{\sigma}_z t}\hat{a} + \epsilon^{*}e^{i\delta t}e^{-i\chi\hat{\sigma}_z t}\hat{a}^{\dagger}, \tag{4.11}$$

where $\delta = \omega_{\mathrm{c}} - \omega_{\mathrm{d}}$ is the cavity-drive detuning, and the subscript "I" labels the interaction picture. In the dispersive-interaction frame, after a time T the state of the full system is described by

$$|\psi'_{\mathrm{D}}(T)\rangle = \hat{U}_{\mathrm{I}}(T,0)|\psi'(0)\rangle = \mathcal{T}\exp\left\{-i\int_0^T \hat{H}_{\mathrm{I}}(t)\right\}|\psi'(0)\rangle, \tag{4.12}$$

where $\mathcal{T}$ is the usual time ordering operator.

To calculate $\hat{U}_{\mathrm{I}}(T,0)$ exactly we will use the Magnus expansion [110], given by

$$\hat{U}_{\mathrm{I}}(T,0) = \exp\left(\sum_{k=1}^{\infty}\Omega_k(T,0)\right) \tag{4.13}$$

where $\Omega_k(T,0)$ is the k'th order Magnus generator. For our system these generators are zero for $k>2$, and so $\hat{U}_{\mathrm{I}}(T,0)$ can be calculated exactly. The first order Magnus generator is given by an expression proportional to the average Hamiltonian

$$\begin{aligned}\Omega_1(T,0) &= -i\int_0^T \mathrm{d}t\ \hat{H}_{\mathrm{I}}(t)\\ &= |g\rangle\langle g|(\alpha_{\mathrm{g}}(T)\hat{a}^\dagger - \alpha_{\mathrm{g}}^*(T)\hat{a}) + |e\rangle\langle e|(\alpha_{\mathrm{e}}(T)\hat{a}^\dagger - \alpha_{\mathrm{e}}^*(T)\hat{a}),\end{aligned} \tag{4.14}$$

where

$$\alpha_{\mathrm{g}}(T) = \frac{-\epsilon^*\left(e^{i(\delta-\chi)T}-1\right)}{\delta-\chi} \quad \text{and} \quad \alpha_{\mathrm{e}}(T) = \frac{-\epsilon^*\left(e^{i(\delta+\chi)T}-1\right)}{\delta+\chi}. \tag{4.15}$$

As $[\hat{H}_{\mathrm{I}}(t_1),\hat{H}_{\mathrm{I}}(t_2)] \propto f(\sigma_z)\otimes\mathbb{I}$ which commutes with $H_{\mathrm{I}}(t_3)$ the Magnus expansion truncates at second order, and the second order generator results in a qubit-state dependent relative Stark phase. Also, as $\Omega_2(T,0)$ commutes with $\Omega_1(T,0)$ the full evolution operator is

$$\begin{aligned}\hat{U}_{\mathrm{I}}(T,0) &= \exp\{\Omega_1(T,0)\}\exp\{\Omega_2(T,0)\}\\ &= \left(|g\rangle\langle g|\hat{D}(\alpha_{\mathrm{g}}(T)) + |e\rangle\langle e|\hat{D}(\alpha_{\mathrm{e}}(T))\right)e^{iF(\sigma_z T)}\end{aligned} \tag{4.16}$$

where $\hat{D}(\beta) = \exp\left\{\beta\hat{a}^\dagger - \beta^*\hat{a}\right\}$ is the usual displacement operator, and $e^{iF(\sigma_z T)}$ is the phase from the $\Omega_2(T,0)$ term, shown explicitly in equation (4.34).

In the lab frame of equation (4.1) we consider an initial state given by $|g,0\rangle$, which is the ground state of the Jaynes-Cummings Hamiltonian. This state is a dark state and therefore invariant under both the transformation into the dispersive frame $\hat{U}_{\mathrm{D}}(t)$ and the transformation into the interaction frame $\exp\left\{i\hat{H}_{\mathrm{D}}t\right\}$, and so in the dispersive-interaction frame the initial state is $|\psi'(0)\rangle = |g,0\rangle$ (we work in the lab frame basis throughout).

We can then calculate the final state in the dispersive-interaction frame

$$|\psi'_{\mathrm{D}}(T)\rangle = \left(|g\rangle\langle g|\hat{D}(\alpha_{\mathrm{g}}(T)) + |e\rangle\langle e|\hat{D}(\alpha_{\mathrm{e}}(T))\right)|g,0\rangle = |g,\alpha_{\mathrm{g}}(T)\rangle, \tag{4.17}$$

where as our initial state is not a qubit superposition state the effect of the second order Magnus term is a global phase that can be ignored. Next we

transform this trivially out of the interaction frame back to the dispersive frame

$$|\psi_{\mathrm{D}}(T)\rangle = \exp\left\{-i\hat{H}_{\mathrm{D}}T\right\}|\psi'_{\mathrm{D}}(T)\rangle = |g\rangle e^{-|\alpha_{\mathrm{g}}(T)|^2}\sum_n \frac{\alpha_{\mathrm{g}}^n(T)}{\sqrt{n!}} e^{-i(\omega_{\mathrm{c}}-\chi)\hat{a}^\dagger\hat{a}T}|n\rangle$$
$$= |g, \alpha_{\mathrm{g}}(T)e^{-i(\omega_{\mathrm{c}}-\chi)T}\rangle = |g, \tilde{\alpha}_{\mathrm{g}}(T)\rangle. \tag{4.18}$$

To return to the lab frame we must apply the inverse dispersive transformation $\hat{U}_{\mathrm{D}}^\dagger$, and using equation (4.8) we see that the final state in the lab frame is

$$|\psi(T)\rangle = \hat{U}_{\mathrm{D}}^\dagger|g, \tilde{\alpha}_{\mathrm{g}}(T)\rangle = e^{-|\tilde{\alpha}_{\mathrm{g}}(T)|^2}\sum_n \frac{\tilde{\alpha}_{\mathrm{g}}^n(T)}{\sqrt{n!}}\hat{U}_{\mathrm{D}}^\dagger|g, n\rangle$$
$$= e^{-|\tilde{\alpha}_{\mathrm{g}}(T)|^2}\sum_n \frac{\tilde{\alpha}_{\mathrm{g}}^n(T)}{\sqrt{n!}}\overline{|g, n\rangle}. \tag{4.19}$$

The qubit-cavity state of equation (4.19) is the dressed coherent state $\overline{|g, \tilde{\alpha}_{\mathrm{g}}(T)\rangle}$, where in general a dressed coherent state has the form

$$\overline{|g/e, \alpha\rangle} = e^{-\frac{|\alpha|^2}{2}}\sum_n \frac{\alpha^n}{\sqrt{n!}}\overline{|g/e, n\rangle}, \tag{4.20}$$

where $\overline{|g/e, n\rangle}$ is given exactly be equation (4.2)/(4.3), and to first order in λ by equation (4.5)/(4.6). To the best of our knowledge this state was first described in Ref. [114]. Schematic diagrams of the dressed coherent states $\overline{|g, \alpha\rangle}$ and $\overline{|e, \alpha\rangle}$ for $|\alpha|^2 = 4$ are shown in FIG. 4.1. The curves in FIG. 4.1 represent the Poissonian weights of the sum in equation (4.20), and highlight the fact that the dressed coherent state has the same distribution of superposition coefficients as the coherent state, only for the dressed states instead of the bare states.

As we have just shown, if the system starts in the state $|g, 0\rangle$ then the final state of the system after a classical cavity drive of length T will be the dressed coherent state $\overline{|g, \tilde{\alpha}_{\mathrm{g}}(T)\rangle}$. Similarly, if the system starts in its first excited state, given by $\overline{|e, 0\rangle}$ in the lab frame, then the final state after classical drive will be the state $\overline{|e, \tilde{\alpha}_{\mathrm{e}}(T)\rangle}$ (see appendix 4.A for further details). We will now discuss an intuitive physical understanding of the dressed coherent state, and compare the analytic results to full numerical simulations.

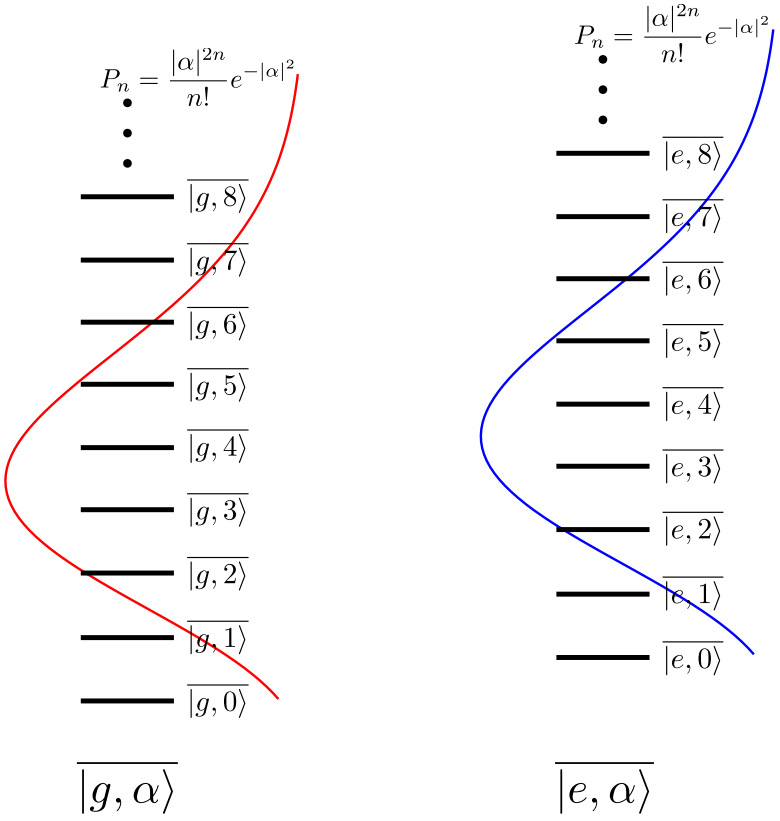

Figure 4.1: Schematic diagrams of the dressed coherent states $\overline{|g,\alpha\rangle}$ and $\overline{|e,\alpha\rangle}$ for $|\alpha|^2 = 4$. The red and blue curves are the Poisson distribution of superposition coefficients, $P_n = |\overline{\langle g/e, n|g/e,\alpha\rangle}|^2$.

4.3.2 Effective Qubit Drive

To understand the dressed coherent state for $\lambda \ll 1$ it is useful to expand the state of equation (4.20) in powers of λ to obtain

$$\begin{aligned}\overline{|g,\beta\rangle} &= e^{-\frac{|\beta|^2}{2}} \sum_n \frac{\beta^n}{\sqrt{n!}} \left(\left(1-\lambda^2\frac{n}{2}\right)|g,n\rangle - \lambda\sqrt{n}|e,n-1\rangle\right) + \mathcal{O}\left(\lambda^3\right) \\ &= \left(|g\rangle - \lambda\beta|e\rangle\right)|\beta\rangle - \frac{\lambda^2}{2} e^{-\frac{|\beta|^2}{2}} \sum_n \frac{\beta^n}{\sqrt{(n-1)!}}\sqrt{n}|g,n\rangle + \mathcal{O}\left(\lambda^3\right),\end{aligned} \tag{4.21}$$

and we see that to lowest nontrivial order in λ the qubit is effectively in the superposition state $\left(|g\rangle - \lambda\beta|e\rangle\right)/\sqrt{\mathcal{N}}$, with the normalization factor $\mathcal{N} = 1+\lambda^2|\beta|^2$. Thus, to lowest order in λ, when the qubit-cavity system is driven by a classical cavity drive (creating a dressed coherent state) the qubit is

effectively weakly driven on resonance via the Hamiltonian (in the interaction picture)

$$\hat{H}_{\text{Eff}} = q_0\hat{\sigma}^- + q_0^*\hat{\sigma}^+, \tag{4.22}$$

for a time T as before, where the effective qubit drive strength is given by $q_0 = (i\beta^*\lambda)/T$ for the dressed coherent state $\overline{|g,\beta\rangle}$.

It is important to note that under the dispersive approximation the cavity drive of equation (4.10) is only the leading order term, and that the next order correction in the dispersive frame, of order λ, is a qubit drive. However, this drive is at a frequency ω_{d}, which will not be resonant with the qubit transition frequency, and as a result this qubit drive has no net effect on relevant timescales. For this reason we have not included this off-resonant qubit drive in our analtyical calculations.

The effective resonant qubit drive described here by equation (4.22) is not due to this first order term in the dispersive approximation of the cavity drive Hamiltonian, as it occurs even when only the zeroth order term of the dispersive frame cavity drive is considered, as in equation (4.10). It is uniquely an effect of considering the lab frame state for qubit-cavity interaction with a driven cavity, and results from interactions between the cavity and the qubit.

4.3.3 Numerical Simulations

In section 4.3.1 we have shown that under the dispersive approximation done completely, the final state in the lab frame of a qubit-cavity system after a classical cavity drive is a dressed coherent state. While for $\lambda \ll 1$ and $|\alpha|^2 \ll n_{\text{crit}}$ it is sufficient to keep terms up to order λ^2 and obtain the Hamiltonian of equation (4.7), it is worthwhile to examine what effect the neglected higher order terms have on the final state. To do so, we numerically investigate time evolution induced by the Hamiltonian

$$\hat{H}_{\text{T}}(t) = \omega_{\text{c}}\hat{a}^\dagger\hat{a} - \frac{\omega_{\text{q}}}{2}\hat{\sigma}_z + g\left(\hat{\sigma}^-\hat{a}^\dagger + \hat{\sigma}^+\hat{a}\right) + \left(\epsilon e^{i\omega_{\text{d}}t}\hat{a} + \epsilon^* e^{-i\omega_{\text{d}}t}\hat{a}^\dagger\right)\Theta(t-T), \tag{4.23}$$

for the lab frame initial states $\overline{|g,0\rangle}$ and $\overline{|e,0\rangle}$, with $\omega_{\text{d}} = \omega_{\text{c}} - \chi$ and $\omega_{\text{d}} = \omega_{\text{c}} + \chi$ respectively. We simulate over a range of λ, ϵ, and target $\tilde{\alpha}_{\text{g/e}}(T)$ to see how these parameters affect the accuracy of the dressed coherent state.

We compare the numerically created states with the dressed coherent states $\overline{|g,\tilde{\alpha}_{\text{g}}(T)\rangle}$ and $\overline{|e,\tilde{\alpha}_{\text{e}}(T)\rangle}$, as well as the undressed product states $|g,\tilde{\alpha}_{\text{g}}(T)\rangle$ and $|e,\tilde{\alpha}_{\text{e}}(T)\rangle$ (all in the lab frame), by calculating the overlap

fidelities

$$\mathcal{F}_{\mathrm{D}}^{g/e}(|\alpha|^2,\epsilon,\lambda) = \left|\langle\psi(T)||\overline{g/e,\tilde{\alpha}_{\mathrm{g/e}}(T)}\rangle\right|^2, \tag{4.24}$$

$$\mathcal{F}^{g/e}(|\alpha|^2,\epsilon,\lambda) = \left|\langle\psi(T)||g/e,\tilde{\alpha}_{\mathrm{g/e}}(T)\rangle\right|^2, \tag{4.25}$$

where $|\psi(T)\rangle$ is the state created by numerical simulation, and we have set that for either initial state the target coherent state amplitude is the same, i.e. $|\tilde{\alpha}_{\mathrm{g}}(T)| = |\tilde{\alpha}_{\mathrm{e}}(T)| = |\alpha(T)|$. The phase of $\alpha(T)$ has no impact on the fidelity and so the fidelity depends only on $|\alpha|^2$. The results are shown in FIGs. 4.2 and 4.3.

Figures 4.2(a), 4.3(a), and 4.3(b) show $1 - \mathcal{F}_{\mathrm{D}}^{g/e}(|\alpha|^2,\epsilon,\lambda)$ for varying $|\alpha|^2$, λ, and ϵ respectively, with the non-varying parameters held at the constant values indicted on the figures. Fidelities for both the ground or excited dressed coherent state are plotted. Due to decreasing validity of the dispersive approximation, both FIGs. 4.2(a) and 4.3(a) show a decreasing overlap as either $|\alpha|^2$ or λ increase. As is to be expected, increasing λ is more detrimental to the agreement between the numerical state and the dressed coherent state, as a larger λ requires fewer photons in the cavity for terms beyond order λ^2 in the full Hamiltonian to become relevant. For increasing $|\alpha|^2$, FIG. 4.2(a) shows that even for a high average photon number of $|\alpha|^2 = 9$ the numerical state still has an overlap greater than 90% with a dressed coherent state.

Interestingly, FIG. 4.3(b) shows that for increasing drive strength ϵ, the overlap between the dressed coherent state and the numerical state actually increases. This can likely be understood by competition between the cavity drive and higher order effects beyond the dispersive approximation, which will both be off-diagonal in the basis of equation (4.7). The stronger the drive, the more it dominates this competition, which therefore diminishes the effect of the higher order correction terms, leading to a state closer to the dressed coherent state.

Finally, FIG. 4.2(b) shows the difference in fidelity between the dressed coherent state and the undressed product state, i.e.

$$\text{Overlap Difference} = \mathcal{F}_{\mathrm{D}}^{g/e}(|\alpha|^2,\epsilon,\lambda) - \mathcal{F}^{g/e}(|\alpha|^2,\epsilon,\lambda), \tag{4.26}$$

as a function of $|\alpha|^2$. As can be seen, the difference is always positive, and the dressed coherent state is always a better description of the numerical state than the undressed product state.

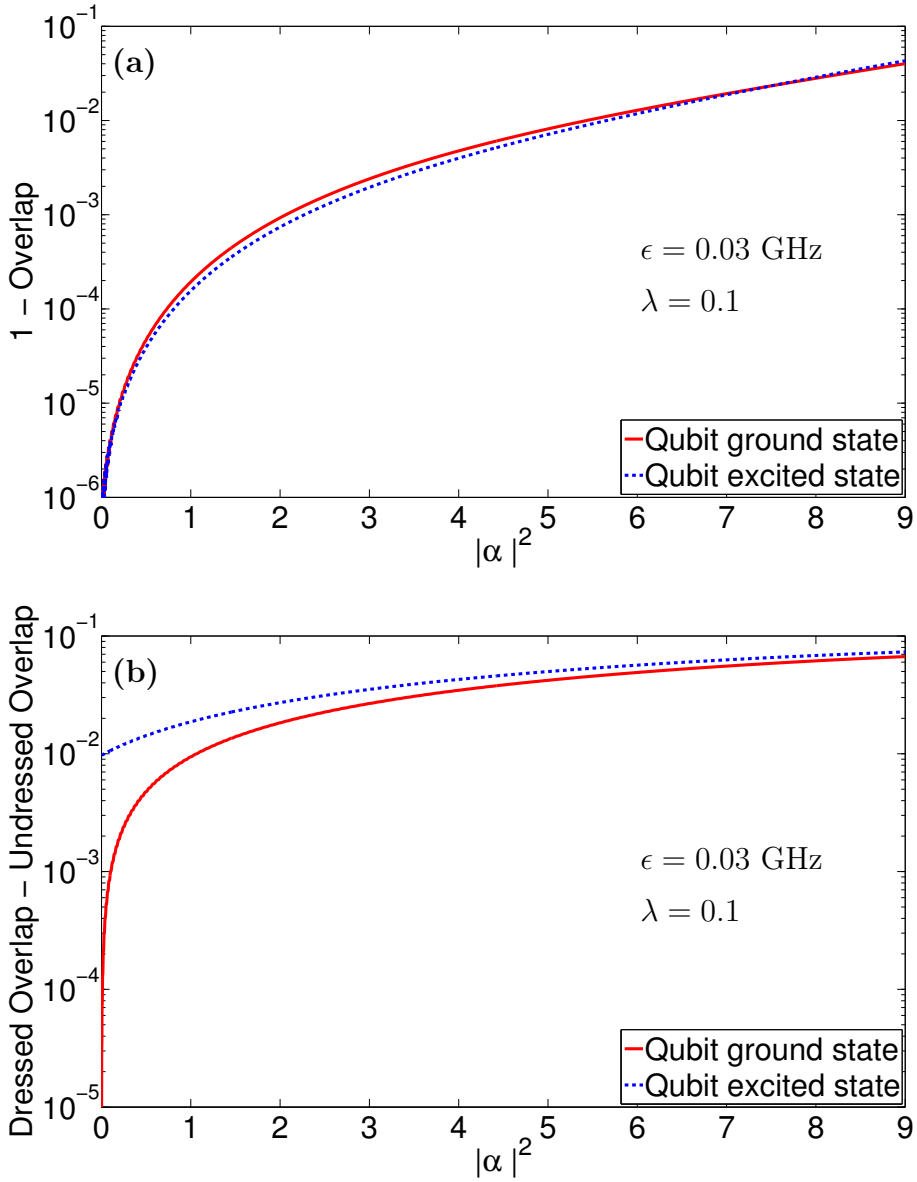

Figure 4.2: **(a)** Comparison of the numerical state created by simulation of equation (4.23) with the dressed coherent state and **(b)** the difference in overlap with the numerical state between the dressed coherent state and the undressed product state, both as a function of photon number $|\alpha|^2$, with ϵ and λ constant. Values of $|\alpha|^2$, λ, and ϵ chosen to be commensurate with current experiments. Additional phase matching was required to obtain high fidelity (see appendix 4.B).

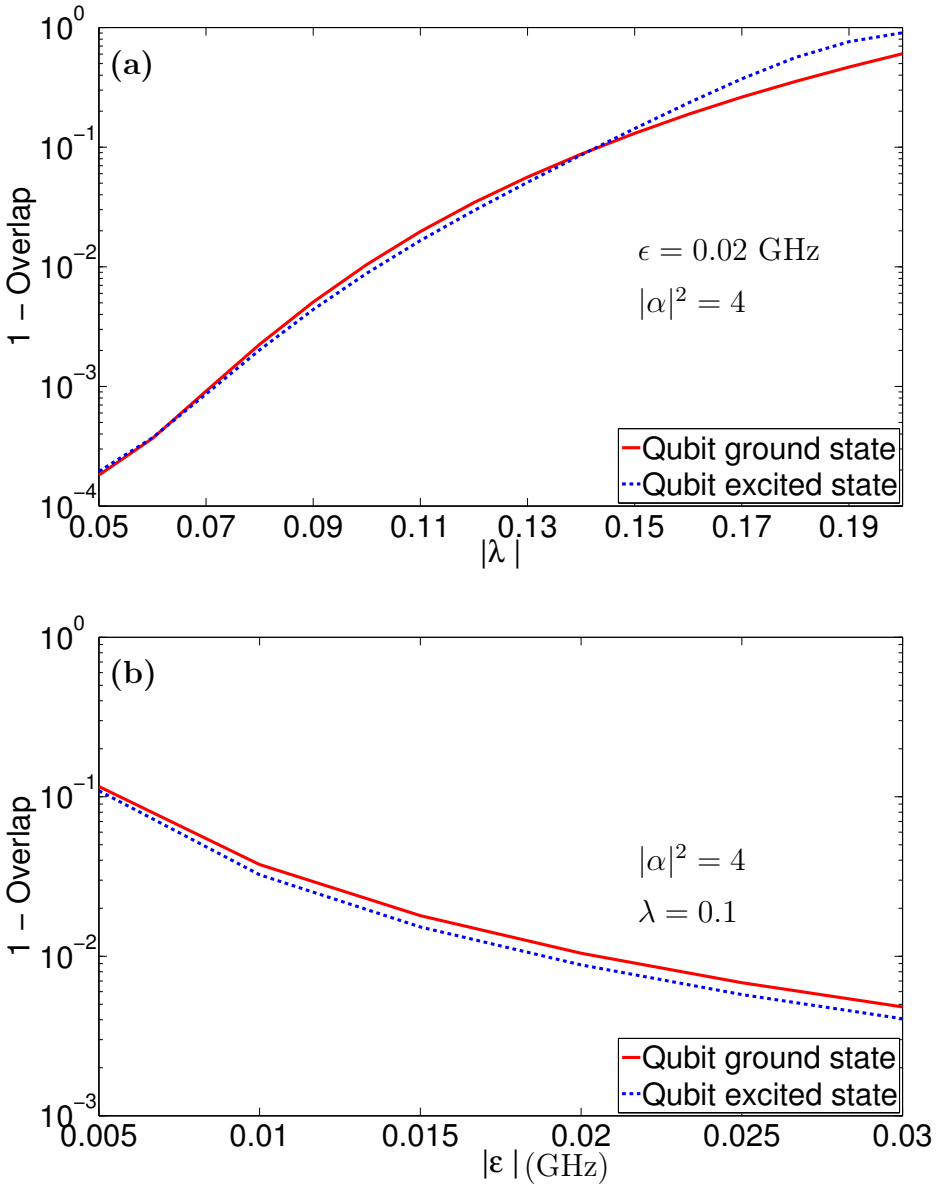

Figure 4.3: Comparison of the numerical state created by simulation of equation (4.23) with the dressed coherent state as a function of **(a)** λ, with ϵ and $|\alpha|^2$ constant, and **(b)** drive strength ϵ, with $|\alpha|^2$ and λ constant. Values of $|\alpha|^2$, λ, and ϵ chosen to be commensurate with current experiments. Additional phase matching was required to obtain high fidelity (see appendix 4.B).

4.4 Implications and Applications

4.4.1 Qubit Operations

In this section we examine a simple case of qubit operations performed on a dressed coherent state to emphasize the dependence of these operations on both the amplitude and phase of the cavity state. Such interactions could occur in a set-up that involved parallel operations on a qubit and a cavity used as a bus [117] or as a quantum memory [118]. We consider a primitive for qubit operations that, while itself not necessarily useful or interesting, elucidates the relevant physics involved, such that useful and interesting applications may be developed from it in future work. Starting in the dressed coherent state $\overline{|g,\beta\rangle}$ (created as described in section 4.3.1), we attempt to rotate the reduced state of the qubit to as close to the excited state as possible. We will show that the excitation probability will depend on both the amplitude and phase of β.

We begin by expanding the inital dressed coherent state $\overline{|g,\beta\rangle}$ to lowest order in λ, as in equation (4.21). In this case, the reduced state of the qubit is a weakly rotated qubit state, with the phase of this rotation proportional to the phase of β. For a weakly rotated qubit state, the probability amplitude upon further rotating the qubit depends on the phase of the applied drive relative to the phase of the initial qubit rotation, and therefore, the success of rotating to the excited state from the state $\overline{|g,\beta\rangle}$ will depend on the phase of β. For purely real (imaginary) β, the reduced qubit state lies in the x-z (y-z) plane on the Bloch sphere, and rotation about the x (y) axis cannot transform the qubit state to the state $|e\rangle$, while rotation about the y (x) axis can. For general β the superposition is along the plane defined by the z axis and the line $\{(x,y) = (\cos(\phi_\beta)s, \sin(\phi_\beta)s),\ \forall s \in \mathbb{R}\}$ in the x-y plane, which depends on the phase of β, given by ϕ_β. In this case perfect state transfer to $|e\rangle$ is not possible by rotation along any axis other than that defined by $\phi_\beta + \pi/2$, given by the line $\{(x,y) = (\sin(\phi_\beta)s, \cos(\phi_\beta)s),\ \forall s \in \mathbb{R}\}$.

More rigorously, we consider the qubit-drive Hamiltonian to first order in the dispersive frame given by

$$\hat{H}_{\mathrm{Q}} = \eta e^{-i\omega t}\hat{\sigma}^{+} + \eta^{*} e^{i\omega t}\hat{\sigma}^{-}. \tag{4.27}$$

In the interaction picture with respect to the dispersive Hamiltonian of equation (4.7), this Hamiltonian becomes

$$\hat{H}'_{\mathrm{Q}} = \eta e^{i\nu t} e^{i2\chi\hat{n}t}\hat{\sigma}^{+} + \eta^{*} e^{-i\nu t} e^{-i2\chi\hat{n}t}\hat{\sigma}^{-}, \tag{4.28}$$

where $\hat{n} = \hat{a}^{\dagger}\hat{a}$ and $\nu = \omega_{\mathrm{q}} + \chi - \omega$. To calculate the evolution operator, we follow the same procedure as in section 4.3.1 using the Magnus expansion.

Unfortunately, the Magnus generators Ω_n do not vanish for any finite order n, due to the nonlinearity of the qubit. To account for this we choose our evolution time to be short enough (roughly one period for the drive frequency ω) that Magnus terms beyond first order have minimal contribution to the evolution, as the magnitude of their effects is small and only becomes relevant after accumulating for a long period of time. With this in mind, the analytical results presented below are meant to be instructive and to highlight the important physical effects, rather than to have high accuracy.

The result of this calculation (see appendix 4.C for further details) is a very complicated expression for the excited state probability as a function of time, given by equation (4.45). In order to gain some intuitive understanding of the rigorous result, we set $\omega = \omega_q$ and go to the limit where $\chi, \lambda \to 0$, in which case, the probability of finding the qubit in the excited state at time τ is given by

$$\begin{aligned} P_e(\tau) = &\left(1-\lambda^2\right)\sin^2(\eta\tau) + \lambda^2|\beta|^2\cos(2\eta\tau) \\ &+ \lambda\sin(2\eta\tau)\left(\mathrm{Im}(\beta e^{-i\varphi})\cos(\Delta\tau) + \mathrm{Re}(\beta e^{-i\varphi})\sin(\Delta\tau)\right), \end{aligned} \tag{4.29}$$

where $e^{i\varphi} = \eta/|\eta|$, and $\Delta = \omega_q - \omega_c$ as before. From the last term in equation (4.29) we see that the excited state probability depends not only on the photon number in the cavity, but also the interplay between the coherent state phase and the phase of the drive, through the unequal dependence on $\mathrm{Re}(\beta e^{-i\varphi})$ and $\mathrm{Im}(\beta e^{-i\varphi})$. This effect can be understood as interference between the effective qubit drive of equation (4.22) caused by the dressed coherent state and the applied qubit drive of equation (4.27), in a manner similar to coherent destruction of tunneling [119].

Unfortunately, while easy to understand, equation (4.29) is not very accurate in the relevant parameter regimes, and the truncation of the Magnus expansion becomes less valid for longer times. However, the analytical calculations leading to equation (4.29) were done to distill the relevant physical effects and present them in an understandable manner, not to obtain highly accurate results. To accurately test the phase dependence effects, we numerically simulate a qubit-cavity system with classical qubit drive (without making the dispersive approximation). As an initial state, we start with the state created by simulation of equation (4.23) of section 4.3.3, which has high overlap with a dressed coherent state. Figure 4.4 shows the excited state probability as a function of time, starting in a dressed coherent state with either purely real or imaginary β, and with a purely real qubit drive η.

In addition to photon number effects, where the qubit resonance frequency is modified by the photon number in the cavity [120], FIG. 4.4 shows that the excited state probability's time evolution depends also on the phase of the

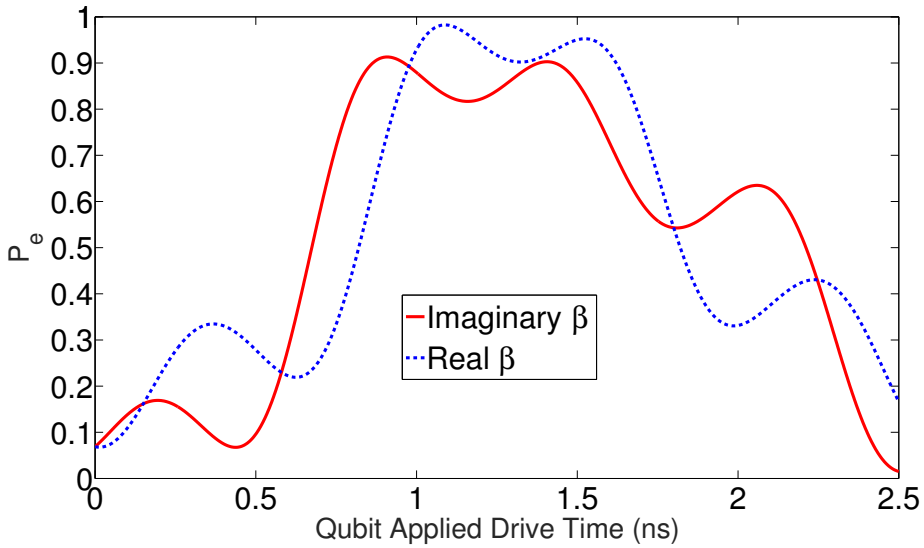

Figure 4.4: Qubit excited state probability as a function of the time of the applied qubit drive, starting in a dressed coherent state with either purely imaginary β or purely real β. The drive strength is strong, $|\eta| = 0.1\omega_{\mathrm{q}}$, so that phase effects are clearly visible. The drive frequency is set to the qubit frequency, $\omega = \omega_{\mathrm{q}}$, η is purely real (i.e. $|\eta| = \eta$), and $\lambda = 0.1$ as elsewhere.

dressed coherent state amplitude β. This agrees with the intuitive conclusions drawn previously, using the approximation of equation (4.21), where one considers the dressed coherent state to be a coherent state in the cavity, and a weakly rotated qubit.

4.4.2 Dispersive Multi-Qubit Readout with a Threshold Detector - Limited Contrast

In recent proposals for dispersive single qubit readout [47], and qubit parity readout [121], protocols were developed that conditionally populate the cavity dependent on the state (parity) of the qubit(s), after which, by using a threshold photon counter to distinguish between the qubit dependent cavity states, the state (parity) of the qubit(s) can be non-destructively measured. A subsequent coherent cavity drive of opposite phase removes the cavity occupation. Such conditional cavity occupation can be achieved by setting $\omega_{\mathrm{d}} = \omega_{\mathrm{c}} - \chi$ in equation (4.15), and the correct choice of T such that $\tilde{\alpha}_{\mathrm{g}}(T) \neq 0$ while $\tilde{\alpha}_{\mathrm{e}}(T) = 0$.

For single-qubit readout, starting from an initial state in the lab frame

of either $|g,0\rangle$ or $|e,0\rangle$ and using equations (4.19) and (4.38), after classical cavity drive the qubit state dependent qubit-cavity states are

$$|\psi(T)\rangle = \overline{|g,\tilde{\alpha}_g(T)\rangle}, \tag{4.30}$$

$$|\Psi(T)\rangle = \cos(\lambda)\,\overline{|e,0\rangle} - e^{i(\omega_q+\chi)}\sin(\lambda)\,\hat{U}_D^\dagger|g\rangle|\xi(T)\rangle, \tag{4.31}$$

for the suitable choice of T that ensures $\tilde{\alpha}_e(T) = 0$. Misidentification of the qubit excited state as the ground state occurs when there is spurious photon population in the cavity when the qubit is in its excited state. As can be calculated using equation (4.31) this spurious photon population is given by

$$\begin{aligned} N &= \langle\Psi(T)|\hat{a}^\dagger\hat{a}|\Psi(T)\rangle \\ &\approx \sin^2(\lambda)\left(\cos^2(\lambda)\,\langle 1|\hat{a}^\dagger\hat{a}|1\rangle + \langle g|\langle\xi(T)|\hat{U}_D\hat{a}^\dagger\hat{a}\hat{U}_D^\dagger|g\rangle|\xi(T)\rangle\right) \\ &\approx \sin^2(\lambda)\left(\cos^2(\lambda) + \langle\xi(T)|\hat{a}^\dagger\hat{a}|\xi(T)\rangle\right) \\ &= \sin^2(\lambda)\left(\cos^2(\lambda) + 1 + |\alpha_g|^2\right) \end{aligned} \tag{4.32}$$

where in the first approximation we have ignored the cross terms as the photon occupation of $|\xi(T)\rangle$ is much greater than 1, and in the second approximation we have assumed the dispersive transformation only slightly modifies the average photon number of $|\xi(T)\rangle$. The photon occupation of $|\xi(T)\rangle$ is high since it is the single photon Fock state displaced by $\hat{D}(\alpha_g(T))$, and $\alpha_g(T) > 0$ for this protocol. Extending this effect to multiple qubits in their excited states explains the even parity misidentification error for four qubit parity measurement seen in Ref. [121], as it is the four-qubit generalization of the state $|\xi(T)\rangle$ that leads to spurious detections when the qubits are in an even parity state. The exact value of this error is dependent on the nature of the threshold photon counter used [59, 88].

4.5 Conclusion

In the work presented here, we have undertaken a critical and careful examination of the dispersive limit, dispersive approximation, and the dispersive Hamiltonian, in order to understand the distinction and commonalities between these commonly used terms. We have found that one obtains the dispersive Hamiltonian after making the dispersive approximation, which requires both being in the dispersive limit of the Jaynes-Cummings interaction, and a frame transformation to the dispersive frame. The dispersive Hamiltonian therefore describes evolution of the system in the dispersive frame, and in order to obtain results valid in the lab frame, one must apply the inverse frame transformation.

This has a profound effect on the description of the system state, and in particular, we have found that after a classical drive is applied to the cavity, the state of the system in the lab frame is accurately described by the dressed coherent state $\overline{|g/e,\alpha\rangle}$, not, as typically used, the product state $|g/e\rangle|\alpha\rangle$. The entanglement present in the dressed coherent state will affect all future operations on the qubit and the cavity. We have shown how this is relevant to rotations of the qubit state, in particular that the probability of rotating the qubit from its ground to excited state (or vice versa) depends on the phase difference between α and the applied qubit drive. We have also explained the limit in measurement contrast for readout of the qubit state via a cavity and a threshold photon counter, reported in Ref. [121]. Future work will continue to explore the effects of the dressed coherent state on contemporary quantum information protocols.

Acknowledgements

The authors acknowledge insightful discussions with Bruno G. Taketani. Supported by the Army Research Office under contract W911NF-14-1-0080 and the European Union through ScaleQIT. LCGG acknowledges support from NSERC through an NSERC PGS-D.

Appendix

4.A Dressed Coherent State for An Excited Qubit

In this appendix we consider starting in the initial state in the lab frame of the bare excited qubit state $|e,0\rangle$, which can be prepared by initialization to the state $|g,0\rangle$ followed by a fast, nonadiabatic pulse on the qubit. In the dispersive frame the initial state will be $|\Psi_{\rm D}(0)\rangle = U_{\rm D}|e,0\rangle = \cos(\lambda)\,|e,0\rangle - \sin(\lambda)\,|g,1\rangle$. Transforming into the interaction frame, the state is unchanged since $t=0$. To calculate the final state, we will need the second order Magnus generator, given by

$$\Omega_2(T,0) = -\frac{1}{2}\int_0^T \mathrm{d}t_1 \int_0^{t_1} \mathrm{d}t_2 \ \Big[\hat{H}_{\rm I}(t_1), \hat{H}_{\rm I}(t_2)\Big] = i\frac{|\epsilon|^2}{\chi^2}\Big(\sin(\chi T\sigma_z) - \chi T\sigma_z\Big) \tag{4.33}$$

From this we can calculate the qubit-state dependent phase due to the second order Magnus generator, given by

$$e^{iF(\sigma_z T)} = \exp\left(i\frac{|\epsilon|^2}{\chi^2}\Big(\sin(\chi T\sigma_z) - \chi T\sigma_z\Big)\right), \tag{4.34}$$

and make the identification

$$F(\sigma_z T) = \frac{|\epsilon|^2}{\chi^2}\Big(\sin(\chi T\sigma_z) - \chi T\sigma_z\Big). \tag{4.35}$$

Now using equation (4.16), at $t=T$ the system state in the dispersive-interaction frame is given by

$$|\Psi'_{\rm D}(T)\rangle = \cos(\lambda)\,|e,\alpha_{\rm e}(T)\rangle - e^{i[F(T)-F(-T)]}\sin(\lambda)\,|g\rangle\hat{D}(\alpha_{\rm g}(T))|1\rangle, \tag{4.36}$$

where we have factored out a global phase. Transforming back into the dispersive frame we have:

$$\begin{aligned}|\Psi_{\rm D}(T)\rangle &= \cos(\lambda)\,|e,\tilde{\alpha}_{\rm e}(T)\rangle \\ &\quad - e^{i(\omega_{\rm q}+\chi)T}e^{i2F(T)}\sin(\lambda)\,|g\rangle e^{-i\left(\omega_{\rm c}\hat{a}^\dagger\hat{a} - \chi\hat{\sigma}_z\hat{a}^\dagger\hat{a}\right)T}\hat{D}(\alpha_{\rm g}(T))|1\rangle \\ &= \cos(\lambda)\,|e,\tilde{\alpha}_{\rm e}(T)\rangle - e^{iG(T)}\sin(\lambda)\,|g\rangle|\xi(T)\rangle,\end{aligned} \tag{4.37}$$

where $\tilde{\alpha}_{\mathrm{e}}(T) = \alpha_{\mathrm{e}}(T)e^{-i(\omega_{\mathrm{c}}+\chi)T}$, $G(T) = (\omega_{\mathrm{q}} + \chi)T + 2F(T)$, and $|\xi(T)\rangle = e^{-i\left(\omega_{\mathrm{c}}\hat{a}^\dagger\hat{a} - \chi\hat{\sigma}_z\hat{a}^\dagger\hat{a}\right)T}\hat{D}(\alpha_{\mathrm{g}}(T))|1\rangle$ is the displaced single photon Fock state. Finally, transforming back into the lab frame gives

$$\begin{aligned}|\Psi(T)\rangle &= \hat{U}_{\mathrm{D}}^\dagger\left(\cos(\lambda)\,|e,\tilde{\alpha}_{\mathrm{e}}(T)\rangle - e^{iG(T)}\sin(\lambda)\,|g\rangle|\xi(t)\rangle\right)\\ &= \cos(\lambda)\,\overline{|e,\tilde{\alpha}_{\mathrm{e}}(T)\rangle} - e^{iG(T)}\sin(\lambda)\,\hat{U}_{\mathrm{D}}^\dagger|g\rangle|\xi(t)\rangle,\end{aligned} \tag{4.38}$$

where as before we have made the identification that $\hat{U}_{\mathrm{D}}^\dagger|e,\tilde{\alpha}_{\mathrm{e}}(T)\rangle = \overline{|e,\tilde{\alpha}_{\mathrm{e}}(T)\rangle}$ to first order in λ. If $\lambda \ll 1$ such that $\sin(\lambda) \approx 0$, then as before $|\Psi(T)\rangle$ is a dressed coherent state. Additionally, if as an initial state we use $|\Psi(0)\rangle = \overline{|e,0\rangle}$ instead of the bare excited state $|e,0\rangle$, then as $\hat{U}_{\mathrm{D}}\overline{|e,0\rangle} = |e,0\rangle$ the term proportional to $\sin(\lambda)$ in equation (4.38) disappears, and $|\Psi(T)\rangle$ contains only the dressed coherent state $\overline{|e,\tilde{\alpha}_{\mathrm{e}}(T)\rangle}$. The dressed initial state is closer to experimental reality as it is an eigenstate of the Hamiltonian, however, the calculation for the bare initial state $|\Psi(0)\rangle = |e,0\rangle$ was shown for completeness, as some experimental protocols can prepare this state, and as from the solution for the bare initial state the solution for the dressed initial state is trivial to obtain.

4.B Corrections to the Phase of the Dressed Coherent State Due to Nonlinear Terms

In the expected parameter regime, FIGs. 4.2 and 4.3 demonstrate excellent agreement between the state created by a numerical simulation of the Jaynes-Cummings Hamiltonian and the dressed coherent state. However, to obtain this high fidelity, it was necessary to include effects beyond the dispersive Hamiltonian to correctly match the phase of the dressed coherent state amplitude $\tilde{\alpha}_{\mathrm{g/e}}(T)$ with the numerical state. In particular, following Ref. [122], we include the nonlinear term proportional to $\Delta\lambda^4$ in the classical equations of motion for the amplitudes $\tilde{\alpha}_{\mathrm{g/e}}(T)$ and obtain the approximate solutions

$$\tilde{\alpha}_{\mathrm{g}}(T) = \alpha_{\mathrm{g}}(T)\exp\left(-i\left(\omega_{\mathrm{c}} - \chi + \zeta\frac{\langle\hat{n}(T)\rangle}{2}\right)T\right), \tag{4.39}$$

$$\tilde{\alpha}_{\mathrm{e}}(T) = \alpha_{\mathrm{e}}(T)\exp\left(-i\left(\omega_{\mathrm{c}} + \chi - \zeta\left(\frac{\langle\hat{n}(T)\rangle}{2} + 1\right)\right)T\right), \tag{4.40}$$

where $\zeta = \Delta\lambda^4$, $\langle\hat{n}(T)\rangle = \langle\hat{a}^\dagger\hat{a}\rangle(T)$ is the average photon number in the cavity at time T, and $\alpha_{\mathrm{g/e}}(T)$ are defined as before in equation (4.15). Using these modified coherent state amplitudes in equations (4.19) and (4.38) gives the excellent overlap with the numerical states seen in FIGs. 4.2 and 4.3.

We emphasize that the nonlinear corrections have only been used to correct the classical solution for $\tilde{\alpha}_{g/e}(T)$, and that to lowest order the nonlinearity modifies only the phase and not the amplitude of the dressed coherent states. Furthermore, the squeezing Hamiltonian of the nonlinearity is not considered in our analytical calculations (as this would modify the state so that it was no longer a dressed coherent state), and while its effect is small, we suspect it to be the leading cause of the less than unit fidelity seen in FIG. 4.2 and 4.3.

4.C Driven Qubit Excited State Probability

To first order in the Magnus expansion, the qubit-drive evolution operator is

$$\begin{aligned}\hat{U}_{\mathrm{Q}}(\tau,0) &= \exp\left\{-i\Omega_1(\tau,0)\right\}\\ &= \cos\left(|\eta b(\hat{n},\tau)|\left(\nu+2\chi\hat{n}\right)^{-1}\right)\mathbb{I}\\ &+ \sin\left(|\eta b(\hat{n},\tau)|\left(\nu+2\chi\hat{n}\right)^{-1}\right)\left((\eta b(\hat{n},\tau))^{*}\sigma^{-}-\eta b(\hat{n},\tau)\sigma^{+}\right)|\eta b(\hat{n},\tau)|^{-1},\end{aligned} \tag{4.41}$$

where we have defined the operator function $b(\hat{n},\tau)=1-e^{i(\nu+2\chi\hat{n})\tau}$. Starting from the initial state $|\psi'_{\mathrm{D}}(0)\rangle=|g,\beta\rangle$ in the dispersive-interaction frame, the state after a time τ of the applied qubit-drive is

$$\begin{aligned}|\psi'_{\mathrm{D}}(\tau)\rangle &= \hat{U}_{\mathrm{Q}}(\tau,0)|\psi'_{\mathrm{D}}(0)\rangle\\ &= e^{\frac{-|\beta|^2}{2}}\sum_k \frac{\beta^k}{\sqrt{k!}}\Bigg(\cos\left(\frac{|\eta b(k,\tau)|}{\nu+2k\chi}\right)|g,k\rangle\\ &- i\sin\left(\frac{|\eta b(k,\tau)|}{\nu+2k\chi}\right)e^{i\varphi}e^{i(\nu+2k\chi)\tau/2}|e,k\rangle\Bigg)\end{aligned} \tag{4.42}$$

where $e^{i\varphi}=\eta/|\eta|$, and we have used the fact that $b(k,\tau)/|b(k,\tau)|=ie^{i(\nu+2k\chi)\tau/2}$. Transforming out of the interaction frame, we arrive at the state in the dispersive frame (after factoring out a global phase)

$$\begin{aligned}|\psi_{\mathrm{D}}(\tau)\rangle &= \hat{U}_{\mathrm{I}}^{\dagger}(\tau,0)|\psi'_{\mathrm{D}}(\tau)\rangle\\ &= e^{\frac{-|\beta|^2}{2}}\sum_k \frac{\tilde{\beta}^k}{\sqrt{k!}}\Bigg(\cos\left(\frac{|\eta b(k,\tau)|}{\nu+2k\chi}\right)|g,k\rangle\\ &- i\sin\left(\frac{|\eta b(k,\tau)|}{\nu+2k\chi}\right)e^{i\varphi}e^{-i\Sigma\tau/2}|e,k\rangle\Bigg)\end{aligned} \tag{4.43}$$

where $\tilde{\beta} = \beta e^{-i\omega_c \tau}$ absorbs the rotation of the cavity state in phase space, and $\Sigma = \omega_q + \chi + \omega + 2k\chi = \nu + 2k\chi + 2\omega$. Finally, transforming back into the lab frame, we end up with the state

$$\begin{aligned}
&|\psi_D(\tau)\rangle = \hat{U}_D^\dagger(\tau,0)|\psi_D(\tau)\rangle \\
&= e^{\frac{-|\beta|^2}{2}} \sum_k \frac{\tilde{\beta}^k}{\sqrt{k!}} \Bigg[\cos\Big(\tfrac{|\eta b(k,\tau)|}{\nu+2k\chi}\Big)\Big(\cos\big(\lambda\sqrt{k}\big)|g,k\rangle - \sin\big(\lambda\sqrt{k}\big)|e,k-1\rangle\Big) \\
&- i \sin\Big(\tfrac{|\eta b(k,\tau)|}{\nu+2k\chi}\Big) e^{i\varphi} e^{-i\Sigma\tau/2}\Big(\cos\big(\lambda\sqrt{k+1}\big)|e,k\rangle + \sin\big(\lambda\sqrt{k+1}\big)|g,k+1\rangle\Big)\Bigg].
\end{aligned} \tag{4.44}$$

Now we can calculate the probability at a given time τ that the qubit is in the excited state, given by $P_e(\tau) = \langle\psi_D(\tau)||e\rangle\langle e| \otimes \mathbb{I}|\psi_D(\tau)\rangle$. Using equation (4.44) we calculate this to be

$$\begin{aligned}
&P_e(\tau) = e^{-|\beta|^2} \sum_k \frac{|\beta|^{2k}}{k!}\Big(\cos^2\Big(\tfrac{|\eta b(k,\tau)|}{\nu+2k\chi}\Big)\sin^2\big(\lambda\sqrt{k}\big) + \sin^2\Big(\tfrac{|\eta b(k,\tau)|}{\nu+2k\chi}\Big)\cos^2\big(\lambda\sqrt{k+1}\big)\Big) \\
&+ 2e^{-|\beta|^2} \sum_k \frac{|\beta|^{2k}}{k!\sqrt{k+1}} \cos\Big(\tfrac{|\eta b(k+1,\tau)|}{\nu+2(k+1)\chi}\Big)\sin\big(\lambda\sqrt{k+1}\big)\sin\Big(\tfrac{|\eta b(k,\tau)|}{\nu+2k\chi}\Big)\cos\big(\lambda\sqrt{k+1}\big)\mathrm{Im}\big[\tilde{\beta} e^{-i\varphi} e^{i\Sigma\tau/2}\big].
\end{aligned} \tag{4.45}$$

Equation (4.45) is quite cumbersome, and to gain some intuitive understanding, we set $\omega = \omega_q$ and examine the $\chi, \lambda \to 0$ limit, which results in equation (4.29).

Chapter 5

Coherent Feedback Improved Qubit Initialization in the Dispersive Regime

Luke C. G. Govia and Frank K. Wilhelm

Abstract

Readout of the state of a superconducting qubit by homodyne detection of the output signal from a dispersively coupled microwave resonator is a common technique in circuit quantum electrodynamics, and is usually claimed to be quantum non-demolition (QND) up to the same order of approximation as in the dispersive approximation. However, in this chapter we show that only in the limit of infinite measurement time is this protocol QND, as the formation of a dressed coherent state in the qubit-cavity system applies an effective rotation to the qubit state. We show how this rotation can be corrected by a coherent operation, leading to improved qubit initialization by measurement and coherent feedback.

5.1 Introduction

For most quantum information and computing protocols measurement is a necessary component, either to extract the answer to a computation, or as an operation in the protocol, such as for entanglement generation or gate operations. In addition, many protocols benefit from so called quantum non-demolition (QND) measurement, where the Hamiltonian describing the measurement operator commutes with the self-Hamiltonian of the system [46]. As a result, perfect QND measurement maximally dephases the system in its eigenbasis, and the system state is projected onto an eigenstate when the measurement result is observed. Alternatively, one can think of a QND measurement as having only the minimal (required by quantum mechanics) back action on the system it measures.

In the field of circuit quantum electrodynamics (cQED), the state of a superconducting qubit is typically measured in its eigenbasis by homodyne detection of the phase of the output signal through a cavity dispersively coupled to the qubit [39]. Due to the small signal strength exciting the cavity, it is necessary to amplify the signal using a low noise (near quantum limited) parametric amplifier based on the nonlinearity induced by a Josephson junction [123, 124, 125, 126, 127, 128]. In recent years this measurement scheme has been a great success, with highlights that include the observation of qubit quantum jumps [70], heralded initialization via measurement [71, 72], entanglement generation between qubits [50, 51], quantum teleportation [74], and readout fidelity greater than 99% [75].

Under the dispersive approximation this readout scheme was believed to be QND, as in the dispersive frame the qubit-cavity coupling is diagonal and commutes with the system self-Hamiltonian. However, it was recently shown [129] that for a semi-classically driven cavity, the joint system of the qubit-cavity in the lab frame is an entangled state known as the dressed coherent state. To lowest order, this entanglement results in a rotation of the qubit state that depends on the coherent state amplitude in the cavity. As a result, dispersive measurement as previously proposed is not perfectly QND, even up to the same order of approximation as the dispersive approximation, except in the limit of infinite measurement time. This poses problems for schemes that require perfect QNDness, such as those performing heralded initialization or entanglement generation [71, 72, 93].

In this chapter we examine the dispersive qubit readout protocol and account for the effects of the formation of dressed coherent states during the protocol. In particular, we describe the effective coherent qubit rotation that depends on both the amplitude and phase of the applied cavity drive. This rotation is equivalent to a change of the measurement basis, and, as it is

coherent, it can be corrected for by unitary feedback. This opens up the possibility for true QND measurement by introducing coherent feedback.

5.2 Analytic Model

We consider a system consisting of a single qubit coupled to a microwave resonator (cavity), as described by the familiar Jaynes-Cummings Hamiltonian [37]

$$\hat{H} = \omega_{\mathrm{c}}\hat{a}^{\dagger}\hat{a} - \frac{\omega_{\mathrm{q}}}{2}\hat{\sigma}_z + g\left(\hat{\sigma}^{-}\hat{a}^{\dagger} + \hat{\sigma}^{+}\hat{a}\right), \tag{5.1}$$

where $\hat{a}$ and $\hat{a}^{\dagger}$ are the usual bosonic annihilation and creation operators for the cavity, $\hat{\sigma}_z$ is the Pauli matrix whose eigenstates are the qubit logical states, $\hat{\sigma}^{\pm}$ are the qubit raising and lowering operators, $\omega_{\mathrm{c/q}}$ are the cavity and qubit frequencies, g is the Jaynes-Cummings coupling strength, and we set $\hbar = 1$ from here on. This Hamiltonian describes evolution in the lab frame, by which we mean we have not described any of the system's evolution by a (possibly time dependent) rotation of Hilbert space.

After the dispersive frame transformation, in the limit $\lambda = g/\Delta < 1$, where $\Delta = \omega_{\mathrm{q}} - \omega_{\mathrm{c}}$, the Jaynes-Cummings Hamiltonian reduces to the dispersive Hamiltonian

$$\hat{H}_{\mathrm{D}} = \omega_{\mathrm{c}}\hat{a}^{\dagger}\hat{a} - \frac{\omega_{\mathrm{q}} + \chi}{2}\hat{\sigma}_z - \chi\hat{\sigma}_z\hat{a}^{\dagger}\hat{a}, \tag{5.2}$$

where $\chi = g^2/\Delta$, and we have kept terms only up to second order in λ. The dispersive frame transformation, followed by the discarding of terms beyond second order in λ is commonly called the dispersive approximation. Under the dispersive approximation, the system eigenstates in the lab frame of equation (5.1) are [9]

$$\overline{|g,n\rangle} = \cos\left(\lambda\sqrt{n}\right)|g,n\rangle - \sin\left(\lambda\sqrt{n}\right)|e,n-1\rangle, \tag{5.3}$$

$$\overline{|e,n-1\rangle} = \cos\left(\lambda\sqrt{n}\right)|e,n-1\rangle + \sin\left(\lambda\sqrt{n}\right)|g,n\rangle, \tag{5.4}$$

which are referred to as the dressed eigenstates, and it is worth pointing out that $\overline{|g,0\rangle} = |g,0\rangle$, i.e. the dressed and undressed ground states are the same as $|g,0\rangle$ is dark.

The last required ingredient for dispersive qubit-state readout is a classical cavity drive, described by the Hamiltonian

$$\hat{H}_{\mathrm{d}}(t) = 2\cos(\omega_{\mathrm{d}}t)\left(\epsilon\hat{a} + \epsilon^{*}\hat{a}^{\dagger}\right), \tag{5.5}$$

in the lab frame. Under the dispersive approximation this Hamiltonian is unaffected to lowest order in λ, and the leading order correction term is both damped by the small parameter λ and oscillates quickly provided $\omega_\mathrm{d} \neq \omega_\mathrm{q}$. Now, if we consider photons from the applied drive that interact with the qubit-cavity system, when they exit the cavity they will carry qubit information with them which can be used to read out the state of the qubit. In particular, by setting $\omega_\mathrm{d} = \omega_\mathrm{c}$ the qubit state information is contained only in the phase of the signal exiting the cavity, as described in Ref. [39]. These statements will be made more concrete shortly.

As was shown in [129], if the system starts in either initial state $\overline{|g/e, 0\rangle}$ (see appendix 5.C for the bare excited state as the initial state), then after applying a cavity drive of the form of equation (5.5) for a time T the state of the qubit-cavity system in the lab frame will be the dressed coherent state $\overline{|g/e, \alpha_{g/e}(T)\rangle}$, defined by

$$\overline{|g/e, \alpha_{g/e}(T)\rangle} = e^{-\frac{|\alpha_{g/e}(T)|^2}{2}} \sum_n \frac{\alpha_{g/e}(T)^n}{\sqrt{n!}} \overline{|g/e, n\rangle}, \tag{5.6}$$

where $\alpha_{g/e}(T)$ are given by

$$\begin{aligned} \alpha_\mathrm{g}(T) &= \frac{\epsilon^*}{\chi}\left(e^{-i\chi T} - 1\right) e^{-i(\omega_\mathrm{c} - \chi)T} = -\frac{2i\epsilon^*}{\chi} \sin\left(\frac{\chi}{2}T\right) e^{-i(\omega_\mathrm{c} - \frac{\chi}{2})T}, \\ \alpha_\mathrm{e}(T) &= \frac{-\epsilon^*}{\chi}\left(e^{i\chi T} - 1\right) e^{-i(\omega_\mathrm{c} + \chi)T} = -\frac{2i\epsilon^*}{\chi} \sin\left(\frac{\chi}{2}T\right) e^{-i(\omega_\mathrm{c} + \frac{\chi}{2})T}, \end{aligned} \tag{5.7}$$

for $\omega_\mathrm{d} = \omega_\mathrm{c}$ as used for dispersive readout. The phase factors $e^{-i(\omega_\mathrm{c} \pm \chi)T}$ are due to the cavity self-Hamiltonian as well as the dispersive interaction. The dressed coherent state is entangled, and correctly accounts for the correlations created between the qubit and the cavity during the applied classical drive.

To first order in λ, both dressed coherent states can be approximated by (see appendix 5.A for further details)

$$\overline{|g, \alpha_g(T)\rangle} = \left(|g\rangle - \lambda \alpha_g(T)|e\rangle\right) |\alpha_g(T)\rangle / \sqrt{\mathcal{N}} + \mathcal{O}(\lambda^2), \tag{5.8}$$

$$\overline{|e, \alpha_e(T)\rangle} = \left(|e\rangle + \lambda \alpha_e^*(T)|g\rangle\right) |\alpha_e(T)\rangle / \sqrt{\mathcal{N}} + \mathcal{O}(\lambda^2), \tag{5.9}$$

where $\mathcal{N} = 1 + \lambda^2 |\alpha_{g/e}(T)|^2$, and even for $\lambda \ll 1$ we can keep the term proportional to $\lambda|\alpha_{g/e}(T)|$ as $|\alpha_{g/e}(T)|$ can be large. This approximation gives a good intuitive picture of the effect of an applied cavity drive on a qubit-cavity system described in the lab frame. The cavity is driven to a coherent state (as expected), while the qubit state is rotated a small amount. This rotation depends on the coherent state amplitude $\alpha_{g/e}(T)$, and therefore on the amplitude, phase, and duration of the applied cavity drive.

To connect to dispersive readout [39], we introduce a cavity decay mechanism via the cavity-environment coupling operator $\hat{a} + \hat{a}^\dagger$, described for an empty cavity by the quality factor Q_F. For an approximately Ohmic environment around the cavity frequency, such as for an open transmission line, the decay rate is defined in terms of the quality factor by $\kappa(\omega_\mathrm{c}) = \omega_\mathrm{c}/Q_\mathrm{F}$. For a coupled qubit-cavity system, following the dressed decoherence model of [43, 89], in addition to cavity decay there will also be cavity-mediated qubit decay (indirect Purcell decay [43]). To lowest order in λ (as shown in [43, 89]), for an approximately Ohmic environment around the qubit frequency, this occurs at a rate $\gamma_\mathrm{P} = \lambda^2(\omega_\mathrm{q} + \chi)/Q_\mathrm{F}$ regardless of the cavity photon number (photon number effects become relevant at higher orders of λ). In experiment, Purcell decay can be almost completely removed by appropriate filtering of the cavity output at the qubit frequency, a technique known as Purcell filtering [130, 75].

In the eigenbasis of the Jaynes-Cummings Hamiltonian, the two decay mechanisms described above amount to the following. "Cavity decay" is the dressed eigenstate transition $\overline{|g/e, n+1\rangle} \to \overline{|g/e, n\rangle}$, which effectively preserves the qubit state, while Purcell decay is the dressed eigenstate transition $\overline{|e, n\rangle} \to \overline{|g, n\rangle}$, which effectively preserves the photon number in the cavity. All other transitions have zero matrix elements with the cavity-environment coupling operator and are therefore forbidden.

Initially, let us assume that we can neglect Purcell decay, as would be the case if a suitable Purcell filter is connected to the cavity, as has been achieved in state of the art dispersive readout [130, 75]. In addition, we assume that the cavity only begins decaying after the state $\overline{|g/e, \alpha_{g/e}(T)\rangle}$ has been created, and we assume a temperature of zero. For this simplified case, given that only transitions of the form $\overline{|g/e, n+1\rangle} \to \overline{|g/e, n\rangle}$ are allowed, we see that the dressed coherent state will decay similarly to a coherent state in an isolated cavity, such that after a time τ of decay the qubit-cavity state will be

$$\begin{aligned}&\overline{|g, \alpha_g(T)e^{-\frac{\kappa}{2}\tau}e^{-i(\omega_\mathrm{c}-\chi)\tau}\rangle} \\ &= \left(|g\rangle - \lambda\alpha_g(T)e^{-\frac{\kappa}{2}\tau}e^{-i(\omega_\mathrm{c}-\chi)\tau}|e\rangle\right)|\alpha_g(T)e^{-\frac{\kappa}{2}\tau}e^{-i(\omega_\mathrm{c}-\chi)\tau}\rangle/\sqrt{\mathcal{N}(\tau)} + \mathcal{O}(\lambda^2),\end{aligned} \tag{5.10}$$

$$\begin{aligned}&\overline{|e, \alpha_e(T)e^{-\frac{\kappa}{2}\tau}e^{-i(\omega_\mathrm{c}+\chi)\tau}\rangle} \\ &= \left(|e\rangle + \lambda\alpha_e^*(T)e^{-\frac{\kappa}{2}\tau}e^{i(\omega_\mathrm{c}+\chi)\tau}|g\rangle\right)|\alpha_e(T)e^{-\frac{\kappa}{2}\tau}e^{-i(\omega_\mathrm{c}+\chi)\tau}\rangle/\sqrt{\mathcal{N}(\tau)} + \mathcal{O}(\lambda^2),\end{aligned} \tag{5.11}$$

which is just a dressed coherent state with a damped amplitude $|\alpha_{g/e}(T)|e^{-\frac{\kappa}{2}\tau}$.

Following equations (5.10) and (5.11), after a cavity decay of time τ the

initial qubit states $|g/e\rangle$ have been mapped approximately to

$$|g\rangle \rightarrow \left(|g\rangle - \lambda|\alpha|e^{-i(\varphi_\epsilon+\pi/2)}e^{-i\varphi_g T}e^{-\frac{\kappa}{2}\tau}e^{-i\varphi'_g\tau}|e\rangle\right)/\sqrt{\mathcal{N}(\tau)}, \tag{5.12}$$

$$|e\rangle \rightarrow \left(|e\rangle + \lambda|\alpha|e^{i(\varphi_\epsilon+\pi/2)}e^{i\varphi_e T}e^{-\frac{\kappa}{2}\tau}e^{i\varphi'_e\tau}|g\rangle\right)/\sqrt{\mathcal{N}(\tau)}, \tag{5.13}$$

where we have used the fact that $\alpha_{g/e}(T)$ differ in phase only to define $\alpha = |\alpha_{g/e}(T)|$ and the phase factor $-(\varphi_\epsilon + \pi/2)$ of $-i\epsilon^*$, as well as the dynamical phase factors $\varphi_{g/e} = \omega_c \mp \frac{\chi}{2}$ and $\varphi'_{g/e} = \omega_c \mp \chi$. The measured phases of the output signal jump sharply when the drive pulse is turned off, with the coherent states rotating around phase space at frequencies $\varphi_{g/e}$ for times $t \leq T$ and at frequencies $\varphi'_{g/e}$ for times $\tau = t - T > 0$.

The qubit state maps of equations (5.12) and (5.13) can alternatively be understood as qubit-cavity interactions during the cavity drive changing the basis of qubit measurement, with measurement of the cavity phase φ_g/φ'_g for a total time $T+\tau$ corresponding to the qubit state $|g\rangle - \lambda|\alpha|e^{-i\varphi_g T}e^{-\frac{\kappa}{2}\tau}e^{-i\varphi'_g\tau}|e\rangle$ and a similar result for the measurement of φ_e/φ'_e. Only in the $\tau \rightarrow \infty$ limit does the basis of measurement become $\{|g\rangle, |e\rangle\}$ and the measurement QND.

The key observation in this work is that the change of basis of measurement is a coherent rotation error applied to the qubit output state. As this error in the qubit state is coherent, it can be actively corrected for by a single qubit rotation that applies the inverse of the unitary map of equation (5.12) or (5.13). This conditional rotation to correct the output state is defined by the unitary operators

$$\hat{U}_g(T,\tau,|\alpha|) = \exp\left\{i\left(\cos(\Sigma_g)\hat{\sigma}_y - \sin(\Sigma_g)\hat{\sigma}_x\right)\theta_g\right\} \quad \tan(\theta_g) = \lambda|\alpha|e^{-\frac{\kappa}{2}\tau}, \tag{5.14}$$

$$\hat{U}_e(T,\tau,|\alpha|) = \exp\left\{i\left(\cos(\Sigma_e)\hat{\sigma}_y - \sin(\Sigma_e)\hat{\sigma}_x\right)\theta_e\right\} \quad \tan(\theta_e) = \lambda|\alpha|e^{-\frac{\kappa}{2}\tau}, \tag{5.15}$$

where $\Sigma_g = \varphi_g T + \varphi'_g\tau + \varphi_\epsilon + \pi/2$ and $\Sigma_e = \varphi_\epsilon + \pi/2 + \varphi_e T + \varphi'_e\tau$.

While this erroneous qubit rotation scales as λ and $e^{-\frac{\kappa}{2}\tau}$ and is therefore small, it is an effect that will propagate throughout a computation, affecting the fidelity of all subsequent gates and measurements. Therefore, the observation that it can be easily corrected for is a useful one, especially in architectures where qubit measurements are used as a means of initialization at the beginning of a computation [71, 72], or used during the computation to stabilize error correction codes [49], and in light of the fact that dispersive qubit readout fidelity approaches ever higher values [75].

5.3 Numerical Simulations

In order to relax our previous assumption of an initially closed cavity, and to consider effects beyond first order in λ, we numerically simulate the cavity drive and decay process with the Purcell filtered master equation (see appendix 5.B for further details, and appendix 5.D for simulations with Purcell decay)

$$\dot{\rho}(t) = -i\left[\hat{H}_{\mathrm{T}}(t), \rho(t)\right] + \kappa\left(\left(1 + n_{\mathrm{th}}(\omega_{\mathrm{c}}, \mathrm{T})\right)\mathcal{D}\left[\hat{a}_{\mathcal{C}}\right] + n_{\mathrm{th}}(\omega_{\mathrm{c}}, \mathrm{T})\mathcal{D}\left[\hat{a}_{\mathcal{C}}^{\dagger}\right]\right)\rho(t), \tag{5.16}$$

where the operator $\hat{a}_{\mathcal{C}}$ of equation (5.34) describes only cavity decay, $n_{\mathrm{th}}(\omega, \mathrm{T})$ is the Bose distribution at frequency ω and temperature T, and $\mathcal{D}(x)\rho$ is the dissipator defined by

$$\mathcal{D}(x)\rho = x\rho x^{\dagger} - \frac{1}{2}\left\{x^{\dagger}x, \rho\right\}. \tag{5.17}$$

Here the total system Hamiltonian describes the full Jaynes-Cummings interaction between the qubit and the cavity as well as the classical cavity drive, and is given by

$$\hat{H}_{\mathrm{T}}(t) = \omega_{\mathrm{c}}\hat{a}^{\dagger}\hat{a} - \frac{\omega_{\mathrm{q}}}{2}\hat{\sigma}_z + g\left(\hat{\sigma}^{-}\hat{a}^{\dagger} + \hat{\sigma}^{+}\hat{a}\right) + \left(\epsilon e^{i\omega_{\mathrm{d}}t}\hat{a} + \epsilon^{*}e^{-i\omega_{\mathrm{d}}t}\hat{a}^{\dagger}\right)\Theta(t - T), \tag{5.18}$$

where $\Theta(x)$ is the Heaviside step function. We simulate the evolution for the initial states $\overline{|g, 0\rangle}$ and $\overline{|e, 0\rangle}$, with the temperature set at either T = 0 or T = 100 mK. The results are shown in FIGs. 5.1 and 5.2.

FIG. 5.1(a) shows the cavity occupation during the readout protocol. As expected, after an initial ring-up phase, once the drive is turned off the cavity occupation decays. Decay stops once the steady state is reached, which is $\overline{|g, 0\rangle}$ or $\overline{|e, 0\rangle}$ for T = 0 and thermally broadened versions of these states for T = 100 mK. FIG. 5.1(b) shows $1 - P(t)$, where $P(t)$ is the purity of the state, defined for a reduced qubit state $\rho(t)$ by $P(t) = \mathrm{Tr}[\rho(t)^2]$. Unit purity indicates a pure state. As can be seen, for T = 0 the states remain very close to a pure state at all times, verifying the analytic results of equations (5.10) and (5.11). Even for T = 100 mK the states remain > 90% pure for either initial state.

As the states remain mostly pure during the protocol, it is possible to correct the qubit state error by the unitaries of equations (5.14) and (5.15), as described previously. To quantify this correction we use the overlap between the desired state ($|g\rangle$ or $|e\rangle$) and the simulated reduced qubit state $\rho(t)$. We measure the overlap before correction

$$\mathcal{F}_{\nu}(\tau) = \mathrm{Tr}\left[|\nu\rangle\langle\nu|\rho(t)\right], \tag{5.19}$$

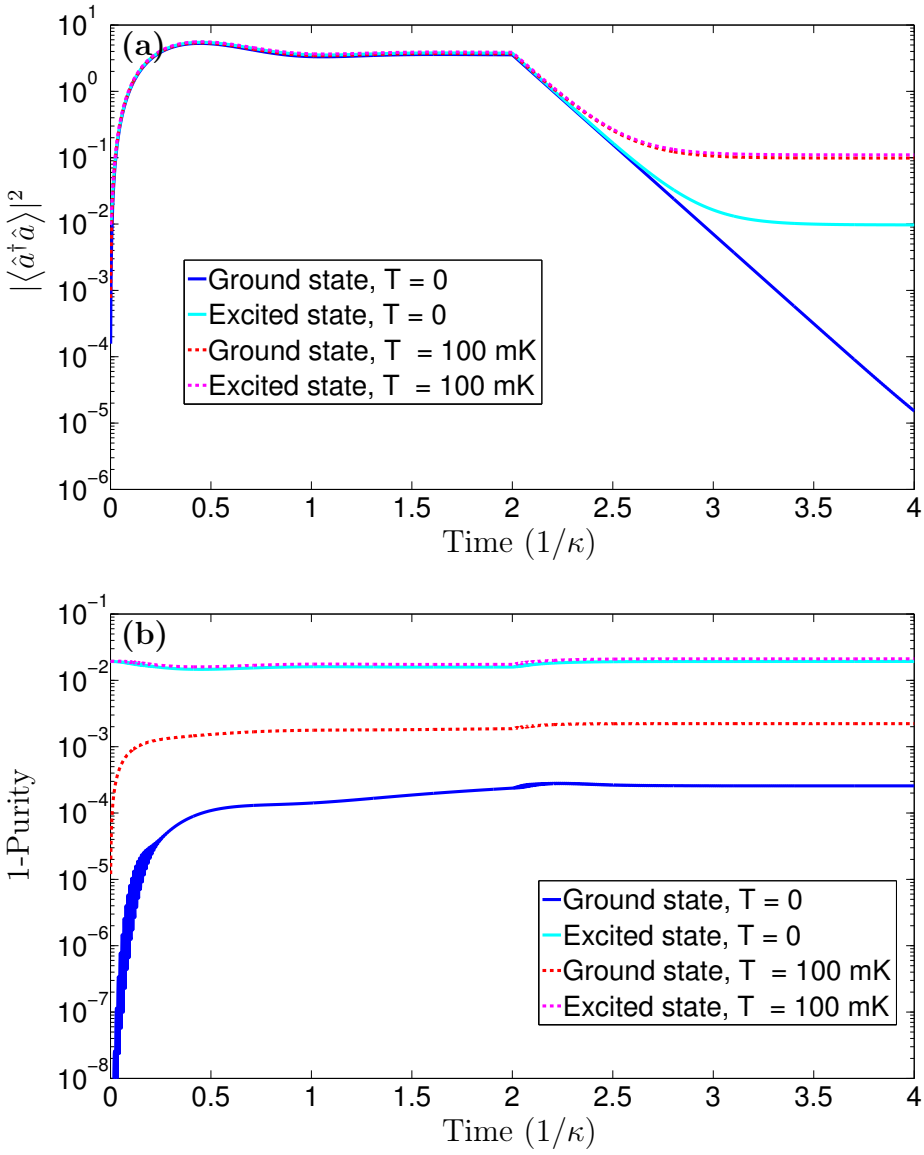

Figure 5.1: **(a)** Cavity occupation, and **(b)** $1 - P(t)$ for T = 0 and T = 100 mK for both initial states. A drive strength of $|\epsilon|/2\pi = 0.04$ GHz, a cavity decay rate of $1/\kappa = 100$ ns, and $|\lambda| = 0.1$ were used for these simulations.

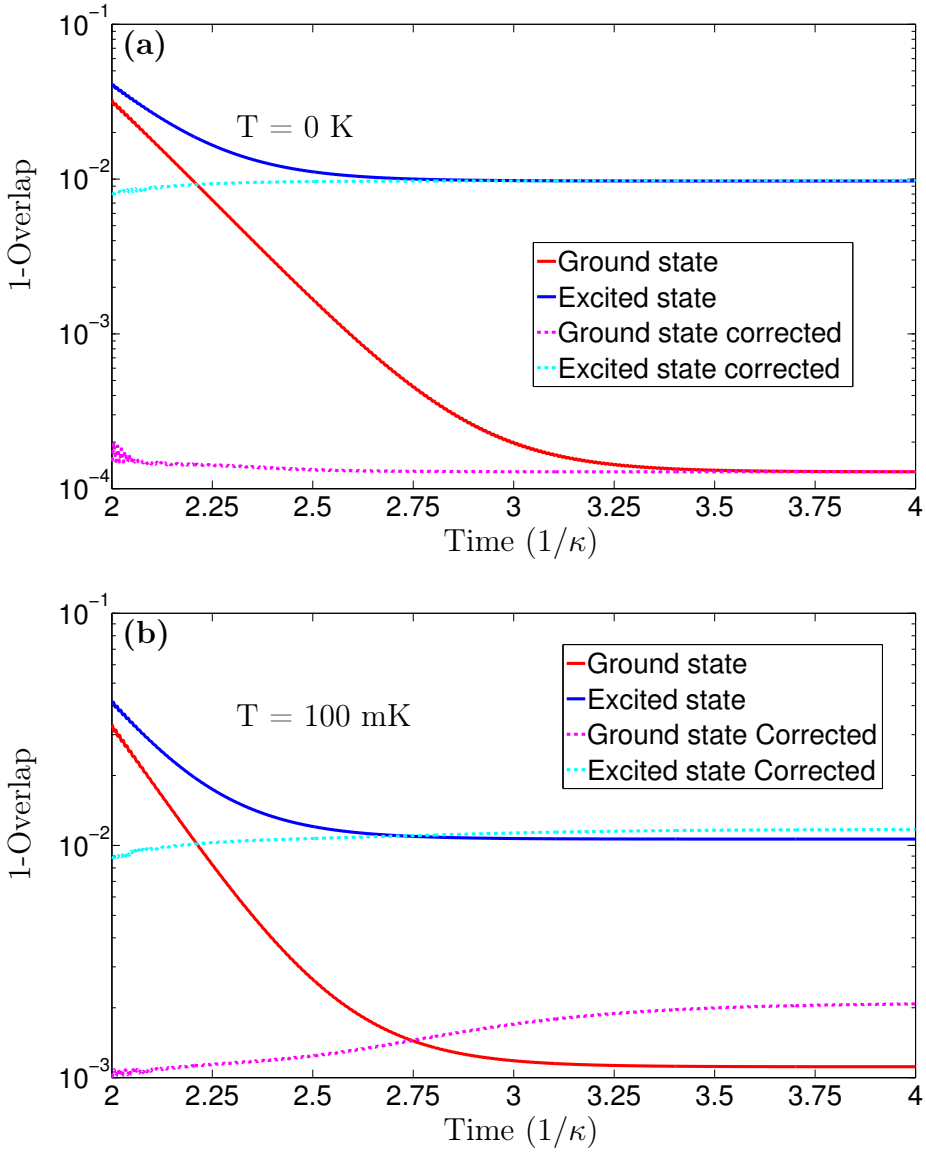

Figure 5.2: $1-\mathcal{F}_\nu(\tau)$ and $1-\mathcal{F}_\nu^{\mathrm{C}}(\tau)$ are shown in **(a)** for T = 0 and **(b)** for T = 100 mK. A drive strength of $|\epsilon|/2\pi = 0.04$ GHz, a cavity decay rate of $1/\kappa = 100$ ns, and $|\lambda| = 0.1$ were used for these simulations.

where the subscript $\nu \in \{g, e\}$ indicates whether we started in $\overline{|g,0\rangle}$ or $\overline{|e,0\rangle}$, and the overlap after correction

$$\mathcal{F}_\nu^{\mathrm{C}}(\tau) = \mathrm{Tr}\left[|\nu\rangle\langle\nu|\hat{U}_\nu\rho(t)\hat{U}_\nu^\dagger\right]. \tag{5.20}$$

FIG. 5.2(a) shows the overlap error for both the uncorrected and the corrected state for T = 0, and as can be seen $\mathcal{F}_\nu^{\mathrm{C}}(\tau) \geq \mathcal{F}_\nu(\tau)$ for all time (to within numerical precision of the simulations). For T = 100 mk, as shown in FIG. 5.2(b), this is not the case as within roughly 75 ns the qubit state loses enough coherence that the unitary correction actually worsens the overlap.

For both system temperatures the greatest benefit from correction is seen early on in the decay time, long before the cavity occupation has reached steady state. Typically one would wait for the cavity to be unoccupied before further operations on the qubit are preformed, as cavity photons are still interacting with the qubit. However, in set-ups with tunable coupling between the cavity and the qubit [131, 132, 133], it would be possible to turn off the interaction between the cavity and the qubit once enough measurement data has been accumulated and then correct the final state of the qubit. In this way one would could achieve both more accurate and faster initialization of the qubit state via measurement and unitary correction. A similar initialization scheme involving both cavity and qubit control has recently been implemented [134].

The analytic expressions of equations (5.14) and (5.15) for the correction unitaries correctly calculate the amplitude of the rotation, described by the angles θ_g and θ_e. Unfortunately, due to higher order nonlinear effects in the full Hamiltonian the analytic phases Σ_g and Σ_e do not give good results. To solve this problem, we performed a brute force optimization over the phase of the rotation to obtain the excellent results shown in FIGs. 5.2(a) and 5.2(b).

5.4 Conclusion

In conclusion, we have shown that during the most commonly used dispersive readout protocol for superconducting qubits a coherent rotation error is applied to the qubit and the measurement scheme is not QND for any finite measurement time. This coherent rotation causes errors in repeated measurements and in qubit initialization; however, as we have shown, it can be corrected for by unitary feedback. This correction is most advantageous early on in the decay time, and, in experiments with tunable qubit-cavity coupling, our scheme shows promising results for faster and more accurate qubit initialization.

Acknowledgements

The authors acknowledge insightful discussions with Bruno G. Taketani, Daniel Sank, and Karl-Peter Marzlin. Supported by the Army Research Office under contract W911NF-14-1-0080 and the European Union through ScaleQIT. LCGG acknowledges support from NSERC through an NSERC PGS-D.

Appendix

5.A First Order Approximation of the Dressed Coherent States

For the ground qubit dressed coherent state, we have

$$\begin{aligned}\overline{|g,\alpha\rangle} &= e^{-\frac{|\alpha|^2}{2}} \sum_n \frac{\alpha^n}{\sqrt{n!}} \overline{|g,n\rangle} \\ &= e^{-\frac{|\alpha|^2}{2}} \sum_n \frac{\alpha^n}{\sqrt{n!}} \left(\cos\left(\lambda\sqrt{n}\right)|g,n\rangle - \sin\left(\lambda\sqrt{n}\right)|e,n-1\rangle\right) \\ &= e^{-\frac{|\alpha g|^2}{2}} \sum_n \frac{\alpha^n}{\sqrt{n!}} \left(\left(1-\frac{n\lambda^2}{2}\right)|g,n\rangle - \lambda\sqrt{n}|e,n-1\rangle\right) + \mathcal{O}(\lambda^3).\end{aligned} \tag{5.21}$$

Tracing out the cavity we obtain

$$\begin{aligned}\mathrm{Tr}_{\mathrm{C}}\left[\overline{|g,\alpha\rangle\langle g,\alpha|}\right] &= \left(1-\lambda^2|\alpha|^2\right)|g\rangle\langle g| + \lambda^2|\alpha|^2|e\rangle\langle e| \\ &\quad - \lambda\alpha^*|g\rangle\langle e| - \lambda\alpha|e\rangle\langle g| + \mathcal{O}(\lambda^3) \\ &= \left(|g\rangle - \lambda\alpha|e\rangle\right)\left(\langle g| - \lambda\alpha^*\langle e|\right) - \lambda^2|\alpha|^2|g\rangle\langle g| + \mathcal{O}(\lambda^3).\end{aligned} \tag{5.22}$$

We now approximate this minimally mixed state by a pure state to obtain

$$\overline{|g,\alpha\rangle} = \left(|g\rangle - \lambda\alpha|e\rangle\right)/\sqrt{\mathcal{N}} + \mathcal{O}(\lambda^2), \tag{5.23}$$

where $\mathcal{N} = 1+\lambda^2|\alpha|^2$ is the normalization.

Now for the excited qubit dressed coherent state, we begin with

$$\begin{aligned}\overline{|e,\alpha\rangle} &= e^{-\frac{|\alpha|^2}{2}} \sum_n \frac{\alpha^n}{\sqrt{n!}} \overline{|e,n\rangle} \\ &= e^{-\frac{|\alpha|^2}{2}} \sum_n \frac{\alpha^n}{\sqrt{n!}} \left(\cos\left(\lambda\sqrt{n+1}\right)|e,n\rangle + \sin\left(\lambda\sqrt{n+1}\right)|g,n+1\rangle\right) \\ &= e^{-\frac{|\alpha|^2}{2}} \sum_n \frac{\alpha^n}{\sqrt{n!}} \left(\left(1-\frac{(n+1)\lambda^2}{2}\right)|e,n\rangle + \lambda\sqrt{n+1}|g,n+1\rangle\right) + \mathcal{O}(\lambda^3).\end{aligned} \tag{5.24}$$

Tracing out the cavity we obtain

$$\begin{aligned}\mathrm{Tr_C}\left[\overline{|e,\alpha\rangle\langle e,\alpha|}\right] &= \left(1-\lambda^2(1+|\alpha|^2)\right)|e\rangle\langle e| + \lambda^2(1+|\alpha|^2)|g\rangle\langle g| \\ &+ \lambda\alpha^*|g\rangle\langle e| + \lambda\alpha|e\rangle\langle g| + \mathcal{O}(\lambda^3) \\ &= \left(|e\rangle + \lambda\alpha^*|g\rangle\right)\left(\langle e| + \lambda\alpha\langle g|\right) + \lambda^2|g\rangle\langle g| - \lambda^2(1+|\alpha|^2)|e\rangle\langle e| + \mathcal{O}(\lambda^3).\end{aligned} \tag{5.25}$$

Making the same approximation as for the previous case, we arrive at the pure state

$$\overline{|e,\alpha\rangle} = \left(|e\rangle + \lambda\alpha^*|g\rangle\right)/\sqrt{\mathcal{N}} + \mathcal{O}(\lambda^2), \tag{5.26}$$

where, as before, $\mathcal{N}$ is the normalization.

5.B Numerical Master Equation

To derive the master equations of equations (5.16) and (5.38) we begin by considering the system-bath Hamiltonian

$$\hat{H}_\mathrm{E} = \hat{H}_\mathrm{T}(t) + \sum_k \eta_k \hat{b}_k^\dagger \hat{b}_k + \sum_k g_k \left(\hat{a} + \hat{a}^\dagger\right)\left(\hat{b}_k + \hat{b}_k^\dagger\right) \tag{5.27}$$

where the second term in equation (5.27) is the bath self-Hamiltonian, and the third term the system-bath coupling. To derive an effective master equation for the system, it is appropriate to work in the instantaneous eigenbasis of $\hat{H}_\mathrm{T}(t)$; however, to simply things we will derive the master equation in the eigenbasis of $\hat{H}$ of equation (5.1). The difference between these two is a frame transformation by a time dependent cavity displacement, which for the parameter regime under consideration is inconsequential to the applicability of the master equation obtained.

Following the procedure of [43] we derive an effective evolution equation for the system (ignoring the coherent evolution for the time being)

$$\begin{aligned}
\dot{\rho}(t) = &\sum_{j,k>j}\sum_{n,m>n} C_{jk}C^*_{nm}\Big(|j\rangle\langle k|\rho(t)|m\rangle\langle n| - |m\rangle\langle n||j\rangle\langle k|\rho(t)\Big)e^{i(\Delta_{jk}-\Delta_{nm})t} \\
&\times \int_0^\infty ds\,\Big\langle \hat{b}(s)\hat{b}^\dagger(0)\Big\rangle e^{-i\Delta_{jk}t} \\
&+ \sum_{j,k>j}\sum_{n,m>n} C_{jk}C^*_{nm}\Big(|j\rangle\langle k|\rho(t)|m\rangle\langle n| - \rho(t)|m\rangle\langle n||j\rangle\langle k|\Big)e^{i(\Delta_{jk}-\Delta_{nm})t} \\
&\times \int_0^\infty ds\,\Big\langle \hat{b}(0)\hat{b}^\dagger(s)\Big\rangle e^{i\Delta_{nm}t} \\
&+ \sum_{j,k>j}\sum_{n,m>n} C^*_{jk}C_{nm}\Big(|k\rangle\langle j|\rho(t)|n\rangle\langle m| - |n\rangle\langle m||k\rangle\langle j|\rho(t)\Big)e^{-i(\Delta_{jk}-\Delta_{nm})t} \\
&\times \int_0^\infty ds\,\Big\langle \hat{b}^\dagger(s)\hat{b}(0)\Big\rangle e^{i\Delta_{jk}t} \\
&+ \sum_{j,k>j}\sum_{n,m>n} C^*_{jk}C_{nm}\Big(|k\rangle\langle j|\rho(t)|n\rangle\langle m| - \rho(t)|n\rangle\langle m||k\rangle\langle j|\Big)e^{-i(\Delta_{jk}-\Delta_{nm})t} \\
&\times \int_0^\infty ds\,\Big\langle \hat{b}^\dagger(0)\hat{b}(s)\Big\rangle e^{-i\Delta_{nm}t}
\end{aligned} \tag{5.28}$$

where $\{|j\rangle\}$ is the eigenbasis of $\hat{H}$ ordered in increasing eigenenergy and given to first order in λ by equations (5.3) and (5.4), Δ_{jk} is the frequency difference between the j'th and k'th eigenstate (Bohr frequency), $\hat{b}(s) = \sum_k g_k\hat{b}_k e^{-i\eta_k t}$ is the time dependent bath lowering operator, and $C_{jk} = \langle j|\left(\hat{a}+\hat{a}^\dagger\right)|k\rangle$. We have also assumed that the bath state is a stationary state of the bath self-Hamiltonian.

Unlike in [43], it is not possible to make a rotating wave approximation, as in the parameter regime under consideration the eigenspectrum of $\hat{H}$ has many nearly degenerate transitions. Instead, it is possible to derive a Lindblad form master equation in a way similar to that done in the singular coupling limit [41] by assuming that the nearly degenerate transitions are actually degenerate. We notice that the coefficients C_{jk} are nonzero if $|j\rangle = \overline{|g/e,n\rangle}$ and $|k\rangle = \overline{|g/e,n\pm1\rangle}$, or if $|j\rangle = \overline{|g/e,n\rangle}$ and $|k\rangle = \overline{|e/g,n\rangle}$, while all other C_{jk} are zero. The former case is what we have been calling cavity decay, while the latter case is Purcell decay, and for each decay type the energy difference Δ_{jk} between adjacent states is approximately constant (ω_c in the former case and ω_q in the latter).

Therefore, we can split the sums of equation (5.28) into two parts, and make a secular approximation to neglect the fast oscillating cross terms be-

tween decay types to arrive at the equation

$$\begin{aligned}\dot{\rho}(t) = &\sum_{j,k>j}^{\mathcal{C}}\sum_{n,m>n}^{\mathcal{C}} C_{jk}C^*_{nm}\Big(|j\rangle\langle k|\rho(t)|m\rangle\langle n| - \frac{1}{2}\Big\{|m\rangle\langle n||j\rangle\langle k|, \rho(t)\Big\}\Big)\\ &\times\left(1+n_{\rm th}(\omega_{\rm c},{\rm T})\right)J(\omega_{\rm c})\\ &+\sum_{j,k>j}^{\mathcal{C}}\sum_{n,m>n}^{\mathcal{C}} C^*_{jk}C_{nm}\Big(|k\rangle\langle j|\rho(t)|n\rangle\langle m| - \frac{1}{2}\Big\{|n\rangle\langle m||k\rangle\langle j|, \rho(t)\Big\}\Big)\\ &\times n_{\rm th}(\omega_{\rm c},{\rm T})J(\omega_{\rm c})\\ &+\sum_{j,k>j}^{\mathcal{P}}\sum_{n,m>n}^{\mathcal{P}} C_{jk}C^*_{nm}\Big(|j\rangle\langle k|\rho(t)|m\rangle\langle n| - \frac{1}{2}\Big\{|m\rangle\langle n||j\rangle\langle k|, \rho(t)\Big\}\Big)\\ &\times\left(1+n_{\rm th}(\omega_{\rm q},{\rm T})\right)J(\omega_{\rm q})\\ &+\sum_{j,k>j}^{\mathcal{P}}\sum_{n,m>n}^{\mathcal{P}} C^*_{jk}C_{nm}\Big(|k\rangle\langle j|\rho(t)|n\rangle\langle m| - \frac{1}{2}\Big\{|n\rangle\langle m||k\rangle\langle j|, \rho(t)\Big\}\Big)\\ &\times n_{\rm th}(\omega_{\rm q},{\rm T})J(\omega_{\rm q}),\end{aligned} \tag{5.29}$$

where we have ignored the Lamb shifts, and the superscripts $\mathcal{C}$ and $\mathcal{P}$ indicate summation over cavity decay transitions and over Purcell decay transitions respectively. Following the usual procedure of Fermi's golden rule we have made the identification

$$\int_0^\infty ds\left(\left\langle\hat{b}(s)\hat{b}^\dagger(0)\right\rangle e^{-i\omega t} + \left\langle\hat{b}(0)\hat{b}^\dagger(s)\right\rangle e^{i\omega t}\right) = \left(1+n_{\rm th}(\omega,{\rm T})\right)J(\omega), \tag{5.30}$$

$$\int_0^\infty ds\left(\left\langle\hat{b}^\dagger(s)\hat{b}(0)\right\rangle e^{i\omega t} + \left\langle\hat{b}^\dagger(0)\hat{b}(s)\right\rangle e^{-i\omega t}\right) = n_{\rm th}(\omega,{\rm T})J(\omega), \tag{5.31}$$

where $J(\omega)$ is the spectral density of the bath, and $n_{\rm th}(\omega)$ is the Bose function evaluated at frequency ω and temperature T.

If we choose a global Ohmic spectral density $J(\omega) = \omega/Q_{\rm F}$, then using the relations

$$\begin{aligned}&\sum_{j,k>j} C_{jk}|j\rangle\langle k| = \hat{a},\\ &\sum_{j,k>j} C_{kj}|k\rangle\langle j| = \sum_{j,k>j} C^*_{jk}|k\rangle\langle j| = \hat{a}^\dagger.\end{aligned} \tag{5.32}$$

we can write equation (5.29) in Lindblad form

$$\begin{aligned}\dot{\rho}(t) = \kappa \left((1 + n_{\text{th}}(\omega_{\text{c}}, \text{T}))\, \mathcal{D}\left[\hat{a}_{\mathcal{C}}\right] + n_{\text{th}}(\omega_{\text{c}}, \text{T}) \mathcal{D}\left[\hat{a}_{\mathcal{C}}^{\dagger}\right] \right) \rho(t) \\ + \gamma_{\text{P}} \left((1 + n_{\text{th}}(\omega_{\text{q}}, \text{T}))\, \mathcal{D}\left[\hat{a}_{\mathcal{P}}\right] + n_{\text{th}}(\omega_{\text{q}}, \text{T}) \mathcal{D}\left[\hat{a}_{\mathcal{P}}^{\dagger}\right] \right) \rho(t) \end{aligned} \tag{5.33}$$

where $\kappa = \omega_{\text{c}}/Q_{\text{F}}$ is the cavity decay rate and $\gamma_{\text{P}} \approx \lambda^2 \omega_{\text{q}}/Q_{\text{F}}$ is the Purcell decay rate. The operators $\hat{a}_{\mathcal{C}}$ and $\hat{a}_{\mathcal{P}}$ are defined by

$$\hat{a}_{\mathcal{C}} = \sum_{j,k>j}^{\mathcal{C}} C_{jk} |j\rangle\langle k| = \hat{a} - \sum_{j,k>j}^{\mathcal{P}} C_{jk} |j\rangle\langle k|, \tag{5.34}$$

$$\hat{a}_{\mathcal{P}} = \sum_{j,k>j}^{\mathcal{P}} C_{jk} |j\rangle\langle k| = \hat{a} - \sum_{j,k>j}^{\mathcal{C}} C_{jk} |j\rangle\langle k|, \tag{5.35}$$

and describe the cavity and Purcell decay processes respectively.

Equation (5.33) is valid for $t \ll t_{\text{ME}}$, where $t_{\text{ME}} = 1/\omega_{\text{max}}$ describes the timescale over which $e^{i(\Delta_{jk} - \Delta_{nm})t} = e^{i\omega_{\text{max}} t}$ is no longer unity, with ω_{max} the largest degeneracy between transitions that were assumed to be degenerate. For cavity decay $\omega_{\text{max}} \propto N\chi\lambda^2$, while for Purcell decay $\omega_{\text{max}} \propto N\chi$, with N the photon number of the largest occupied state. For the parameters under consideration ($\chi \leq 10$ MHz, $\lambda \leq 10^{-1}$) we have $t_{\text{ME}} \sim 10/N$ μs for cavity decay, and $t_{ME} \propto 100/N$ ns for Purcell decay. For typical experimental parameters the simulation length is on the order of 100s of nanoseconds, well below the limit imposed by cavity decay for reasonable values of N, but unfortunately on the same order as that set by Purcell decay. As such, we expect that the simulations of equation (5.33) are somewhat nonphysical; however, as the Purcell decay rate is quite small, we do expect the results to remain mostly trustworthy.

If instead of choosing a global Ohmic spectral density, we choose a spectral density for which $J(\omega_{\text{c}}) = \omega_{\text{c}}/Q_{\text{F}}$ but $J(\omega_{\text{q}}) \approx 0$, such as has been achieved in contemporary dispersive readout schemes by a filter [130, 75], then the resulting Lindblad equation contains only cavity decay, and is given by

$$\dot{\rho}(t) = \kappa \left((1 + n_{\text{th}}(\omega_{\text{c}}, \text{T}))\, \mathcal{D}\left[\hat{a}_{\mathcal{C}}\right] + n_{\text{th}}(\omega_{\text{c}}, \text{T}) \mathcal{D}\left[\hat{a}_{\mathcal{C}}^{\dagger}\right] \right) \rho(t). \tag{5.36}$$

This is the master equation used in the main text to described dispersive readout in a Purcell filtered system.

5.C Readout of the Undressed Qubit Excited State

In the main text we considered starting with the excited initial state $\overline{|e,0\rangle}$, which is the first excited state in the energy eigenbasis of the qubit-cavity system. However, for some quantum information protocols it is advantageous to work in the qubit logical basis, where the logical excited state is the state $|e,0\rangle$. Such a state can be prepared by initializing the qubit-cavity system into its ground state $|g,0\rangle$, followed by a short non-adiabatic qubit pulse that flips the state of the qubit.

If we now attempt to read out the state of the qubit, from Ref. [129] we see that starting in the state $|e,0\rangle$, after an applied cavity drive of the form of equation (5.5) the state of the system is

$$\begin{aligned}|\Psi(T)\rangle =& \cos(\lambda)\,\overline{|e,\alpha_{\mathrm{e}}(T)\rangle} \\ &- e^{iG(T)}\sin(\lambda)\,\hat{U}_{\mathrm{D}}^{\dagger}|g\rangle e^{-i\left(\omega_{\mathrm{c}}\hat{a}^{\dagger}\hat{a}-\chi\hat{\sigma}_{z}\hat{a}^{\dagger}\hat{a}\right)T}\hat{D}(\alpha'_{\mathrm{g}}(T))|1\rangle,\end{aligned} \tag{5.37}$$

where $\alpha'_{\mathrm{g}}(T) = \epsilon^{*}\left(e^{-i\chi T}-1\right)/\chi$, $\hat{D}(\beta)$ is the usual displacement operator for a harmonic oscillator, $\hat{U}_{\mathrm{D}} = \exp\left\{\lambda\left(\hat{\sigma}^{+}\hat{a}-\hat{\sigma}^{-}\hat{a}^{\dagger}\right)\right\}$ is the dispersive frame transformation operator, and $e^{iG(T)}$ is a relative qubit phase whose form is unimportant. From equation (5.37) we see that the final state contains a component for which the qubit is in its ground state, and the phase of the cavity signal for this component will be close to φ_g, measurement of which indicates the qubit is in its ground state. This introduces the possibility of misidentifying the qubit state; however, the amplitude of the ground state component is small as it as scales with $\sin^2(\lambda) \approx \lambda^2$. Nevertheless, this sets a fundamental limit for the readout fidelity of the undressed excited state via standard dispersive readout as presented here, and partly explains the unequal readout fidelities reported in [75].

After sufficiently long measurement of the phase φ_e, the state of equation (5.37) will have collapsed to the dressed coherent state $\overline{|e,\alpha_{\mathrm{e}}(T)\rangle}$, and the rest of the readout and coherent feedback protocol can occur as described in the main text, without further modification.

5.D Purcell Decay

To examine the effect of Purcell decay we simulate the unfiltered master equation

$$\dot{\rho}(t) = -i\left[\hat{H}_{\mathrm{T}}(t), \rho(t)\right] + \kappa\left(\left(1 + n_{\mathrm{th}}(\omega_{\mathrm{c}}, \mathrm{T})\right)\mathcal{D}\left[\hat{a}_{\mathcal{C}}\right] + n_{\mathrm{th}}(\omega_{\mathrm{c}}, \mathrm{T})\mathcal{D}\left[\hat{a}_{\mathcal{C}}^{\dagger}\right]\right)\rho(t) + \gamma_{\mathrm{P}}\left(\left(1 + n_{\mathrm{th}}(\omega_{\mathrm{q}}, \mathrm{T})\right)\mathcal{D}\left[\hat{a}_{\mathcal{P}}\right] + n_{\mathrm{th}}(\omega_{\mathrm{q}}, \mathrm{T})\mathcal{D}\left[\hat{a}_{\mathcal{P}}^{\dagger}\right]\right)\rho(t), \tag{5.38}$$

where the operator $\hat{a}_{\mathcal{P}}$ of equation (5.35) describes Purcell decay. As before, we simulate the evolution for the initial states $\overline{|g,0\rangle}$ and $\overline{|e,0\rangle}$, at a temperature T = 0. The overlap error for the uncorrected and corrected states are shown in FIG. 5.3.

As can be seen, for the initial state $\overline{|g,0\rangle}$ the results remain unchanged, as Purcell decay only minimally affects the decay of states of the form $\overline{|g,\alpha\rangle}$. Coherent feedback can still be used in this case to correct the qubit state, with excellent improvement in the overlap. For $\overline{|e,0\rangle}$ the results are quite different from that of FIG. 5.2(a), as Purcell decay drives the system to the global ground state $\overline{|g,0\rangle}$ and, as such the qubit state decays. In this case the coherent correction does little good, as the qubit state is lost by Purcell decay.

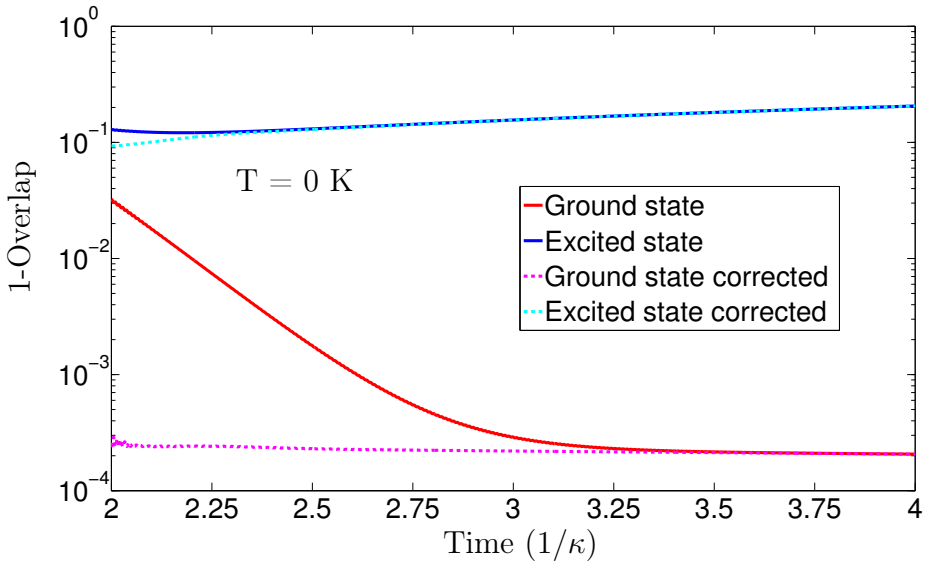

Figure 5.3: $1 - \mathcal{F}_{\nu}(\tau)$ and $1 - \mathcal{F}_{\nu}^{\mathrm{C}}(\tau)$ for T = 0. A drive strength of $|\epsilon|/2\pi = 0.04$ GHz, a cavity decay rate of $1/\kappa = 100$ ns, and $|\lambda| = 0.1$ were used for this simulation.

Chapter 6

Generating Nonclassical States from Classical Radiation by Subtraction Measurements

Luke C. G. Govia, Emily J. Pritchett, Frank K. Wilhelm

There are more things in heaven and earth,
Horatio, Than are dreamt of in your philosophy.
-William Shakespeare

Abstract

We describe the creation of nonclassical states of microwave radiation via ideal dichotomic single photon detection, i.e., a detector that only indicates presence or absence of photons. Ideally, such a detector has a back action in the form of the subtraction operator (bare lowering operator). Using the nonlinearity of this back action, it is possible to create a large family of nonclassical states of microwave radiation, including squeezed and multi-component cat states, starting from a coherent state. We discuss the applicability of this protocol to current experimental designs of Josephson Photomultipliers (JPMs).

Published in New Journal of Physics **16**, 045011 (2014). An early version of parts of this chapter appears in my M.Sc. thesis, Theory and Applications of Josephson Photomultipliers, University of Waterloo, Ontario, Canada.

6.1 Introduction

The generation of nonclassical states of radiation is an important test of the foundations of quantum mechanics and a necessary precursor to implementing quantum communication and computation protocols in many architectures [135, 136, 137]. While the methodology for creating nonclassical radiation at optical wavelengths has been studied extensively [138, 139, 140, 107, 141], the technology to create quantum states with larger and larger wavelengths has recently become available with advances in cavity- and circuit-QED.

In this paper we present a novel way to generate a family of nonclassical states of microwave radiation in a long wavelength resonator using only detection by an ideal binary detector, such as the Josephson Photomultiplier (JPM). The protocol only involves radiating a microwave cavity with coherent radiation and post selection based on single photon detection, without further manipulation. In addition, our protocol applies to any detection mechanism with a back action resembling that of the subtraction operator (equation (6.1)) and so can be generalized to other quantum systems, in particular, other superconducting circuits where strong photon-detector coupling is possible [142, 67, 68]. Recent proposals have established an analogous detection scheme in cavity-QED, broadening the range of application of our results [143, 108].

In the microwave regime of cavity-QED/circuit-QED squeezed states [144, 145, 146] and cat-like states [113, 147] of microwave radiation have been generated by the Kerr interaction between a cavity/transmission line and coupled atoms/superconducting qubits. Multi-component cat states have also been produced in circuit-QED using a gate-based construction [67, 68]. We show how these nonclassical states can be created in circuit-QED by a measurement based protocol, and add a new class of nonclassical states to the list, the generalized squeezed states, which so far have only been proposed in theory [148, 149].

The JPM, a current biased Josephson junction related to the phase qubit, has been shown experimentally [54] and theoretically [59, 58, 53] to be an effective single microwave photon counter. Previously, we have shown that for a JPM under optimal conditions (long relaxation time, short pure dephasing time, and a small dark count rate) the back action of photon detection is the photon subtraction operator [59],

$$\hat{B} \equiv \sum_{n=1}^{\infty} |n-1\rangle\langle n|, \tag{6.1}$$

a nonlinear operator that can be related to the photon lowering operator

by $\hat{a} = \hat{B}\sqrt{\hat{n}}$, but cannot be expressed as a linear combination of photon creation and annihilation operators. Also, note that $\hat{B}$ is not invertible, and hence not unitary. The JPM can be seen in this regime as an ideal dichotomic detector (see 6.A for further information), providing information about the presence or absence of photons but not revealing their number beyond that. Unlike traditional intensity meausurements, a measurement with subtraction operator back action has no corresponding classical observable, and as such has the potential to turn classical states into nonclassical ones.

6.2 Protocols for Nonclassical State Generation

In this paper we show how to use the noncommuntativity of the detection back action with coherent displacement pulses to achieve single mode quadrature squeezing of an input coherent state as well as to generate other nonclassical states, namely generalized squeezed states and squeezed multi-component Schrödinger cat states [138]. The subtraction operator is phase squeezing in particular as it removes the phases of the lower energy Fock states in the original coherent state superposition without changing the phases of the higher energy Fock states - which become the lower energy states - to compensate. Note that a special case of the second step of our protocol is already known in quantum optics: subtracting a photon from a squeezed vacuum state produces a low-power cat (kitten) state [107].

6.2.1 Squeezed States

The generation of squeezed states of microwave radiation using JPMs follows a simple protocol. The cavity is initially prepared in a coherent state, $|\alpha\rangle = \hat{D}(\alpha)|0\rangle = e^{-\frac{|\alpha|^2}{2}} \sum_{n=0}^{\infty} \frac{\alpha^n}{\sqrt{n!}}|n\rangle$ where $\alpha \equiv |\alpha|e^{i\varphi_\alpha}$, and is coupled to one or more detectors, each acting with back action $\hat{B}$ on the cavity after a photon is detected. Mathematically a coherent displacement such as this is represented by the displacement operator $\hat{D}(\alpha) = e^{\left(\alpha\hat{a}^\dagger - \alpha^*\hat{a}\right)}$. After N photons are counted (either by N detectors, or less if fast detector reset is possible), a further displacement pulse is applied such that the state is centred around $-\alpha$ in phase space. After N further photon detections are observed, the resulting state is a squeezed state. The optimal choice of N will be discussed shortly.

Starting from the coherent state input, the probability for N photons to

be detected is

$$P_N \equiv 1 - e^{-|\alpha|^2} \sum_{n=0}^{N-1} \frac{|\alpha|^{2n}}{n!} = 1 - \frac{\Gamma(N, |\alpha|^2)}{\Gamma(N)} \tag{6.2}$$

where $\Gamma(N, |\alpha|^2)$ is the upper incomplete gamma function of N and $|\alpha|^2$ [150]. $P_N \sim |\alpha|^{2N}/N!$ as $|\alpha| \to 0$; however, at $|\alpha|^2 \approx N$ P_N jumps rapidly towards unity, and so can be made arbitrarily close to unity with higher power coherent pulses (see 6.C for further detail).

It is straightforward to calculate the normalized post measurement cavity state after N detections,

$$\rho' \equiv \frac{\hat{B}^N |\alpha\rangle\langle\alpha| \hat{B}^{\dagger N}}{P_N}, \tag{6.3}$$

and the average photon number $n_1 \equiv \langle a^\dagger a \rangle_{\rho'}$ is given by

$$n_1 = \frac{|\alpha|^2 \left(1 - \frac{\Gamma(N-1,|\alpha|^2)}{\Gamma(N-1)}\right) - N\left(1 - \frac{\Gamma(N,|\alpha|^2)}{\Gamma(N)}\right)}{P_N}, \tag{6.4}$$

which can also be numerically evaluated. After N detections, the next step is to displace the state by an amount $\alpha_1 = -\sqrt{n_1} e^{i\varphi_\alpha} - \alpha$, so that the resulting state will be centred in phase space around $-\alpha$. For this displaced state, N photon detection events will occur with probability P'_N [1] , and the renormalized cavity state will have the form

$$\rho'' \equiv \frac{\hat{B}^N D(\alpha') \rho' D(\alpha')^\dagger \hat{B}^{\dagger N}}{P'_N}. \tag{6.5}$$

We will now show that the state ρ'' is a squeezed state.

To quantify the amount of squeezing, we calculate the variance of the squeezed quadrature

$$\Delta p^2 = \mathrm{Tr}[\rho'' \hat{p}^2] - \mathrm{Tr}[\rho'' \hat{p}]^2. \tag{6.6}$$

The quadrature observable $\hat{p}(\varphi_a)$ is defined by $\hat{p}(\varphi_a) = \frac{i}{\sqrt{2}} \left(\hat{a}^\dagger e^{i\varphi_\alpha} - \hat{a} e^{-i\varphi_\alpha}\right)$, where $\hat{a}$ is the annihilation operator for the cavity microwave mode. The phase shift $e^{-i\varphi_\alpha}$ accounts for the fact that this protocol squeezes along the phase space axis complementary to that defined by the phase of the input

[1] for which the analytic expression is cumbersome and not instructive but, as is the case for P_N, $P'_N \to 1$ for $|\alpha| \to \infty$.

coherent state. Anything less than $\Delta p^2 = \frac{1}{2}$ indicates a squeezed state. The amount of squeezing is expressed in dB, by calculating

$$S(\Delta p) \equiv 10\log_{10}\left(\frac{\Delta p^2}{\Delta p^2_{\text{norm}}}\right) = 10\log_{10}\left(2\Delta p^2\right). \tag{6.7}$$

In addition, we can calculate how far the state ρ'' deviates form a minimal uncertainty state by calculating $\Delta x \Delta p$ (where $\hat{x} = \frac{1}{\sqrt{2}}\left(\hat{a}e^{-i\varphi_\alpha} + \hat{a}^\dagger e^{i\varphi_\alpha}\right)$ is the conjugate observable to $\hat{p}$). Figures 6.1(a) and 6.1(b) show $S(\Delta p)$ and $\Delta x \Delta p$ respectively as functions of α and the number of detection events on either side of the displacement, N.

As can be see in figure 6.1(a), the maximum amount of squeezing possible on a given input state $|\alpha\rangle$ increases monotonically with $|\alpha|^2$, proportional to the power of the input pulse. Interestingly, for a given α, there exists a finite N that achieves a global minimum in Δp^2. One would be tempted to use this value of N in the protocol to create ρ''; however, as can be seen in figure 6.1(b), there are other concerns.

As figure 6.1(b) shows, for a given α, $\Delta x \Delta p$ is not monotonic in N. Since we want ρ'' to be as close to a minimal uncertainty state as possible, while still maintaining a significantly squeezed quadrature, the optimal choice of N for the protocol would be at the $\Delta x \Delta p$ local minima shown in figures 6.1(a) and 6.1(b) by the white curve. While this does not minimize Δp^2 (and therefore maximize squeezing), it achieves a significantly squeezed state ρ'' that is as close to being a minimal uncertainty state as is possible, which is what we consider optimal.

6.2.2 Generalized Squeezed States

Other nonclassical states of microwave radiation having $\varphi_k \equiv 2\pi/k$ rotational symmetry in phase space result from generalizing this procedure (see figure 6.2). The squeezed state protocol discussed previously involves detecting the cavity state while centred at two points on a line through the origin of phase space, i.e., the case $k = 2$. To generalize this protocol, we detect N photons at k positions equally spaced around a circle of radius $|\alpha|$ in phase space, and take the first position on the positive real axis for simplicity.

There are k steps to this generalized protocol, and for $j = 0, 1, ..k-1$, the jth step is to: 1) displace by α_j so that the cavity state is centred around $|\alpha|e^{ij\varphi_k}$, 2) detect N photons, and 3) displace by α'_j, such that the cavity state is centred around the origin, where the coherent displacements parameters

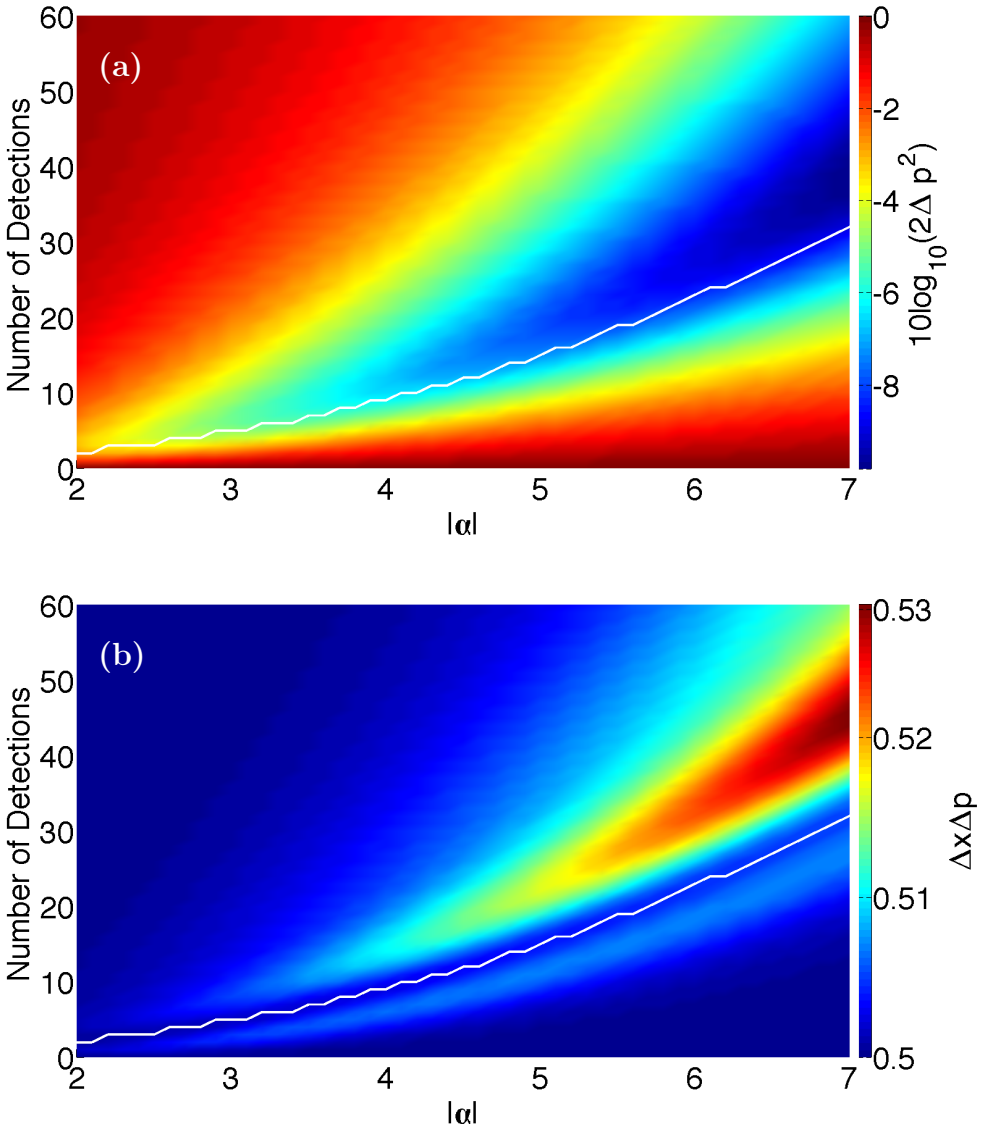

Figure 6.1: **(a)** $S(\Delta p)$ and **(b)** $\Delta x \Delta p$ of the state ρ'', as functions of α and the number of detection events, N. $\varphi_\alpha = 0$ for both figures. The white curve indicates the value of N that gives a local minimum in $\Delta x \Delta p$, while maintaining a squeezed Δp^2.

are

$$\alpha_j = |\alpha| e^{ij\varphi_k} \tag{6.8}$$

$$\alpha'_j = -\delta_j e^{ij\varphi_k} \tag{6.9}$$

$$\delta_j \approx \sqrt{n_j}. \tag{6.10}$$

The amplitude of the displacement to the origin, δ_j, is approximately the square root of the photon number left in the cavity after N detections, with a small correction accounting for the asymmetry of the intermediate states of the protocol.

Finally, after detecting N photons at all k positions, we obtain the generalized squeezed state with k-fold symmetry, ρ_k. The detection stage at each position transforms ρ_{j1} to ρ_{j2} according to

$$\rho_{j2} \equiv \frac{\hat{B}^N \rho_{j1} \hat{B}^{\dagger N}}{P_N^j}, \tag{6.11}$$

where P_N^j is the probability of detecting N photons from the state ρ_{j1}. The entire protocol will complete with success probability

$$\text{Prob(success)} = \prod_{j=0}^{k-1} P_N^j, \tag{6.12}$$

which can be made close to unity (see 6.C).

As mentioned previously, the case $k = 2$ ($\varphi_k = \pi$) corresponds to the creation of the vacuum with squeezed quadratures. We find high (here and henceforth meaning above 99%) overlap with

$$|\Psi_2\rangle = S(z)|0\rangle = e^{-\frac{1}{2}\left(z(\hat{a}^\dagger)^2 - z^*(\hat{a})^2\right)}|0\rangle \tag{6.13}$$

by numerically searching over N and z, where $S(z)$ is the ordinary squeezing operator with complex squeezing parameter z. In general, for $k \geq 2$, the states created by this protocol have high overlap with the analytic states

$$|\Psi_k\rangle = S^{(k)}(z)|0\rangle = e^{-\frac{1}{2}\left(z(\hat{a}^\dagger)^k - z^*(\hat{a})^k\right)}|0\rangle, \tag{6.14}$$

where $S^{(k)}(z)$ is called a generalized squeezing operator with complex parameter z [148, 149]. The first three operators of this class are

$$S^{(0)}(z) = e^{-\text{Im}[z]}\mathbb{I}, \; S^{(1)}(z) = D\left(-\frac{z}{2}\right) \text{ and } S^{(2)}(z) = S(z), \tag{6.15}$$

where $S(z)$ is the squeezing operator of equation (6.13).

Consider the final state after displacing to the origin ρ_k. To find z, we impose the condition that ρ_k and $|\Psi_k\rangle$ have the same average photon number by setting

$$\langle\Psi_k|\hat{a}^\dagger\hat{a}|\Psi_k\rangle = \left\langle\hat{a}^\dagger\hat{a}\right\rangle_{\rho_k}. \tag{6.16}$$

This results in excellent fidelity between the states, quantified by

$$\mathrm{F}\left[\rho_k\right] \equiv \mathrm{Tr}\left\{\rho_k |\Psi_k\rangle\langle\Psi_k|\right\}. \tag{6.17}$$

In fact, for $k = 2, 3, 4$ the fidelity is greater than 99% in each case for various values of $|\alpha|$. The Wigner functions of these states are shown in the left column of figure 6.2.

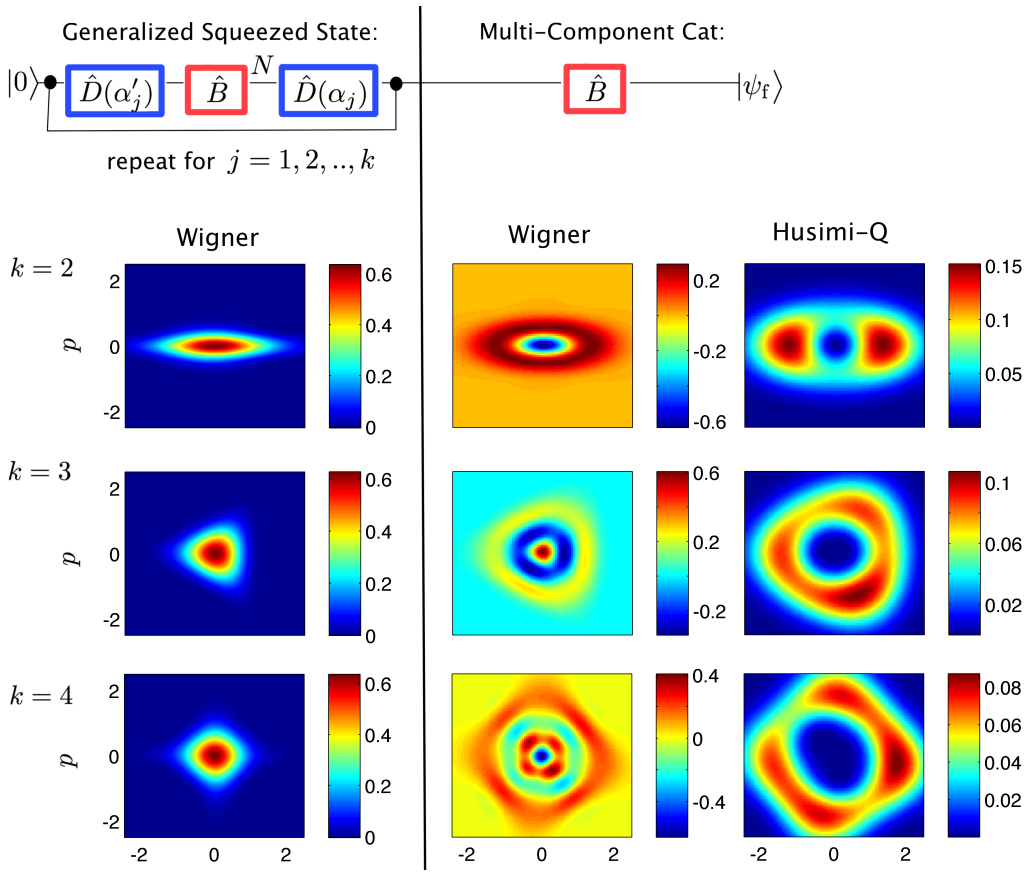

Figure 6.2: (upper) a schematic description of the state preparation protocol. (lower) Wigner representations (first and second columns) and Husmi Q representations (third column) of the $k = 2$, $k = 3$, and $k = 4$ generalized squeezed vacuum states (first column) and squeezed k-component Schrödinger cat states (second and third columns). The Wigner functions have been scaled such that they correspond to the quadrature opertors defined previously scaled by a factor of $1/\sqrt{2}$. Note that the second column has non-uniform colour bars for its figures in order to highlight all relevant information. 6.D contains a table of the fidelities, success probabilities, and α, δ, and N values for these states, as well as the fit parameters z and β.

To verify that these states are indeed nonclassical, a suitable nonclassicality witness can be used. For this purpose, we use the entanglement potential of [151], where a nonzero entanglement potential indicates that a state is nonclassical. Indeed, as can be calculated numerically, the states created by the generalized protocol all have nonzero entanglement potential (see 6.B).

Since the first displacement stage of each step ensures the average photon number of each state ρ_{j1} is on the order of $|\alpha|^2$, each P_N^j can be quite large, and as a result, the generalized protocol can have a significant probability of success. For example, for the modest $|\alpha|$ of the states shown in figure 6.2, the success probabilities are all greater than 99%. Furthermore, the success probability will grow monotonically with $|\alpha|$, and so can be increased by increasing the initial input state power.

6.2.3 Squeezed Multi-Component Cat States

It is known in quantum optics [107] that subtracting a photon from a squeezed vacuum produces an odd Schrödinger cat state. This concept can be generalized, such that subtracting a photon from a generalized squeezed vacuum of k-fold symmetry (the output state ρ_k of our protocol in 6.2.2) leaves a squeezed, k-component Schrödinger cat state in the cavity. We note that while having some similarity to the optical setting, our protocol does not require a beam splitter or a photon number resolving detector, instead, it simply requires the subtraction of one more photon from the squeezed states created by the protocol described in the previous section.

If we remove one more photon from the final state ρ_k, the resulting state has the form

$$\rho_k' = \frac{\hat{B}\rho_k\hat{B}^\dagger}{P_1^k}\,, \tag{6.18}$$

where P_1^k is the probability of a single photon being detected from state ρ_k. This procedure produces states of high overlap with

$$|\Psi_k'\rangle = S^{(k)}(z)\sum_{j=0}^{k-1} e^{ij(\varphi_k+\pi)}|\beta e^{ij(\varphi_k+\pi)}\rangle, \tag{6.19}$$

where now both $z \in \mathbb{C}$ and $\beta \in \mathbb{R}$ must be found numerically. These states all have non-zero entanglement potential, and are therefore nonclassical states of microwave radiation (see 6.B).

For $k = 2$, this additional detection will create a state very close to a squeezed odd Schrödinger cat state

$$|\Psi_2'\rangle = S^{(2)}(z)\left(|\beta\rangle - |-\beta\rangle\right). \tag{6.20}$$

For $k = 3$ and $k = 4$, we have

$$|\Psi_3'\rangle = S^{(3)}(z)\left(e^{-i\frac{\pi}{3}}|\beta e^{-i\frac{\pi}{3}}\rangle + e^{i\frac{\pi}{3}}|\beta e^{i\frac{\pi}{3}}\rangle - |-\beta\rangle\right) \tag{6.21}$$

$$|\Psi_4'\rangle = S^{(4)}(z)\left(|\beta\rangle + i|i\beta\rangle - |-\beta\rangle - i|-i\beta\rangle\right). \tag{6.22}$$

The $k = 3$ state is the state formed when the operator $S^{(3)}(z)$ is applied to a voodoo cat state [68]. The $k = 4$ state is the operator $S^{(4)}(z)$ applied to a coherent superposition of four out of phase coherent states, known as a compass state, which is known to have favourable decoherence properties [152, 113]. The Wigner and Husimi Q functions of these squeezed multi-component cat states are shown in the middle and right columns of figure 6.2 respectively, all of which have greater than 94% fidelity with (6.20), (6.21), and (6.22).

We have plotted both representations of these states as they highlight distinct information about the state. The Q function emphasizes the cat-like properties of the final state, while the Wigner function makes apparent the similarity between the final state and a $k-1$ photon Fock state, squeezed to the same order in k. The highly nonclassical nature of the state is also made evident by the large negative region of its Wigner function.

The probability of successful generation of these multi-component cat states is

$$\text{Prob(success)}' = P_1^k \prod_{j=0}^{k-1} P_N^j. \tag{6.23}$$

Unfortunately, the P_1^k are often very small, and for the squeezed multi-component cat states shown in figure 6.2 this results in a much lower success probability than the generalized squeezed vacuum. Optimization of this success probability is discussed in appendices 6.C and 6.D.

6.3 Discussion

6.3.1 Experimental Implementation

In regards to experimental implementation of this protocol with JPMs, superconducting microwave resonators are currently fabricated with Q-factors approaching 10^7, which in the microwave regime will lead to cavity lifetimes on the order of 10^5ns [153]. Thus, when JPMs with short T_2 are used [59], we can conservatively expect that as many as 10^2 to 10^3 measurements can be performed in the lifetime of the cavity. Practically, space requirements on a chip require a fast reset strategy for the JPMs, which is currently being developed [154].

For a realistic implementation of this protocol via JPMs, one must also consider the possibility of energy dissipation and dark counts in the JPMs. The behaviour of a JPM under such conditions has previously been discussed in [59, 58], and as such, we will highlight only the key point here. Both energy relaxation in the detector, and dark counts can be treated on the same footing. Energy relaxation corresponds to an unregistered measurement, and dark counts to false positives. One can thus adjust the number of measurements according to these rates to approach the desired number of $\hat{B}$-applications.

In the presence of dark counts and energy relaxation, one must describe the state of the cavity by a classically mixed state, with mixture components corresponding to different photon numbers in the cavity. However, in line with the standard interpretation of quantum mechanics, this mixing is only a lack of complete information on the observer's part, not on the action of the JPM. During each step of the protocol a definite number of photons is removed from the cavity, leaving it in a pure state. While we may be unaware of this exact number, unless this number plays a significant role in the success and performance of our protocol, or to further applications of the states created, then the mixture components are practically indistinguishable.

To that effect, as is illustrated in figure 6.1(a), the asymmetric squeezing performed at the j'th step is a smooth and slowly varying function of N, and as such is only minimally affected by a small change in N. Thus, the protocol is generally robust to the effects of energy relaxation and dark counts, provided these effects are small. Only the final detection used to generate squeezed multi-component cat states is sensitive to small perturbations in N, with an odd number of detections producing states of the form seen in equation (6.19).

Photon lifetimes are in general a limiting factor for nonclassical states, but these have been reported to be very long in circuit QED (on the order of 100 μs in [113]), and given the fast measurement times of our protocol, the cavity lifetime will affect our protocol less than others. In addition, some of the nonclassical states created by our protocol are robust to photon loss. For example, the even k-th order squeezed states are robust to single photon loss [118].

6.3.2 Applications

The generalized squeezed states have applications in continuous variable quantum computing [155]. Our protocol provides a simple way to obtain the necessary single mode squeezing and nonlinearity: by applying the generalized squeezed state protocols for $k = 2$ and $k \geq 3$ respectively. In par-

ticular, implementing the nonlinearity is often the technological bottleneck, as it cannot be created using linear optics alone [156], and our proposal is to use the nonlinear transformation performed by our protocol for $k \geq 3$ in place of traditional nonlinear interactions (such as Kerr-like interactions). In this regard, our protocol has the potential to be more efficient and require less technological overhead than most known methods to implement the nonlinearity [156, 157].

The squeezed multi-component Schrödinger cat states (SMCS) have applications in metrology, in particular for phase estimation using a Mach-Zehnder interferometer set up. It has recently been shown that cat states can be used in combination with linear optics to create Entangled Coherent states (ECS), and that phase estimation using these ECS outperforms that using NOON states [158]. The performance difference is especially significant at low photon number, and/or when photon loss is considered. It is an emerging and active area of research to see if an improvement in phase estimation can be gained by using SMCS in place of cat states in this scheme.

6.3.3 Conclusions

In conclusion, we have shown how a combination of strongly coupled photon counting and coherent displacement can be used to create nonclassical states of radiation with high probability (greater than 99% for the generalized squeezed states), and with high fidelity (greater than 99% for the generalized squeezed states, and greater than 94% for the squeezed multi-component cats). This protocol can be realized in circuit QED using Josephson photomultipliers.

Acknowledgements

We acknowledge instructive discussions with F.W. Strauch, R. McDermott, and B.G. Taketani. Research supported by DARPA within the QuEST program and NSERC Discovery grants. LCGG was supported by the Ontario Graduate Scholarship Program.

Appendix

6.A The Josephson Photomultiplier

The Josephson Photomultipler consists of a current biased Josephson junction which can be completely described by the phase difference across the junction, and its conjugate momentum (related to the charge difference across the junction). Such a system has a potential energy (as a function of phase) which has the so called "tilted washboard" shape:

$$U(\phi) \approx -I_{\mathrm{c}} \cos\phi - I_{\mathrm{b}}\phi \tag{6.24}$$

where I_{c} is the junction critical current and I_{b} is the applied bias current.

The system thus has an infinite number of local energy minima which have one or more metastable bound states. The applied bias current determines the number of bound states, and during operation the JPM is biased such that the potential minimum working point contains only two metastable bound states. Additionally, during operation, the bias current is finely tuned such that the energy difference between the metastable bound states is equal to the photon energy of the microwave cavity coupled to the JPM. It is important to note that the control offered by the applied bias makes the JPM tunable, allowing one to bring it in and out of strong coupling with the microwave cavity.

The detection mechanism of the JPM relies on the fact that the bound states of the potential well are metastable, and have finite quantum tunnelling rates out of the potential well. These rates increase exponentially as the excitation number in the potential well increases. When there are only two metastable states in the potential well, tunnelling out of the ground state is exponentially suppressed, and all observed tunnelling events can be attributed to incident microwave radiation exciting the JPM into the excited metastable state, and this state then tunnelling out of the potential well. A tunnelling event results in a large voltage change across the circuit, and as a result can be detected by external classical circuitry. We can thus equate a tunnelling event with a single photon detection.

In reference [59] the back action of the JPM onto the microwave cavity was thoroughly examined, taking into account the relevant physical processes occurring (JPM relaxation and pure dephasing, and tunnelling out of the metastable ground state). We will briefly summarize the points relevant to this work.

Photon detection by a JPM approaches the dichotomic detection of the subtraction operator when the JPM and the cavity are allowed to interact for a long enough time (typically several Rabi periods) before the tunnelling event occurs. This is achieved when the coupling strength between the JPM and the cavity is comparable to the tunnel rate out of the first excited metastable state, as achieved in [54]. This "long" interaction time removes any photon number information in the measurement time coming from the $\sqrt{n}g$ dependent oscillation periods of the Fock states.

However, the long interaction time with the JPM results in the reduction of the coherence between cavity Fock states after measurement, something that is not caused by the subtraction operator. To counteract this affect, a JPM with a short T_2 time can be used, since pure dephasing effectively kills the cavity coherence damping effect of the JPM (see [59], figure 3(b)). In the extreme case where the cavity-JPM interaction is itself incoherent, the subtraction operator back action is obtained.

6.B Nonclassicality

The entanglement potential is both a nonclassicality witness and measure, and as such can be used to examine how the nonclassicality changes with the number of detections at each step of the generalized protocol. It is defined as

$$\mathrm{EP}[\rho] \equiv \log_2 ||\sigma_\rho^{T_A}||_1, \tag{6.25}$$

where $\sigma_\rho = U_{\mathrm{BS}} (\rho \otimes |0\rangle\langle 0|) U_{\mathrm{BS}}^\dagger$, for U_{BS} the unitary transformation of a 50:50 beam splitter, and $\sigma_\rho^{T_A}$ is the partial transpose of σ_ρ [159]. Figure 6.3 shows the entanglement potential of the generalized squeezed states and the multi-component cat states (for $k = 2, 3, 4$) as a function of the number of detections at each step. As can be seen, for the squeezed state ($k = 2$), the maximum value of EP occurs around the optimal value of N determined in the main text.

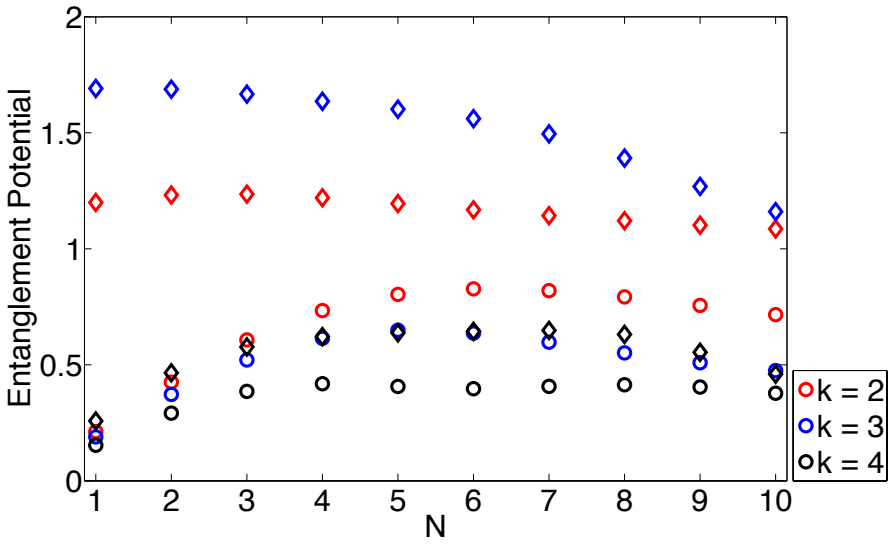

Figure 6.3: This figure shows entanglement potential (EP) of the states created by the generalized protocol (for $k = 2, 3, 4$) as a function of the number of detections, N, performed at each step in the protocol. The generalized squeezed states are the circles, and the diamonds correspond to the squeezed multi-component cat states. These states all have $|\alpha| = 3$.

6.C Success Probability vs. Fidelity

Due to the noncommutivity of the subtraction operator and coherent displacement, finding a simple closed form analytic solution for the success probability of our protocols (equations (6.12) and (6.23)) may not be possible. However, we can examine the behaviour of P_N of equation (6.2) to understand how the total detection probability scales with $|\alpha|^2$. As can be seen in figure C1(a), P_N rapidly approaches unity for $|\alpha|^2 > N$. As a result of this, it is possible to achieve very high success probabilities for the generalized squeezed state protocol. For the squeezed multi-component cat states, the limiting factor remains P_1^k, which can be quite small.

In addition to success probability, one also wishes to maximize the fidelity with the target analytic states. In the $k = 2$ case, we find that this is achieved when, for a given $|\alpha|$, N lies nearly along the minimal uncertainty curve of figure 6.1(b). This curve is well approximated by $q(|\alpha|) = a|\alpha|^2 + b|\alpha| + c$, where $a, b, c \in \mathbb{R}$ can be found numerically. Since N must be an integer, we set

$$N = \lceil q(|\alpha|) \rceil, \tag{6.26}$$

where $\lceil * \rceil$ rounds up to the nearest integer. It is worth examining what effect this has on the success probability of P_N, now defined by

$$P_N = 1 - \frac{\Gamma(\lceil q(|\alpha|) \rceil, |\alpha|^2)}{\Gamma(\lceil q(|\alpha|) \rceil)}. \tag{6.27}$$

This is plotted in figure C1(b), along with the continuous version of equation (6.27), where N is allowed to take non-integer values. As the figures show, the success probability approaches unity with increasing $|\alpha|$. It is therefore possible to maximize both fidelity and success probability in the $k = 2$ case, for both the squeezed state and Schrödinger cat state.

For $k > 2$ there is no known analog of the minimal uncertainty curve of figure 6.1(b), however, numerical results have shown that it is possible to achieve high fidelity and success probability using N and $|\alpha|$ similar to that of the $k = 2$ case, i.e. near to the minimal uncertainty curve.

6.D Numerical Results

In figure 6.2, we have given examples of a generalized squeezed vacuum and a squeezed/multi-component cat, for $k = 2, 3, 4$. Each of these examples is found by a numerical fit over the parameters in the protocol: the field amplitude α, the number of photon subtractions at each position N, and the small corrections for photon loss, δ_1, .., δ_k. For each of the examples in Fig. 6.2, we have locally minimized the error function

$$\epsilon = 1 - F[\rho_k, \rho_k^{\mathrm{t}}] \tag{6.28}$$

over the set of parameters $\mathcal{P} = \{x_i\}$ necessary to define ρ_k – the final state produced in our protocol – and the target state $\rho_k^{\mathrm{t}} = |\Psi_k\rangle\langle\Psi_k|$. The fidelity F is as defined in equation (6.17). We have given examples only for $N = 16$ ($N = 6$ in the case of the 4-component cat state) to reduce this parameter space. Although this choice is somewhat arbitrary, it generally predicts reasonably small error for $|\alpha| \in [3, 10]$, an experimentally accessible range.

In the case of the generalized squeezed vacuum states, we constrain the squeezing parameter z, all that is necessary to specify the target state, so that

$$\langle \hat{n} \rangle_{\rho_k} = \langle \hat{n} \rangle_{\rho_k^{\mathrm{t}}}. \tag{6.29}$$

There remains $k+1$ unconstrained parameters determining the error function:

$$\epsilon^k \equiv \epsilon^k(\alpha, \delta_1, .., \delta_k). \tag{6.30}$$

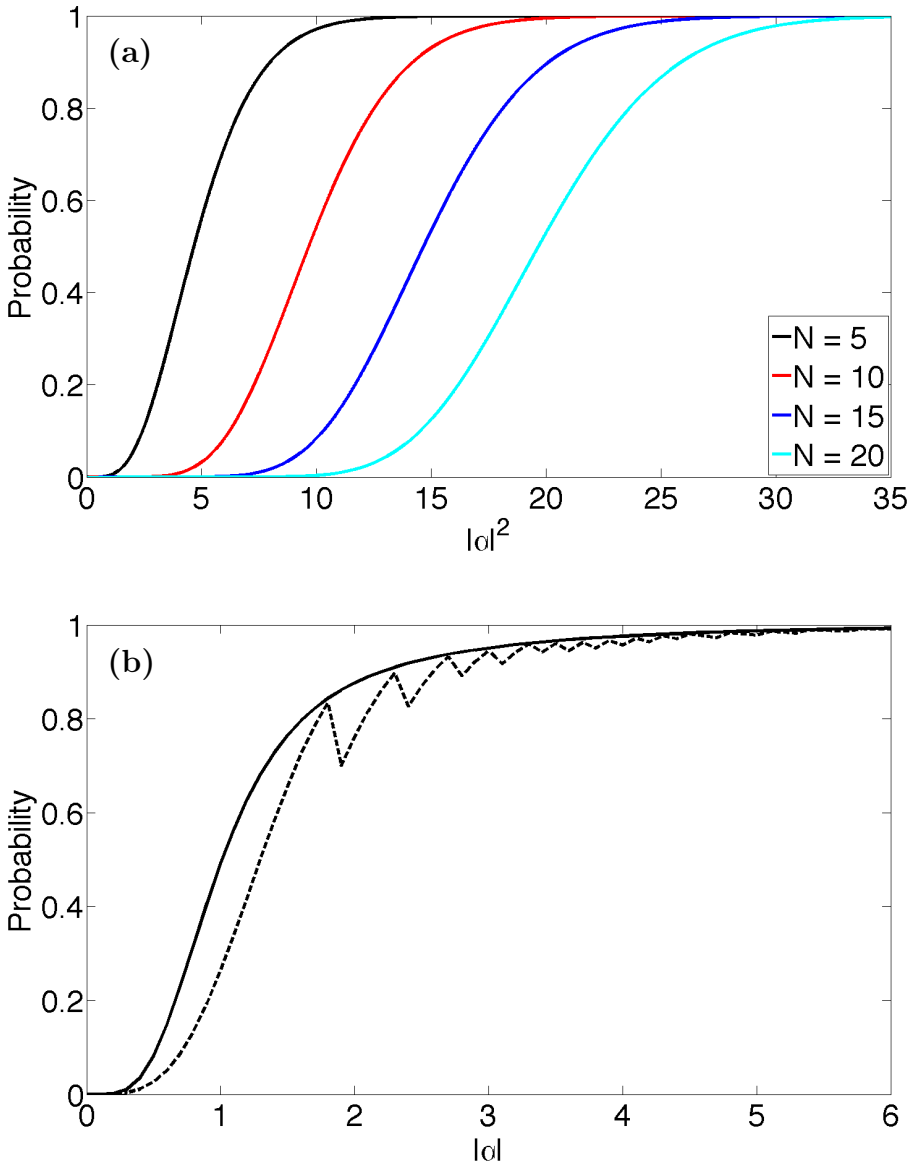

Figure 6.4: The success probability of the first step of the protocol as a function of input coherent state power. In **(a)** for several values of fixed N, and in **(b)** for N assumed to vary quadratically as $q(|\alpha|)$. The solid line in **(b)** is for N taking real values, and the dashed line for N taking only integer values.

In the case of multi-component/squeezed cats, two parameters specify ρ_k^{t}, z and the cat-state amplitude β. In this case, β is constrained according to equation (6.29), and we add z to the set of parameters over which we

	generalized squeezed vacuums			
k=2	$\alpha = 5.7389$			
	$\delta_1 = 1.6786$	$\delta_2 = 1.7227$		
	$z = 0.7063$			
	$P = 0.9951$	$\epsilon^{(2)} = 1.7 \times 10^{-3}$		
k=3	$\alpha = 6.6999$			
	$\delta_1 = 1.1782$	$\delta_2 = 1.1536$	$\delta_3 = 1.1532$	
	$z = -0.185$			
	$P = 1.0000$	$\epsilon^{(3)} = 4.5 \times 10^{-4}$		
k=4	$\alpha = 5.9999$			
	$\delta_1 = 1.2138$	$\delta_2 = 1.2166$	$\delta_3 = 1.2047$	$\delta_4 = 1.2193$
	$z = 1.4776$			
	$P = 0.9999$	$\epsilon^{(4)} = 6.1 \times 10^{-3}$		
	squeezed multi-component cats			
k=2	$\alpha = 3.8480$			
	$\delta_1 = 1.9783$	$\delta_2 = 1.5670$		
	$z = -3.8667$	$\beta = 2.00$		
	$P = 0.2478$	$\epsilon^{(2)} = 2.0 \times 10^{-3}$		
k=3	$\alpha = 7.5000$			
	$\delta_1 = 1.582$	$\delta_2 = 1.1522$	$\delta_3 = 1.1482$	
	$z = 4.4 \times 10^{-2}$	$\beta = 6.0 \times 10^{-5}$		
	$P = 0.0037$	$\epsilon^{(3)} = 4.4 \times 10^{-3}$		
k=4	$\alpha = 3.5500$			
	$\delta_1 = 0.9451$	$\delta_2 = 0.9518$	$\delta_3 = 0.9393$	$\delta_4 = 0.9401$
	$z = 0.0014$	$\beta = 1.56$		
	$P = 0.0025$	$\epsilon^{(4)} = 5.6 \times 10^{-2}$		

Figure 6.5: Protocol parameters α and $\{\delta_j\}$, target state parameter(s) z (and β), error ϵ^k, and corresponding success probability P for each of the examples given in Fig. 6.2. $N = 16$ in all cases except for the 4-component cat, in which case $N = 6$.

minimize the error:

$$\epsilon^k \equiv \epsilon^k(z, \alpha, \delta_1, .., \delta_k). \tag{6.31}$$

Figure 6.5 contains the parameter values, ϵ^k, and success probabilities P for each of the cases shown in figure 6.2.

Note that the error function equation (6.28) is multimodal, so we have not likely found a global maximum in state fidelity. Generally, the detection probability is also multimodal when the integer nature of N is considered, e.g. see dotted curve in figure 6.4(b), so the detection probabilities listed here are not likely maximal and depend sensitively on the choice of N. While our choice $N = 16$ is well-suited for $k = 2$, other values would likely optimize the cat-state detection probabilities for different k. We leave the optimal value of N for a given k as an open question.

Conclusion

Quantum information and computing promise a wide range of potential applications and uses, with the potential to revolutionize research in not only physics, but other areas of science, including biology and chemistry. However, before useful quantum computers are developed, a myriad of challenges must be overcome, many of which are likely not yet even known. A central challenge is how one can continue to control and measure with high fidelity the components of a quantum computer as this computer grows in size. At the time of writing of this thesis, state of the art quantum computers have on the order of ten qubits, while hundreds or thousands of qubits will be needed for a useful quantum computer. Solving this and other challenges has driven research for the last several decades, which has led to much success, and, as a bonus, a better understanding of the fundamental behavior of nature on quantum scales. In this thesis, developing scalable measurement protocols was a major focus, as was a careful examination of the fundamental limits on measurement fidelity set by the auxiliary quantum systems used to measure the qubits in a superconducting quantum computer. Both of these research directions combat the challenge of scaling up measurement protocols, and are potentially one piece towards a useful quantum computer.

Chapter 2 proposes a novel readout scheme for superconducting qubits, using a diserpsively coupled microwave cavity and a Josephson photomultiplier (JPM). This protocol achieves both fast and accurate single-shot measurement of the qubit state, with a measurement contrast of 95% in 150 ns, by encoding the state of the qubit in the average photon number in the cavity and distinguishing between high and low power cavity pointer states using the JPM. Continuing the study of quantum measurement, chapter 3 proposes a measurement protocol for the parity of N qubits, which can be implemented in any physical system where strong dispersive coupling between qubits and electromagnetic fields in a cavity can be achieved. By mapping the qubit parity information to the average photon number of a cavity coherent state, while storing information that distinguishes between states with the same parity in the coherent state phase, this protocol determines the qubit parity

by cavity measurement with a phase insensitive threshold photon counter. In so doing the protocol implements a quantum non-demolition measurement of the parity, while erasing all other qubit state information.

Both single-qubit readout and multi-qubit parity readout are important components to many quantum information protocols, such as some error correction schemes and heralded initialization. The protocols presented in chapters 2 and 3 offer several advantages over existing schemes. These include the fact that they are quantum non-demolition, which is especially relevant to parity measurement, and that due to their limited resource footprint in both hardware and software, they may prove to be intrinsically easier to scale with system size. However, open questions remain. It is not well understood what constraints using a dispersively coupled cavity to measure qubit observables puts on the achievable measurement fidelity. In particular, to what extent corrections beyond the second order dispersive Hamiltonian are relevant to present day experiments is an active area of study. The limits imposed by these corrections on qubit measurement fidelity is also unknown. In a broader sense, these open questions are related to the question of whether or not it is better to take the bare qubit basis or the dressed qubit-cavity basis as the logical basis for a quantum computer. Only within the last few years has sufficiently strong dispersive coupling been achieved that this question now begins to become relevant to current experiments.

In chapter 4 the connection between the bare and dressed logical bases is explored by calculating the state formed in the lab frame when a dispersively coupled qubit-cavity system is driven by a classical cavity drive. We find that the state created is a Poissonian distributed superposition of the dressed eigenstates, which we name the dressed coherent state. Even though all corrections beyond the dispersive approximation were ignored, this state still exhibits nontrivial qubit-cavity entanglement. As a result of this, future and simultaneous qubit operations have a dependence on both the phase and amplitude of the effective coherent state in the cavity. How to use this advantageously in a quantum information protocol remains an open quesiton.

Chapter 5 applies the concept of the dressed coherent state to standard dispersive readout, where the qubit state is encoded in the phase of the signal exiting the coupled cavity, which can be measured using homodyne techniques. As a result of the formation of a dressed coherent state, we find that readout of the qubit state this way is not intrinsically quantum non-demolition, except in the limit of infinite measurement time. However, we propose a technique to mitigate this effect by coherent feedback on the qubit, and this technique can be used to achieve faster and more accurate qubit initialization. When enough photons are in the cavity the dressed coherent state stops being an adequate description of the qubit-cavity system, and what the

full quantum description of the system is in this regime remains unknown. Further study is needed to understand this regime, as many contemporary readout schemes are beginning to operate with high average photon numbers in the cavity.

Finally, chapter 6 presents a protocol for the generation of nonclassical states of electromagnetic radiation inside a cavity, using only classical cavity drive and nonlinear photon detection. In particular, the nonlinear detector must perform an ideal vacuum detection, with no photon number resolving ability, such as can be achieved in some regimes of operation of the JPM. Examples of the states this protocol can create include the generalized squeezed states and multi-component Schrödinger cat states, which have applications in quantum metrology and continuous variable quantum computing. Future areas of work in this research direction include characterization of the full class of states that can be created using this protocol, and understanding how best to implement ideal vacuum detection under realistic experimental conditions.

Quantum information science will continue to be an active area of research for the foreseeable future. While recent progress, especially in superconducting circuits, is extremely promising, considerable technological and fundamental challenges still exist, and it is unlikely that a useful quantum computer will be developed in the near future. However, the study of quantum information science pushes the boundaries of our understanding of nature. Understanding the details of simple systems at the accuracy required for computation can often lead to novel insights into the behavior of these systems, such as has been presented in this thesis. As a result, despite limited practical applications in the near future, quantum information remains a valuable research direction. While it may be decades before the first real-world applications of quantum information are commonplace, the deeper understanding of nature that we gain along the way is invaluable, and justifies the field in its own right.

Publication List

Published

1. Luke C. G. Govia, Emily J. Pritchett, Canran Xu, B. L. T. Plourde, Maxim G. Vavilov, Frank K. Wilhelm, and R. McDermott
High-fidelity qubit measurement with a microwave-photon counter
Phys. Rev. A **90**, 062307 (2014)

2. Luke C. G. Govia, Emily J. Pritchett, and Frank K. Wilhelm
Generating nonclassical states from classical radiation by subtraction measurements
New J. Phys. **16** 045011 (2014)

Submitted

3. Luke C. G. Govia, Emily J. Pritchett, B.L.T. Plourde, Maxim G. Vavilov, R. McDermott, and Frank K. Wilhelm
Scalable two- and four-qubit parity measurement with a threshold photon counter
arXiv:1502.03340 (2015)

In Preparation

4. Luke C. G. Govia and Frank K. Wilhelm
Entanglement Generated by the Dispersive Interaction: The Dressed Coherent State

5. Luke C. G. Govia and Frank K. Wilhelm
Coherent Feedback Improved Qubit Initialization in the Dispersive Regime

Previous Publications

6. Luke C. G. Govia, Emily J. Pritchett, Seth T. Merkel, Deanna Pineau, and Frank K. Wilhelm
   Theory of Josephson photomultipliers: Optimal working conditions and back action
   Phys. Rev. A **86**, 032311 (2012)

Appendices

Appendix A

Numerical Simulation of the Master Equation

The numerical work in this thesis involved simulation of the master equation

$$\dot{\rho}(t) = -i[\hat{H}(t), \rho(t)] + \sum_{\mu} \gamma_{\mu} \left(\hat{L}_{\mu} \rho(t) \hat{L}_{\mu}^{\dagger} - \frac{1}{2} \left\{ \hat{L}_{\mu}^{\dagger} \hat{L}_{\mu}, \rho(t) \right\} \right), \tag{A.1}$$

and the technique used to do so will be briefly outlined here. The first step in solving such an operator differential equation is to vectorize the equation, converting the matrix ρ to the vector $\vec{\rho}$ by stacking its rows on top of one another, such as:

$$\rho = \begin{pmatrix} \rho_{11} & \rho_{12} & \rho_{13} \\ \rho_{21} & \rho_{22} & \rho_{23} \\ \rho_{31} & \rho_{32} & \rho_{33} \end{pmatrix} \longmapsto \mathrm{vec}(\rho) \equiv \vec{\rho} = \begin{pmatrix} \rho_{11} \\ \rho_{12} \\ \rho_{13} \\ \rho_{21} \\ \rho_{22} \\ \rho_{23} \\ \rho_{31} \\ \rho_{32} \\ \rho_{33} \end{pmatrix} \tag{A.2}$$

The vectorized master equation has the form

$$\dot{\vec{\rho}}(t) = \hat{\mathcal{L}} \vec{\rho}(t), \tag{A.3}$$

where, using the identity $\mathrm{vec}(ABC) = A \otimes C^{\mathrm{T}}\vec{B}$, the superoperator $\hat{\mathcal{L}}$ is given by

$$\begin{aligned}\hat{\mathcal{L}} = &-i\left(\hat{H}(t)\otimes\mathbb{I} - \mathbb{I}\otimes\hat{H}(t)^{\mathrm{T}}\right)\\ &+\sum_{\mu}\gamma_{\mu}\left(\hat{L}_{\mu}\otimes\hat{L}_{\mu}^{*} - \frac{1}{2}\left(\hat{L}_{\mu}^{\dagger}\hat{L}_{\mu}\otimes\mathbb{I} + \mathbb{I}\otimes\left(\hat{L}_{\mu}^{\dagger}\hat{L}_{\mu}\right)^{*}\right)\right).\end{aligned} \tag{A.4}$$

Vectorization is necessary to allow for easy application of numerical differential equation solvers, such as those implementing Runge-Kutta algorithms [160]. Also, in the case where the Hamiltonian is time independent the vectorized master equation can be solved directly by exponentiation as

$$\vec{\rho}(t) = e^{\hat{\mathcal{L}}t}\vec{\rho}(0). \tag{A.5}$$

While vectorization is necessary to simulate the master equation using most standard numerical techniques, it limits the dimension of the system Hilbert space that can be simulated. For a Hilbert space of dimension d, the density matrix ρ and the Lindblad operators $\hat{L}_{\mu}$ are $d \times d$ matrices, while the vectorized Lindblad generator $\hat{\mathcal{L}}$ is a $d^2 \times d^2$ matrix. Therefore, it becomes difficult to store $\hat{\mathcal{L}}$ in memory and operate on it at a rate much faster than it does for either ρ or $\hat{L}_{\mu}$.

To avoid this problem, a hybrid technique was employed that avoids the calculation of $\hat{\mathcal{L}}$ directly. This technique involves a function that given a vectorized density matrix $\vec{\rho}(t)$, calculates the vectorized derivative $\dot{\vec{\rho}}(t)$ by the following protocol:

1. Convert $\vec{\rho}(t)$ back to $\rho(t)$ by unstacking its rows.
2. Calculate the derivative $\dot{\rho}(t)$ using equation (A.1).
3. Vectorize the derivative $\dot{\rho}(t)$ and output $\dot{\vec{\rho}}(t)$.

Now, if the numerical differential equation solver is linked to this function it can calculate $\dot{\vec{\rho}}(t)$ without ever constructing or operating on $\hat{\mathcal{L}}$, avoiding the problems previously discussed. For the work done in this thesis, employing this technique has allowed for the simulation on a single desktop computer of time-dependent systems with a Hilbert space dimension of 800.

It is worthwhile to briefly comment on the running time required to calculate the derivative for the fully vectorized algorithm versus the unvectorized algorithm presented here. In the most naïve implementation, the hardest part in the calculation for the vectorized algorithm is the multiplication of a $d^2 \times d^2$ matrix by a $d^2 \times 1$ vector, for which the running time is $\mathcal{O}((d^2)^2) = \mathcal{O}(d^4)$.

For the unvectorized algorithm, the most computational intensive component is the matrix multiplication for all d^2 components of the sum in the dissipator, for each of which the running time is $\mathcal{O}(d^3)$, giving a total running time of $\mathcal{O}(d^5)$. However, often the number of distinct Lindblad operators with nonzero γ_μ does not scale as $\mathcal{O}(d^2)$, in which case the running time of the unvectorized algorithm decreases. A lower bound of $\mathcal{O}(d^3)$ is achieved for a constant number of Lindblad operators, as is the case, for example, for a harmonic oscillator coupled to a bosonic bath.

Bibliography

[1] Richard P. Feynman. Simulating physics with computers. *International Journal of Theoretical Physics*, 21(6-7):467–488, 1982.

[2] David Deutsch. Quantum theory, the church-turing principle and the universal quantum computer. *Proceedings of the Royal Society of London A: Mathematical, Physical and Engineering Sciences*, 400(1818):97–117, 1985.

[3] David Deutsch and Richard Jozsa. Rapid solution of problems by quantum computation. *Proceedings of the Royal Society of London A: Mathematical, Physical and Engineering Sciences*, 439(1907):553–558, 1992.

[4] Lov K. Grover. A fast quantum mechanical algorithm for database search. In *Proceedings of the Twenty-eighth Annual ACM Symposium on Theory of Computing*, STOC '96, pages 212–219, New York, NY, USA, 1996. ACM.

[5] Peter W. Shor. Polynomial-time algorithms for prime factorization and discrete logarithms on a quantum computer. *SIAM Review*, 41(2):303–332, 1999.

[6] Daniel Loss and David P. DiVincenzo. Quantum computation with quantum dots. *Phys. Rev. A*, 57:120–126, Jan 1998.

[7] M.A. Nielsen and I.L. Chuang. *Quantum Computation and Quantum Information*. Cambridge University Press, Cambridge, UK, 2000.

[8] M.O. Scully and S. Zubairy. *Quantum Optics*. Cambridge University Press, 1997.

[9] S. Haroche and J.-M. Raimond. *Exploring the Quantum: Atoms, Cavities, and Photons*. Oxford University Press, Oxford, 2006.

[10] M. Fox. *Quantum Optics : An Introduction*. Oxford Master Series in Physics. OUP Oxford, 2006.

[11] M.H. Devoret. Quantum fluctuations in electrical circuits. In *Les Houches Session LXIII, Quantum Fluctuations*, pages 351–386, 1995.

[12] R. J. Glauber. Coherent and incoherent states of the radiation field. *Phys. Rev.*, 131:2766–2788, 1963.

[13] E. C. G. Sudarshan. Equivalence of semiclassical and quantum mechanical descriptions of statistical light beams. *Phys. Rev. Lett.*, 10:277–279, Apr 1963.

[14] Vittorio Giovannetti, Seth Lloyd, and Lorenzo Maccone. Quantum metrology. *Phys. Rev. Lett.*, 96:010401, Jan 2006.

[15] Samuel L. Braunstein and Carlton M. Caves. Statistical distance and the geometry of quantum states. *Phys. Rev. Lett.*, 72:3439–3443, May 1994.

[16] E. Wigner. On the quantum correction for thermodynamic equilibrium. *Phys. Rev.*, 40:749–759, Jun 1932.

[17] Various. *Springer Handbook of Atomic, Molecular and Optical Physics*. Springer, 2006.

[18] Kôdi Husimi. Some formal properties of the density matrix. *Proceedings of the Physico-Mathematical Society of Japan. 3rd Series*, 22(4):264–314, 1940.

[19] R.J. Schoelkopf and S.M. Girvin. Wiring up quantum systems. *Nature*, 451:664–669, 2008.

[20] Y. Makhlin, G. Schön, and A. Shnirman. Quantum-state engineering with Josephson-junction devices. *Rev. Mod. Phys.*, 73:357–400, 2001.

[21] M.H. Devoret and J.M. Martinis. Implementing qubits with superconducting integrated circuits. *Quantum Inf. Process.*, 3:163, 2004.

[22] J. Clarke and F.K. Wilhelm. Superconducting quantum bits. *Nature*, 453:1031–1042, 2008.

[23] M.H. Devoret and R.J. Schoelkopf. Superconducting circuits for quantum information: An outlook. *Science*, 339:1169–1174, 2013.

[24] B. D. Josephson. Possible new effects in superconductive tunnelling. *Phys. Lett.*, 1:251–253, 1962.

[25] J. M. Martinis, S. Nam, J. Aumentado, and C. Urbina. Rabi oscillations in a large Josephson junction qubit. *Phys. Rev. Lett*, 89:117907, 2002.

[26] Y. Nakamura, Y. A. Pashkin, and J. S. Tsai. Coherent control of macroscopic quantum states in a single-Cooper-pair box. *Nature*, 398:786–788, 1999.

[27] V. Bouchiat, D. Vion, P. Joyez, D. Esteve, and M. H. Devoret. Quantum coherence with a single Cooper pair. *Phys. Scripta*, T76:165, 1998.

[28] J. E. Mooij, T. P. Orlando, L. Levitov, L. Tian, C. H. van der Wal, and S. Lloyd. Josephson persistent current qubit. *Science*, 285:1036, 1999.

[29] J.A. Schreier, A.A. Houck, J. Koch, D.I. Schuster, B.R. Johnson, J.M. Chow, J.M. Gambetta, J. Majer, L. Frunzio, M.H. Devoret, S.M. Girvin, and R.J. Schoelkopf. Suppressing charge noise decoherence in superconducting charge qubits. *Phys. Rev. B*, 77:180502, 2008.

[30] J. Koch, T.M. Yu, J. Gambetta, A.A. Houck, D.I. Schuster, J. Majer, A. Blais, M.H. Devoret, S.M. Girvin, and R.J. Schoelkopf. Charge-insensitive qubit design derived from the Cooper pair box. *Phys. Rev. A*, 76:042319, 2007.

[31] R. Barends, J. Kelly, A. Megrant, D. Sank, E. Jeffrey, Y. Chen, Y. Yin, B. Chiaro, J. Mutus, C. Neill, P. O'Malley, P. Roushan, J. Wenner, T. C. White, A. N. Cleland, and John M. Martinis. Coherent josephson qubit suitable for scalable quantum integrated circuits. *Phys. Rev. Lett.*, 111:080502, Aug 2013.

[32] M. R. Geller, E. J. Pritchett, A. T. Sornborger, and F. K. Wilhelm. Quantum computing with superconductors i: Architectures. *NATO Science Series II: Mathematics, Physics and Chemistry*, 244:171–194, 2006.

[33] F. Motzoi, J. M. Gambetta, P. Rebentrost, and F. K. Wilhelm. Simple pulses for elimination of leakage in weakly nonlinear qubits. *Phys. Rev. Lett.*, 103:110509, 2009.

[34] T. Niemczyk, F. Deppe, H. Huebl, E. P. Menzel, F. Hocke, M. J. Schwarz, J. J. Garcia-Ripoll, D. Zueco, T. Hummer, E. Solano, A. Marx, and R. Gross. Circuit quantum electrodynamics in the ultrastrong-coupling regime. *Nat Phys*, 6(10):772–776, 10 2010.

[35] H. Paik, D.I. Schuster, L.S. Bishop, G. Kirchmair, G. Catelani, A.P. Sears, B.R. Johnson, M.J. Reagor, L. Frunzio, L.I. Glazman, S.M. Girvin, M.H. Devoret, and R.J. Schoelkopf. Observation of high coherence in Josephson junction qubits measured in a three-dimensional circuit QED architecture. *Phys. Rev. Lett.*, 107:240501, 2011.

[36] Yu Chen, D. Sank, P. O'Malley, T. White, R. Barends, B. Chiaro, J. Kelly, E. Lucero, M. Mariantoni, A. Megrant, C. Neill, A. Vainsencher, J. Wenner, Y. Yin, A. N. Cleland, and John M. Martinis. Multiplexed dispersive readout of superconducting phase qubits. *Applied Physics Letters*, 101(18):–, 2012.

[37] E.T. Jaynes and F.W. Cummings. Comparison of quantum and semiclassical radiation theories with application to the beam maser. *IEEE Proc.*, 51:89, 1963.

[38] LongBao Yu, NingHua Tong, ZhengYuan Xue, ZiDan Wang, and ShiLiang Zhu. Simulation of the spin-boson model with superconducting phase qubit coupled to a transmission line. *Science China Physics, Mechanics and Astronomy*, 55(9):1557–1561, 2012.

[39] A. Blais, R. S. Huang, A. Wallraff, S. M. Girvin, and R. J. Schoelkopf. Cavity quantum electrodynamics for superconducting electrical circuits: An architecture for quantum computing. *Phys. Rev. A*, 69:062320, 2004.

[40] Robert Alicki and K. Lendi. *Quantum Dynamical Semigroups and Applications*, volume 717 of *Lecture Notes in Physics*. Springer-Verlag Berlin Heidelberg, 2007.

[41] Heinz-Peter Breuer and Francesco Petruccione. *The Theory of Open Quantum Systems*. Oxford University Press, 2006.

[42] E.B. Davies. Markovian master equations. *Communications in Mathematical Physics*, 39(2):91–110, 1974.

[43] Félix Beaudoin, Jay M. Gambetta, and A. Blais. Dissipation and ultrastrong coupling in circuit qed. *Phys. Rev. A*, 84:043832, Oct 2011.

[44] Maximilan G. Schultz. *On Master Equations and Rate Equations in Molecular Electronics: There and Back Aagin*. PhD thesis, Freie Universität Berlin, 2009.

[45] H. Wiseman and G. Milburn. *Quantum Measurement and Control*. Cambridge University Press, 2010.

[46] Vladimir B. Braginsky and Farid Ya. Khalili. *Quantum Measurement*. Cambridge University Press, New York, NY, USA, 1992.

[47] Luke C. G. Govia, Emily J. Pritchett, Canran Xu, B. L. T. Plourde, Maxim G. Vavilov, Frank K. Wilhelm, and R. McDermott. High-fidelity qubit measurement with a microwave-photon counter. *Phys. Rev. A*, 90:062307, Dec 2014.

[48] Bixuan Fan, Göran Johansson, Joshua Combes, G. J. Milburn, and Thomas M. Stace. Nonabsorbing high-efficiency counter for itinerant microwave photons. *Phys. Rev. B*, 90:035132, Jul 2014.

[49] Austin G. Fowler, Matteo Mariantoni, John M. Martinis, and Andrew N. Cleland. Surface codes: Towards practical large-scale quantum computation. *Phys. Rev. A*, 86:032324, Sep 2012.

[50] D Ristè, M Dukalski, C A Watson, G de Lange, M J Tiggelman, Ya M Blanter, K W Lehnert, R N Schouten, and L DiCarlo. Deterministic entanglement of superconducting qubits by parity measurement and feedback. *Nature*, 502(7471):350–4, October 2013.

[51] Jerry M. Chow, Jay M. Gambetta, Easwar Magesan, David W. Abraham, Andrew W. Cross, B R Johnson, Nicholas A. Masluk, Colm A. Ryan, John A. Smolin, Srikanth J. Srinivasan, and M Steffen. Implementing a strand of a scalable fault-tolerant quantum computing fabric. *Nat Commun*, 5:4015, 06 2014.

[52] Robert H. Hadfield. Single-photon detectors for optical quantum information applications. *Nat Photon*, 3(12):696–705, 12 2009.

[53] B. Peropadre, G. Romero, G. Johansson, C. M. Wilson, E. Solano, and J. J. García-Ripoll. Approaching perfect microwave photodetection in circuit qed. *Phys. Rev. A*, 84:063834, Dec 2011.

[54] Y.-F. Chen, D. Hover, S. Sendelbach, L. Maurer, S. T. Merkel, E. J. Pritchett, F. K. Wilhelm, and R. McDermott. Microwave photon counter based on Josephson junctions. *Phys. Rev. Lett.*, 107:217401, 2011.

[55] Sankar R. Sathyamoorthy, L. Tornberg, Anton F. Kockum, Ben Q. Baragiola, Joshua Combes, C.M. Wilson, Thomas M. Stace, and G. Johansson. Quantum nondemolition detection of a propagating microwave photon. *Phys. Rev. Lett.*, 112:093601, Mar 2014.

[56] R. Hanbury Brown and R. Q. Twiss. Correlation between photons in two coherent beams of light. *Nature*, 177(4497):27–29, 01 1956.

[57] Guilhem Ribeill, Ivan Pechenezhski, Ted Thorbeck, Caleb Howington, Matthew Hutchings, Luke Govia, Frank Wilhelm, BLT Plourde, and Robert McDermott. Qubit readout with josephson photomultipliers. *Bulletin of the American Physical Society*, 60, 2015.

[58] A. Poudel, R. McDermott, and M. G. Vavilov. Quantum efficiency of a microwave photon detector based on a current-biased josephson junction. *Phys. Rev. B*, 86:174506, Nov 2012.

[59] Luke C. G. Govia, Emily J. Pritchett, Seth T. Merkel, Deanna Pineau, and Frank K. Wilhelm. Theory of josephson photomultipliers: Optimal working conditions and back action. *Phys. Rev. A*, 86:032311, Sep 2012.

[60] A. Wallraff, D.I. Schuster, A. Blais, L. Frunzio, R.S. Huang, J. Majer, S. Kumar, S.M. Girvin, and R.J. Schoelkopf. Strong coupling of a single photon to a superconducting qubit using circuit quantum electrodynamics. *Nature*, 431:162, 2004.

[61] A. Wallraff, D. I. Schuster, A. Blais, L. Frunzio, J. Majer, M. H. Devoret, S. M. Girvin, and R. J. Schoelkopf. Approaching unit visibility for control of a superconducting qubit with dispersive readout. *Phys. Rev. Lett.*, 95:060501, 2005.

[62] D. I. Schuster, A. Wallraff, A. Blais, L. Frunzio, R. S. Huang, J. Majer, S. M. Girvin, and R. J. Schoelkopf. ac Stark shift and dephasing of a superconducting qubit strongly coupled to a cavity field. *Phys. Rev. Lett.*, 94:123602, 2005.

[63] J. Majer, J.M. Chow, J.M. Gambetta, J. Koch, B.R. Johnson, J.A. Schreier, L. Frunzio, D.I. Schuster, A.A. Houck, A. Wallraff, A. Blais, M.H. Devoret, S.M. Girvin, and R.J. Schoelkopf. Coupling superconducting qubits via a cavity bus. *Nature*, 449:443–447, 2007.

[64] L. DiCarlo, J.M. Chow, J.M. Gambetta, L.S. Bishop, B.R. Johnson, D.I. Schuster, J. Majer, A. Blais, L. Frunzio, S.M. Girvin, and R.J.

Schoelkopf. Demonstration of two-qubit algorithms with a superconducting quantum processor. *Nature*, 460:240–244, 2009.

[65] L. DiCarlo, M.D. Reed, L. Sun, B.R. Johnson, J.M. Chow, J.M. Gambetta, L. Frunzio, S.M. Girvin, M.H. Devoret, and R. J. Schoelkopf. Preparation and measurement of three-qubit entanglement in a superconducting circuit. *Nature*, 467:574–578, 2010.

[66] J.M. Chow, J.M. Gambetta, A.D. Corcoles, S.T. Merkel, J.A. Smolin, C. Rigetti, S. Poletto, G.A. Keefe, M.B. Rothwell, J.R. Rozen, M.B. Ketchen, and M. Steffen. Universal quantum gate set approaching fault-tolerant thresholds with superconducting qubits. *Phys. Rev. Lett.*, 109:060501, 2012.

[67] M. Hofheinz, E. M. Weig, M. Ansmann, R. C. Bialczak, E. Lucero, M. Neeley, A. D. O'Connell, H. Wang, J. M. Martinis, and A. N. Cleland. Generation of Fock states in a superconducting quantum circuit. *Nature*, 454:310–314, 2008.

[68] Max Hofheinz, H. Wang, M. Ansmann, Radoslaw C. Bialczak, Erik Lucero, M. Neeley, A. D. O'Connell, D. Sank, J. Wenner, John M. Martinis, and A. N. Cleland. Synthesizing arbitrary quantum states in a superconducting resonator. *Nature*, 459(7246):546–549, 05 2009.

[69] Jay Gambetta, W A Braff, A Wallraff, S M Girvin, and R J Schoelkopf. Protocols for optimal readout of qubits using a continuous quantum nondemolition measurement. *Phys. Rev. A*, 76(1):012325, July 2007.

[70] R. Vijay, D. H. Slichter, and I. Siddiqi. Observation of Quantum Jumps in a Superconducting Artificial Atom. *Phys. Rev. Lett.*, 106(11):110502, March 2011.

[71] J. E. Johnson, C. Macklin, D. H. Slichter, R. Vijay, E. B. Weingarten, J. Clarke, and I. Siddiqi. Heralded state preparation in a superconducting qubit. *Phys. Rev. Lett.*, 109:050506, 2012.

[72] D. Ristè, J. G. van Leeuwen, H.-S. Ku, K. W. Lehnert, and L. DiCarlo. Initialization by measurement of a superconducting quantum bit circuit. *Phys. Rev. Lett.*, 109:050507, 2012.

[73] R. Vijay, C. Macklin, D.H. Slichter, S.J. Weber, K.W. Murch, R. Naik, A.N. Korotkov, and I. Siddiqi. Stabilizing Rabi oscillations in a superconducting qubit using quantum feedback. *Nature*, 490:77–80, 2012.

[74] L Steffen, Y Salathe, M Oppliger, P Kurpiers, M Baur, C Lang, C Eichler, G Puebla-Hellmann, A Fedorov, and A Wallraff. Deterministic quantum teleportation with feed-forward in a solid state system. *Nature*, 500(7462):319–22, August 2013.

[75] Evan Jeffrey, Daniel Sank, J. Y. Mutus, T. C. White, J. Kelly, R. Barends, Y. Chen, Z. Chen, B. Chiaro, A. Dunsworth, A. Megrant, P. J. J. O'Malley, C. Neill, P. Roushan, A. Vainsencher, J. Wenner, A. N. Cleland, and John M. Martinis. Fast accurate state measurement with superconducting qubits. *Phys. Rev. Lett.*, 112:190504, May 2014.

[76] S. Shankar, M. Hatridge, Z. Leghtas, K.M. Sliwa, A. Narla, U. Vool, S.M. Girvin, K. Frunzio, M. Mirrahimi, and M.H. Devoret. Autonomously stabilized entanglement between two superconducting quantum bits. *Nature*, 504:419, 2013.

[77] H.-A. Bachor and T.C. Ralph. *A Guide to Experiments in Quantum Optics*. Wiley-VCH, 2004.

[78] K.K. Likharev and V.K. Semenov. RSFQ logic/memory family: A new Josephson-junction technology for sub-terahertz-clock-frequency digital systems. *IEEE Trans. Appl. Supercond.*, 1:3, 1991.

[79] M. Tinkham. *Introduction to Superconductivity*. McGraw-Hill, New York, 1996.

[80] U. Weiss. *Quantum Dissipative Systems*. World Scientific Publishing Company, 4th edition, Mar 2012.

[81] Alexander N. Korotkov. Quantum efficiency of binary-outcome detectors of solid-state qubits. *Phys. Rev. B*, 78:174512, Nov 2008.

[82] G. Romero, J. J. García-Ripoll, and E. Solano. Microwave photon detector in circuit QED. *Phys. Rev. Lett.*, 102:173602, 2009.

[83] Christian Kraglund Andersen, Gregor Oelsner, Evgeni Il'ichev, and Klaus Mølmer. Quantized resonator field coupled to a current-biased josephson junction in circuit qed. *Phys. Rev. A*, 89:033853, Mar 2014.

[84] W. H. Zurek. Pointer basis of quantum apparatus: Into what mixture does the wave packet collapse? *Phys. Rev. D*, 24:1516–1525, Sep 1981.

[85] P. Bertet, A. Auffeves, P. Maioli, S. Osnaghi, T. Meunier, M. Brune, J. M. Raimond, and S. Haroche. Direct measurement of the wigner function of a one-photon fock state in a cavity. *Phys. Rev. Lett.*, 89:200402, Oct 2002.

[86] Sebastien Gleyzes, Stefan Kuhr, Christine Guerlin, Julien Bernu, Samuel Deleglise, Ulrich Busk Hoff, Michel Brune, Jean-Michel Raimond, and Serge Haroche. Quantum jumps of light recording the birth and death of a photon in a cavity. *Nature*, 446(7133):297–300, 03 2007.

[87] R. McDermott, R. W. Simmonds, M. Steffen, K. B. Cooper, K. Cicak, K. D. Osborn, S. Oh, D. P. Pappas, and J. M. Martinis. Simultaneous state measurement of coupled Josephson phase qubits. *Science*, 307:1299–1302, 2005.

[88] Luke C G Govia, Emily J Pritchett, and Frank K Wilhelm. Generating nonclassical states from classical radiation by subtraction measurements. *New Journal of Physics*, 16(4):045011, 2014.

[89] Eyob A. Sete, Jay M. Gambetta, and Alexander N. Korotkov. Purcell effect with microwave drive: Suppression of qubit relaxation rate. *Phys. Rev. B*, 89:104516, Mar 2014.

[90] Alberto Peruzzo, Jarrod McClean, Peter Shadbolt, Man-Hong Yung, Xiao-Qi Zhou, Peter J. Love, Alán Aspuru-Guzik, and Jeremy L. O'Brien. A variational eigenvalue solver on a photonic quantum processor. *Nat Commun*, 5:4213, 07 2014.

[91] Daniel Gottesman and Isaac L. Chuang. Demonstrating the viability of universal quantum computation using teleportation and single-qubit operations. *Nature*, 402(6760):390–393, 11 1999.

[92] C. W. J. Beenakker, D. P. DiVincenzo, C. Emary, and M. Kindermann. Charge detection enables free-electron quantum computation. *Phys. Rev. Lett.*, 93:020501, Jul 2004.

[93] Chantal L. Hutchison, J. M. Gambetta, Alexandre Blais, and F. K. Wilhelm. Quantum trajectory equation for multiple qubits in circuit qed: Generating entanglement by measurement. *Canadian Journal of Physics*, 87(3):225–231, 2009.

[94] Rusko Ruskov and Alexander N. Korotkov. Entanglement of solid-state qubits by measurement. *Phys. Rev. B*, 67:241305, Jun 2003.

[95] Simon E. Nigg and S. M. Girvin. Stabilizer quantum error correction toolbox for superconducting qubits. *Phys. Rev. Lett.*, 110:243604, Jun 2013.

[96] Brian Vlastakis, Gerhard Kirchmair, Zaki Leghtas, Simon E Nigg, Luigi Frunzio, S M Girvin, Mazyar Mirrahimi, M H Devoret, and R J Schoelkopf. Deterministically encoding quantum information using 100-photon Schrödinger cat states. *Science*, 342(6158):607–10, November 2013.

[97] David P DiVincenzo and Firat Solgun. Multi-qubit parity measurement in circuit quantum electrodynamics. *New Journal of Physics*, 15(7):075001, July 2013.

[98] L. Tornberg, Sh. Barzanjeh, and David P. DiVincenzo. Stochastic-master-equation analysis of optimized three-qubit nondemolition parity measurements. *Phys. Rev. A*, 89:032314, Mar 2014.

[99] F. Mallet, F.R. Ong a.d A. Palacios-Laloy, F. Nguyen, P. Bertet, D. Vion, and D. Esteve. Single-shot qubit readout in circuit quantum electrodynamics. *Nat. Phys.*, 5:791, 2009.

[100] Y. Kubo, F. R. Ong, P. Bertet, D. Vion, V. Jacques, D. Zheng, A. Dréau, J.-F. Roch, A. Auffeves, F. Jelezko, J. Wrachtrup, M. F. Barthe, P. Bergonzo, and D. Esteve. Strong coupling of a spin ensemble to a superconducting resonator. *Phys. Rev. Lett.*, 105:140502, Sep 2010.

[101] J. D. Pritchard, J. A. Isaacs, M. A. Beck, R. McDermott, and M. Saffman. Hybrid atom-photon quantum gate in a superconducting microwave resonator. *Phys. Rev. A*, 89:010301, Jan 2014.

[102] S. D. Hogan, J. A. Agner, F. Merkt, T. Thiele, S. Filipp, and A. Wallraff. Driving rydberg-rydberg transitions from a coplanar microwave waveguide. *Phys. Rev. Lett.*, 108:063004, Feb 2012.

[103] T. Frey, P. J. Leek, M. Beck, A. Blais, T. Ihn, K. Ensslin, and A. Wallraff. Dipole coupling of a double quantum dot to a microwave resonator. *Phys. Rev. Lett.*, 108:046807, Jan 2012.

[104] R Miller, T E Northup, K M Birnbaum, A Boca, A D Boozer, and H J Kimble. Trapped atoms in cavity QED: coupling quantized light and matter. *Journal of Physics B: Atomic, Molecular and Optical Physics*, 38(9):S551–S565, May 2005.

[105] Javier Miguel-Sánchez, Andreas Reinhard, Emre Togan, Thomas Volz, Atac Imamoglu, Benjamin Besga, Jakob Reichel, and Jérôme Estève. Cavity quantum electrodynamics with charge-controlled quantum dots coupled to a fiber Fabry–Perot cavity. *New Journal of Physics*, 15(4):045002, April 2013.

[106] J. Kelly, R. Barends, A. G. Fowler, A. Megrant, E. Jeffrey, T. C. White, D. Sank, J. Y. Mutus, B. Campbell, Yu Chen, Z. Chen, B. Chiaro, A. Dunsworth, I. C. Hoi, C. Neill, P. J. J. O/'Malley, C. Quintana, P. Roushan, A. Vainsencher, J. Wenner, A. N. Cleland, and John M. Martinis. State preservation by repetitive error detection in a superconducting quantum circuit. *Nature*, 519(7541):66–69, 03 2015.

[107] M. Dakna, T. Anhut, T. Opatrný, L. Knöll, and D.-G. Welsch. Generating schrödinger-cat-like states by means of conditional measurements on a beam splitter. *Phys. Rev. A*, 55:3184–3194, Apr 1997.

[108] Daniel K. L. Oi, Václav Potoček, and John Jeffers. Nondemolition measurement of the vacuum state or its complement. *Phys. Rev. Lett.*, 110:210504, May 2013.

[109] Fabien Boitier, Jean-Baptiste Dherbecourt, Antoine Godard, and Emmanuel Rosencher. Infrared quantum counting by nondegenerate two photon conductivity in gaas. *Applied Physics Letters*, 94(8):–, 2009.

[110] Wilhelm Magnus. On the exponential solution of differential equations for a linear operator. *Communications on Pure and Applied Mathematics*, 7(4):649–673, 1954.

[111] I. Serban, B. L. T. Plourde, and F. K. Wilhelm. Quantum nondemolition-like fast measurement scheme for a superconducting qubit. *Phys. Rev. B*, 78:054507, Aug 2008.

[112] D. Meschede, H. Walther, and G. Müller. One-atom maser. *Phys. Rev. Lett.*, 54:551–554, Feb 1985.

[113] Gerhard Kirchmair, Brian Vlastakis, Zaki Leghtas, Simon E. Nigg, Hanhee Paik, Eran Ginossar, Mazyar Mirrahimi, Luigi Frunzio, S. M. Girvin, and R. J. Schoelkopf. Observation of quantum state collapse and revival due to the single-photon kerr effect. *Nature*, 495(7440):205–209, 03 2013.

[114] Eyob A. Sete, Andrei Galiautdinov, Eric Mlinar, John M. Martinis, and Alexander N. Korotkov. Catch-disperse-release readout for superconducting qubits. *Phys. Rev. Lett.*, 110:210501, May 2013.

[115] V. Peano and M. Thorwart. Dynamical bistability in the driven circuit qed. *EPL (Europhysics Letters)*, 89(1):17008, 2010.

[116] V. Peano and M. Thorwart. Quasienergy description of the driven jaynes-cummings model. *Phys. Rev. B*, 82:155129, Oct 2010.

[117] Andrei Galiautdinov, Alexander N. Korotkov, and John M. Martinis. Resonator–zero-qubit architecture for superconducting qubits. *Phys. Rev. A*, 85:042321, Apr 2012.

[118] Zaki Leghtas, Gerhard Kirchmair, Brian Vlastakis, Robert J. Schoelkopf, Michel H. Devoret, and Mazyar Mirrahimi. Hardware-efficient autonomous quantum memory protection. *Phys. Rev. Lett.*, 111:120501, Sep 2013.

[119] F. Grossmann, T. Dittrich, P. Jung, and P. Hänggi. Coherent destruction of tunneling. *Phys. Rev. Lett.*, 67:516–519, Jul 1991.

[120] D. I. Schuster, A. A. Houck, J. A. Schreier, A. Wallraff, J. M. Gambetta, A. Blais, L. Frunzio, J. Majer, B. Johnson, M. H. Devoret, S. M. Girvin, and R. J. Schoelkopf. Resolving photon number states in a superconducting circuit. *Nature*, 445(7127):515–518, 02 2007.

[121] L. C. G. Govia, E. J. Pritchett, B. L. T. Plourde, M. G. Vavilov, R. McDermott, and F. K. Wilhelm. Scalable two- and four-qubit parity measurement with a threshold photon counter. February 2015.

[122] Maxime Boissonneault, J. M. Gambetta, and Alexandre Blais. Dispersive regime of circuit qed: Photon-dependent qubit dephasing and relaxation rates. *Phys. Rev. A*, 79:013819, Jan 2009.

[123] I. Siddiqi, R. Vijay, F. Pierre, C. M. Wilson, M. Metcalfe, C. Rigetti, L. Frunzio, and M. H. Devoret. Rf-driven josephson bifurcation amplifier for quantum measurement. *Phys. Rev. Lett.*, 93:207002, Nov 2004.

[124] M. A. Castellanos-Beltran and K. W. Lehnert. Widely tunable parametric amplifier based on a superconducting quantum interference device array resonator. *Appl. Phys. Lett.*, 91:083509, 2007.

[125] N. Bergeal, F. Schackert, M. Metcalfe, R. Vijay, V. E. Manucharyan, L. Frunzio, D. E. Prober, R. J. Schoelkopf, S. M. Girvin, and M. H. Devoret. Phase-preserving amplification near the quantum limit with a josephson ring modulator. *Nature*, 465(7294):64–68, 05 2010.

[126] J. Y. Mutus, T. C. White, R. Barends, Yu Chen, Z. Chen, B. Chiaro, A. Dunsworth, E. Jeffrey, J. Kelly, A. Megrant, C. Neill, P. J. J. O'Malley, P. Roushan, D. Sank, A. Vainsencher, J. Wenner, K. M. Sundqvist, A. N. Cleland, and John M. Martinis. Strong environmental coupling in a josephson parametric amplifier. *Applied Physics Letters*, 104(26):–, 2014.

[127] Kevin O'Brien, Chris Macklin, Irfan Siddiqi, and Xiang Zhang. Resonant phase matching of josephson junction traveling wave parametric amplifiers. *Phys. Rev. Lett.*, 113:157001, Oct 2014.

[128] T. C. White, J. Y. Mutus, I. C. Hoi, R. Barends, B. Campbell, Yu Chen, Z. Chen, B. Chiaro, A. Dunsworth, E. Jeffrey, J. Kelly, A. Megrant, C. Neill, P. J. J. O'Malley, P. Roushan, D. Sank, A. Vainsencher, J. Wenner, S. Chaudhuri, J. Gao, and John M. Martinis. Traveling wave parametric amplifier with Josephson junctions using minimal resonator phase matching. arXiv:1503.04364, 2015.

[129] Luke C G Govia and Frank K Wilhelm. Entanglement generated by the dispersive interaction: The dressed coherent state. In preparation.

[130] M.D. Reed, B.R. Johnson, A.A. Houck, L. DiCarlo, J.M. Chow, D.I. Schuster, L. Frunzio, and R.J. Schoelkopf. Fast reset and suppressing spontaneous emission of a superconducting qubit. *Appl. Phys. Lett.*, 96:203110, 2010.

[131] J. Wenner, Yi Yin, Yu Chen, R. Barends, B. Chiaro, E. Jeffrey, J. Kelly, A. Megrant, J. Y. Mutus, C. Neill, P. J. J. O'Malley, P. Roushan, D. Sank, A. Vainsencher, T. C. White, Alexander N. Korotkov, A. N. Cleland, and John M. Martinis. Catching time-reversed microwave coherent state photons with 99.4absorption efficiency. *Phys. Rev. Lett.*, 112:210501, May 2014.

[132] Yu Chen, C. Neill, P. Roushan, N. Leung, M. Fang, R. Barends, J. Kelly, B. Campbell, Z. Chen, B. Chiaro, A. Dunsworth, E. Jeffrey, A. Megrant, J. Y. Mutus, P. J. J. O'Malley, C. M. Quintana, D. Sank, A. Vainsencher, J. Wenner, T. C. White, Michael R. Geller, A. N. Cleland, and John M. Martinis. Qubit architecture with high coherence and fast tunable coupling. *Phys. Rev. Lett.*, 113:220502, Nov 2014.

[133] S. Zeytinoglu, M. Pechal, S. Berger, A. A. Abdumalikov Jr., A. Wallraff, and S. Filipp. Microwave-induced amplitude and phase tunable qubit-resonator coupling in circuit quantum electrodynamics. arXiv:1502.03692, February 2015.

[134] K. Geerlings, Z. Leghtas, I. M. Pop, S. Shankar, L. Frunzio, R. J. Schoelkopf, M. Mirrahimi, and M. H. Devoret. Demonstrating a driven reset protocol for a superconducting qubit. *Phys. Rev. Lett.*, 110:120501, Mar 2013.

[135] E. Knill, R. Laflamme, and G.J. Milburn. A scheme for efficient quantum computing with linear optics. *Nature*, 409:46, 2001.

[136] S.L. Braunstein and P. van Loock. Quantum information with continuous variables. *Rev. Mod. Phys.*, 77:513, 2005.

[137] N. Gisin, R. Ribordy, W. Tittel, and H. Zbinden. Quantum cryptography. *Rev. Mod. Phys.*, 74:145, 2002.

[138] A. I. Lvovsky and M. G. Raymer. Continuous-variable optical quantum-state tomography. *Rev. Mod. Phys.*, 81:299–332, Mar 2009.

[139] Alexei Ourjoumtsev, Rosa Tualle-Brouri, Julien Laurat, and Philippe Grangier. Generating optical schrödinger kittens for quantum information processing. *Science*, 312(5770):83–86, 2006.

[140] Zheng Shi-Biao. Preparation of multicomponent schrödinger cat states through resonant atom-field interaction. *Communications in Theoretical Physics*, 43(6):1105, 2005.

[141] Jaromír Fiurášek, Raúl García-Patrón, and Nicolas J. Cerf. Conditional generation of arbitrary single-mode quantum states of light by repeated photon subtractions. *Phys. Rev. A*, 72:033822, Sep 2005.

[142] M. K. Akhlaghi, A. H. Majedi, and J. S. Lundeen. Nonlinearity in single photon detection: Modeling and quantum tomography. *Optics Express*, 19(22):21305–21312, 2011.

[143] J. M. Raimond, C. Sayrin, S. Gleyzes, I. Dotsenko, M. Brune, S. Haroche, P. Facchi, and S. Pascazio. Phase space tweezers for tailoring cavity fields by quantum zeno dynamics. *Phys. Rev. Lett.*, 105:213601, Nov 2010.

[144] M. A. Castellanos-Beltran, K. D. Irwin, G. C. Hilton, L. R. Vale, and K. W. Lehnert. Amplification and squeezing of quantum noise with a tunable josephson metamaterial. *Nat Phys*, 4(12):929–931, 12 2008.

[145] C. Eichler, D. Bozyigit, C. Lang, M. Baur, L. Steffen, J. M. Fink, S. Filipp, and A. Wallraff. Observation of two-mode squeezing in the microwave frequency domain. *Phys. Rev. Lett.*, 107:113601, Sep 2011.

[146] C. M. Wilson, G. Johannsson, A. Pourkabirian, J.R. Johannson, T. Duty, F. Nori, and P. Delsing. Observation of the dynamical casimir effect in a superconducting circuit. *Nature*, 479:376, 2011.

[147] Samuel Deleglise, Igor Dotsenko, Clement Sayrin, Julien Bernu, Michel Brune, Jean-Michel Raimond, and Serge Haroche. Reconstruction of non-classical cavity field states with snapshots of their decoherence. *Nature*, 455(7212):510–514, 09 2008.

[148] Samuel L. Braunstein and Robert I. McLachlan. Generalized squeezing. *Phys. Rev. A*, 35:1659–1667, Feb 1987.

[149] Samuel L. Braunstein and Carlton M. Caves. Phase and homodyne statistics of generalized squeezed states. *Phys. Rev. A*, 42:4115–4119, Oct 1990.

[150] George B. Arfken, Hans J. Weber, and Frank E. Harris. *Mathematical Methods for Physicists: A Comprehensive Guide*. Academic Press, 7 edition, January 2012.

[151] János K. Asbóth, John Calsamiglia, and Helmut Ritsch. Computable measure of nonclassicality for light. *Phys. Rev. Lett.*, 94:173602, May 2005.

[152] W. H. Zurek. Sub-planck structure in phase space and its relevance for quantum decoherence. *Nature*, 412(6848):712–717, August 2001.

[153] A. Megrant, C. Neill, R. Barends, B. Chiaro, Yu Chen, L. Feigl, J. Kelly, Erik Lucero, Matteo Mariantoni, P. J. J. O'Malley, D. Sank, A. Vainsencher, J. Wenner, T. C. White, Y. Yin, J. Zhao, C. J. Palmstrøm, John M. Martinis, and A. N. Cleland. Planar superconducting resonators with internal quality factors above one million. *Applied Physics Letters*, 100(11):113510, 2012.

[154] R. McDermott, 2012. private communication.

[155] Seth Lloyd and Samuel L. Braunstein. Quantum computation over continuous variables. *Phys. Rev. Lett.*, 82:1784–1787, Feb 1999.

[156] Stephen D. Bartlett and Barry C. Sanders. Universal continuous-variable quantum computation: Requirement of optical nonlinearity for photon counting. *Phys. Rev. A*, 65:042304, Mar 2002.

[157] G. J. Milburn and D. F. Walls. Quantum nondemolition measurements via quadratic coupling. *Phys. Rev. A*, 28:2065–2070, Oct 1983.

[158] Jaewoo Joo, William J. Munro, and Timothy P. Spiller. Quantum metrology with entangled coherent states. *Phys. Rev. Lett.*, 107:083601, Aug 2011.

[159] G. Vidal and R. F. Werner. Computable measure of entanglement. *Phys. Rev. A*, 65:032314, Feb 2002.

[160] J. R. Dormand and P. J. Prince. A family of embedded Runge-Kutta formulae. *Journal of Computational and Applied Mathematics*, 6:19–26, 1980.